Advancing Chemiresistive and Field-Effect Based Electronic Noses via Nanomaterial Synthesis, Digital Printing, and Machine Learning

Zur Erlangung des akademischen Grades eines

DOKTORS DER INGENIEURWISSENSCHAFTEN (Dr.-Ing.)

von der KIT-Fakultät für Elektrotechnik und Informationstechnik des Karlsruher Instituts für Technologie (KIT)

angenommene

DISSERTATION

von

M.Sc. Hankun Yang

geboren in Beijing, V.R. China

Tag der mündlichen Prüfung: 21. April 2026
Hauptreferent: Prof. Dr. Uli Lemmer
Korreferent: Prof. Dr. Manfred Kohl

Abstract

Odor recognition plays a crucial role across diverse sectors, including environmental monitoring, food quality control, and health diagnostics. Conventional analytical instruments, such as gas chromatography or mass spectrometry, remain limited by high cost, complexity, and lack of portability, which have fueled the development of electronic nose (eNose) technology. An eNose is an artificial olfactory system designed to mimic the pattern-recognition capabilities of the biological olfactory system using sensor arrays and machine-learning algorithms. However, to achieve reliable, fast, and energy-efficient odor detection under real-world conditions, for example, variable humidity, significant challenges remain regarding sensitivity, selectivity, and interference. Furthermore, higher sensor performance, such as more precise classification of different gases and odors, combined with higher sensitivities, is always in demand. Additionally, for rapidly developing systems, conventional CMOS-based approaches offer limited flexibility, leading to long, costly invoicing cycles. Motivated by these demands and inspired by the biological olfactory system, this dissertation advances the state of the art in chemiresistive and chemically-sensitive field-effect transistor (ChemFET)-based eNose technologies. This is accomplished by converging developments in nanomaterial synthesis, sensor technology, and machine learning. Additionally, digital printing is used in parts for a fast, flexible fabrication route.

To maintain stable and reliable eNose operation, accurate and independent monitoring of relative humidity (RH), one of the most interfering environmental variables, is essential. Additionally, in a broader context, relative humidity is not only required for a comfortable environment but also critical in various industrial processes. Therefore, in the first part of the thesis, a vanadium pentoxide (V_2O_5) nanofiber (NF)-based relative humidity sensor was developed.

The V_2O_5 NFs are synthesized by precursor-based electrospinning (ES) followed by thermal annealing. Subsequently, their chemical composition, microstructure, and NF morphology are systematically analyzed across a range of annealing temperatures. At an optimal temperature of 500 °C, the resulting chemiresistive sensor can be operated at room temperature and exhibits a linear humidity response over 10 RH% to 90 RH%, with a high relative sensitivity (1.427). Furthermore, the V_2O_5 NF sensor demonstrates pronounced selectivity toward water vapor with negligible cross-sensitivity to several target gases, underscoring its suitability for integration into humidity-compensated gas and eNose platforms.

Building on metal oxide (MOX)-based 1D nanomaterials, a chemiresistive eNose is developed in a subsequent step. For this, vapor-liquid-solid grown tin dioxide (SnO_2) nanowires (NWs), optimally with sub-200 nm diameter, form subsensors of the eNose. The resulting sensor array exhibits strong analyte sensitivity, particularly for isopropyl alcohol (IPA), and accurate gas classification using linear

discriminant analysis (LDA). Its applicability is further demonstrated for indoor mold detection, targeting the harmful mold species *Stachybotrys chartarum* (*S. chartarum*) and *Chaetomium globosum* (*C. globosum*) cultivated on distinct culture media. Through systematic data partitioning and ensemble building, the eNose achieves a top F1-score of 0.986. These findings support the use of the eNose for rapid and reliable detection and identification of mold across diverse environments.

Finally, the dissertation advances toward a ChemFET-based eNose, combining inkjet printing (IJP) and aerosol jet printing (AJP) to exploit their complementary strengths in depositing nanometer-thick In_2O_3 thin films (TFs) and micrometer-thick Ag electrodes. The ChemFET exhibits an exceptionally high relative response of approximately 200.0 to IPA and benzene compared to the baseline signal at reference conditions. A single room temperature (RT)-operated ChemFET sensor without UV activation or heating generates sufficient signal features via voltage modulation, enabling gas classification. Random Forest (RF) outperforms the conventional LDA in regards to classification accuracy. Moreover, to the authors' knowledge, this is the first time that a correlation between the gate-source voltage and the feature importance has been established. A comprehensive comparison between the SnO_2 NW chemiresistor and the In_2O_3 TF ChemFET highlights the design trade-offs between sensitivity, selectivity, and classification performance.

Kurzfassung

Die Geruchserkennung spielt eine entscheidende Rolle in zahlreichen Bereichen, darunter Umweltüberwachung, Lebensmittelqualitätskontrolle und Gesundheitsdiagnostik. Konventionelle analytische Instrumente wie Gaschromatographie-Massenspektrometrie sind aufgrund hoher Kosten, Komplexität und mangelnder Portabilität eingeschränkt, was die Entwicklung der elektronischen Nase-Technologie vorangetrieben hat. Elektronische Nasen (eNasen) sind künstliche olfaktorische Systeme, welche die Mustererkennungsfähigkeiten des biologischen Geruchssinns mithilfe von Sensorarrays und maschinellen Lernalgorithmen nachahmen. Um jedoch eine zuverlässige, schnelle und energieeffiziente Geruchserkennung unter realen Bedingungen, wie beispielsweise bei variabler Luftfeuchtigkeit, zu erreichen, bestehen weiterhin große Herausforderungen hinsichtlich Empfindlichkeit, Selektivität und Interferenzen. Darüber hinaus wird stets eine höhere Sensorleistung gefordert, etwa durch genauere Klassifizierung verschiedener Gase und Gerüche bei gleichzeitig höherer Empfindlichkeit. Für insbesondere schnell entwickelnde Systeme bieten herkömmliche CMOS-basierte Ansätze zudem nur begrenzte Flexibilität, was zu langen und kostspieligen Entwicklungszyklen führt. Motiviert durch diese Anforderungen und inspiriert vom biologischen Geruchssystem, leistet diese Dissertation einen Beitrag zum Stand der Technik in der chemiresistiven und CHEMFET-basierten eNase-Technologie. Dies wird durch die Zusammenführung von Fortschritten in der Nanomaterialsynthese, der Sensortechnologie und dem maschinellen Lernen erreicht. Zusätzlich wird der digitale Druck teilweise eingesetzt, um eine schnelle und flexible Herstellungsroute zu ermöglichen.

Für den stabilen und zuverlässigen Betrieb einer eNase ist eine präzise und unabhängige Überwachung der relativen Luftfeuchtigkeit, einer der störanfälligsten Umweltgrößen, unerlässlich. Darüber hinaus ist die relative Luftfeuchtigkeit nicht nur für ein angenehmes Raumklima erforderlich, sondern auch für zahlreiche industrielle Prozesse von entscheidender Bedeutung. Daher wurde im ersten Teil der Arbeit ein Vanadiumpentoxid-(V_2O_5)-Nanofaser-basierter Feuchtigkeitssensor entwickelt. Die V_2O_5-Nanofasern werden mittels einer präkursorbasierten Elektrospinnen-Methode synthetisiert und anschließend getempert. Ihre chemische Zusammensetzung, Mikrostruktur und Morphologie werden systematisch bei unterschiedlichen Temperaturbereichen untersucht. Bei einer optimalen Temperatur von 500 °C kann der resultierende chemiresistive Sensor bei Raumtemperatur betrieben werden und zeigt eine hochlineare Signalantwort im Bereich von 10 RH% bis 90 RH% mit einer hohen relativen Empfindlichkeit (1,427). Darüber hinaus weist der Sensor eine ausgeprägte Selektivität gegenüber Wasserdampf auf, mit vernachlässigbarer Kreuzempfindlichkeit gegenüber mehreren Zielgasen, was seine Eignung für die Integration in feuchtigkeitskompensierte Gas- und eNase-Plattformen unterstreicht.

Aufbauend auf oxidbasierten eindimensionalen Nanomaterialien wird im nächsten Schritt eine chemiresistive eNase entwickelt. Hierbei bilden im Dampf-Flüssig-Fest-Verfahren gezüchtete Zinnoxid-(SnO_2)-Nanodrähte mit einem Durchmesser unter 200 nm die einzelnen Subsensoren der eNase. Das

resultierende Sensorarray zeigt eine hohe Analytempfindlichkeit, insbesondere für Isopropanol, sowie eine präzise Gasklassifizierung mittels linearen Diskriminanzanalysen. Seine Anwendbarkeit wird zudem für die Erkennung von Schimmel in Innenräumen demonstriert, wobei die schädlichen Schimmelarten Stachybotrys und Chaetomium auf unterschiedlichen Nähruntergründen eindeutig nachgewiesen und zugleich unterschieden werden können. Durch systematische Datenpartitionierung und Ensemblebildung erreicht die eNase ein maximales F1-Maß von 0,986. Diese Ergebnisse belegen die Eignung der eNase für eine schnelle und zuverlässige Erkennung und Identifikation von Schimmel in den verschiedensten Umgebungen.

Abschließend wird in dieser Arbeit eine chemisch sensitiver Feldeffekttransistor (ChemFET)-basierte eNase entwickelt, bei der Tintenstrahl- und Aerosolstrahldruck kombiniert werden, um deren komplementäre Vorteile beim Aufbringen von nanometerdünnen In_2O_3-Filmen und mikrometerdicken Ag-Elektroden zu nutzen. Der ChemFET zeigt eine außergewöhnlich hohe relative Signalantwort von etwa 200,0 gegenüber Isopropanol und Benzol im Vergleich zum Basissignal unter Referenzbedingungen. Ein einzelner bei Raumtemperatur betriebener ChemFET-Sensor ohne UV-Aktivierung oder Beheizung erzeugt durch Spannungsmodulation ausreichend viele Signalmerkmale, um eine Gasklassifizierung zu ermöglichen. Das Random-Forest-Verfahren übertrifft die konventionelle lineare Diskriminanzanalyse hinsichtlich der Klassifikationsgenauigkeit. Zudem konnte erstmals eine Korrelation zwischen der Gate-Source-Spannung und der Merkmalswichtigkeit nachgewiesen werden.

Ein umfassender Vergleich zwischen dem SnO_2-Nanodraht-Chemiresistor und dem In_2O_3-Dünnschicht-ChemFET verdeutlicht die Designkompromisse zwischen Empfindlichkeit, Selektivität und Klassifikationsleistung.

Table of Contents

Abbreviations and Nomenclature

Abbreviations

3DMM2O 3D Matter Made to Order

AJ aerosol jet
  AJP aerosol jet printing
ANN artificial neural network
avg. average

BET Brunauer-Emmett-Teller
BJT bipolar junction transistor

C. globosum *Chaetomium globosum*
CAD computer-aided design
CC BY 4.0 Creative Commons Attribution 4.0 International License
CI confidence interval
CM confusion matrix
CMOS complementary metal-oxide-semiconductor
CNN convolutional neural network
CNT carbon nanotube
CSP chemiresistive sensor platform
CV cross-validation
  LOOCV leave-one-out cross-validation
  LpOCV leave-p-out cross-validation

DB decision boundary
DMC Dimatix Materials Cartridge
DMF dimethylformamide
DoD drop-on-demand
DT decision tree
DXF Drawing Exchange Format

E-field electric field
EDS energy-dispersive X-ray spectroscopy
Electron Microscopy
  SEM scanning electron microscopy

FE-SEM field-emission scanning electron microscopy
TEM transmission electron microscopy
ELM extreme learning machine
eNose electronic nose
ES electrospinning

FET field-effect transistor
ChemFET chemically-sensitive field-effect transistor
IGFET insulated-gate field-effect transistor
JFET junction field-effect transistor
MOSFET metal-oxide-semiconductor field-effect transistor
FIB focused ion beam
FKM fluorocarbon-based fluoroelastomer materials

GCMS gas chromatography mass spectrometry
GMS gas mixing system

humidity
AH absolute humidity
RH relative humidity
SH saturation humidity

IDE interdigitated electrodes
IHE Institute of Radio Frequency Engineering and Electronics
IJ inkjet
CIJ continuous inkjet
IJP inkjet printing
PIJ piezoelectric inkjet
TIJ thermal inkjet
IMT Institute of Microstructure Technology
INT Institute of Nanotechnology
IoT internet-of-thing
IPA isopropyl alcohol
IQR interquartile range
ITO indium tin oxide
IUPAC International Union of Pure and Applied Chemistry

KAMINA Karlsruher Mikronase
KamObs Kamina Observer
KIT Karlsruhe Institute of Technology

LDA linear discriminant analysis
LED light-emitting diode
LHS left-hand side
LoD limit of detection

LSTM long short-term memory
LTI Light Technology Institute

MEMS micro-electromechanical systems
MFC mass flow controller
MLP multilayer perceptron
MOX metal oxide
  TMOX transition metal oxide

NF nanofiber
NHC negative humidity coefficient
NP nanoparticle
NR nanorod
NS nanosheet
NT nanotube
NW nanowire

OR olfactory receptor
OSN olfactory sensory neurons

PA pneumatic atomizer
PAN polyacrylonitrile
PC personal computer
PCA principal component analysis
PCB printed circuit board
PDMS polydimethylsiloxane
PHC positive humidity coefficient
PID proportional-integral-derivative control mechanism
PNG Portable Network Graphics
PTFE polytetrafluoroethylene
PVT physical vapor transport

QF quality factor

RF Random Forest
RHS right-hand side
RR relative response
RT room temperature

S. chartarum *Stachybotrys chartarum*
SAD selected area diffraction
SD standard deviation
SI International System of Units
SLS solution-liquid-solid
SMR softmax regression

SQ separation quotient
SVM support vector machine

TF thin film
TFT thin-film transistor

UA ultrasonic atomizer
USB Universal Serial Bus
UV ultraviolet

VLS vapor-liquid-solid
VOC volatile organic compound
  MVOC microbial volatile organic compound

XPS X-ray photoelectron spectroscopy
XRD X-ray diffraction

ZIM Zentrale Innovationsprogramm Mittelstand

Nomenclature

Due to the large number of nomenclatures and the unavoidable overlap in character usage across domains, the nomenclatures are categorized into physical (variables, constants, and subscripts) and data analysis-related (variables, subscripts, and operators). Physical quantities are given by:

Symbol | base or derived SI unit | description.

Alternative units used in this work, which are not directly apparent from the SI units, are separately provided in square brackets, including the conversion factor.

Data analysis variables are given by:

Symbol | membership declaration | description | definition or range (optional).

Physical
  A (m^2) area
  C (F) electrical capacitance
  c (1) mole fraction concentration [$1\,\mathrm{ppm} = 10^{-6}$]
  D (m) diameter
  d (m) distance/spacing/thickness
  DPI (1) dots per inch
  E ($\mathrm{V\,m^{-1}}$) electric field strength
  e ($1.602\,176\,634 \times 10^{-19}$ C) elemental charge
  g_t ($\mathrm{A\,V^{-1}}$) transconductance (FET)

H Humidity
  H_{abs} ($\mathrm{kg\,m^{-3}}$) absolute humidity
  H_{rel} (%) relative humidity [RH%]
  H_{sat} ($\mathrm{kg\,m^{-3}}$) saturation humidity
h (m) height
I (A) electrical current
l (m) length
m (kg) mass
M_{W} ($\mathrm{kg\,mol^{-1}}$) molecular weight
P (W) power
p (Pa) pressure [$1\,\mathrm{bar} = 1 \times 10^5\,\mathrm{Pa}$]
Q ($\mathrm{m^3\,s^{-1}}$) volumetric flow rate [$1\,\mathrm{sccm} = 1 \times 10^{-6}\,\mathrm{m^3\,s^{-1}}$]
R (Ω) resistance
r (m) radius
Re (1) Reynolds number
T (°C) temperature
t (s) time
U (V) voltage
V ($\mathrm{m^3}$) volume
v ($\mathrm{m\,s^{-1}}$) velocity
w (m) width
We (1) Weber number
γ ($\mathrm{J\,m^{-2}}$) surface tension
ε_0 ($8.854\,187\,818\,8 \times 10^{-12}\,\mathrm{F\,m^{-1}}$) electric constant or vacuum permittivity
ε_r (1) relative permittivity
η (Pa s) dynamic viscosity
λ (m) wave length
μ ($\mathrm{m^2\,V^{-1}\,s^{-1}}$) charge carrier mobility
ρ ($\mathrm{kg\,m^{-3}}$) density
σ ($\mathrm{S\,m^{-1}}$) electrical conductivity
τ (s) time constant

Subscripts

0 base(line) or reference
abs absolute
anl annealing
atm atomizer (AJP)
ch channel (FET)
crit critical
DS drain-source (FET)
GS gate-source (FET)
m mass-specific
min minimum / minimal

plate plate
recov recovery
rel relative
resp response
sat saturation
sht sheath (AJP)
th threshold
tot total

Machine Learning and Statistical Notation

C ($\mathbb{N}$) number of classes = $|\mathbb{G}|$
$\mathbb{F}$ ($|\mathbb{F}| = N$) set of features
F1 ($\mathbb{R}$) F1-score $\in [0, 1]$
FI ($\mathbb{R}$) feature importance $\in [0, 1]$
$\mathbb{G}$ set of classes
$\mathbb{I}$ observation index set
M ($\mathbb{N}$) number of observation samples $|\mathbb{I}|$
N ($\mathbb{N}$) number of features
N' ($\mathbb{N}$) number of used discriminants (LDA)
PRC ($\mathbb{R}$) precision $\in [0, 1]$
REC ($\mathbb{R}$) recall $\in [0, 1]$
$\boldsymbol{S}$ ($\mathbb{R}^{(N,N)}$) scatter matrix (LDA)
  $\boldsymbol{S}_\mathrm{B}$ between-class scatter matrix
  $\boldsymbol{S}_\mathrm{T}$ total scatter matrix
  $\boldsymbol{S}_\mathrm{W}$ within-class scatter matrix
$\boldsymbol{X}$ ($\mathbb{R}^{M \times N}$) feature matrix
$\boldsymbol{x}$ ($\mathbb{R}^N$) observation vector
$\boldsymbol{y}$ ($\mathbb{G}^M$) label array
z ($\mathbb{R}$) z-score $\in [0, 1]$
$\boldsymbol{\mu}$ ($\mathbb{R}^N$) total observation mean

Data analysis subscripts

c class specific
med median
pred predicted (label)
test test
train training
true true (label)

Operators

$|\cdot|$ cardinality (number of elements of a set), e.g. $|\{A, B, C\}| = 3$
$\mathcal{E}(\cdot)$ expected value
$\mathcal{I}(\cdot)$ Iverson bracket $\mathcal{I}(P) = \begin{cases} 1 & \text{if } P \text{ is true} \\ 0 & \text{otherwise} \end{cases}$

$\text{med}(\cdot)$ median

1. Introduction

> *Did you ever try to measure a smell? Can you tell whether one smell is just twice as strong as another. Can you measure the difference between one kind of smell and another. It is very obvious that we have very many different kinds of smells, all the way from the odor of violets and roses up to asafetida. But until you can measure their likenesses and differences you can have no science of odor. If you are ambitious to found a new science, measure a smell.*
>
> — Alexander Graham Bell, *Discovery and Invention*, 1914

Olfactory sensing, or the sense of smell, is an intricate chemosensory process that evolved with various functions, which are crucial for the survival and reproduction of many species [9]. Its primordial functions include communication, identification of nutritional resources, selection of suitable mates, and perception of impending danger, such as toxins and predators [9]. Even in modern societies, many functions remain vital for us humans. Olfaction enhances flavor perception during eating and guides food choices by signaling edibility or spoilage, directly affecting appetite and intake [10]. Moreover, olfaction affects social relationships across different stages of life, particularly during partner selection, the prenatal period, and the postnatal period [10]. Most recently, as evidenced by the Coronavirus disease 2019 (COVID-19) pandemic, a reduction or complete loss of olfactory sensation severely interferes with daily activities and ultimately leads to a significant decline in quality of life and negatively impacts psychological well-being [11].

Historically, humans have harnessed biological olfactory sensing to overcome their own limitations, employing animals such as dogs for tasks requiring superior scent detection, from tracking game and fugitives in ancient hunting societies to detecting explosives and drugs in modern applications [12]. The expensive and sought-after delicacy, black truffles, is traditionally found by pigs [13]. Today, gas and odor sensors are used for many industrial applications, such as quality control and spoilage detection in food processing, locating the source of prohibited contraband (e.g., explosives and drugs), location of survivors (of natural disasters), environmental monitoring, and early diagnosis of diseases [14–17]. Hence, the continuous advancement of gas and odor-sensing systems remains indispensable.

1.1. State of the Art

The traditional approach is to characterize the elemental or molecular composition of the odor by precisely determining the concentration of individual components. For this approach, the gas chromatography mass spectrometry (GCMS) remains the de facto gold standard for accurately determining

individual gas components, enabling detailed and effective chemical analysis of complex compositions [17, 18]. Despite its high sensitivity and specificity, it has several limitations. First, GCMS systems are expensive devices [17, 19]. Moreover, it entails high operational costs, particularly for service, consumables, gas supplies, and sample preparation [19]. Delicate sample preparation is not only expensive but also time-consuming, accounting for approximately 60 % of the total laboratory time [18]. Additionally, it is a major source of error, accounting for approximately 30 % of total errors [18]. Therefore, it is the de facto bottleneck, which limits the throughput of GCMS systems. Standard GCMS setups are large devices which are unsuitable for portable, point-of-need applications [17, 19]. Mobile versions with smaller footprints, such as the E^2M system from Bruker, exist but weigh 37 kg per unit [20]; further miniaturization is desired. Furthermore, in addition to large molecules or thermally unstable compounds, the GCMS exhibits limited compatibility with highly polar molecules, which is a large part of relevant odorants [21, 22].

In contrast, the electronic nose (eNose) approach analyzes the entire odorant mixture, without detailed information on individual components or their concentrations. The "fingerprint" of the odor is captured as the characteristic sub-sensor signal pattern, which can then be identified using pattern recognition methods. This approach emerged as a paradigm-shifting alternative to bridge the critical gap between laboratory accuracy and cost-effectiveness, while ensuring mobile, easy-to-use functionality. As the name suggests, the eNose technology is a bio-inspired approach where arrays of chemical sub-sensor are coupled with sophisticated pattern recognition algorithms to collectively "smell" and recognize complex gas mixtures. The earliest work on the eNose technology dates back to Wilkens and Hatman in 1964 [21]. The field has matured substantially over four decades, evolving from large, expensive, power-hungry research instruments to compact, portable, and energy-efficient devices with current trends of wireless computing and integration with internet-of-thing (IoT) platforms [23]. In addition to the sensor and the pattern recognition algorithm, a complete macro-architecture of an eNose system comprises the gas sampling system and the readout electronics [24]. Nevertheless, these components are not discussed further here, as they are not the primary focus of this work.

The single (sub-)sensors of the eNose can employ various technologies to convert odorant compositions into electrical signals. They can be categorized into the principal working domains: mechanical (surface acoustic wave and quartz microbalance) [25, 26], electrical (resistive, capacitive, and field-effect-based) [27–29], optical (colorimetric, fluorescence-, polarization-, and absorbance-based) [14, 30, 31], and biological [32].

Currently, chemiresistive sensor technology dominates the commercial gas sensor market, while semiconducting metal oxide (MOX), carbon nanotube (CNT), and conductive polymers are the most widely used chemiresistive materials [27, 33, 34]. MOX sensors are characterized by high sensitivity, long lifespan, high durability, fast response times, and inexpensive manufacturing. Accounting for approximately 88 % of the MOX sensors, n-type materials, such as (sorted in descending frequency) SnO_2, ZnO, TiO_2, WO_3, In_2O_3, Fe_2O_3, MoO_3, and V_2O_5, dominate the research landscape [35]. In contrast, p-type MOXs only accounts for approximately 12 % where CuO and NiO are the most represented materials [35]. Moreover, the materials can be further modified by doping, incorporating metallic nanoparticles (NPs), or creating complex composites to tailor the sensor's sensitivity to specific analytes. The requirements for pure single-gas sensing applications differ from those of an eNose system. For a

single-gas sensor, the sensitivity to the target gas is desired to be as high as possible, whereas cross-sensitivity should be minimized. In contrast, for eNoses, individual subsensors should show differences in sensitivity towards a certain gas, whereas the average difference in sensitivity towards certain gases is not of particular interest. Therefore, a multi-step approach is to integrate multiple materials on a single chip to enhance classification capability [36]. Specialized sensor materials, such as polyaniline, have been reported to achieve relative responses (RRs) exceeding 300 % for specific odorants [37]. RR describes the sensor response of the target analyte compared to the baseline response of a reference analyte.

In addition to chemical composition, material morphology affects several sensing properties. 1D nanomaterials form dense and porous networks with large surface to volume ratios and show significantly increased sensitivity compared to 2D thin films at the cost of increased limit of detection (LoD) and signal noise [38]. Surprisingly, the response and recovery times remain similar despite deep and convoluted channel paths.

More recently, chemically-sensitive field-effect transistor (ChemFET) technology has emerged as a promising alternative. As the name suggests, they are based on field-effect transistors (FETs) and achieve sensing via one or multiple FET characteristics such as threshold voltage (shift), Dirac point shift, carrier mobility, contact potential difference, and time constant spectrum [39]. Compared with chemiresistive sensors, they offer the major advantage of measuring multiple parameters. Moreover, if the fabrication method is complementary metal-oxide-semiconductor (CMOS) compatible, small sensor sizes and high yields can be achieved [40]. Various gas-sensing FET structures exist and are categorized by gate position: back-gate, top-gate, dual-gate, and floating-gate [39]. As with chemiresistors, surface modifications may improve gas-specific sensitivity. For example, in the case of Au decorated Si nanowire (NW), reports show extremely high relative response (RR) (compared to baseline signal) towards NH_3 of around 35 at 50 ppm [40].

The eNose technology is tightly coupled with machine learning, which should map the often high-dimensional multivariate data to discrete class predictions. Machine learning has evolved significantly over the past decades, and numerous algorithms have been applied to eNose applications. Various supervised methods can be used for classification, including neural networks, decision tree (DT), principal component analysis (PCA), linear discriminant analysis (LDA), and ensemble methods. LDA stands out as a versatile and tried-and-tested method for eNose applications. Additionally, a confidence-interval-dependent decision boundary can be implemented for novelty detection [41], which is critical for practical eNose applications where previously unknown odors may be encountered. Traditional dimensionality reduction methods such as principal PCA and LDA are widely used, (power) efficient, and straightforward, but struggle with complex non-linear sensor signal patterns and temporal variability [42, 43]. Conversely, support vector machine (SVM), DT, and Random Forest (RF) can handle more complex data but may struggle with highly overlapping data [43, 44]. Artificial neural network (ANN) based methods, including multilayer perceptron (MLP), extreme learning machine (ELM), convolutional neural network (CNN), and long short-term memory (LSTM), have been reported to be able to handle complex non-linear data but require extensive training of non-transparent and non-interpretable models [45–47]. The optimal classification algorithm is selected and optimized depending on the eNose system and the specific application.

At Karlsruhe Institute of Technology (KIT), the chemiresistive eNose technology, especially in combination with LDA, has a long history resulting in the famous Karlsruher Mikronase (KAMINA) and its applications include early fire detection, air quality monitoring, food freshness assessment, and soil and water polution analysis [48–57].

1.2. Motivation

Despite significant developments and maturation of chemiresistive and ChemFET based eNose technologies, persistent challenges continue to limit their practical deployment and unrestricted commercial success.

First, humidity, which can vary independently of the target odorants in a real-world environment, is a major source of interference for humidity sensors, alongside temperature and atmospheric pressure [58, 59]. The interference can be expressed as baseline drift, cross-sensitivity, and degraded sensor specificity [58]. Secondly, there is a persistent desire for higher sensitivity, recognition accuracy, and reliability, which are constrained by the chemical selectivity of eNoses. Its lack of sensor diversity and specificity compared to biological "lock-and-key" receptors hinders robust pattern recognition under real-world variability. Finally, traditional microfabrication techniques such as photolithography and sputtering remain expensive and material-inefficient for prototyping diverse, customizable sensors, thereby limiting rapid, cost-effective iteration.

This thesis addresses these limitations and challenges through contributions from distinct domains: nanomaterial synthesis, fabrication methods, sensor technology, machine learning, and application. First, V_2O_5 nanofibers are developed via a facile electrospinning (ES) synthesis route to enable gas-independent humidity monitoring, ensuring stable and reliable eNose applications for the subsequent technologies. Next, optimized vapor-liquid-solid (VLS) grown SnO_2 nanowires are used as the sensing material to achieve improved sensitivity and classification performance. Finally, this work introduces digital inkjet and aerosol jet printing as transformative fabrication methods that enable efficient, requirement-specific fabrication, resulting in a multi-component field-effect-based sensor architecture, which explores multi-dimensional voltage modulation as an alternative to conventional sub-sensor arrays. These solutions collectively advance the eNose technology toward reliable, for diverse applications.

1.3. Structure of the Thesis

Chapter 1 Introduction This chapter provides an overview of the state-of-the-art eNose systems. Various sensor technologies, in addition to machine learning methods, are discussed and compared. Following this, the thesis aims to present challenges and issues with the proposed solutions. Finally, this section outlines the thesis structure.

Chapter 2 Fundamentals This chapter examines various fundamental aspects of eNose technology. First, a brief introduction of the gas compositions and humidity is presented. After the connections and distinctions among the biological noses are concisely established, the relevant eNose sensor technologies of this thesis, namely chemiresistors and ChemFET, are comprehensively discussed. Important sensing properties and metrics, along with the machine learning methods employed, are presented in the final two sections.

Chapter 3 Experimental In this chapter, the most relevant experimental methods are presented and discussed, with the focus on nanomaterial synthesis and digital printing. The general working principle is shown, along with device-specific details. The actual process parameters and case-dependent differences are stated in the corresponding main chapters.

Chapter 4 Relative Humidity Sensing Using Electrospun V_2O_5 Nanofibers The relevant eNose technologies, chemiresistor and ChemFET, in this work are both sensitive to humidity, which may negatively interfere with the actual sensing process. Therefore, in a first step, a reliable relative humidity sensor based on electrospun V_2O_5 nanofibers (NFs) is presented in this chapter. A connection between the critical synthesis parameter, annealing temperature, materials' chemical composition, NF morphology, microcrystalline structure, and humidity-sensing performance is established. Ultimately, under optimal synthesis conditions, a high-performance, efficient humidity sensor was fabricated with minimal cross-sensitivity to the tested gases. The findings of this chapter are expected to facilitate the future deployment of the humidity-sensitive eNose technology in field applications.

Chapter 5 Chemiresistive Electronic Nose using SnO_2 Nanowires for Gas Sensing and Mold-Detection The first eNose system, using VLS-grown SnO_2 NWs, is fabricated, evaluated using standard test gases, and applied to detect and identify harmful indoor mold species. The sensor successfully classifies the gases using LDA. Mold detection and identification pose a greater challenge, requiring dedicated modifications and extensions to the LDA algorithm. Ultimately, using the optimized methods, the eNose reliably detects and identifies mold species across various growth media. The detailed comparison of this chemiresistive SnO_2-NW based eNose technology with the ChemFET and literature reports is postponed to the next chapter.

Chapter 6 Digitally Printed Single-ChemFET-based Electronic Nose In this chapter, a hybrid printing approach that leverages the advantages of inkjet printing (IJP) and aerosol jet printing (AJP) is used to fabricate a ChemFET sensor. The two distinct printing technologies satisfy the vastly different requirements of individual components. The resulting ChemFET sensor exhibits exceptionally high sensitivity to the tested gases, while being operated power-efficiently at room temperature (RT) without external excitation. Moreover, a single ChemFET can generate sufficient features to distinguish among the tested gases when combined with an appropriate machine learning method. From these methods, interesting correlations between different operation points and the feature importances are established. Finally, the ChemFET and the chemiresistive SnO_2 sensor from the previous chapter are compared with one another and with other reported sensors.

Chapter 7 Conclusion and Outlook This chapter summarizes the key results of this dissertation and outlines potential directions for future research.

2. Fundamentals

In this chapter, the fundamental aspects of the electronic nose (eNose) technology are thoroughly discussed. First, the theory of gas composition is introduced. Additionally, the subtopic humidity is discussed separately, with distinct quantities given its prevalence. Next, the human olfactory system is presented as an example to introduce the eNose technology. Subsequently, the fundamentals of the eNose, including its sensing technology and principles, are discussed in detail. Special emphasis is placed on chemiresistive and field-effect-based technologies, given their relevance to this work. Thereafter, several gas-sensing characteristics and metrics, including response, recovery, and sensitivity, are examined. Finally, the chapter concludes with the machine learning section, which focuses on the two classification algorithms, linear discriminant analysis (LDA) and Random Forest (RF), as well as general procedures and quantities.

2.1. Gas Composition and Humidity

General Gas Composition An odor is generally composed of different gas components at different concentrations. Therefore, an odor is precisely characterized by the i-th gas component and by its corresponding amount N_i. The total pressure p is therefore equal to the sum of the partial pressure p_i of each component according to Equation 2.1.

$$p_i = \frac{N_i}{N} p = c_i p \tag{2.1}$$

Here, the ratio $N_i N^{-1}$ is the mole fraction of the i-th gas and is a measurement of the concentration c_i. For analyte gases, this mole fraction is usually tiny. Hence, a purely numerical unit such as ppm $= 10^{-6}$ (parts-per-million) is commonly used for convenience. *l*ikewise, but less common, are parts-per-billion (ppb $= 10^{-9}$), ppt (ppt $= 10^{-12}$), and parts-per-quadrillion (ppq $= 10^{-15}$), which are used for even smaller concentrations. It is noted here that these parts-per notations are not part of the International System of Units (SI). Under known conditions, different but equivalent concentration units, such as volume fraction, mass fraction, mass-to-volume ratio, and partial pressure, can be converted to one another.

Zero and Reference Air Zero air (or pure air) is a loosely defined term that generally describes atmospheric air free of impurities. Impurities include dust, aerosols, and other volatile anthropogenic contaminants such as NO, NO_2, SO_2, and non-methane hydrocarbons [60]. The composition of the dry atmospheric air is listed in decreasing order of concentration in Table 2.1 and is considered

approximately constant [60]. In this work, zero air, optionally humidified, is used as the reference air for baseline sensor measurements.

Table 2.1: Concentrations of the major components of pure dry air [60].

Gas	Molecule	Concentration [ppm]
nitrogen	N_2	78084
oxygen	O_2	20946
argon	Ar_2	934
carbon dioxide	CO_2	330
neon	Ne	18.2
helium	He	5.24
methane	CH_4	1.6
krypton	Kr	1.14
hydrogen	H_2	0.5
nitrous oxide	N_2O	0.3
xenon	Xe	0.087

Humidity Humidity is a measure of the water vapor concentration in the air. The water content in the air can similarly be described using the previously discussed quantities, such as mole fractions. Despite this, a mass-to-volume concentration quantity has prevailed for absolute humidity (AH) (H_{abs}) and saturation humidity (SH) (H_{sat}). The unit of both these quantities is [$\mathrm{kg\,m^{-3}}$]. AH is defined as the ratio between the mass of water vapor $m_{\mathrm{H_2O}}$ contained in a volume V according to Equation 2.2 [61].

$$H_{\text{abs}} = \frac{m_{\mathrm{H_2O}}}{V} \tag{2.2}$$

The SH $H_{\text{sat}}(T)$ describes how much water vapor $m_{\mathrm{H_2O}}$ a volume V of air can hold at a specific temperature at maximum [61]. For most situations and applications, the ratio between AH and SH, the relative humidity (RH), is of interest as defined in Equation 2.3 [61].

$$H_{\text{rel}} = \frac{H_{\text{abs}}}{H_{\text{sat}}} \tag{2.3}$$

From here on, the percentual unit of relative humidity is represented by [RH%] to distinguish it clearly from other percentual quantities. Relative humidity has a profound impact on many aspects of everyday life and in many industrial processes. If relative humidity is low, it feels dry because water evaporates more efficiently, and vice versa. The so-called dew point is reached if $H_{\text{rel}} = 100\,\text{RH\%}$. Here, the water begins to condensate or precipitate. If not otherwise stated, the standard relative humidity of 50 RH% is used in this work.

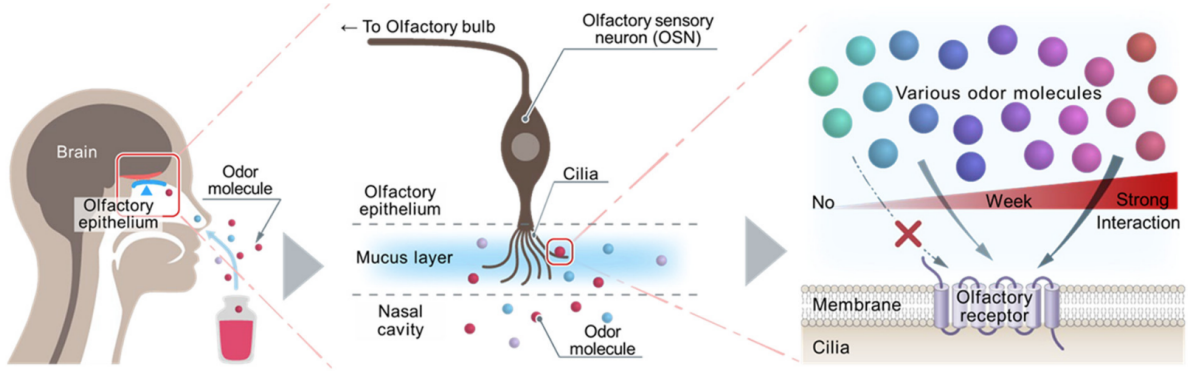

Figure 2.1: Human olfactory system. Left: Odorants entering the nasal cavity are recognized by different ORs in the olfactory epithelium. Middle: Odorants bind to the OR and the OSN transduces the signal to the olfactory bulb. Right: Odorants bind to OR groups with different affinities, thereby enabling pattern recognition of the entire odor. Reprinted from [68] under CC BY 4.0.

2.2. Electronic Nose Technology

The human olfactory system is a sophisticated chemical sensor capable of distinguishing volatile compounds with remarkable sensitivity and selectivity. The electronic nose (eNose) has been developed to mimic the pattern recognition mechanism of the biological olfactory system. This section first introduces the biological nose, using the human nose as an example, and establishes the connection between humans and eNose technology. Next, the eNose is described in detail, including its general operating principle and the various technologies employed. Finally, the two relevant sensing principles, chemiresistive and chemically-sensitive field-effect transistor (ChemFET), are discussed in detail. The machine learning section is discussed separately because of its general applicability and the extent of its theoretical content.

Biological Olfaction - Human as an Example Olfaction is a chemoreceptive process that represents the sense of smell. The human olfactory system exhibits remarkable sensitivity and range. It is commonly estimated that humans can discriminate thousands of odors [62]. Some estimates even place this limit to over a trillion [63]. As depicted in Figure 2.1, odorant molecules (or odorants) bind to olfactory receptors (ORs) in the nasal epithelium and the corresponding olfactory sensory neurons (OSN) triggers signals that travel via the olfactory bulb to the brain for recognition. The interaction between odorants and receptors remains an active area of research. One of the main theories is the docking theory, which describes the selective sensing mechanism of ORs and is analogous to the lock-and-key principle. This is enabled by weak non-covalent interactions, such as dipole-dipole and Van der waals interactions, between the odorant molecules and the ORs [64, 65]. Recently, in 2023, a publication in *Nature* further supports the docking theory [66]. Humans have around 10 to 20 million ORs from which approximately 400 unique types of ORs have been identified [63]. The signal travels from the olfactory bulb to the olfactory cortex, located in the uncus part of the brain. The olfactory cortex resonates if the smell is recognized [67]. Finally, the cortex may send feedback signals to suppress specific responses in the olfactory bulb, thereby enabling olfactory adaptation to background odors.

Basic Principles The eNose is an electronic odor sensor that mimics the human olfactory system and shares many of its principles. The eNose technology differs from sophisticated gas chromatography mass spectrometry (GCMS) instruments in its operating principle, which is the gold standard for gas composition analysis. Instead of analyzing the presence and concentrations of each gas component, the eNose captures odor as an overall impression. The following example conceptualizes the similarity to human olfactory sensing. A human can immediately recognize the smell of a banana, but cannot precisely determine or quantify the concentration of each odorant. The working principle of the eNose and the biological pendant is depicted in Figure 2.2. Odorants originating from the analyte interact with the subsensors in the sensor array. The readout electronics capture and preprocess the response signals from the sub-sensors, thereby forming a signal pattern that is ideally distinct for each odor. Similar to the biological model, the machine learning algorithm must be trained in advance on labeled observations of signal patterns. Afterwards, the previously trained machine learning algorithm can recognize the signal pattern and predict the target label.

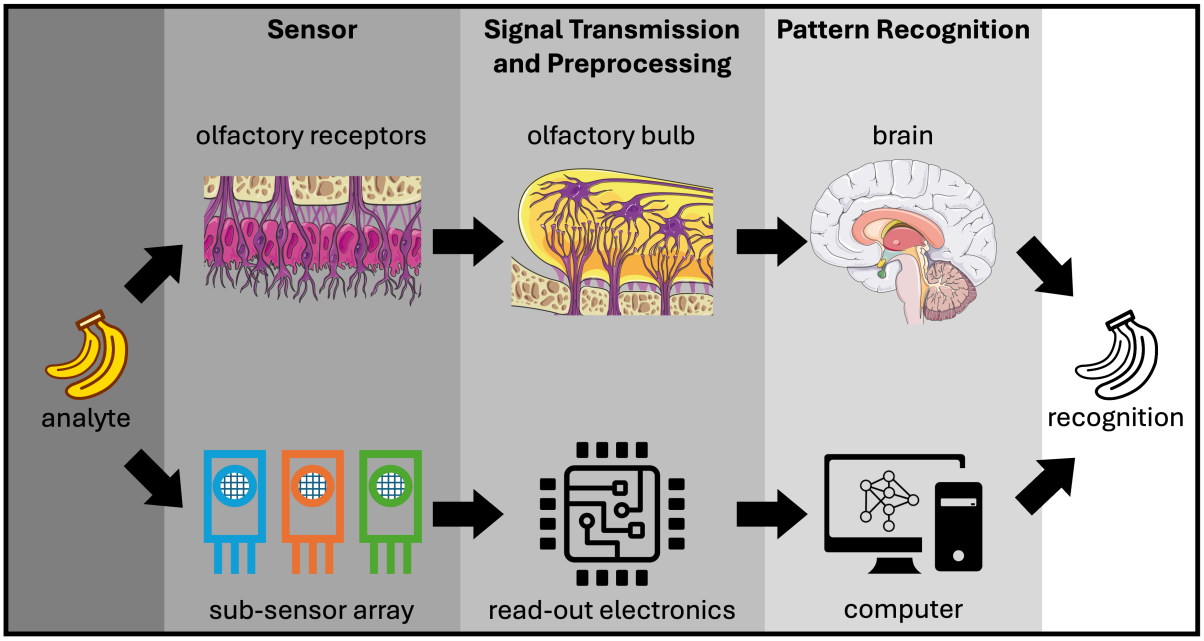

Figure 2.2: Similarities between human olfactory system and eNose. Anatomy images adapted from Servier Medical Art on smart.servier.com

Various sensing technologies and sensing materials are mentioned in the State-of-the-Art (Section 1.1) from which the two relevant sensor technologies, chemiresistors and ChemFETs, are discussed in detail in the following subsections.

2.2.1. Chemiresistor

The basic chemiresistive working principle of semiconducting metal oxides (MOXs) relies on the adsorption of gas molecules, which changes the electrical conductivity. The electrical conductivity σ of a semiconducting MOX is given by Equation 2.4.

$$\sigma = e\,(n\,\mu_{\mathrm{e}} + p\,\mu_{\mathrm{h}}) \tag{2.4}$$

Here, μ_{e} and μ_{h} are the charge carrier mobilities for electrons and holes, respectively. Whereas n and p are the concentrations $[1/\mathrm{m}^3]$ of electrons and holes, respectively. The resistivity is defined as the inverse of the conductivity. The semiconducting MOXs are split into n-type and p-type materials depending on the type of majority charge carriers (electrons vs holes), as previously stated in Section 1.1. Most common representants of n-type MOXs are SnO_2, ZnO, TiO_2, WO_3, In_2O_3, Fe_2O_3, MoO_3, and V_2O_5. Whereas CuO and NiO are common p-type MOXs. If gas molecules adsorb on the surface of the MOX, one of two interactions occurs. Oxidizing gases (electron acceptors) such as NO, NO_2, and O_3 attract electrons, whereas reducing gases (electron donors) such as CO_2 and H_2 donate electrons. These two interactions lead to a positive or negative change in resistivity, depending on the type of MOX [35, 69]. The donated electrons from reducing gases decrease the resistivity of n-type MOXs by increasing electron accumulation. In contrast, they increase the resistivity of p-type MOXs by forming hole depletion regions or reducing hole accumulation. Vice versa, oxidizing gases deplete electrons, thereby increasing the resistivity of n-type MOXs by creating depletion regions. At the same time, p-type MOXs experiences a decrease in resistivity because of hole accumulation. In addition to direct adsorption-induced changes in resistance, gas molecules may indirectly alter resistance by competing with other gases for adsorption sites. One mechanism is competition among molecules of different gases for the limited number of adsorption sites. Alternatively, some gases may react with one another, thereby reducing the effective adsorption concentration of the educt gases. For example, part of the reduction power of CO is attributed to its reaction with oxygen. Figure 2.3 summarizes the four types of interaction. Examples for an oxidizing O_2 adsorption is presented in Equation 2.5 [37].

$$\begin{aligned} \mathrm{O_{2(gas)}} + \mathrm{e^-} &\longrightarrow \mathrm{{O_2}^-_{(ads)}} \\ \mathrm{O_{2(gas)}} + 2\,\mathrm{e^-} &\longrightarrow 2\,\mathrm{O^-_{(ads)}} \\ \mathrm{O_{2(gas)}} + 4\,\mathrm{e^-} &\longrightarrow 2\,\mathrm{O^{2-}_{(ads)}} \end{aligned} \tag{2.5}$$

Here, the (ads) subscript indicates adsorbed molecules. The impact of electron depletion layers on resistance is amplified at interparticle contacts and grain boundaries, which form back-to-back double Schottky barriers in n-type MOX materials. This forms a serial connection path between grains and particles, resulting in a significantly higher sensor sensitivity [35, 69]. In contrast, in p-type contacts, hole accumulation forms parallel conduction paths. Consequently, the resulting sensitivity amplification of a p-type nanomaterial is calculated to be only the square root of the amplification of an identical shaped n-type MOXs [35]. This is the reason for the dominance of n-type materials, whereas p-type semiconductors receive less attention due to their lower gas response [35].

Selectivity For the eNose, differences in subsensors ultimately lead to improved classification. Many methods exist to systematically create differences in sub-sensor, such as filtering, nanoparticle incorporation, heterojunction formation, and external stimuli, such as irradiation and heating [35, 37]. Additionally, some materials uniquely interact with specific gases. For example, CuO, NiO and WO_3 metallic sulfides when exposed to H_2S [37]. A more straightforward approach is to exploit statistical differences in the fabrication process. This effect is particularly pronounced in randomly oriented

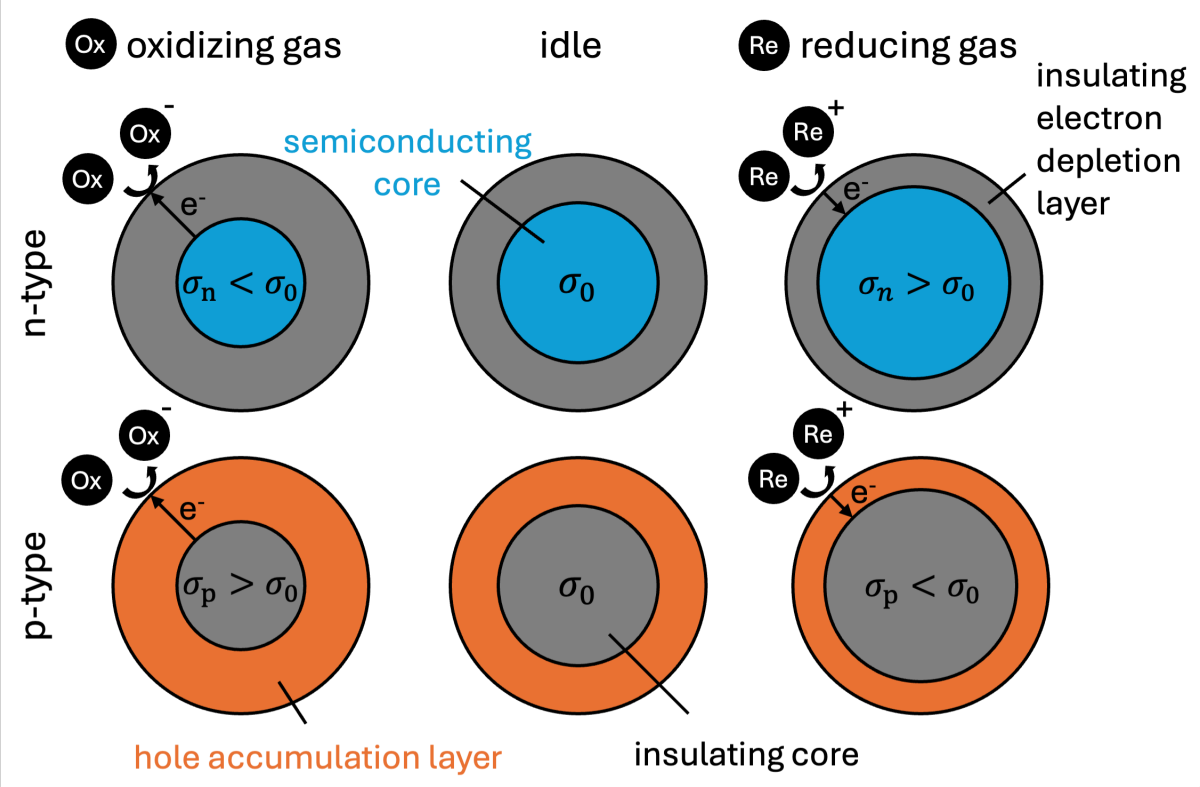

Figure 2.3: Gas interaction with semiconducting MOX chemiresistors. The interactions are separately illustrated for oxidizing and reducing gases with p-type and n-type MOXs.

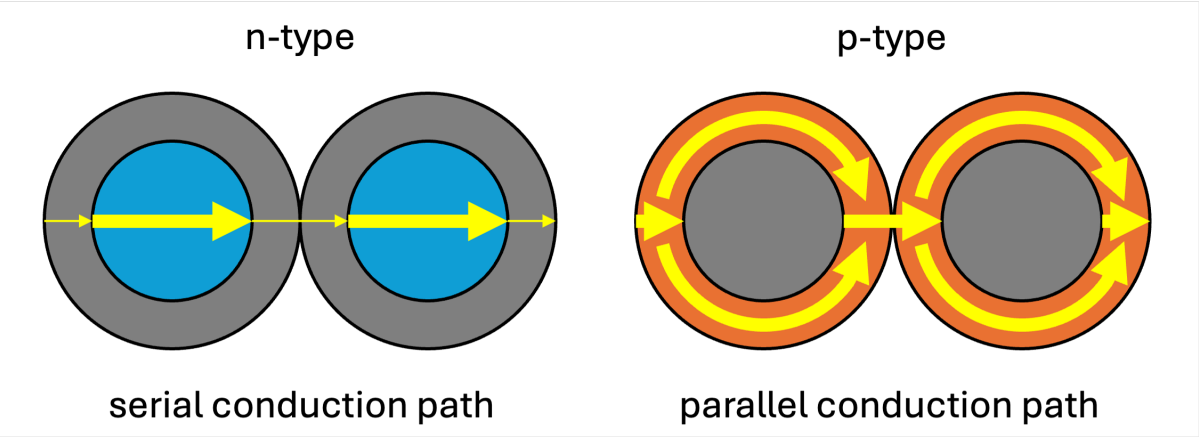

Figure 2.4: Conduction paths of n-type and p-type MOXs at inter-particle contacts and grain boundaries. N-type materials show a serial conduction path due to the high resistive shells, whereas p-type materials exhibit a parallel conduction path through the shell.

networks of 1D materials, such as nanowires (NWs) or nanofibers (NFs). They exhibit intrinsic local heterogeneity in nanomaterial dimensions, material density, pore size, and pore density. However, because the variation is random, the amplitude may vary, necessitating the rejection of poorly performing sensors.

2.2.2. Chemically-Sensitive Field-Effect Transistor (ChemFET)

One of the eNose sensor technologies that is used and developed in this work is the ChemFET. Generally speaking, the ChemFET is a field-effect transistor (FET), which is optimized to work as a chemical sensor. The anticipated advantage of ChemFETs, relevant to this work, is the ability to generate features artificially via voltage modulation. While a multi-sub-sensor configuration is also possible, as in the previously mentioned chemiresistive approach, this work intentionally focuses on a single ChemFET sensor, leveraging the voltage-modulation-generated features. Additionally, compared with other modulation methods, such as UV and heating, voltage modulation is expected to be fast and energy-efficient.

Transistors are fundamental semiconductor devices commonly used as amplifiers and switches. Bipolar junction transistor (BJT) and FET are the two major transistor subclasses that work fundamentally differently. A BJT is a three-terminal device (base, emitter, and collector) which uses a small base current to control a larger collector current. Similarly, a FET is a three- to four-terminal device (gate, source, drain, and optionally bulk) that uses an electric field (E-field) at the gate to control the drain current. BJTs are primarily utilized in linear amplifiers and analog stages because of their high gain, whereas FETs dominate in switching and digital logic applications due to their power efficiency and high switching frequency. FETs can be further divided into a wide range of FET technologies, depending on their categorization by structure, semiconductor material, and application. Most prominent candidates are metal-oxide-semiconductor field-effect transistors (MOSFETs) and junction field-effect transistors (JFETs). A MOSFET can be considered as a material-specific case belonging to the more generalized insulated-gate field-effect transistor (IGFET) family.

Thin Film Transistors While MOSFETs powers the majority of worldwide processors and memory devices, thin-film transistors (TFTs) are widely used in displays [70]. A TFT is a three-terminal device with no p-n junctions as opposed to a MOSFET. The structure of a TFT can be categorized according to the positions of the drain, source, and gate electrodes as shown in Figure 2.5 [71].

Most commonly, the channel is either an inorganic or organic semiconductor. In this work, only semiconducting MOXs- based bottom-gated TFTs are considered, in which the channels are directly exposed to the gaseous analytes. The drain-source current I_{DS} in the linear region can be calculated according to Equation 2.6 [70].

$$I_{DS} = \frac{w}{l}\mu C\left[(U_{GS} - U_{th})U_{DS} - \frac{1}{2}{U_{DS}}^2\right] \tag{2.6}$$

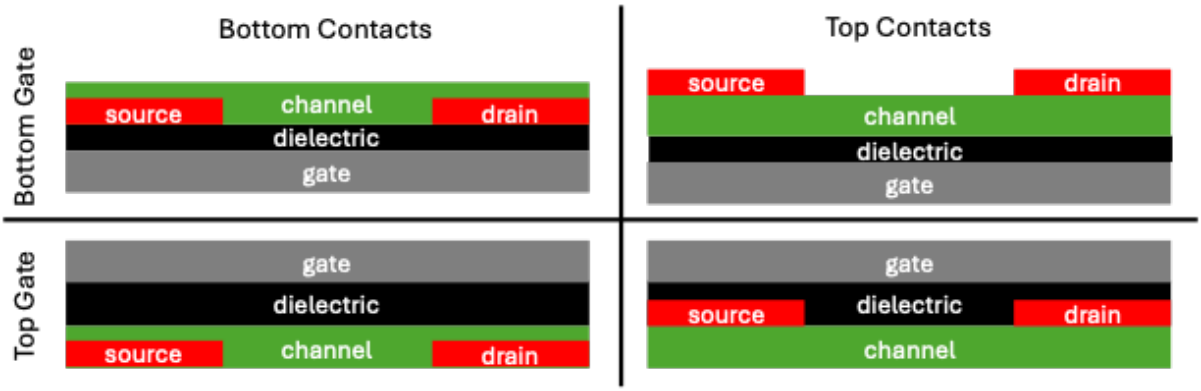

Figure 2.5: Different TFT stack structures. Four types are shown, categorized by the gate and electrode positions.

Here, the w and l are the width and length of the channel, respectively. d is the thickness of the MOX dielectric, $C = \varepsilon_0 \varepsilon_r d^{-1}$ is the area specific gate insulator capacitance, U_{GS} is the gate-source voltage, U_{DS} is the drain-source voltage, U_{th} is the threshold voltage, and μ is the charge carrier mobility. From the transfer characteristics, the transconductance can be calculated by the slope of the IV curve according to Equation 2.7 [70].

$$g_t = \frac{dI_{DS}}{dU_{GS}} \tag{2.7}$$

In the saturation region ($U_{DS} > U_{GS} - U_{th} > 0$), I_{DS} can be approximated by Equation 2.8 and the saturation mobility is given by Equation 2.9 [70].

$$I_{DS} = \frac{w}{2l} \mu C (U_{GS} - U_{th})^2 \tag{2.8}$$

$$\mu_{sat} = \frac{\left(\frac{d\sqrt{I_{DS}}}{dU_{GS}}\right)^2}{\frac{w}{2l}C} \tag{2.9}$$

U_{th} is the threshold gate voltage at which enough charge carriers are accumulated for the source-to-drain channel to form. U_{th} can be calculated either by linear extrapolation of $I_{DS}(U_{GS})$ in the linear region or $\sqrt{I_{DS}(U_{GS})}$ of the saturation region. From a transfer characteristic, the on and off I_{DS} currents can be extracted for a given U_{DS}. Most commonly, the on/off ratio is calculated as a single quantity that describes the ratio of on-to-off current. The gate leakage current or measurement limit primarily determines the off-current. These parameters are important for a switching or amplifying FET; however, for eNose applications, they are only required to define distinct operating regimes, with no specific requirements. At the same time, the on-off-ratio is typically desired to be as high as possible to enable effective transition across widely different operating regions. In contrast, the transconductance g_t on the one hand should not be too high or too low to achieve adequate and continuous change in conductance within a given U_{GS} range.

Gas Sensing Mechanism As previously mentioned, the ChemFET is structured such that the channel is exposed to the analyte gases. In the absence of a gate voltage, the three-terminal ChemFET reduces to a two-terminal chemiresistor. Therefore, the same gas interactions apply, depending on the gas (oxidizing vs. reducing) and the semiconductor type, as discussed in Section 2.2.1. If a metal-semiconductor junction is present, gas adsorption affects the Schottky barrier, thereby modulating current. Moreover, negatively charged gas molecules, which are predominantly the oxygen species $O_2{}^-$, O^-, and O^{2-}, may influence the electrical field in the semiconducting MOX beneath, thereby changing the IV-characteristics [39]. ChemFETs are also used for liquid analytes, but they generally perform significantly better with gaseous samples [72]. For classification purposes, the ChemFET may generate features by systematic modulation. In addition to temperature and UV-irradiation intensity modulation, which chemiresistive eNose systems may also employ, ChemFET may exploit the more power-efficient voltage modulations, including gate-source and drain-source voltages [39]. These modulations create distinct operating regimes that, in turn, may increase selectivity, thereby improving classification performance.

2.3. Sensing Characteristics

2.3.1. Response and Recovery

Response and Recovery When exposing a specific sensor to a particular analyte concentration c, it responds with an absolute signal y_{abs}, which can be of many forms, such as resistance for chemiresistors or current for ChemFETs. For gas sensing purposes, a baseline reference should be established first by measuring a reference gas, yielding the baseline signal $y_{\text{abs},0}$. With these two quantities, a more convenient, comparable, and dimensionless quantity, the relative response (RR), can be calculated according to Equation 2.10.

$$y_{\text{rel}} = \frac{y_{\text{abs}} - y_{\text{abs},0}}{y_{\text{abs},0}} \tag{2.10}$$

For non-negative quantities, such as resistance or conductance, which can respond by decreasing several orders of magnitude ($y_{\text{abs}} \ll y_{\text{abs},0}$) while y_{rel} remains below 1. Therefore, in this case, y_{rel} does not adequately reflect differences between sensors. Therefore, an alternative, yet still dimensionless, approach is to define it simply as the ratio of the absolute response to the absolute baseline response, as shown in Equation 2.11.

$$y_{\text{rel}}* = \begin{cases} y_{\text{abs}}/y_{\text{abs},0} & \text{if } y_{\text{abs}} > y_{\text{abs},0} \\ y_{\text{abs},0}/y_{\text{abs}} & \text{otherwise} \end{cases} \tag{2.11}$$

The second definition $y_{\text{rel}}*$ is especially useful to establish comparability independent of the signal change direction, whereas y_{rel} is more suited for further data analysis, as it retains the directional information. The subsequent quantities presented in this section are independent of which definition is chosen. For future convenience, the RR is given by y.

As depicted in Figure 2.6, the concentration typically changes rapidly at $t = t_0$, which is approximated as a step function. This approximation requires the experimental setup to change the concentration

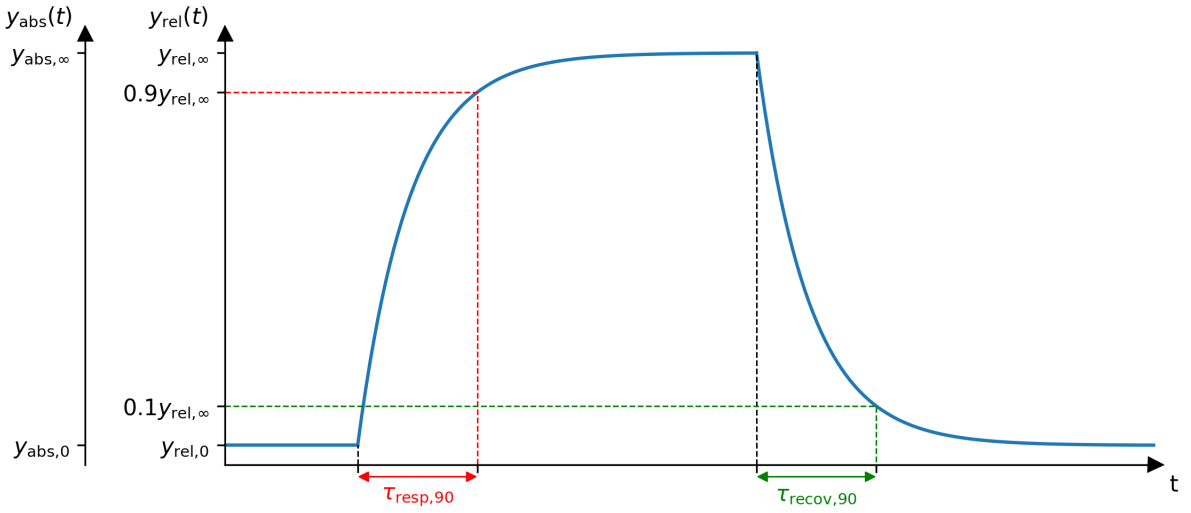

Figure 2.6: Illustration of a conventional signal response and recovery curve. Both the response and recovery are modeled after limited growth functions (refer to Equation 2.13 and Equation 2.15).

significantly faster than the sensor response time. In a real setup, the final recorded response behaviour is a convolution of the gas piping and the eNose system's responses. The signal of the setup changes rapidly after t_0 and stabilizes to a certain final value $y_{abs,\infty}$. During each measurement segment, the signal can be approximated by a limited growth function with a certain time constant τ_{resp} according to Equation 2.12.

$$y_{abs}(t) = (y_{abs,\infty} - y_{abs,0}) \left(1 - e^{-\frac{t}{\tau_{resp}}}\right) + y_{abs,0} \tag{2.12}$$

This equation (Equation 2.12) can be transformed into a simpler form using the RR (Equation 2.10), as shown in Equation 2.13.

$$\begin{aligned} y(t) &= \frac{y_{abs}(t) - y_{abs,0}}{y_{abs,0}} \\ &= \frac{(y_{abs,\infty} - y_{abs,0}) \left(1 - e^{-\frac{t}{\tau_{resp}}}\right) + \cancel{y_{abs,0}} - \cancel{y_{abs,0}}}{y_{abs,0}} \\ &= \frac{y_{abs,\infty} - y_{abs,0}}{y_{abs,0}} \left(1 - e^{-\frac{t}{\tau_{resp}}}\right) \\ &= y_\infty \left(1 - e^{-\frac{t}{\tau_{resp}}}\right) \end{aligned} \tag{2.13}$$

Here, $y_\infty = \lim_{t\to\infty} y(t)$ describes the RR limit, which is theoretically only reached for $t \to \infty$. The response time constant τ_{resp} may differ depending on measurement conditions, analyte, analyte concentration, response, and recovery. At $t = \tau_{resp}$, the RR reaches approximately 63.2 % of y_∞.

As already pointed out in the last paragraph, it would take an infinite amount of time to reach the limit value. Therefore, the response time is defined for a specific point where the RR y reaches a certain percentage of its final stationary y_∞ value. Most commonly, this percentage value is set to 90 % [73],

which is also used for this work. This value can be either extracted graphically after the curve fitting of Equation 2.13 or directly according to Equation 2.14.

$$\begin{aligned} \frac{y(t=\tau_{\text{resp},90})}{y_\infty} &= 1 - e^{-\frac{\tau_{\text{resp},90}}{\tau_{\text{resp}}}} = 0.9 \\ \Rightarrow \tau_{\text{resp},90} &= -\ln(0.1) \cdot \tau_{\text{resp}} \approx 2.3 \cdot \tau_{\text{resp}} \end{aligned} \tag{2.14}$$

Recovery is the process by which the response signal returns to baseline after the analyte concentration is returned to the reference value. Consequently, the RR during recovery is defined according to Equation 2.15 with the time constant τ_{recov}, which is generally not equal to τ_{resp}.

$$y(t) = -y_{\text{rel},\infty}\left(1 - e^{-\frac{t}{\tau_{\text{recov}}}}\right) + y_\infty = y_\infty\, e^{-\frac{t}{\tau_{\text{recov}}}} \tag{2.15}$$

Similar to the response time, the 90 % recovery time $\tau_{\text{recov},90}$ can also either be extracted from the fitted graph or calculated $\tau_{\text{recov},90} \approx 2.3 \cdot \tau_{\text{recov}}$. From here on, any response and recovery response curve which can be approximated by the limited growth functions (Equation 2.13 and Equation 2.15) are described as *conventional*.

2.3.2. Calibration Function and Sensitivity

The calibration function $f(c)$ is defined as the functional relationship between the analyte amount, such as the concentration c, and the expected value of the observed signal $\mathcal{E}(y)$ according to Equation 2.16 [60]. The calibration curve is the graphical display of the calibration function for a particular analyte as depicted in Figure 2.7. In general terms, the calibration function can take any continuous, differentiable form, and the calibration curve can take any shape.

$$f(c) = \mathcal{E}(y(c)) \tag{2.16}$$

Multiple measurements are taken at different concentrations to find the parameters of the calibration function by curve fitting, as shown in Figure 2.7. Sensitivity is defined as the derivation of the calibration function (or the slope of the calibration curve) [60]. It describes how changes in analyte concentration affect the signal output.

$$s(c) = \frac{\mathrm{d}f(c)}{\mathrm{d}c} \tag{2.17}$$

In the case of a linear calibration function, the sensitivity s simplifies to a constant. An additional advantage of using RR to calculate sensitivity is that $s(c)$ is invariant to scaling factors[1] as required according to International Union of Pure and Applied Chemistry (IUPAC) [60]. This scale invariance propagates from the RR to the calibration function to the sensitivity, as shown in Equation 2.18. Here, it

[1] such as an arbitrary signal gain

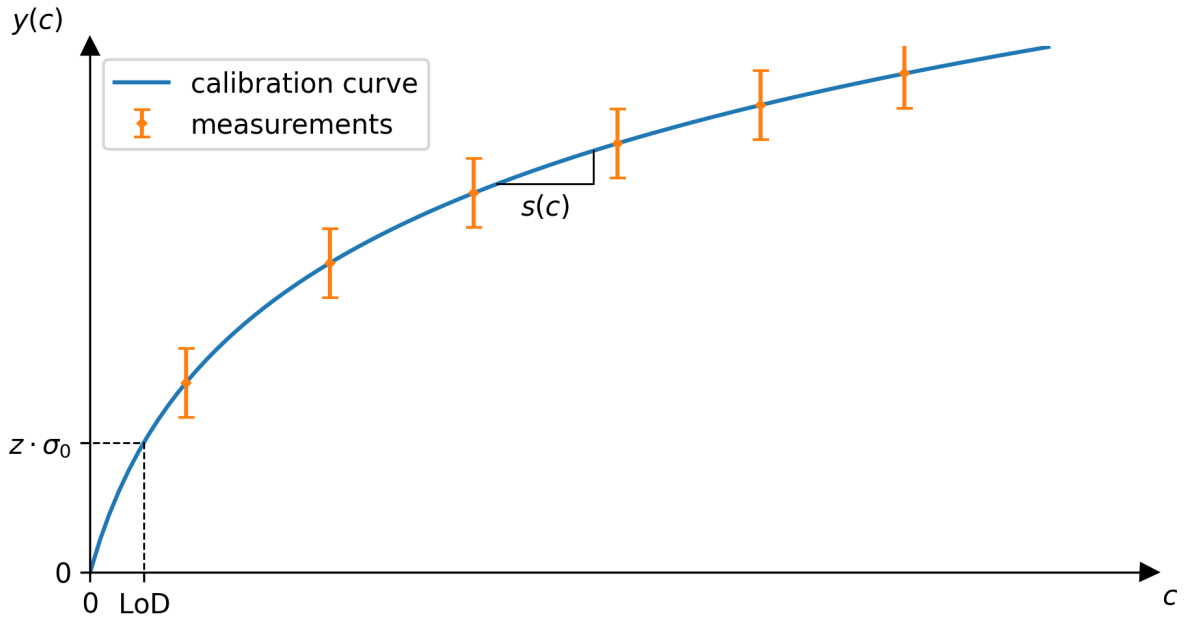

Figure 2.7: Illustration of the calibration curve, sensitivity, and LoD. The curve is created by fitting to actual measurement data. The LoD is calculated on a predetermined $z\sigma$ threshold. The concentration-dependent sensitivity s is the slope of the calibration curve.

is demonstrated that y does not change if the absolute signal values y_{abs} are multiplied by an arbitrary non-zero factor α.

$$s(c) \propto f(c) \propto y = \frac{y_{\text{abs}} - y_{\text{abs},0}}{y_{\text{abs},0}} = \frac{\alpha y_{\text{abs}} - \alpha y_{\text{abs},0}}{\alpha y_{\text{abs},0}} \quad \forall\, \alpha \in \mathbb{R}_{\neq 0} \tag{2.18}$$

2.3.3. Limit of Detection (LoD)

The limit of detection (LoD) is a quantity that describes the lowest concentration of analyte c_{LoD} where the corresponding signal differs from the baseline signal with sufficient statistical significance as depicted in Figure 2.7. Given multiple samples, the expected baseline value is defined as $\mathcal{E}(y_0) = \overline{y}_0$ and the baseline standard deviation (SD) is defined as σ_0. Consequently, the LoD (c_{LoD}) can be found such that Equation 2.19 holds.

$$\mathcal{E}(y(c_{\text{LoD}})) - \mathcal{E}(y_0) = z \cdot \sigma_0 \tag{2.19}$$

Here, z is a z-score which determines the required statistical significance and is fixed to $z = 3$ (corresponds to $\approx 99.73\,\%$) in this work. If the same samples are used to calculate the absolute baseline value $y_{\text{abs},0}$, then $\mathcal{E}(y_0) = 0$ and Equation 2.19 simplifies to $\mathcal{E}(y(c_{\text{LoD}})) = z \cdot \sigma_0$.

2.4. Machine Learning

Machine learning aims to learn from existing data by and subsequently apply the extracted and generalizable information to new data e.g. to predict outcomes. For the eNose application in this work, machine learning algorithms are used to recognize different odors by the output signal pattern from the eNose. Machine learning approaches are categorized into the four main types as listed below [74]:

- Supervised learning: The training data contains the desired outcomes (targets or labels).
- Unsupervised learning: Training data does not contain targets.
- Semi-supervised learning: Training data contains a few targets.
- Reinforcement learning: Learning from reward-based actions.

In this case, only supervised learning is considered for eNose applications.

2.4.1. General Terms and Quantities

Dataset The machine learning algorithm takes the features (inputs) and predicts the target (outputs). Features and targets can be numerical (e.g., integers or floating-point values) or categorical (e.g., strings). In eNose applications for gas recognition, the features are numerical sensor signals, and the targets are labels. From measurements, N outcome variables (also called features) are observed simultaneously, such as resistance or current values. The i-th multivariate observation is consequently represented by the vector $\boldsymbol{x}_i \in \mathbb{R}^N$ according to Equation 2.20.

$$\boldsymbol{x}_i = [x_{i,1}, \ldots, x_{i,j}, \ldots, x_{i,N}]^\top \quad \forall\, i \in \{1, \ldots M\} \text{ and } j \in \{1, \ldots N\} \tag{2.20}$$

All M observations can be packed into an observation matrix $\boldsymbol{X} \in \mathbb{R}^{M \times N}$ with rows of observations and columns of features according to Equation 2.21.

$$\boldsymbol{X} = \begin{bmatrix} \boldsymbol{x}_1^\top \\ \vdots \\ \boldsymbol{x}_i^\top \\ \vdots \\ \boldsymbol{x}_M^\top \end{bmatrix} = \begin{bmatrix} x_{1,1} & \ldots & x_{1,j} & \ldots & x_{1,N} \\ \vdots & \ddots & & & \vdots \\ x_{i,1} & & x_{i,j} & & x_{i,N} \\ \vdots & & & \ddots & \vdots \\ x_{M,1} & \ldots & x_{M,j} & \ldots & x_{M,N} \end{bmatrix} \tag{2.21}$$

For supervised learning, each observation is assigned a label. Given M observations, the label vector $\boldsymbol{y} \in \mathbb{G}^M$ is defined according to Equation 2.22. Here, $\mathbb{G}$ is the set of classes containing $C = |\mathbb{G}|$ unique elements.

$$\boldsymbol{y} = [y_1, \ldots, y_i, \ldots, y_M]^\top \tag{2.22}$$

Consequently, a complete dataset $(\boldsymbol{X}, \boldsymbol{y})$ consists of the observation matrix $\boldsymbol{X}$ and the corresponding label vector $\boldsymbol{y}$ with matching rows $\left(\boldsymbol{x}_i^\top, y_i\right)$. For training and testing, the dataset is split into training and test subsets: $(\boldsymbol{X}_{\text{train}}, \boldsymbol{y}_{\text{train}})$ and $(\boldsymbol{X}_{\text{test}}, \boldsymbol{y}_{\text{test}})$. The training size is defined as the ratio of M_{train}/M. Likewise, the test size is defined as the ratio M_{test}/M, with the sum of the training and test sizes equal to one.

The complete set of indices is denoted by $\mathbb{I} = \{1, \ldots, M\}$, whereas each class c has a unique subset of indices $\mathbb{I}_c \in \mathbb{I} : \boldsymbol{y}_i = c \, \forall \, i \in \mathbb{I}_c$. The union of all class-specific index sets equals the complete set $\mathbb{I} = \bigcup_{c \in \mathbb{G}} \mathbb{I}_c$ and the class-specific index sets are pairwise disjoint $\mathbb{I}_c \cap \mathbb{I}_{c'} = \varnothing \; \forall c \neq c'$. Consequently, the number of observations for each class is given by $M_c = |\mathbb{I}_c|$.

A dataset may be imbalanced, meaning that the counts of observations across classes differ significantly. An imbalanced data set may negatively impact the performance of machine learning models [75–77]. Therefore, it may be useful to balance the data during preprocessing.

Generalization The generalization capability of a machine learning algorithm refers to its predictive performance on independent test data [78]. Models with higher generalization performance can accurately predict new data. Therefore, optimizing the model's generalization capability is desired. This is achieved through training, in which the model's parameters are adjusted using a training dataset. Thereafter, its performance can be evaluated by testing the previously trained model on a distinct, unseen test dataset. The errors made during training and testing are referred to as training and test errors, respectively. Since testing reveals the generalization capability, the test error is also called the generalization error.

Errors: Noise, Bias, and Variance A model's test error can be attributed to three sources: noise, bias, and variance [74]. Any data-collection errors, outliers, and unknown features are classified as noise. Bias occurs when the model's complexity is insufficient to map observation features to targets accurately. For example, given a dataset with an underlying quadratic relationship, a linear model is inadequate. High bias results from an underfit model. In contrast, variance refers to the sensitivity of the data to fluctuations. Overly complex models are prone to variance errors from overfitting. For example, in a linearly distributed dataset, a high-order polynomial model may misinterpret small deviations. During training, the model's complexity increases, and its predictive performance improves, thereby decreasing bias. For some algorithms, if training is not stopped in time, the variance increases due to overfitting. Figure 2.8 depicts the non-monotonic relationship between predictive performance and model complexity, which is called the bias-variance tradeoff.

Cross-Validation (CV) Cross-validation (CV) is one of the most widely used methods to estimate the prediction error. The general idea is to create distinct training and validation datasets. Models are then trained and validated on these datasets. The validation results are then combined (e.g., by averaging) to obtain an estimate of the model's actual predictive performance. The methods can be categorized based on whether they are exhaustive. An exhaustive algorithm generates all possible combinations without randomness. Leave-p-out and leave-one-out CV are members of exhaustive algorithms. In contrast,

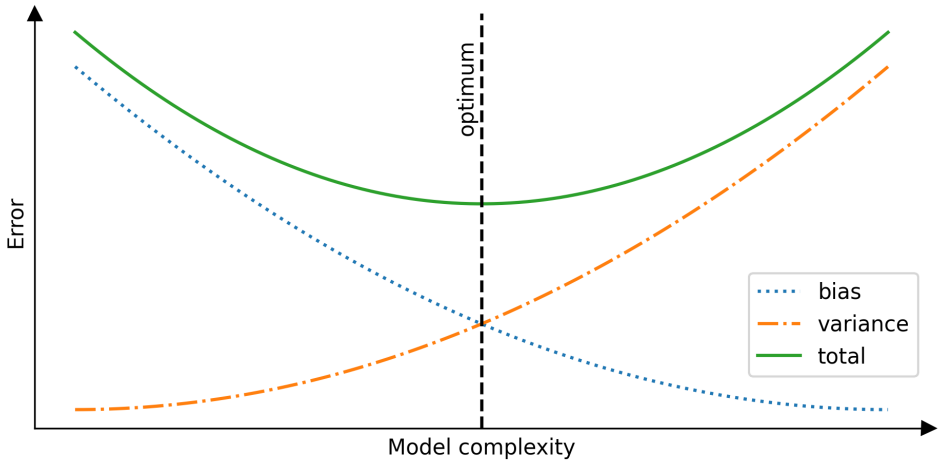

Figure 2.8: Illustration of the bias-variance-tradeoff. At low model complexity, the bias error is high due to inadequate modeling. Increasing the model complexity reduces bias error but increases variance error. At a certain point, an optimal balance between bias and variance is achieved.

non-exhaustive algorithms only test a subset of possibilities, which induces randomness. Monte Carlo and k-fold CV are members of non-exhaustive algorithms.

Leave-p-out cross-validation (LpOCV) iteratively reserves p validation from the dataset. The remaining data is used for training in each iteration. Therefore, due to its exhaustive nature, the number of iterations scales binomially $\binom{M}{p}$, which may become infeasible to compute for large M and certain p.

Leave-one-out cross-validation (LOOCV) is the special LpOCV case where $p = 1$. This means that every observation is used exactly once as a validation observation and $M - 1$ times as a training observation. This limits the number of iterations to M, which is significantly lower than LpOCV yet still higher than for other CV methods.

K-fold CV randomly partitions the dataset into k approximately equally sized groups. Consequently, each partition will contain M/k observations on average. From these partitions, k folds are created, where the i-th fold uses the i-th partition as the validation dataset and the union of the remaining partitions as the training dataset. These partitions are called folds. The model is subsequently trained and tested in each fold. Again, in the special case of $k = 1$, k-fold CV is equivalent to LOOCV.

The Monte Carlo CV repeatedly resamples the dataset to obtain training and validation sets with a predefined test size. In contrast to the k-fold CV, the number of iterations can be selected independently of the test size.

Imbalanced partitioning may occur due to the random nature of the k-fold and the Monte Carlo CV. Therefore, to retain the original distribution, stratification may be used, which ensures that the class distribution in each partition is approximately equal (and thus equal to the original dataset).

LpOCV, LOOCV, and Monte Carlo CV are used for small datasets because many training and test sets are generated. At the same time, this implies that the different iterations are highly interdependent. Conversely, k-fold CV reduces interdependence and is preferred for sufficiently large datasets.

Hyperparameter Hyperparameters are model parameters that define the model's structure or learning process, which are not adjusted during training. Examples of hyperparameters include the number of layers in a multilayer perceptron (MLP) or the maximum tree depth in a decision tree (DT). Hyperparameters are commonly optimized before the actual training process begins. The detailed process is described in Section 2.4.2.

Data Leakage Data leakage refers to information in the training set that is not available at prediction time, leading to overly optimistic performance estimates and overtraining [79]. This may occur if the data pipeline is not carefully designed. There are two types of leakage: feature and training-sample leakage. Feature leakage (column-wise) occurs when some features are included in the training dataset but are unavailable at prediction time. The most obvious and extreme example is when the target is included in the training features. Training sample leakage (row-wise) occurs when, for example, duplicate test dataset samples are included in the training dataset. More subtle are indirect leaks, in which transformed information is introduced into the training dataset. This is the case, for example, when standardization is applied to the entire dataset at once rather than being fit on the training dataset and only applied to the test set.

Outlier and Novelty In a dataset, outliers or anomalies are inconsistencies, describing data points that differ significantly from the rest of the data [74, 80]. In contrast, novelty data are new in that they were not encountered during training. Hence, outlier and novelty detection are similar concepts but with distinct goals. Detecting outliers before training is beneficial for machine learning algorithms that are highly sensitive to outliers, such as LDA. Detecting novelty is practical in gas-sensing applications, where false-positive classifications should be avoided.

Model Performance Metrics To evaluate and compare models, certain metrics need to be calculated. Here, a case with C classes is assumed. Additionally, the true (actual) label array $\boldsymbol{y}_{\text{true}}$ and the predicted label array $\boldsymbol{y}_{\text{pred}}$ are provided from the test. A confusion matrix (CM), also known as an error matrix, is a table that visualizes the predictive performance of an algorithm. The rows of the CM correspond to the actual conditions, whereas the columns correspond to the predicted conditions. When observing individual classes, a binary CM can be created according to Table 2.2. The true positive (TP), true

Table 2.2: Binary CM. This can be applied to a multiclass case, focusing on a single class c and only considering *is c* or *not c*.

	Predicted		
True	c	not c	Total
c	TP	FN	$\text{TP} + \text{FN} = M_c$
not c	FP	TN	$\text{FP} + \text{TN} = M - M_c$
Total	$\text{TP} + \text{FP} = \left\lvert\left\{y \in \boldsymbol{y}_{\text{pred}} \,\middle\vert\, y = c\right\}\right\rvert$	$\text{TP} + \text{FP} = \left\lvert\left\{y \in \boldsymbol{y}_{\text{pred}} \,\middle\vert\, y \neq c\right\}\right\rvert$	$\text{TP} + \text{FN} + \text{FP} + \text{TN} = M$

negative (TN), false positive (FP), and false negative (FN) values of a certain class c can be directly calculated from $\boldsymbol{y}_{\text{true}}$ and $\boldsymbol{y}_{\text{pred}}$ according to Equation 2.23.

$$\begin{aligned} \text{TP} &= \left|\left\{i \in \mathbb{I}_{\text{test}} \mid y_{\text{true},i} = c \text{ and } y_{\text{pred},i} = c\right\}\right| \\ \text{TN} &= \left|\left\{i \in \mathbb{I}_{\text{test}} \mid y_{\text{true},i} \neq c \text{ and } y_{\text{pred},i} \neq c\right\}\right| \\ \text{FP} &= \left|\left\{i \in \mathbb{I}_{\text{test}} \mid y_{\text{true},i} \neq c \text{ and } y_{\text{pred},i} = c\right\}\right| \\ \text{FN} &= \left|\left\{i \in \mathbb{I}_{\text{test}} \mid y_{\text{true},i} = c \text{ and } y_{\text{pred},i} \neq c\right\}\right| \end{aligned} \tag{2.23}$$

Table 2.3 shows the multiclass CM, where the elements $m_{k,k'}$ are the corresponding occurence count according to Equation 2.24.

$$m_{k,k'} = \sum_{i}^{M_{\text{test}}} \mathcal{I}\left(y_{\text{true},i} = c_k \text{ and } y_{\text{pred},i} = c_{k'}\right) \quad \forall k \in \{1, \ldots, C\} \tag{2.24}$$

Some class-specific quantities can therefore be simplified according to Equation 2.25.

Table 2.3: Multiclass CM. Compared to the binary CM (Table 2.2), the multiclass CM does not focus on a single class.

	Predicted			
True	c_1	…	c_C	Total
c_1	m_{11}	…	m_{1C}	$\sum_{k'}^{C} m_{1k'} = M_0$
⋮	⋮	$m_{k,k'}$	⋮	⋮
c_C	m_{C1}	…	m_{CC}	$\sum_{k'}^{C} m_{Ck'} = M_C$
Total	$\sum_{k}^{C} m_{k1}$	…	$\sum_{k}^{C} m_{kC}$	$\sum_{k}^{C}\sum_{k'}^{C} m_{k,k'} = M$

$$\begin{aligned} \text{TP}_k &= \text{TP}_{k'} = m_{k,k} \\ \text{TP}_{k'} + \text{FP}_{k'} &= \sum_{k}^{M} m_{k,k'} \\ \text{TP}_k + \text{FN}_k &= \sum_{k'}^{M} m_{k,k'} = M_k \\ &\forall k, k' \in \{1, \ldots, C\} \end{aligned} \tag{2.25}$$

With these, three important metrics – precision $\in [0, 1]$ (PRC), recall $\in [0, 1]$ (REC), and F1-score $\in [0, 1]$ (F1) – can be calculated with regards to a class k according to Equation 2.26, Equation 2.27, and Equation 2.28, respectively.

$$\text{PRC}_k = \frac{\text{TP}_k}{\text{TP}_k + \text{FP}_k} = \frac{m_{k,k}}{\sum_i m_{i',k}} \tag{2.26}$$

$$\text{REC}_k = \frac{\text{TP}_k}{\text{TP}_k + \text{FN}_k} = \frac{m_{k,k}}{\sum_{j'} m_{i,j'}} = \frac{m_{k,k}}{M_k} \tag{2.27}$$

$$\text{F1}_k = 2\frac{\text{PRC}_k \cdot \text{REC}_k}{\text{PRC}_k + \text{REC}_k} \tag{2.28}$$

$$\forall k \in \mathbb{I}_{\text{test}}$$

For a certain class $c_{k'}$, the PRC analyzes the k'-th column of the multi-class CM, meaning it describes how often $c_{k'}$ is correctly predicted relative to how often $c_{k'}$ is predicted at all. Conversely, REC analyzes rows of the CM and describes how often c_k is correctly predicted relative to how many c_k observations are actually present. Therefore, FPs significantly reduces PRC, whereas FNs severely reduces REC. Consequently, PRC and REC can be selectively used in different cases where one type of error has a higher priority over the other. Two examples are presented next to further illustrate the differences between these two quantities. For spam detection, where it is more detrimental to accidentally put important emails into the spam folder (FPs), the PRC is valued over REC to avoid FPs. In contrast, for preliminary contraband detection, failing to detect the contraband (FN) is much more relevant, as a FP can be easily corrected by further investigations. The F1-score (or more generalized F_β) balances these two quantities by forming the harmonic mean. All three quantities are used to evaluate and compare the models in this work with F1-score as the figure of merit.

2.4.2. Machine Learning Workflow

A generalized workflow structure is presented in the following list [81].

1. Data collection
2. Preprocessing
3. Iterative model optimization
    a) Training
    b) Testing
4. Model deployment

While there is an inherent order, most real-world cases require revisiting previous steps iteratively.

Data collection First, sufficient data must be collected, e.g., through repeated measurements. This typically results in a table consisting of observation rows and feature columns as previously shown in Section 2.4.1.

Preprocessing In most real-world cases, the application of machine learning algorithms directly on the "raw" datasets results in bad performances or even complete failure [81]. Therefore, preprocessing steps, a loose term for all data manipulation steps performed before training the model, are required. Some common preprocessing steps are listed in [82].

- Cleaning and correction: identifying and removing missing, duplicate, irrelevant, or erroneous data
- Transformation: Change of data format, structure, or values
- Augmentation: Addition of artificially modified copies to the training dataset

- Balancing: Mitigation of data distribution imbalances

Training One part of the dataset, $(\boldsymbol{X}_{\text{train}}, \boldsymbol{y}_{\text{train}})$, is used to train the machine learning models, while the other part, $(\boldsymbol{X}_{\text{test}}, \boldsymbol{y}_{\text{test}})$, is reserved for testing. This separation must be strictly upheld to prevent any data leakage as mentioned in Section 2.4.1. If applicable and required, hyperparameters are optimized first, which is called hyperparameter tuning. Given a predefined parameter space (range and resolution), the two most naive optimization algorithms are random search and grid search. As the name suggests, random hyperparameter combinations are selected and evaluated in a random search, whereas the complete parameter space is exhaustively evaluated in a grid search. The models trained with the selected hyperparameters are evaluated via CV. Thereafter, the hyperparameter-optimized models are trained on the entire training dataset.

Testing Finally, the previously trained models are evaluated using the test dataset $(\boldsymbol{X}_{\text{test}}, \boldsymbol{y}_{\text{test}})$. For this, the model is applied to the test input observations $(\boldsymbol{X}_{\text{test}})$ and the resulting predictions $(\boldsymbol{y}_{\text{pred}})$ are recorded. Finally, the classification metrics are calculated using $\boldsymbol{y}_{\text{pred}}$ and $\boldsymbol{y}_{\text{test}}$ $(= \boldsymbol{y}_{\text{true}})$ as previously presented in Section 2.4.1.

2.4.3. Linear Discriminant Analysis

The arithmetic mean vector $\boldsymbol{\mu}$ is calculated according to Equation 2.29, whereas the class-specific arithmetic mean vector $\boldsymbol{\mu}_c$ is calculated according to Equation 2.30.

$$\boldsymbol{\mu} = \frac{1}{M} \sum_{i=1}^{M} \boldsymbol{x}_i \tag{2.29}$$

$$\boldsymbol{\mu}_c = \frac{1}{M_c} \sum_{i \in \mathbb{I}^c} \boldsymbol{x}_i \tag{2.30}$$

LDA is a statistical and supervised classification algorithm that analyzes the differences between two or more classes [83]. It was first introduced by Fisher in 1936 for classifying flowers [84]. LDA remains one of the most widely used algorithms for eNose applications [85, 86]. LDA can be used to evaluate the discriminatory power of the features (discrimination task), and/or to predict the class membership of new observations (classification task) [83]. In this work, both tasks are being used. For classification tasks, the LDA model first reduces dimensionality via a linear mapping. The training of the LDA model is, in fact, to find the transformation matrix of this mapping, such that the separation between the class mean points is maximized. At the same time, the separation of data points within each class is minimized. Details about the calculation and application of the transformation matrix are discussed extensively later. Finally, within the low-dimensional discriminant space, a classification based on distance to the class mean can be applied for prediction. Both the training and application are fast and efficient because the computations are mostly well-understood and well-optimized matrix operations. The LDA's training and prediction procedures are illustrated in a flowchart in Figure 2.9.

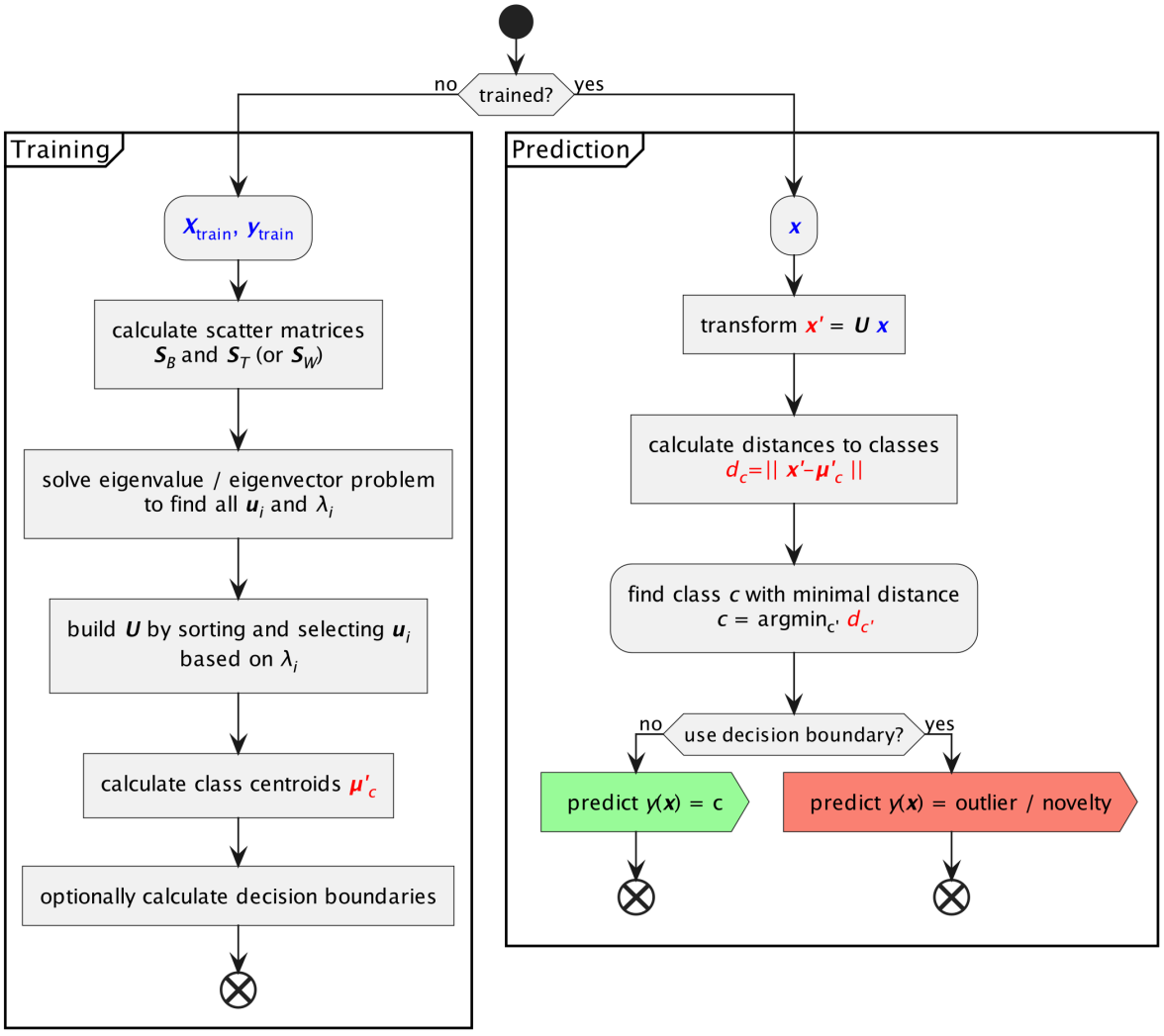

Figure 2.9: LDA activity flow chart. Left: training, right: prediction.

Requirements The reliable usage of LDA has several requirements on the training dataset, especially regarding the number of observations. First, "number of groups should not be larger than the number of describing variables" [83, p. 210] ($C \leq N$). Additionally, each class should contain at least 20 observations for statistically significant results ($M_c \geq 20$)[83]. Moreover, the number of observations should be evenly distributed across the classes (a balanced dataset), which may negatively impact classification performance [75, 76, 83]. Strictly speaking, the feature data needs to be normally distributed because of the underlying mathematical assumptions of the LDA [41]. However, in real-world applications, an exact normal distribution is usually neither given nor realistic. Nonetheless, LDA is tolerant towards slight deviations [41, 87].

Transformation The so-called discriminant features (or simply discriminants) span the discriminant space. By linear transformation, a weight vector $\boldsymbol{u}$ can transform an observation $\boldsymbol{x}$ into a single discriminant feature x' according to Equation 2.31.

$$x' = \boldsymbol{x}^\top \boldsymbol{u} = \underbrace{\boldsymbol{x} \cdot \boldsymbol{u}}_{\text{scalar product}} = \sum_{i=1}^{N} x_i \cdot u_i \tag{2.31}$$

In the more generalized case, a transformation matrix $\boldsymbol{U} = [\boldsymbol{u}_1, \ldots, \boldsymbol{u}_{N'}]$ containing individual weight column vectors u_j, can transform the observation matrix $\boldsymbol{X} \in \mathbb{R}^{MxN}$ into $\boldsymbol{X'} \in \mathbb{R}^{MxN'}$ ($N' \leq \min\{N, C-1\}$) with rows of transformed observations $\boldsymbol{x}_i'^\top \in \mathbb{R}^{N'}$ and columns of discriminant features Equation 2.32.

$$\boldsymbol{X'} = \begin{bmatrix} \boldsymbol{x}_1'^\top \\ \vdots \\ \boldsymbol{x}_i'^\top \\ \vdots \\ \boldsymbol{x}_M'^\top \end{bmatrix} = \begin{bmatrix} \boldsymbol{x}_1 \cdot \boldsymbol{u}_1 & \ldots & \boldsymbol{x}_1 \cdot \boldsymbol{u}_{N'} \\ \vdots & \boldsymbol{x}_i \cdot \boldsymbol{u}_j & \vdots \\ \boldsymbol{x}_M \cdot \boldsymbol{u}_1 & \ldots & \boldsymbol{x}_M \cdot \boldsymbol{u}_{N'} \end{bmatrix} = \boldsymbol{X}\boldsymbol{U} \tag{2.32}$$

The task is now to find the optimal $\boldsymbol{u}$ or rather $\boldsymbol{U}$. There are several equivalent criteria, two of which are presented in Equation 2.33 [41].

$$\arg\max_{\boldsymbol{u}} \frac{\text{between-class scatter}}{\text{within-class scatter}} = \arg\max_{\boldsymbol{u}} \frac{\text{between-class scatter}}{\text{total scatter}} \tag{2.33}$$

To calculate the scatter quantities, the corresponding scatter matrices are defined as follows: the between-class scatter matrix ($\boldsymbol{S}_\text{B}$), the within-class scatter matrix ($\boldsymbol{S}_\text{W}$), and the total scatter matrix ($\boldsymbol{S}_\text{T}$). $\boldsymbol{S}_\text{B}$, $\boldsymbol{S}_\text{W}$, and $\boldsymbol{S}_\text{T}$ are calculated according to Equation 2.34, Equation 2.35, and Equation 2.36, respectively.

$$\boldsymbol{S}_\text{B} = \sum_{c \in \mathbb{G}} M_c \cdot \underbrace{(\boldsymbol{\mu}_c - \boldsymbol{\mu})(\boldsymbol{\mu}_c - \boldsymbol{\mu})^\top}_{\text{class mean scatter mat. of } c} \tag{2.34}$$

$$\boldsymbol{S}_\text{W} = \underbrace{\sum_{c \in \mathbb{G}} \sum_{i \in \mathbb{I}_c} (\boldsymbol{x}_i - \boldsymbol{\mu}_c)(\boldsymbol{x}_i - \boldsymbol{\mu}_c)^\top}_{\text{scatter mat. within class } c} \tag{2.35}$$

$$\boldsymbol{S}_\text{T} = \sum_{i=1}^{M} (\boldsymbol{x}_i - \boldsymbol{\mu})(\boldsymbol{x}_i - \boldsymbol{\mu})^\top = \boldsymbol{X}^* \boldsymbol{X}^{*T} \tag{2.36}$$

Here, the asterisk denotes the variable's centralized version. E.g. $\boldsymbol{x}^* = \boldsymbol{x} - \boldsymbol{\mu}$ and $\boldsymbol{X}^* = \boldsymbol{X} - \boldsymbol{J}_{M,1}\,\boldsymbol{\mu}$, where $j_{m,n} = 1$. The three scatter matrices are not linearly independent, as one can always be expressed as a linear combination of the other two: $\boldsymbol{S}_\text{T} = \boldsymbol{S}_\text{B} + \boldsymbol{S}_\text{W}$. The fractions in Equation 2.33 require either $\boldsymbol{S}_\text{W}$ or $\boldsymbol{S}_\text{T}$. Usually, total scatter is preferred over within scatter for computational stability and a normalization property that will be discussed later. As shown in Equation 2.37, the maximization

problem in Equation 2.33 can be redefined for a single weight vector $\boldsymbol{u}$ (Equation 2.31), $\boldsymbol{S}_\mathrm{B}$ (Equation 2.34), and $\boldsymbol{S}_\mathrm{T}$ (Equation 2.36).

$$\arg\max_{\boldsymbol{u}} \frac{\text{between-class scatter}}{\text{total scatter}}$$

$$\begin{aligned}
&= \arg\max_{\boldsymbol{u}} \frac{\sum_{c\in\mathbb{G}} M_c\,(\boldsymbol{u}^\top\boldsymbol{\mu}_c - \boldsymbol{u}^\top\boldsymbol{\mu})^2}{(\boldsymbol{X}^*\boldsymbol{u})^\top(\boldsymbol{X}^*\boldsymbol{u})} \\
&= \arg\max_{\boldsymbol{u}} \frac{\sum_{c\in\mathbb{G}} M_c\,\boldsymbol{u}^\top(\boldsymbol{\mu}_c - \boldsymbol{\mu})(\boldsymbol{\mu}_c - \boldsymbol{\mu})^\top\boldsymbol{u}}{\boldsymbol{u}^\top\boldsymbol{X}^{*\top}\boldsymbol{X}^*\boldsymbol{u}} \\
&= \arg\max_{\boldsymbol{u}} \frac{\boldsymbol{u}^\top[\sum_{c\in\mathbb{G}} M_c\,(\boldsymbol{\mu}_c - \boldsymbol{\mu})(\boldsymbol{\mu}_c - \boldsymbol{\mu})^\top]\boldsymbol{u}}{\boldsymbol{u}^\top\boldsymbol{X}^{*\top}\boldsymbol{X}^*\boldsymbol{u}} \\
&= \arg\max_{\boldsymbol{u}} \frac{\boldsymbol{u}^\top\boldsymbol{S}_\mathrm{B}\boldsymbol{u}}{\boldsymbol{u}^\top\boldsymbol{S}_\mathrm{T}\boldsymbol{u}} = \arg\max_{\boldsymbol{u}} \mathrm{SQ}(\boldsymbol{u})
\end{aligned} \tag{2.37}$$

The value of the fraction is the separation quotient (SQ), which is an indication of the separation strength of $\boldsymbol{u}$. To solve the maximization of SQ, the equivalent eigenvalue/eigenvector problem can be solved according to Equation 2.38 [41].

$$\boldsymbol{S}_\mathrm{B}\,\boldsymbol{u} = \lambda\,\boldsymbol{S}_\mathrm{T}\,\boldsymbol{u} \iff \boldsymbol{S}_\mathrm{T}^{-1}\,\boldsymbol{S}_\mathrm{B}\,\boldsymbol{u} = \lambda\,\boldsymbol{u} \tag{2.38}$$

For the special case with only two classes, a simpler matrix equation can be solved [41]. The solution of the eigenvalue/eigenvector problem in Equation 2.38 results in $C-1$ pairs of eigenvectors and eigenvalues $\{(\boldsymbol{u}_i, \lambda_i) \mid i \in \{1,\ldots,C-1\}\}$. The eigenvalues λ_i represent the corresponding SQs of $\boldsymbol{u}_i$. They are normalized to the range $[0,1]$ if total scatter is used as in Equation 2.37. Therefore, the pairs $(\boldsymbol{u}_i, \lambda_i)$ are ranked $\lambda_i \geq \lambda_j\ \forall i < j$ such that the top $\boldsymbol{u}_i$ contributes the most to the separation. Generally, only a subset, consisting of the top $N' \in \{1,\ldots,C-1\}$ eigenvectors $\boldsymbol{u}_i$, is used, as leaving some low-ranking ones out may result in a better classification and computational performance [41]. The selected eigenvectors are concatenated as column vectors to the transformation matrix $\boldsymbol{U} \in \mathbb{R}^{N\times N'}$ and can be used as intended (refer to Equation 2.32).

Classification Next, the classification is performed. After transforming the initial N features to N' discriminant features, the data are grouped into clusters, each with a class centroid $\boldsymbol{\mu}_c{}'^\top = \boldsymbol{\mu}_c{}^\top\boldsymbol{U}$ in the discriminant space. Subsequently, any input feature $\boldsymbol{x}$ is predicted as the class with the minimal Euclidean distance d_c according to Equation 2.39.

$$y(\boldsymbol{x}) = \arg\min_c\ d_c = \arg\min_c \left\|\boldsymbol{x}^\top\boldsymbol{U} - \boldsymbol{\mu}_c{}'^\top\right\| \tag{2.39}$$

In real-world cases, especially in eNose applications, outliers and novel observations may occur. The minimal Euclidean distance classification criterion (Equation 2.39) will, without exception, predict one of the C classes, even if the observation is an outlier or a novelty with large Euclidean distances to any class centroids. One method to circumvent this is to implement decision boundaries (DBs) for each class. Each DB is centered around the corresponding class centroid. Now, the minimal Euclidean

distance criterion (Equation 2.39) is only used if the data point is within at least one DB. Otherwise, the data point is considered an outlier or a novelty according to Equation 2.40.

$$y(\boldsymbol{x}) = \begin{cases} \arg\min_c \ d_c & \text{if } \boldsymbol{x}' \text{ inside of the DB of } c \\ \text{novelty/outlier} & \text{otherwise} \end{cases} \tag{2.40}$$

One approach is to construct a multidimensional ellipsoid for each class c where the i-th semi-axis' half-length is calculated according to Equation 2.41.

$$r_{c,i} = \sigma_{c,i} \cdot z \tag{2.41}$$

Here, $\sigma_{c,i}$ is the SD of class c in the i-th discriminant feature and z is a predetermined z-score. Alternatively, the weight vectors $\boldsymbol{u}_i$ can be scaled with $\sqrt{(M-C)/(\lambda_i - \lambda_i^2)}$. This results in spherically distributed data points around each corresponding class centroids on average [41]. The scaling of $\boldsymbol{u}_i$ is possible because SQ is invariant towards multiplication of arbitrary scalars (refer to Equation 2.37). Consequently, the radius of the DB for class c can be calculated depending on a predefined confidence interval (CI) according to Equation 2.42 [41].

$$r_c = \sqrt{\frac{N'(M-C)}{M-C-N'+1} \frac{M_c+1}{M_c} F_{CI}(N', M-C-N'+1)} \tag{2.42}$$

Here, $F_{CI}(\mathrm{DoF}_1, \mathrm{DoF}_2)$ is the quantile of the F-distribution with the corresponding degrees of freedom DoF_1 and DoF_2, which can be found, e.g., in a lookup table.

LDA Plots A LDA-plot (or LDA-display) is a graphical representation of the transformed observations in the LDA space. For this, the data points to be plotted are first mapped to the LDA space by $\boldsymbol{U}$ as shown in Figure 2.10. The data points are typically presented in the first two discriminants, whereas the other discriminants with lower separation power are omitted in the plot. In addition, the class centroids and the previously mentioned decision boundaries are plotted to illustrate the class regions clearly.

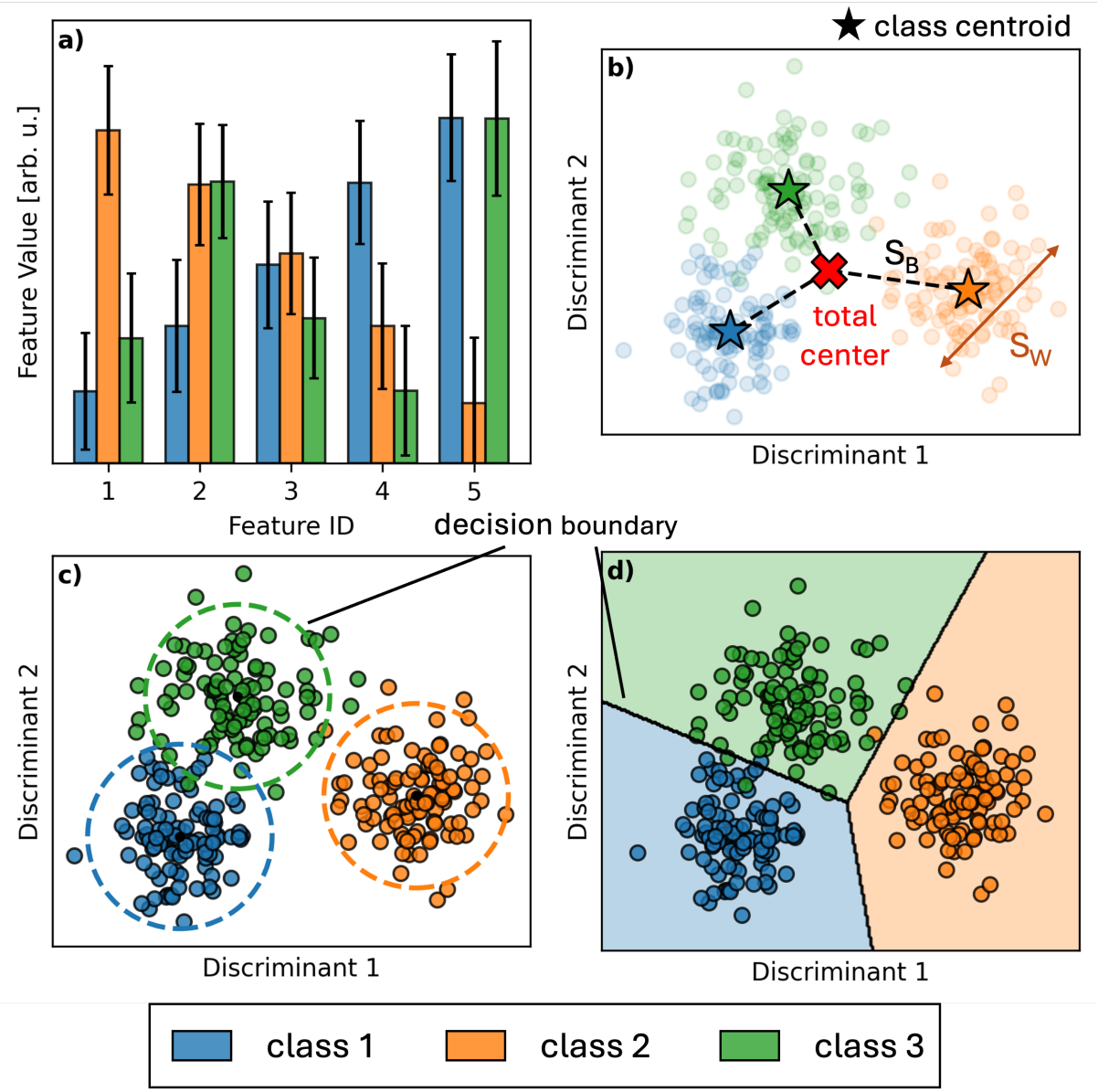

Figure 2.10: Exemplary LDA-Plot. Three exemplary classes (1, 2, and 3) are used. a) Different feature patterns. b) LDA maximizes the between class spread (S_B) to within class spread (S_W) ratio. c) Spherical decision boundary around the class centroids. Observations outside any decision boundary are detected as novelties or outliers. d) If only the minimum distance is used, the hyperplanes between the classes are used as decision boundaries.

2.4.4. Decision Tree and Random Forest

DTs and RFs are closely related machine learning algorithms, where the RF consists of multiple DTs. Therefore, the fundamental basis behind DTs is introduced first.

2.4.4.1. Decision Tree

0 A DT is a machine learning method that, as the name suggests, is structured like a tree. As depicted by Figure 2.11, the decision path starts at the initial root node, traverses through branch nodes, and ends at leaf nodes, which ultimately predicts a class [78, 88]. Generally, a DT can handle both discrete

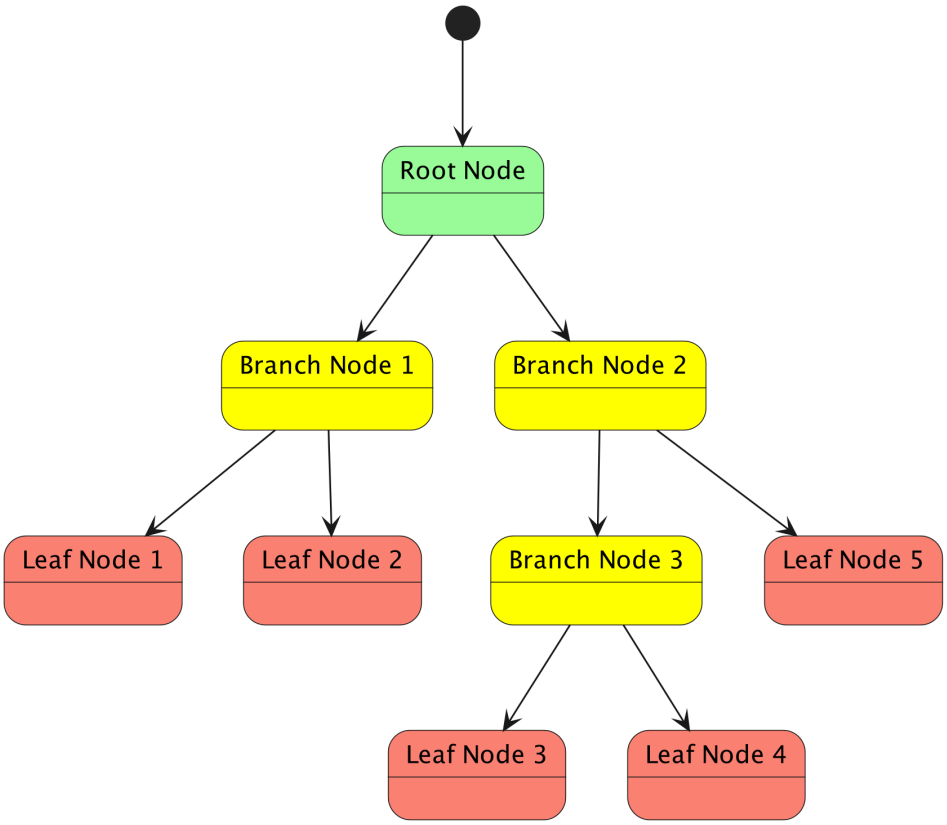

Figure 2.11: DT structure. The decision process starts at the root node (green) and propagates through branch nodes (yellow) to a final leaf node (red) with the final prediction.

(categorical) and continuous features simultaneously. Nodes may be split into more than two child nodes, but this is generally not recommended due to data fragmentation [78]. Additionally, DTs can be utilized either for regression or classification tasks. Only binary splitting and classification DTs with continuous feature values are relevant for this work and are considered for further discussion.

Tree Node Generation To each node o, a data partition $D_o = (\boldsymbol{X}_o, \boldsymbol{y}_o)$ is passed, containing $M_o \leq M$ observations, a subset of features $\mathbb{F}_o \subseteq \mathbb{F}\,(|\mathbb{F}_o| = N_o \leq N)$ and a subset of classes $\mathbb{G}_o \subseteq \mathbb{G}\,(|\mathbb{G}_o| = C_o \leq C)$. The majority class is defined as $c_{maj} = \arg\max_c P_c$, where P_c is the proportion (or occurence probability) of class c according to Equation 2.43.

$$P_c = \frac{1}{M_o} \sum_{y \in \boldsymbol{y}_o} \mathcal{I}\,(y = c) \tag{2.43}$$

For the recursive process, the two termination conditions are introduced first. The primary termination condition is met when there is only one class left ($C_o = 1$), which is naturally c_{maj}. The secondary termination condition is satisfied when no further features remain ($N_o = 0$). In both cases, a leaf node is created and labeled as c_{maj}. Additional termination conditions can be set as hyperparameters, such as the maximum number of leaf nodes.

If no termination condition is met, the initial data partition D_o is divided into multiple sub-partitions $D_{o,i} = \left(\boldsymbol{X}_{o,i}, \boldsymbol{y}_{o,i}\right)$. Each $D_{o,i}$ is passed to a child node, which in turn is attached to the current (parent) node o. If $D_{o,i}$ is empty ($M_{o,i} = 0$), the child node is immediately set as a final leaf node and labeled as c_{maj}. Otherwise, the recursive generation algorithm is applied to the child node. The complete flow chart of the recursion is shown in Figure 2.12.

Splitting In principle, there are many, and in the case of continuous values, infinitely many possible ways to split at each node. Therefore, it is crucial to find the optimal split that yields the best classification result. In the split, the partition D_o is tested on a specific feature f using a threshold k_f for that feature. The optimal split happens when using the splitting criterion, which is the optimal feature and threshold combination $k_{f,\text{opt}}$. The task is now to find $k_{f,\text{opt}}$. For that, D_o is testwise split into $\left\{D_{k_f,1}, D_{k_f,2}\right\}$ for all possible combinations $k_f \in \mathbb{K}_f$ with $f \in \mathbb{F}_o$. The number of unique combinations is therefore given by $\sum_f \left|\mathbb{K}_f\right|$. Here, $\mathbb{K}_f$ is the set of mid-point values constructed from a sorted list of unique values of f. To quantify how good a k_f-split is, an impurity metric Q_{k_f} is calculated. This impurity metric is the weighted sum of the individual impurities of $D_{k_f,i}$ according to Equation 2.44:

$$Q_{k_f} = \frac{1}{2} \sum_{i=1}^{2} M_{k_f,i} \cdot Q(D_{k_f,i}) \tag{2.44}$$

Here, $M_{k_f,i}$ is the number of samples of the corresponding partition $D_{k_f,i}$, where $M_{k_f,1} + M_{k_f,2} = M_o$. The impurity quantifies the uniformity of the proportions of each class in D_o. The impurity reaches its maximum when $P_c = P_{c'} \; \forall \, c \neq c'$ and the lowest when only one class is left $P_c = P_{c_{maj}} = 1$. Low impurity implies high prediction confidence and vice versa. The feature and threshold values that minimize the weighted sum of the child impurities are selected as the splitting criterion.

$$k_{f,\text{opt}} = \arg\min_{k_f} Q_{k_f}$$

Three main impurity metrics exists: misclassification error Q_{mc} (Equation 2.45), Gini index Q_{gini} (Equation 2.46), and entropy Q_{e} (Equation 2.47).

$$Q_{\text{mc}} = 1 - P_{c_{maj}} = \frac{1}{M_o} \sum_{y \in \boldsymbol{y}} \mathcal{I}\left(y \neq c_{maj}\right) \tag{2.45}$$

$$Q_{\text{gini}} = \sum_{c \neq c'} P_c P_{c'} = \sum_{c \in \mathbb{G}} P_c (1 - P_c) \tag{2.46}$$

$$Q_{\text{e}} = -\sum_{c \in \mathbb{G}} P_c \log_2(P_c) \tag{2.47}$$

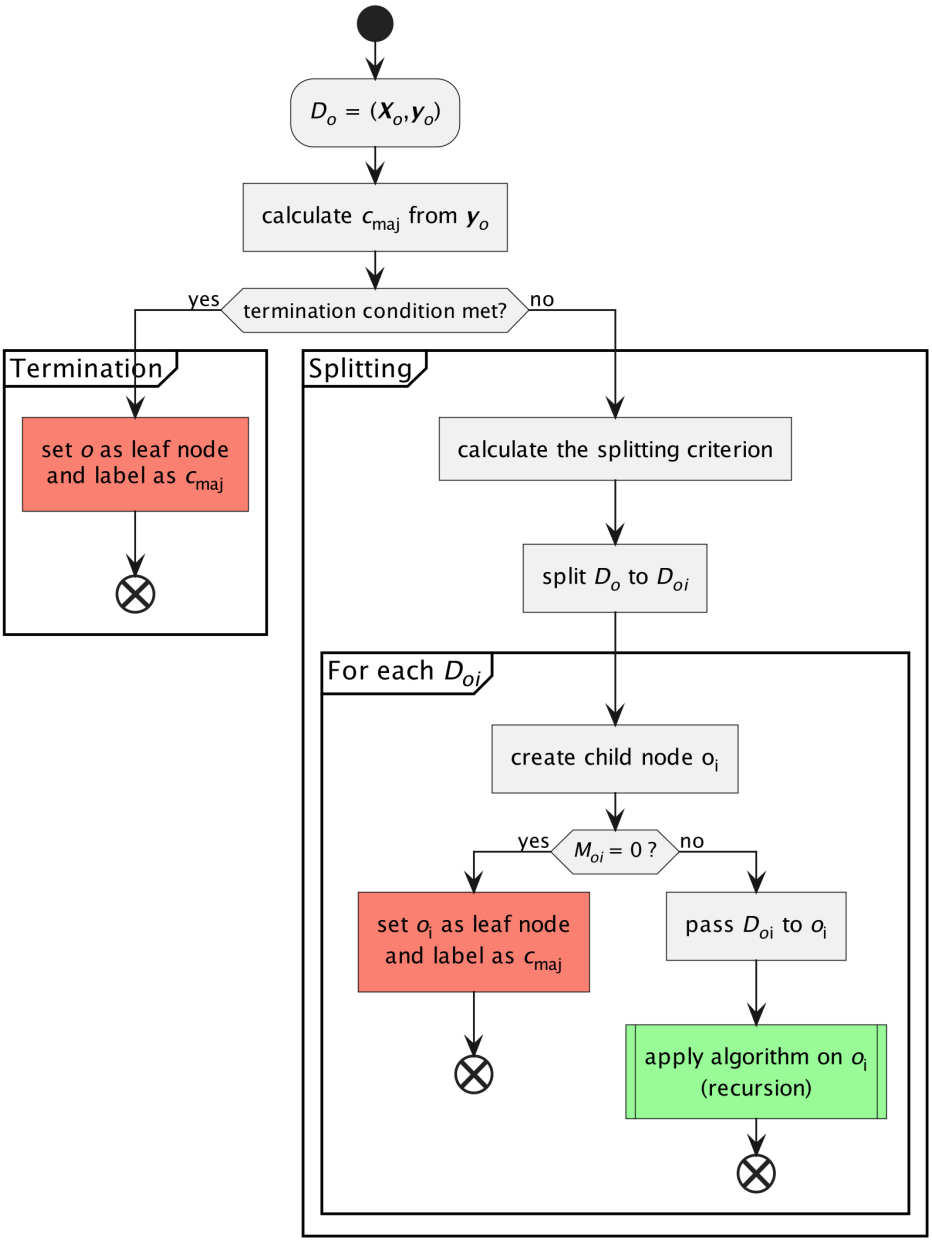

Figure 2.12: Flow chart of the recursive algorithm for node generation and splitting. The green process at the lower right corner calls the procedure itself recursively. Several termination conditions stop the recursion.

For numerical efficiency, the Gini index or entropy is preferred because they are differentiable [78].

DTs mainly face two issues: high variablity and overfitting [78]. The variability stems from the hierarchical structure, in which small changes in the initial input can yield vastly different tree structures and predictions. Overfitting occurs when a DT is overly large (deep) and captures noise or outliers in the training dataset. These limitations have motivated the development of RF, which combines multiple DTs to achieve enhanced robustness and accuracy, and is presented in the next section.

2.4.4.2. Random Forest

RF is a supervised machine learning method and consists of multiple DTs as depicted in Figure 2.13. The random part of an RF comes from the randomness of available training data each DT accesses, which will be discussed in more detail later. While a single decision tree can independently classify data, the RF mitigates the DT-typical problems of high variability and overfitting by using the bagging (bootstrap aggregating) method [78].

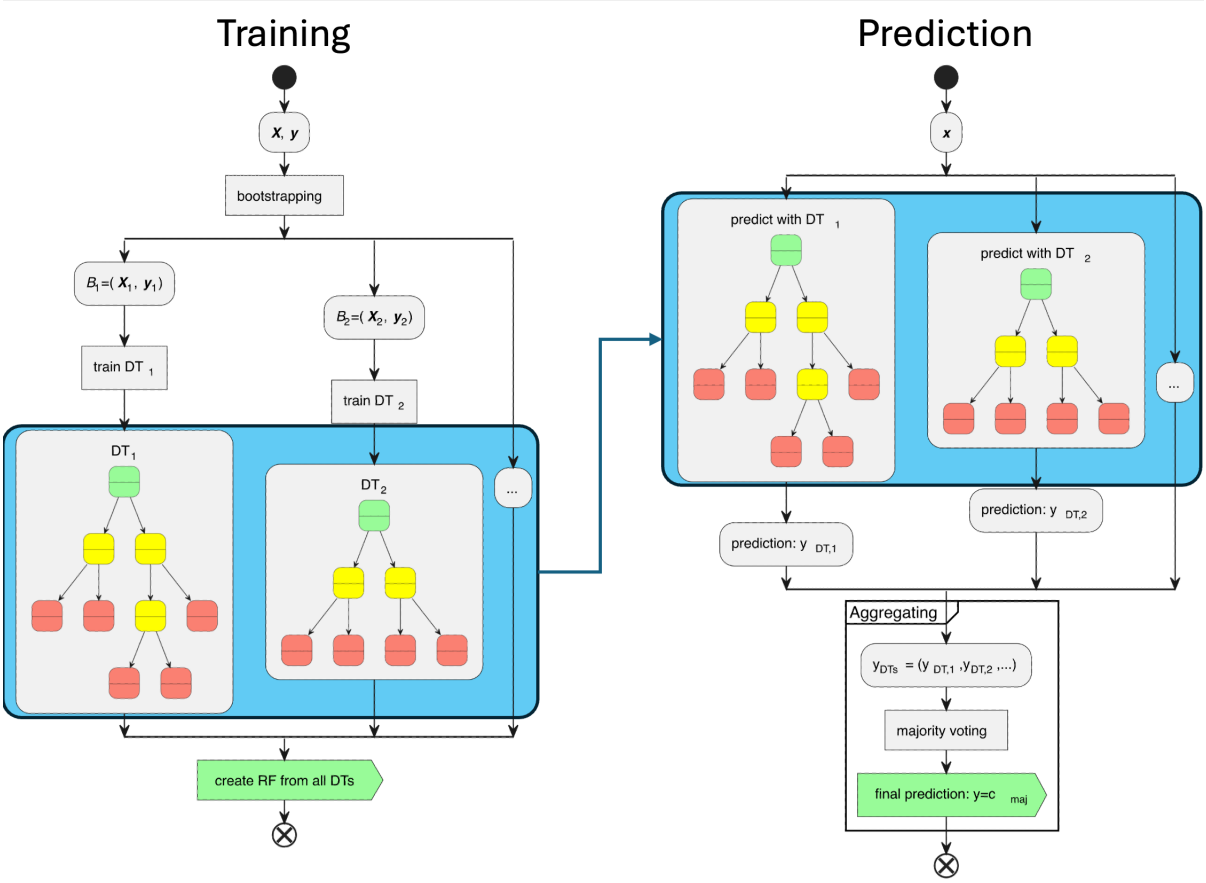

Figure 2.13: RF training and prediction flow chart. During training, the RF trains multiple DTs using the bootstrapped training data. During prediction, the predictions of all DTs are aggregated.

Bagging To construct individual DTs in the RF, the bagging method is used. Bagging refers to **b**ootstrapping and **agg**regat**ing**. Bootstrapping is used to create uniformly resampled datasets $\{B_i = (\boldsymbol{X}_i, \boldsymbol{y}_i) \mid 1 \leq i \leq N_t\}$ for an RF with N_t trees. Each resampled dataset has the same number of observations, $M_t \leq M$, but individual observations may be sampled multiple times. For each B_i, a DT is trained as shown in Figure 2.13. The random forest consists now of all trained DTs: RF = $(\mathrm{DT}_1, \mathrm{DT}_2, \ldots)$. At prediction

time, each tree DT_i makes a individual prediction y_{DT_i} and the combined prediction results of all trees is $\boldsymbol{y}_{\mathrm{DTs}} = (y_{\mathrm{DT}_1}, y_{\mathrm{DT}_2}, \ldots)$. The final aggregated result is obtained by majority voting, as in Equation 2.48.

$$y = \arg\max_{c} \sum_{i=1}^{N_t} \mathcal{I}\left(y_{\mathrm{DT}_i} = c\right) \tag{2.48}$$

2.4.4.3. Hyperparameters

Many hyperparameters can be optimized for DTs and RFs. They mainly address overfitting issues and may also help reduce computation time. For a DT, the main hyperparameter is the maximum depth of trees, which determines the maximum complexity [78]. If the maximum depth is too low, the DT may be too simple to adequately reflect the underlying feature-to-target relationship, leading to underfitting. In contrast, if the maximum depth is not restricted correctly, overfitting may occur. Next, the minimum number of samples required for further splitting can be set. The termination condition is relaxed to stop the splitting process earlier and reduce overfitting. Similarly, the minimum number of samples per leaf node (defaults to 1) can be increased to smooth the DT and reduce overfitting. Additionally, the maximum number of leaf nodes can be reduced further to mitigate overfitting. This number is unrestricted by default. For RF, specifically, the number of trees is the primary hyperparameter that needs to be adjusted depending on the given problem [78]. Too few trees limit the model's complexity and, in turn, negatively impact predictive performance. As the number of trees increases, the predictive performance of an RF improves but eventually stabilizes. Further increasing the number of trees does not (significantly) degrade predictive performance but unnecessarily adds computational complexity and should therefore be avoided.

2.4.4.4. Feature Importance

For a DT, the feature importance (FI) of a specific feature f is calculated by summing the mean decrease in impurity (MDI) of each node that splits using f. The MDI is calculated by subtracting the parent impurity Q_o from the weighted sum of the child impurities $Q(o_{f,i})$ according to Equation 2.49.

$$\mathrm{MDI}_f = \sum_{o \in \mathbb{O}_f} \left(Q_o - \sum_{i=1}^{2} M_{o,i} Q_{o,i} \right) \tag{2.49}$$

Where $\mathbb{O}_f$ is the set of all nodes that split using f. Finally, the feature importances FI_i are normalized according to Equation 2.50 such that $\sum_{i=1}^{N} \mathrm{FI}_{i,\mathrm{norm}} = 1$.

$$\mathrm{FI}_{i,\mathrm{norm}} = \frac{\mathrm{FI}_i}{\sum_{j=1}^{N} \mathrm{FI}_j} \tag{2.50}$$

In this work, feature importance is used to assess the usefulness of certain sub-sensors and operating points.

3. Experimental

This chapter presents the materials and methods used in the fabrication and characterization of chemiresistive and chemically-sensitive field-effect transistor (ChemFET) based electronic nose (eNose) sensors. First, the section on nanomaterial synthesis introduces the preparation of functional nanostructures with tailored morphologies aimed at chemiresistive sensing applications. The chemiresistive nanomaterials are used in combination with the chemiresistive sensor platform (CSP), which is presented in the next section. The following sections on inkjet printing and aerosol jet printing describe the additive manufacturing processes used for patterning and constructing ChemFET devices, with a focus on deposition accuracy, layer homogeneity, and reproducibility. The pre- and postprocessing procedures are explained in detail, as they are critical steps for ensuring device integrity and performance stability. Finally, the gas mixing system (GMS), which supplies the reference and target gases, is presented.

3.1. 1D Nanomaterial Synthesis

Nanomaterials, especially low-dimensional ones, are well-suited for gas sensing applications due to their high surface-to-volume ratios, which lead to higher sensitivities. In this work, the nanomaterials are used for chemiresistive sensing, and their specific synthesis methods are presented in this chapter.

3.1.1. Overview of Nanomaterials

Nanomaterials are characterized by the name-giving property of their nanometer-scale dimensions. A lower limit of approximately 1 nm = 10^{-9} m is set to avoid misclassifications between nanomaterials and atomic or molecular structures[1]. The nanomaterial can be categorized into 0D up to 3D materials as presented in Table 3.1.

Among these nanomaterials, 1D nanostructures, particularly nanowires (NWs) and nanofibers (NFs), have emerged as functional sensing materials for advanced sensing and devices. Networks of NWs or NFs exhibit a high specific surface area and a large surface-to-volume ratio, making them exceptionally valuable for applications spanning optoelectronics, gas sensing, energy storage, and catalysis[93]. The precise distinction between NW and NF is not standardized. Generally, NW refers to a monocrystalline whisker with a loosely defined diameter below around 100 nm to 400 nm [104, 105]. In contrast, a NF may exhibit a polycrystalline hierarchical structure containing substructures with an outer diameter of

[1] Fullerene molecules and graphene are exceptions to this limit [89].

Table 3.1: Overview of nanomaterials and morphologies. The materials are categorized by their dimensionality.

Dim.	Morphology	Material and application example
0D	quantum dot	Cd-based: displays [90]
	fullerene	C_{60}: biosensor [91]
	nanoparticle	Ag: electrode [92]
1D	nanofiber	multimaterial: battery [93]
	nanowire	SnO_2: UV sensor [94]
	nanobelt	SnO_2: gas sensor [95]
	nanorod	V_2O_5: supercapacitor [96]
	nanotube	carbon: chemical (aq) sensor [97]
2D	nanofilms	carbon: capacitors [98]
	nanosheet	TiO_2: gas sensor [99]
3D	nanocubes	carbon: biosensor [100]
	nanocages	Au: drug delivery [101]
	nanoflowers	Pt: catalysis [102]
	nanotetrapods	ZnO: wound care [103]

up to 1000 nm[93]. The hierarchical structure refers to the primary morphology of 1D fibers and to secondary morphologies, such as porosity and particle-like structures. In this work, metal oxides NWs and NFs are primarily used for chemiresistive sensing.

The ability to precisely control their morphology, crystallinity, and composition at the nanoscale has driven intensive research into synthesis methodologies that can reproducibly generate high-quality nanostructures with tailored properties. In the following sections, the two prominent yet complementary synthesis methods, vapor-liquid-solid (VLS) for NWs and electrospinning (ES) for NFs, are presented.

3.1.2. Electrospinning

Electrospinning (ES), also known as electrostatic spinning, is an electrohydrodynamic technique used to synthesize ultrafine wires and fibers in the micro- and nano-scale [93]. An electrospinning device generally consists of a high-voltage power supply, a spinneret (a biological reference and often in the form of a syringe), and a collector (or target) as depicted in Figure 3.1. The ES process initiates when a high-voltage electric field (typically 10 kV to 30 kV) is applied between the polymer solution and the grounded collector. At sufficiently high electric field strengths, exceeding a critical threshold E_{min}, electrostatic forces overcome the surface tension of the polymer solution, causing the formation of a Taylor cone. At the tip of the Taylor cone, a fine jet is accelerated toward the collector, thereby elongating and narrowing. The polymer solution wire accumulates at the stationary or spinning target. Finally, the solvent evaporates, and the polymer solidifies. One of ES' strengths is its versatility regarding material choice. It is particularly fitting for synthesizing metal oxide (MOX) and carbon-based NFs.

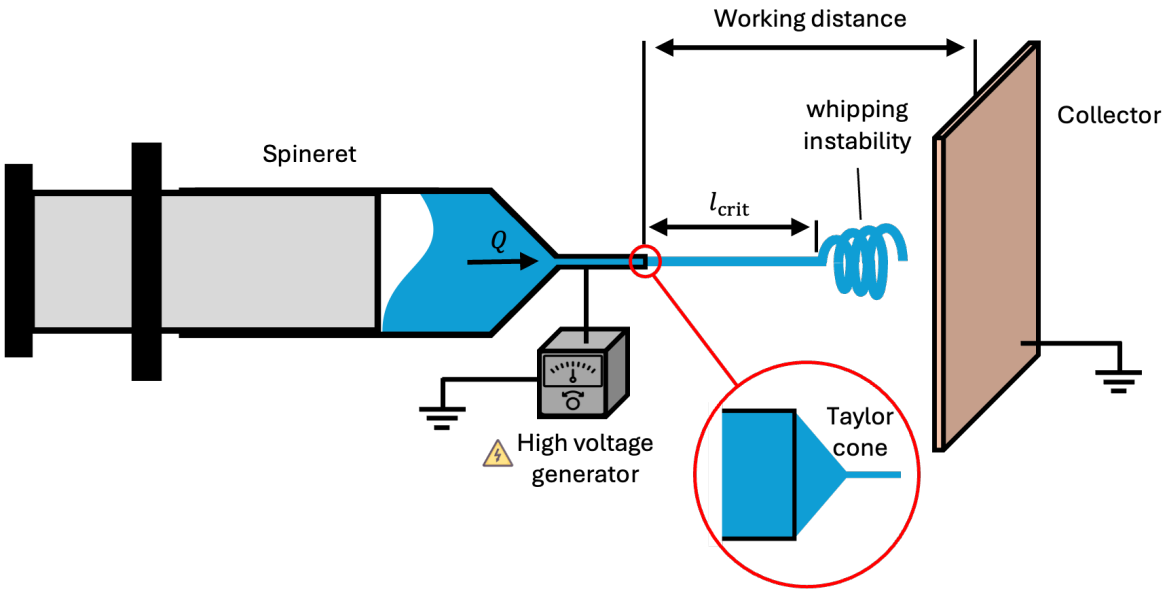

Figure 3.1: Electrospinning setup. The spineret is pushed automatically to create a precise flow rate at its tip Q. Through a high-voltage generator, a potential difference is created between the collector and the spinneret tip. The resulting electric field (E-field) forms a Taylor cone at the tip, which ends in a narrow jet. The jet is accelerated under the E-field and experiences whipping instability after a critical length l_{crit}. Consequently, the fibers randomly accumulate at the collector and are stripped after the ES process.

Taylor Cone At the core of the ES process is the controlled formation of the Taylor cone, which is named after Geoffrey I. Taylor in honor of his revolutionary work in that field [106]. A stable Taylor cone is formed if the electrostatic forces and the hydrostatic forces are in equilibrium, resulting in a thinning of the initial spineret diameter to obtain proper NFs. Under ideal assumptions, "1. an equipotential cone surface, 2. no space charge in the solution, 3. zero pressure difference between the solution and the surrounding air" [93, p. 17], the theoretical semi-vertical angle at the Taylor cone tip (Taylor angle θ) is derived to be 49.3°. For a non-zero pressure difference between the solution and the surrounding air, the Taylor cone is deformed [93].

Jetting Usually, a steady, continuous jet is desired to generate long, uniform NFs. This is only achievable in a limited parameter space that is spanned by the flow rate Q and the E-field E as depicted by the green area in Figure 3.2. If the E-field is below the minimum threshold E_{min}, no jetting occurs. If the E-field is approximately at E_{min} and $Q > Q_{min}$, stable ES is observed. Further increasing Q without matching E will yield undesirable thick fibers. Continuously increasing E will eventually lead to axial instability, resulting in pulsating deposition. These effects are summarized in Table 3.2.[93] During

Table 3.2: Effects of different flow rate and E-field settings on ES. Stable jetting of thin fibers is achieved if the flow rate Q and the E-field E values are not much greater than their minimum threshold.

	$E < E_{min}$	$E \gtrsim E_{min}$	$E \gg E_{min}$
$Q < Q_{min}$	no jet	pulsating	pulsating
$Q \gtrsim Q_{min}$	no jet	fine fibers	multi-jet
$Q \gg Q_{min}$	no jet	dripping	thick fibers

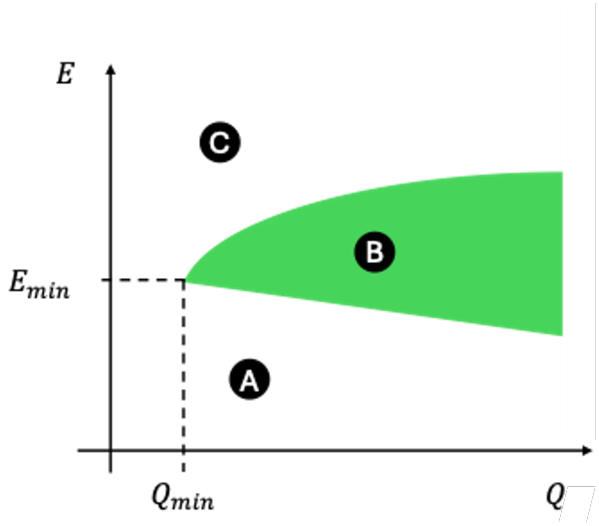

Figure 3.2: Stable jetting in a flow rate and E-field parameter space. A) The E-field is not strong enough to initiate ES; no jet formation and dripping occur. B) the stable region, C) Complex pulsating regime due to E-field induced axial instabilities.

the flight toward the collector, several parallel processes occur. Due to the electric forces acting on the jet, its velocity increases while its diameter shrinks, resulting in a tapered profile. Additionally, a continuous jet will experience whipping instability after a certain critical length l_{crit}. The terminal fiber diameter D scales with multiple parameters including the solutions viscosity η and the surface charge density σ_e (unit: [C m^{-2}]) according to Equation 3.1 [93].

$$D \propto \sqrt{\frac{\eta Q \sigma_e^{0.2}}{{E_{\text{min}}}^2}} \tag{3.1}$$

Collection Upon contact with the collector, which is typically an aluminum plate, fibers are deposited as either random or oriented arrays. For oriented arrays, a rotating collector (e.g., a drum or disk) can be used [93]. Alternatively, a specifically shaped electric field can be used to direct the jet into the desired pattern. The nanofibers can undergo further post-synthesis treatments, such as annealing or sintering. The various post-synthesis treatment methods and parameters also profoundly affect fiber morphology, including porosity and chemical composition.

In this work, the spinneret tip-to-collector voltage, distance, and flow rate are optimized to achieve continuous and stable jetting.

3.1.3. Vapor-Liquid-Solid Process

The vapor-liquid-solid mechanism, first described by Wagner and Ellis in the 1960s [107], provides a controllable approach for synthesizing NWs with precise diameter control and high crystallinity.

General Procedure The VLS process operates through a three-phase system involving a precursor in *vapor* state, a catalyst in *liquid* phase, and the *solid* crystalline nanowire product, thereby giving the name. The synthesis process proceeds through several sequential steps, as depicted in Figure 3.3 a. First, the substrate needs to be coated with a catalyst thin film or nanoparticles (NPs), e.g., by sputtering or evaporation. The catalyst is typically a metal, such as gold, tin, or a transition metal. The precursor is heated to its vaporization temperature, thereby entering the vapor phase. The catalyst liquefies and dewets into tiny droplets on top of the substrate. An incomplete VLS process with visible dewetted Au structures is shown in Figure A6. Liquification is further supported by the Gibbs-Thomson effect, which describes a depression in the melting point of nanomaterials. The precursor vapor dissolves into the liquid catalyst droplet, raising the precursor concentration above its saturation concentration. Consequently, nucleation and growth occur preferentially at the solid-liquid interface because the thermodynamic barrier to crystal formation is lower than that for homogeneous nucleation in the vapor phase. As material continues to crystallize at the solid-liquid interface, the droplet is elevated, creating a quasi-one-dimensional growth morphology. This continuous process of precursor vapor dissolution and interface crystallization drives nanowire growth while maintaining a constant diameter, which is primarily determined by the catalyst particle size.

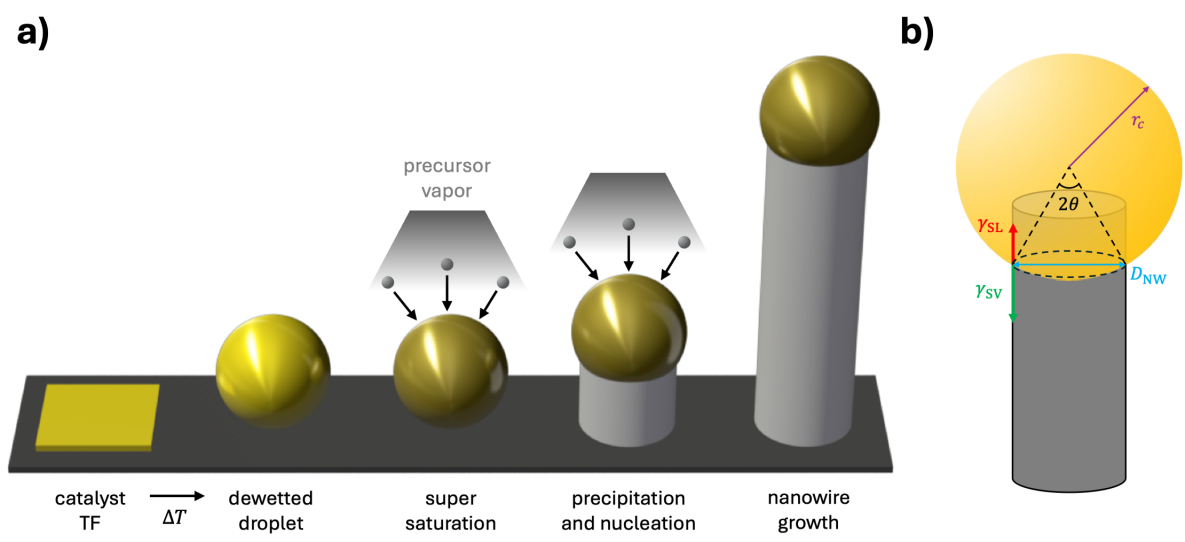

Figure 3.3: NW growth mechanism during the VLS process. a) Individual steps of the VLS process. b) Geometric model of the catalyst droplet and the NW during growth.

Dimensions The catalyst droplet and the NW are geometrically modeled as a sphere and a cylinder, respectively, as shown in Figure 3.3 b [108]. A virtual cone is constructed from the sphere center and the intersection circle between the sphere and the cylinder. Consequently, the NW diameter D_{NW} can be calculated by the apex angle θ of the cone and the catalyst radius r_c according to $D_{NW} = 2\sin(\theta)\, r_c$. At equilibrium state, the relationship between the apex angle and the catalyst droplet surface tension (γ), the internal tension between the catalyst droplet and the solid surface (γ_{SL}) and the internal tension between the vapor and the surface (γ_{SV}) can be established according to Equation 3.2.

$$\gamma \sin(\theta) + \gamma_{SL} - \gamma_{SV} = 0 \tag{3.2}$$

It is shown that the NW diameter D_{NW} is proportional to the catalyst droplet diameter D_c as shown in Equation 3.3.

$$D_{NW} = \frac{\gamma_{SV} - \gamma_{SL}}{\gamma} D_c \propto D_c \tag{3.3}$$

The NW length l_{NW}, on the other hand, linearly correlates with the local precursor vapor concentration c_{pc}, which decreases with increasing source-to-target (or precursor-to-substrate) distance d according to Equation 3.4 [108].

$$l_{NW} \propto c_{pc} \propto e^{-kd} \tag{3.4}$$

Both c_{pc} and l_{NW} are dependent on the vapor flow rate (or molecule velocity), the vapor diffusion speed, and the precursor adsorption speed, which are incorporated in the constant k. The spatial density of VLS grown NWs primarily depends on the density of the catalyst droplets in addition to a distance-dependent constant [108].

Standard Process for SnO_2 NWs The experimental VLS setup (refer to Figure 3.4) and the standard process used in this work for the synthesis of SnO_2 NWs are described in the following. The setup consists of a tube furnace with a quartz tube, a vacuum pump, a manometer, and two MFCs connected to the Ar and O_2 gas flasks. First, a ceramic boat was filled with two spatula tips of the precursor SnO powder. The precursor boat was then placed in the quartz tube and positioned at the center of the furnace, where the highest temperature was achieved. The temperature profile can be fit by a 4th degree polynomial, where the temperature drops by approximately 150 °C at a 100 mm distance from the center [109]. The quartz tube has an inner diameter of approximately 40 mm. Next, a pre-coated (Au, 5 nm) Si substrate was placed on a secondary ceramic boat and positioned in the gas-flow direction behind the precursor boat. The quartz tube is then connected to the vacuum pump, and the MFCs are sealed with flange gaskets at both ends. Finally, the two manual valves are opened to connect the MFCs with the Ar and O_2 gas bottles. The vacuum pump, the manometer, and the MFCs are PID controlled. As presented in Figure 3.5, the VLS process is divided into four phases: 1. purging, 2. temperature ramping, 3. main VLS step, and 4. cool down. Ar is constantly supplied at 50 sccm in all phases. In the first phase, the oven tube is evacuated (to approximately 3 mbar) and heated to 300 °C. This phase purged the oven of residual impurities, especially water. At the same time, Au droplets are generated by dewetting without initiating chemical reactions of the precursor material [94]. In the second phase, the pressure is rised to 300 mbar (by accumulating Ar) and the temperature raised linearly to $T_{VLS} = 1040$ °C over a duration of 40 min. In the third (main) phase, the VLS process takes place at the constant temperature of $T_{VLS} = 1040$ °C and over a duration of 60 min. Under these conditions, the SnO precursor evaporates, adsorbs into, and consequently supersaturates the Au droplets as described previously. Subsequently, crystallization occurs at the liquid-solid interface, forming the SnO_2 NWs. Equation 3.5 presents the corresponding disproportionation[2] reaction [110].

$$2\,SnO\,(g) \xrightarrow{\text{disproportionation}} Sn\,(l) + SnO_2\,(s) \tag{3.5}$$

[2] Disproportionation regarding the oxidation state as defined by International Union of Pure and Applied Chemistry (IUPAC) [60].

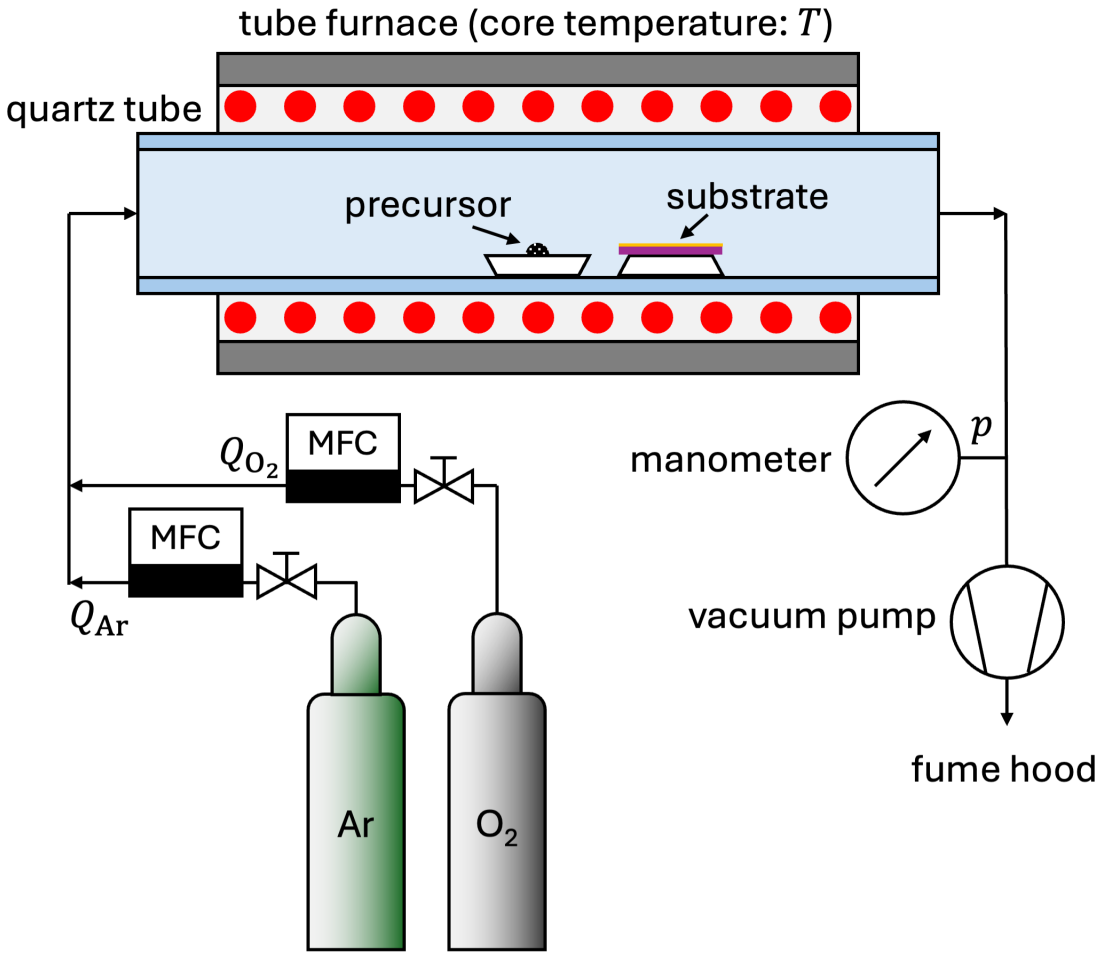

Figure 3.4: VLS setup. A temperature-resistant quartz tube is placed inside a tube furnace. During operation, the Ar and O_2 flows are controlled precisely using mass flow controllers (MFCs). The pressure is proportional-integral-derivative control mechanism (PID) controlled by a manometer in combination with a vacuum pump. The furnace and the exhaust are placed inside a fume hood.

During the third phase, 0.5 sccm O_2 is additionally supplied to further shift the chemical equilibrium towards SnO_2. Finally, in the last phase, the substrates were allowed to cool to approximately room temperature (RT) for at least 5 hours. The substrates are removed from the quartz tube, and the collected NWs are stripped from the substrates for further usage. The stripping must be performed with extra care to avoid breaking the substrate surface and edges and consequently introducing impurities.

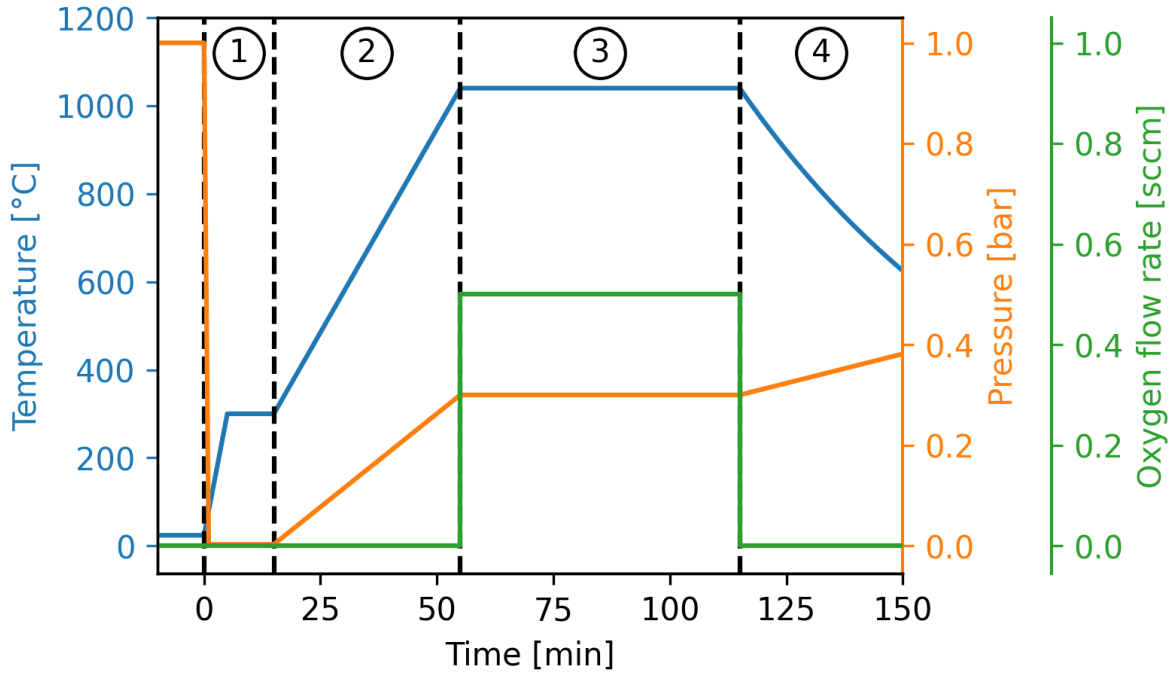

Figure 3.5: VLS process parameters. Process parameters include temperature (blue), pressure (orange), and O_2 flow rate (green). The complete process is divided into four distinct phases: 1. purging (15 min), 2. temperature ramping (40 min), 3. main VLS (60 min), and 4. cool down ($\geq$ 300 min).

3.2. Chemiresistive Sensor Platform (CSP)

Within the scope of this work, all chemiresistive sensors are based on a custom chemiresistive sensor platform (CSP). This platform was previously developed at Karlsruhe Institute of Technology (KIT), which has been successfully deployed in several eNose applications [109, 111, 112]. The CSP consists of 17 Au interdigitated electrodes (IDE) which are 50 µm wide and 50 µm apart from each other as shown in Figure 3.6. The electrodes are approximately 4 µm thick. If not otherwise stated, the chemiresistive sensing material is deposited by mask-assisted drop casting onto the IDE area.

Chemiresistive Material Deposition The chemiresistive sensing 1D nanomaterials used in this work aggregate into fuzzy networks, making them difficult to handle during subsequent deposition steps. Therefore, they are first dispersed in a carrier solvent, such as isopropyl alcohol (IPA), using various methods, such as magnetic stirring or an ultrasonic bath. NWs grown on a single 10 mm × 10 mm substrate were dispersed in approximately 0.5 mL. thereby creating a heterogeneous suspension. No targeted attempts were made to stabilize the suspension, such as electrostatic stabilization via peptization or steric stabilization, and significant sedimentation occurs when the suspension is allowed to rest due to density differences and nanomaterial size. Therefore, immediately after stirring, the suspension was withdrawn with a pipette and then drop-cast onto the IDE sensing area. Extra care has been taken to ensure that the pipette was drawing suspension from approximately the middle of the suspension height to avoid capturing larger and heavier sediments. To increase the nanomaterial

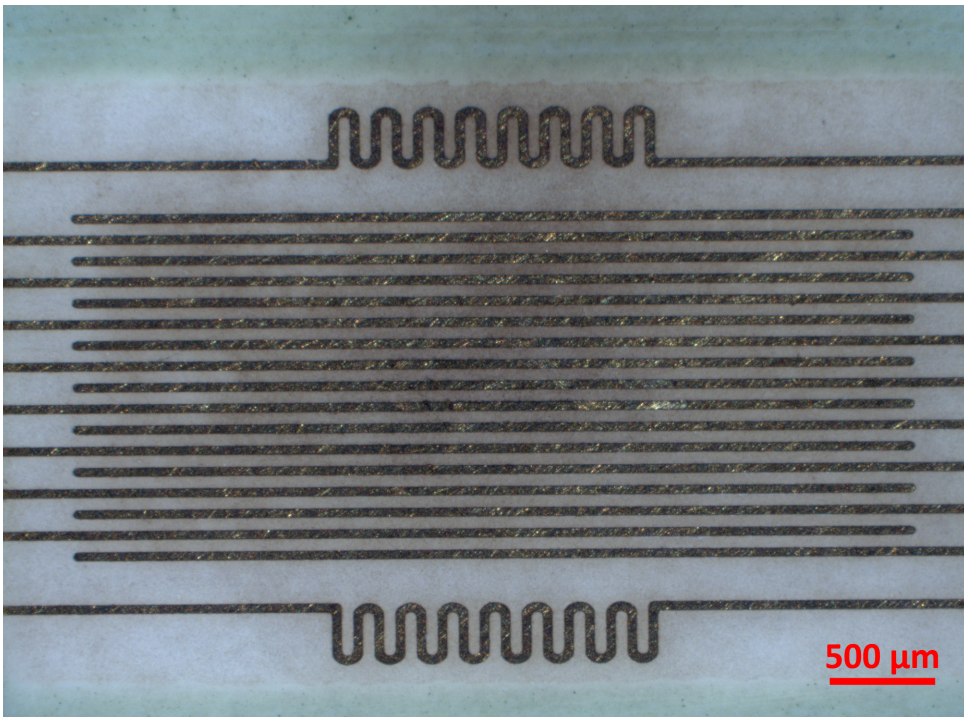

Figure 3.6: Closeup image of the IDE area of the CSP. 17 (straight) separately connected Au electrodes are visible. The top and bottom meander-shaped electrodes can be powered for heating, but are never used in this work.

concentration and prevent material from leaking onto other sensor components, a custom 3D-printed, gasket-sealed mask is used, as depicted in Figure 3.7. Finally, the deposited material is allowed to dry naturally under ambient conditions. 1D nanomaterials naturally adhere to the CSP surface due to several mechanisms such as "Van der Waals, electrostatic, capillary, hydrogen bonding, and/or chemical interactions" [113], in addition to mechanical interlocking [114]. The CSP can be reused. For this, the IDE area needs to be thoroughly cleaned with IPA and lint-free tissues.

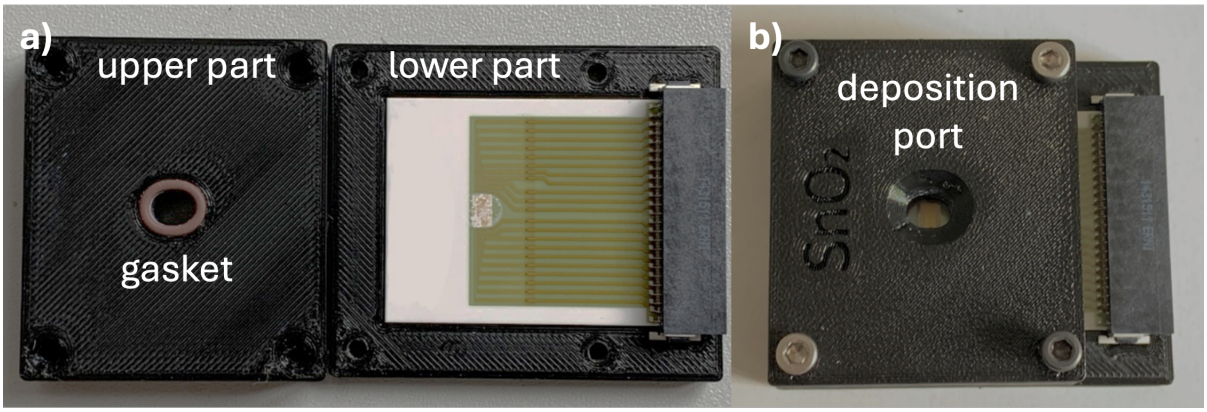

Figure 3.7: CSP chip and mask. a) CSP residing in the lower part of the deposition mask. b) Closed mask ready for drop-casting. Adapted from [7]

.

Read-out and Logging During operation, the resistance values of each sub-sensor were recorded using a custom electronic readout system provided by SMELLDECT GmbH, and the data were recorded by the custom Kamina Observer (KamObs) software on a laboratory PC. The range was limited from 0.1 kΩ to 1 GΩ. All 16 sub-sensors are being measured approximately once per second. However, this period increases to around 40 s as the resistance approaches the previously mentioned upper device limit of 1 GΩ. The continuously recorded data can be considered three-dimensional (time, sub-sensor index, and resistance value), as illustrated in Figure 3.8 a. Therefore, a single data point ($\boldsymbol{x}_i$) at a certain

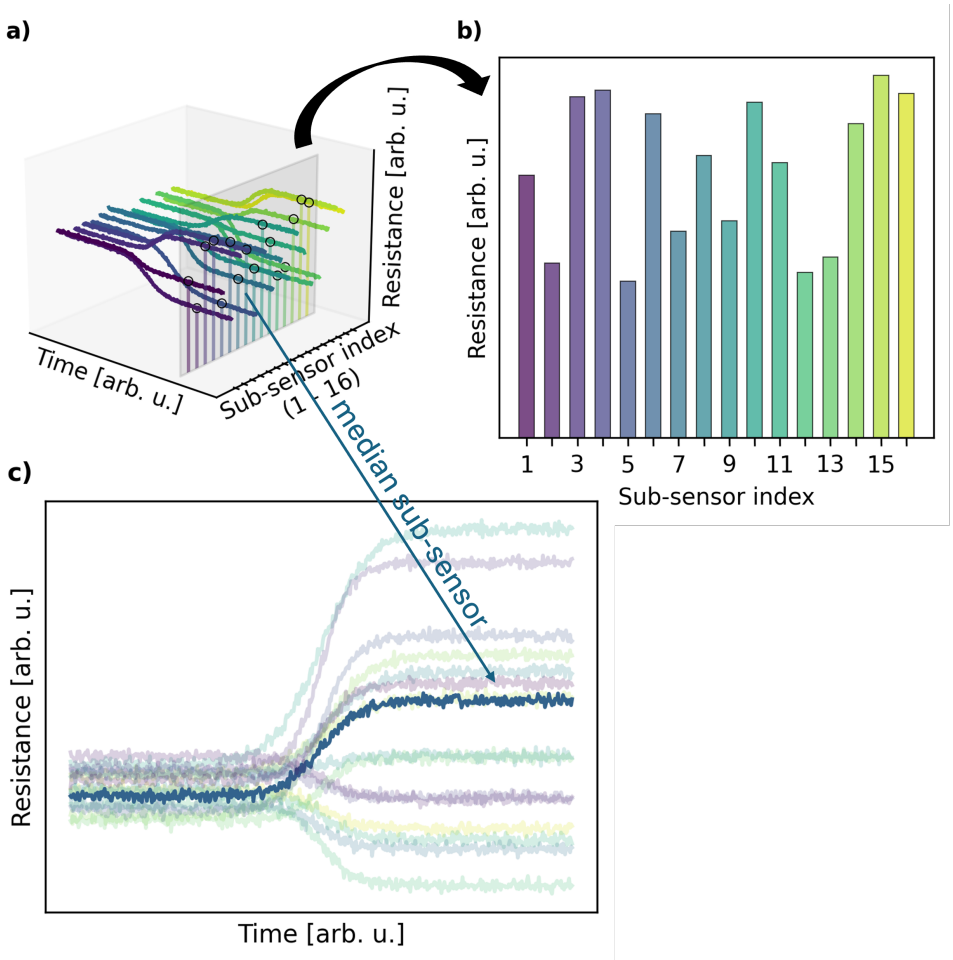

Figure 3.8: Illustration of the data structure of the CSP. a) Transient sensor signal in 3D space (time, sub-sensor, and resistance). A single point in time is represented by the plane and is shown again in b). In this work, the transient signal is usually represented by the median sensor as depicted in c) to avoid over-cluttered plots from all the sub-sensors.

.

point in time (t_i) is represented by 16 resistance values as illustrated by Figure 3.8 b. When showing the transient response of the sensors, only the median sensor's signal is displayed for clarity, as shown in Figure 3.8 c. The procedure for finding the median sensor is described below. Given a continuos set observations $\boldsymbol{X} \in \mathbb{R}^{M \times N}$, ($N = 16$ sub-sensors) the j-th sensors transient signal is represented by the

j-th column of $\boldsymbol{X}$. First the sub-sensors' mean values are calculated from the rows ($\boldsymbol{x}_i \in \mathbb{R}^{1\times N}$) of $\boldsymbol{X}$ according to Equation 3.6.

$$\boldsymbol{\mu} = [\mu_1, \ldots, \mu_j, \ldots \mu_N] = \frac{1}{M}\sum_{i=1}^{M} \boldsymbol{x}_i \tag{3.6}$$

Finally, the median sensor's index j_{med} is determined using Equation 3.7.

$$j_{\text{med}} = \arg\min_j |\mu_j - \text{med}(\boldsymbol{\mu})| \tag{3.7}$$

3.3. Substrate Preprocessing for Digital Printing

This section describes the nessesary processing steps which precedes the digital printing processes, used for the fabrication of ChemFETs.

Substrate Dicing Substrates are diced into the desired dimensions. This research-level approach contrasts with the industrial-scale standard of structuring first and dicing later. Silicon wafers are diced by a wafer saw in an automated fashion, whereas glass substrates are manually cut using a diamond cutter.

Cleaning Special care is taken to ensure the substrate remains as clean as possible during each processing step. Any surface contaminants, impurities, or defects may cause ununiformities during subsequent steps. This is especially critical during the deposition of nanometer-thick thin films, as described in Section 3.4 for inkjet printing. Therefore, diced substrates are processed in a cleanroom unless otherwise stated.

The substrates are cleaned in an ultrasonic cleaner, which generates temporary micrometer-sized air bubbles called cavitation bubbles. The eventual collapse of cavitation generates high temperatures and pressures, which in turn clean the surface of the submerged object. The substrates are ultrasonically cleaned at full power, first submerged in acetone for 10 min and then in isopropyl alcohol (IPA) for 10 min. The substrates are thoroughly dried after each cleaning step. The described cleaning process is used for all bare substrates unless otherwise stated.

Plasma Treatment For many wet-deposition methods, such as spin-coating, drop-casting, and various printing techniques, the substrate surface must be specifically treated to ensure proper wetting behavior. In this work, this is achieved by O_2 plasma activation (PlasmaFlecto, plasma technology GmbH, Germany). If not otherwise stated, the following standard parameters are used.

- Pressure: 0.3 mbar
- Pressure stabilization duration: 10 s
- Power: 100 %

3.4. Inkjet Printing

3.4.1. Introduction

Inkjet printing (IJP) is an established and widely used printing technology, mainly known for printing documents and photos. As fitting to its name, IJP ejects droplets of ink for printing. Although the first of its kind was invented in 1858 by William Thomson[3], the commercial launch was not until the 1950s and 60s.[115].

Generally, an inkjet (IJ) printer consists of a tank reservoir, a printhead, and a motorized stage as depicted in Figure 3.9 a. To print a structure, the printhead is synchronized with the stage's motion and ejects drops only at the desired positions.

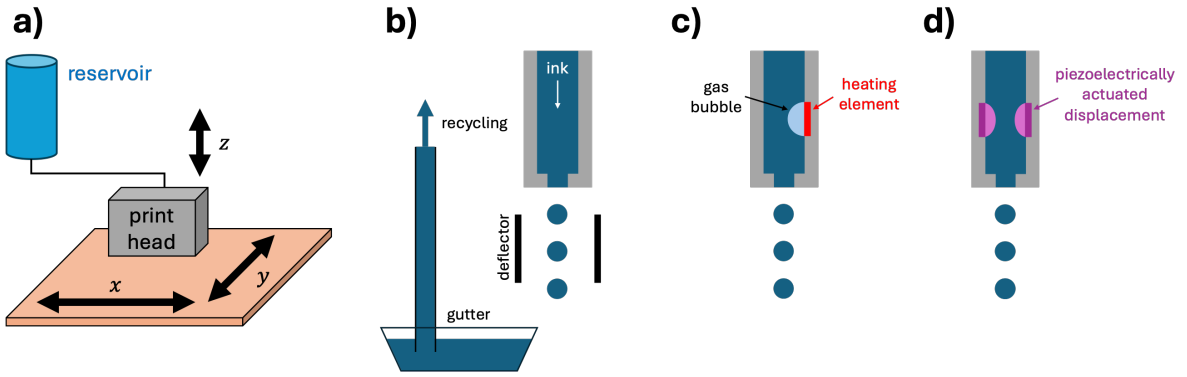

Figure 3.9: Technology overview of IJP. a) General structure of a IJ printer. b) continuous inkjet (CIJ). c) drop-on-demand (DoD): thermal droplet generation. d) DoD: piezoelectric droplet generation.

Overview IJP Technologies Generally, an IJP's printhead consists of multiple nozzles. IJ is divided into two categories, CIJ and DoD, depending on the interruption technology [115–117]. In CIJ, the nozzles continuously jet during operation, and the drops deposit on the target by default, as shown in Figure 3.9 b. To stop specific nozzles from printing, the falling droplets are deflected and intercepted by a gutter. The collected ink can be recycled to improve material efficiency. In contrast to CIJ systems, DoD systems generate and eject individual droplets only as required. This approach further reduces material waste.

Two main droplet generation technologies exist for DoD IJP, thermal inkjet (TIJ) and piezoelectric inkjet (PIJ) [115]. For TIJ, at least one component of the ink is heated locally above its boiling point, thus forming an expanding bubble that pushes out the drop as depicted in Figure 3.9 c. TIJ is further categorized based on the position of the heater: roof-shooter, side-shooter, and suspended heater. PIJ uses a piezoelectric element that deforms directly under electrical actuation as depicted in Figure 3.9 d. PIJ is further categorized by the deformation mode: squeezing, bending, pushing, or shearing [115].

[3] Later known as Lord Kelvin, after whom the absolute temperature unit, the kelvin, is named.

The piezoelectric printheads are further classified into squeeze, push, shear, and bend modes. TIJ components are exposed to frequent and significant thermal changes, which lead to lower life-span expectations compared to PIJ [115, 117].

Ink Compatibility For a stable printing process, IJP imposes limitations on ink properties, which depend on the specific technology. This tight dependence is caused by multiple factors across different stages of the printing process, including ink flow, droplet formation, flight, impact, and distribution. Therefore, the ink formulation must fulfil the complex requirements and be optimized. Two crucial dimensionless ink parameters determine the printability: the Reynolds number (Re) and the Weber number (We).

The first parameter, the Reynolds number, is defined as the quotient between inertial and viscous forces according to Equation 3.8.

$$\mathrm{Re} = \frac{\rho v l}{\eta} \tag{3.8}$$

Here for IJP, ρ [kg m^{-3}] is the inks density, v [m s^{-1}] is the velocity of the droplets, η [Pa s] is the inks dynamic viscosity, and l [m] is a characteristic length which equals the nozzle diameter for a circular orifice. For small Re values, the viscous forces dominate, thereby a laminar flow is observed. In contrast, large Re values predict turbulent flow, where inertial forces dominate. For a given system, a threshold value, the so-called critical Reynolds number, can be found, which separates laminar and turbulent flow.

Because of the small nozzle diameters and droplets, the surface tension is not negligible. Therefore, the second parameter, the Weber number, is the ratio of inertial to surface-tension forces as defined in Equation 3.9 [117].

$$\mathrm{We} = \frac{\rho v^2 l}{\gamma} \tag{3.9}$$

Here for IJP, γ [N m^{-1}] is the surface tension of the ink. If We is too small, surface tension prevents proper droplet formation and ejection. In contrast, at high We values, droplets will form and eject, but collisions of ejected droplets with the surface cause splashing. A combined metric Z, which is the reciprocal of the Ohnesorge number Oh, can be calculated, which is defined by Equation 3.10 [117].

$$Z = \frac{\mathrm{Re}}{\sqrt{\mathrm{We}}} = \frac{\sqrt{\gamma \rho l}}{\eta} \tag{3.10}$$

With these quantities, a printable parameter region can be found as illustrated in Figure 3.10 [117].

3.4.2. Experimental Setup

IJP is conducted in a cleanroom with a controlled ambient temperature of around 21 °C to 22 °C and relative humidity of around 40 RH% to 50 RH% [117]. The complete setup is shown in Figure 3.11. The research-grade DoD IJ printer Pixdro LP50 (SUSS MicroTec), in combination with the micro-electromechanical systems (MEMS)- based Dimatix Materials Cartridge (DMC) (Fujifilm), is used for all

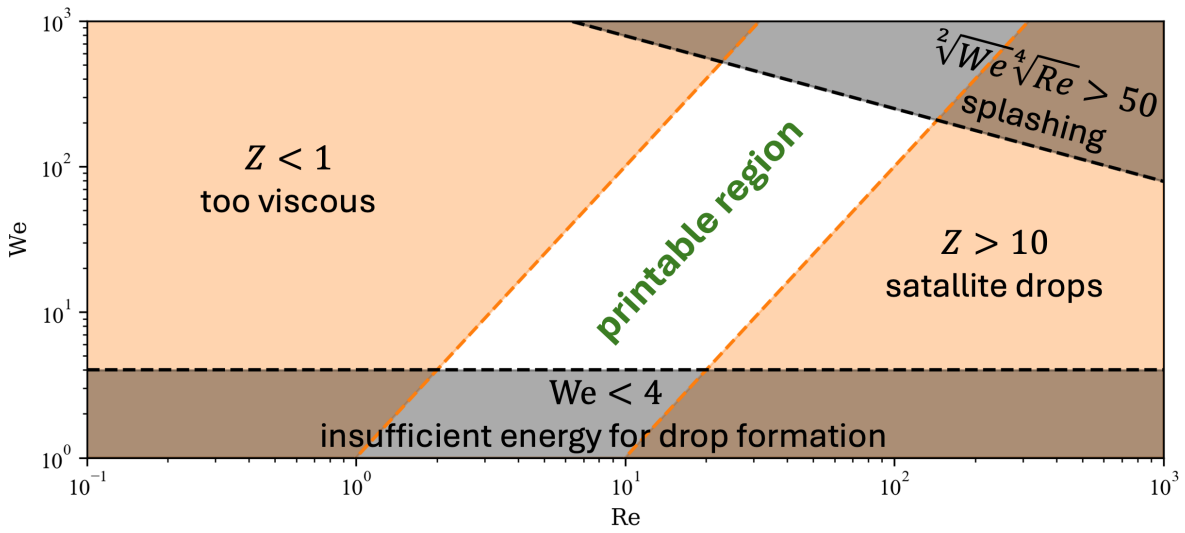

Figure 3.10: Ink printability diagram for IJP. The parameter space is span by the Reynolds number Re and Weber number (We). To the left ($Z < 1$), the ink fails to eject due to too high viscosity. In contrast to the right ($Z > 10$), satellite droplets emerge alongside the primary droplet. To the top ($We^{1/2}Re^{1/4} > 50$) splashing occurs when the droplets land on the target. Conversely, on the bottom We < 4, droplet formation is hindered by insufficient kinetic energy. The center region (white) represents the area of printable parameter combinations.

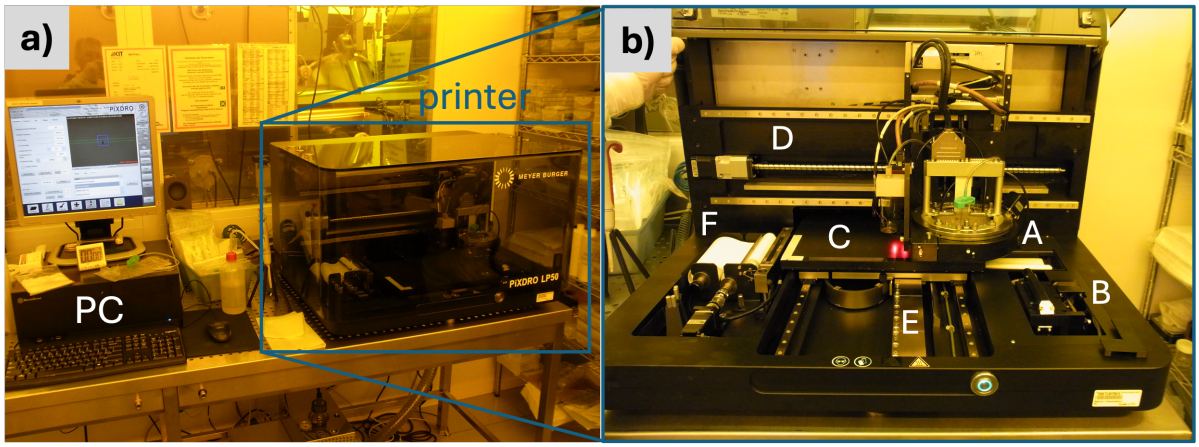

Figure 3.11: IJ printer setup at LTI. a) Overview showing the closed printer and the pc. b) Closeup view of the opened printer with the following components: (A) printhead assembly, (B) droplet camera, (C) plate, (D) x-axis linear motor, (E) y-axis linear motor, (F) automatic wiping system.

IJP processes. The DMC consists of 16 nozzles and comes in a 10 pL (DMC 11610) or 1 pL (DMC 11601) version. The ink is stored in a 5 mL syringe barrel rather than in the included cartridge reservoir. Other parts of the syringe, such as the plunger or the needle, were not used. The syringe was connected to the printhead via an approximately 10 mm to 15 mm polytetrafluoroethylene (PTFE) tube. Inks are filtered at least once through a 0.2 µm PTFE membrane filter before usage to prevent nozzle clogging. The filtered ink was added to the syringe barrel via a pipette. Next, the top of the syringe barrel was connected to the pressure control system, which applies a relatively small underpressure in the mbar range to prevent ink leakage and increase repeatability.

During operation, a predefined voltage pulse profile induces mechanical deformation of the piezoelectric component in each enabled nozzle of the printhead. The pulse profile can be divided into three phases:

1. precondition phase,
2. ejection phase, and
3. recovery phase.

An exemplary pulse profile is presented in Figure 3.12. The entire pulse profile can be characterized

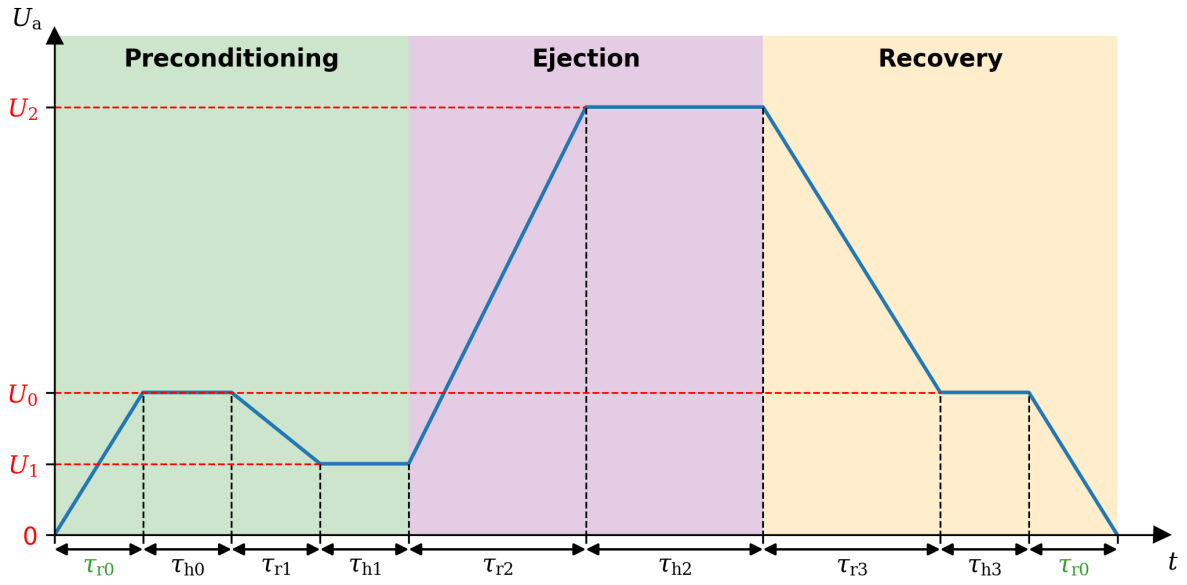

Figure 3.12: General voltage profile of the DMC printhead. The voltage profile is split into the preconditioning (green), ejection (purple) and recovery phase (yellow).

by 11 parameters: three positive voltages $U_i \in \{U_1, U_2, U_3\}$, four ramping durations, and four holding durations.

During the precondition phase (green), the minor voltage pulses only "tickle" the nozzle without actual droplet ejection. This keeps the ink moving inside the nozzle to prevent drying and particle settling [118]. This phase is parameterized by two voltages (U_0 and U_1), ramp durations (τ_{r0} and τ_{r1}), and hold durations (τ_{h0} and τ_{h1}). Next, the droplet is ejected during the ejection phase (purple). This phase is parameterized by U_2, which is usually the highest voltage inside the pulse, and the ramp duration τ_{r2} and the hold duration τ_{h2}. Finally, the system returns to its idle state, and the reservoir refills the nozzle during the recovery phase (yellow). During the recovery phase, the voltage is first ramped (down) to U_0 (from the preconditioning phase) with τ_{r3} as the ramp duration. Subsequently the voltage is held for τ_{h3} and ramped to 0 V with a ramp duration of τ_{r0} (from the preconditioning phase). Alternatively, τ_{r0} can be set to zero so that U_0 is constantly held between pulses.

τ_{pulse} is the duration of the complete pulse profile, and the complete pulse profile is repeated for a specific ejection frequency. It is ensured that the ejection frequency does not exceed τ_{pulse}^{-1} in addition to the

device limit. The underpressure, voltage pulse profile, ejection frequency, and nozzle temperature need to be optimized for each distinct ink (composition and concentration) to ensure proper inkjetting.

For this purpose, droplet ejection is closely observed using a camera synchronized to the ejection frequency. A time offset is manually adjusted to ensure the camera captures the droplets after a specific delay following ejection. The optimization of these parameters is typically performed in order of phase importance: the ejection phase, then the preconditioning phase, and finally the recovery phase, which has the least impact on droplet generation. If drop ejection is treated as the primary optimization task, the following sub-optimizations are performed in any order:

- increase positional stability of the droplets
- adjust droplet velocity
- eliminate satellite droplets
- minimize flight path skewness
- adjust droplet volume/size

The exact optimization procedure does not follow a strict systematic procedure. Rather, the parameters are adjusted iteratively through trial and error, and previously optimized parameters often need to be reconsidered and readjusted. Not all nozzles are guaranteed to perform identically under a given parameter set. Therefore, optimization is typically performed to achieve optimal performance across most nozzles. Bad nozzles that do not reliably eject satisfactory droplets with minimal tilt can be deactivated. A lower number of enabled nozzles generally increases the print duration. After the printhead optimization, the actual printing can be performed. The targeted layout is imported into the software. The line resolutions or dots per inch (DPI) in both directions are defined independently (DPI_x and DPI_y). In contrast, the ejection frequency is indirectly inferred from the print speed setting.

For a thin film, the DPI is limited by the continuity of the thin film on the lower side and by overflowing on the larger side. In between, the layer thickness h and the print speed are defined, whereas the DPI settings are set according to Equation 3.11.

$$h \propto \frac{V_{\mathrm{tot}}}{A} \propto \left(\mathrm{DPI}_x \cdot \mathrm{DPI}_y\right) V_{\mathrm{drop}} \tag{3.11}$$

The term $(\mathrm{DPI}_x \cdot \mathrm{DPI}_y)$ can be interpreted as the average dots per square inch, $\frac{V_{\mathrm{tot}}}{A}$ is the total amount of ink volume per area, and V_{drop} is the droplet volume. The printer prints exclusively in one direction (x or y) while moving in between the printed lines in the orthogonal direction. Before actual droplet ejection, the printhead is accelerated to the final speed. Additionally, the print can be performed in one direction or in both directions. The combination of both settings is shown in Figure 3.13 a. Bi-directional printing reduces printing duration but may cause line shifts if droplet flight timing is not properly calculated and set. In contrast, uni-directional printing takes longer, but flight time does not need to be adjusted. By default, a line in the print direction is printed by a single nozzle. To mitigate line patterns arising from unreliable nozzles or nozzles with different skewness of droplet flight paths, the quality factor (quality factor (QF), defaults to 1) can be increased. QF determines the number of nozzles used to print a

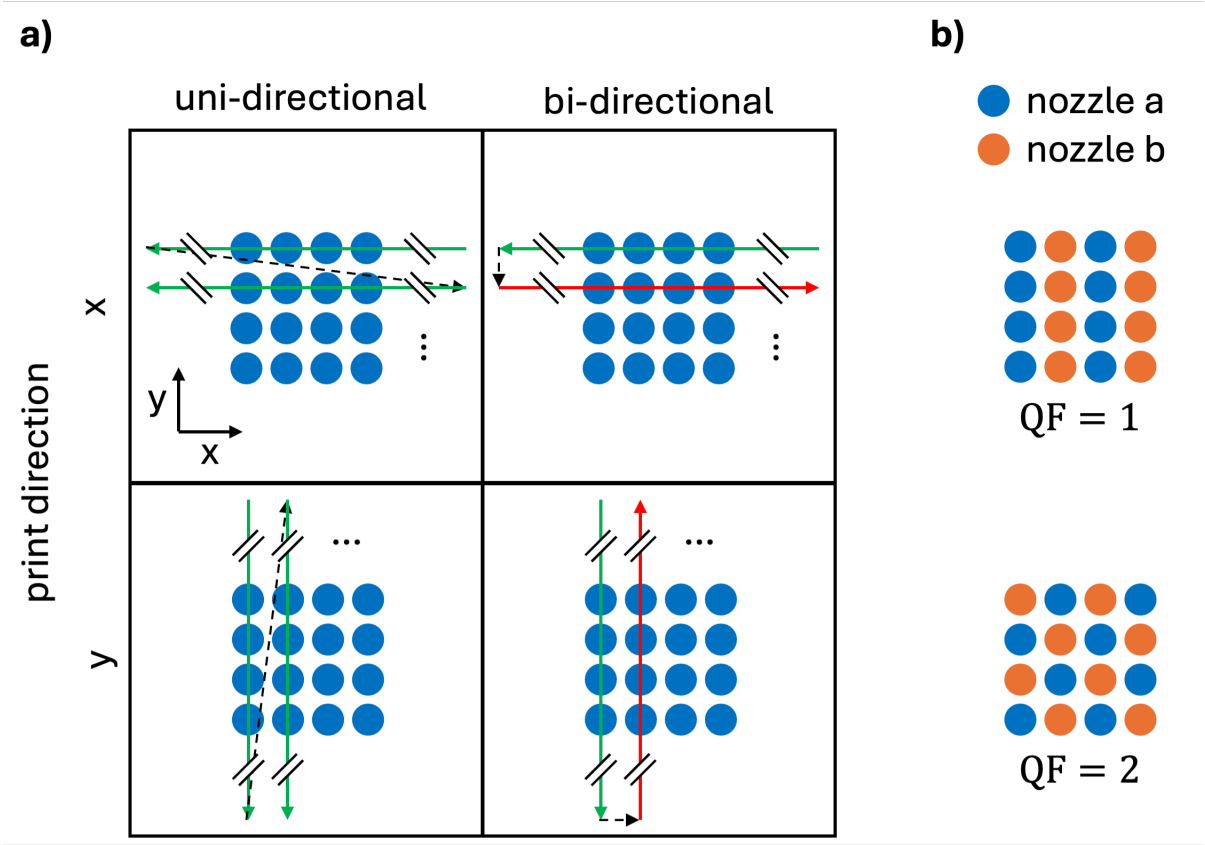

Figure 3.13: Illustration of IJP movement settings. a) Print direction b) Quality factor.

single line in the print direction. The difference between $QF = 1$ and $QF = 2$ is presented in Figure 3.13 b. The print duration increases for larger QF values because the same printline needs to be printed repeatedly using different nozzles. If not otherwise stated, all stable inkjetting nozzles are used in this work. The Pixdro LP50 allows rotation of the printhead around the z-axis. This can be used to further adjust nozzle spacing for printing complete patches in one go. The substrate is placed and aligned on the motorized XY stage, which can be heated to control the substrate temperature. The substrate temperature, in turn, affects the printed structure, including evaporation conditions and the coffee-ring effect.

Precise layouts are designed parametrically with micrometer precision in Inventor (Autodesk). Next, the layout is exported as a Drawing Exchange Format (DXF) (2018) file. Python (3.13.0), ezdxf (1.4.3), and PIL (11.0.0) are used to convert the DXF file to a Portable Network Graphics (PNG) image with a black background and white structures. Finally, the PNG file is imported into Pixdro and optionally scaled for subsequent use.

3.5. Aerosoljet Printing

Aerosol jet printing (AJP), first developed by Optomec Inc. in the 2000s, is a novel digital printing technology that uses streams of micron-sized aerosols to deposit material [119, 120]. This allows AJP to continuously print structures with a resolution of down to 10 µm. AJP offers two major advantages (comapred to IJP). First, depending on the atomization method used, inks with viscosities ranging from 1 cP to 1000 cP can be printed [121]. Second, the continuous jetting mechanism enables efficient printing of uniform traces and lines, for example, as interconnects [120, 121]. Despite these advantages, AJP remains primarily a research-level fabrication tool that awaits industrial transition due to reproducibility issues [92, 122]. In this work, the aerosol jet (AJ) printer AJ 5X (Optomec, Decathlon version 1.0) is used in combination with the KEWA software. The general working principle of the AJ system is explained in the following section and depicted in Figure 3.14. First, the ink is atomized into a fine

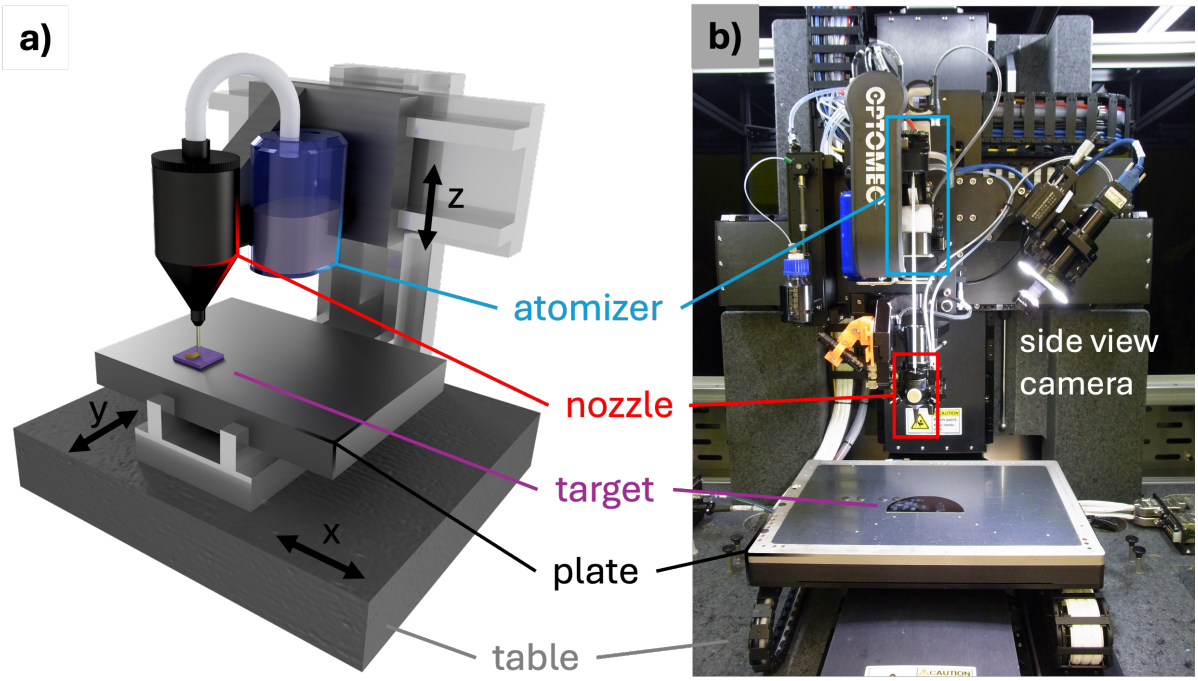

Figure 3.14: AJ setup overview. a) 3D illustration of the main components of the AJ printer. b) The Optomec AJ 5X (Optomec) located in the cleanroom at Light Technology Institute (LTI).

aerosol mist. The AJ 5X system has two mechanisms that can be used separately or in combination to interrupt the aerosol jet; these will be discussed in greater detail later. This aerosol mist is subsequently transported by an inert gas stream that a bubbler has previously humidified. Unsuitable droplets, with respect to size or mass, in the aerosol stream are filtered out. At the tip of the nozzle, the aerosol jet stream is focused and protected by a secondary, enveloping sheath gas stream. The sheath gas stream guides the aerosol jet stream onto the target. Finally, a shutter mechanism can interrupt the aerosol jet stream to pause the print. For precise deposition, the system uses a linear stage with x, y, and z axes, achieving a repeatable positional accuracy of ±5 µm and a repeatability of ±2 µm [123]. The details

of the critical processes – atomization, interruption, and aerodynamic focusing – are discussed in the following subsections.

3.5.1. Aerosol Generation

Ultrasonic Atomizer The atomizer converts liquid ink into aerosol. This is achieved either ultrasonically or pneumatically. The ultrasonic atomizer (UA), as shown in Figure 3.15, consists of an ink vial with a polymer diaphragm at its bottom. The ink vial is partially submerged in a water bath. An ultrasonic transducer is installed at the bottom, similar to an ultrasonic cleaner. When the transducer is activated, mechanical energy is transferred from the water to the diaphragm and ultimately to the ink. As a result, a standing wave forms at the center. Consequently, droplets form by a combination of instabilities in the capillary standing waves and acoustic cavitations [124].

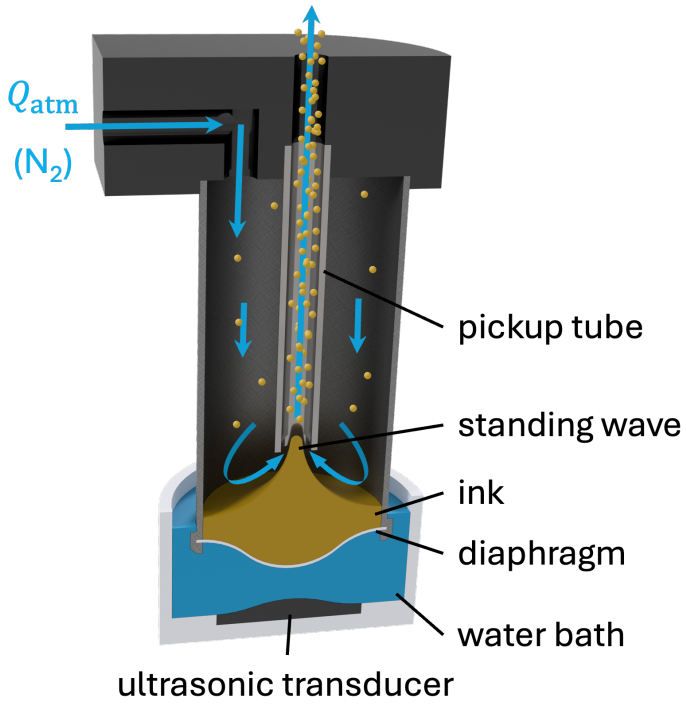

Figure 3.15: 3D illustration of the UA. Aerosols are generated ultrasonically via instabilities in the capillary standing waves and acoustic cavitations. The carrier gas stream Q_{atm} transports the aerosols to the nozzle.

Pneumatic Atomizer In contrast, the pneumatic atomizer (PA) uses the Venturi effect to generate a low-pressure, high-velocity air stream at the narrowed section [92], as shown in Figure 3.16. The Venturi effect, based on Bernoulli's principle, describes the change in fluid pressure (Δp) as it passes through different cross-sectional areas (A_0 and A_1) as described by Equation 3.12.

$$\Delta p = p_0 - p_1 = \frac{1}{2}\rho\left(\frac{1}{A_1^2} - \frac{1}{A_0^2}\right)Q^2 \tag{3.12}$$

Consequently, ink is drawn into the narrow section of the Venturi tube by the underpressure (p_1) and nebulized upon release.

Comparison Both atomization methods have complementary advantages and drawbacks, and are chosen based on the use case. The UA the standing wave is only suited for inks with a viscosity up to approximately 20 cP. As this limit is approached, the number of generated aerosols drops quickly. In contrast, the PA can handle inks with much higher viscosities up to 1000 cP. Therefore, for high viscosity inks, the PA must be used. But, using the PA results in a higher material waste. This is because a large portion of the initial air stream used to atomize the ink is filtered out to achieve a suitable nozzle exit flow rate. Additionally, the PA system is more complex, with more parameters, and requires longer setup and cleaning processes. For inks with a viscosity below 20 cP, the ultrasonic atomizer is preferred for its simplicity and ink efficiency. Although the pneumatic atomizer was used to test-print

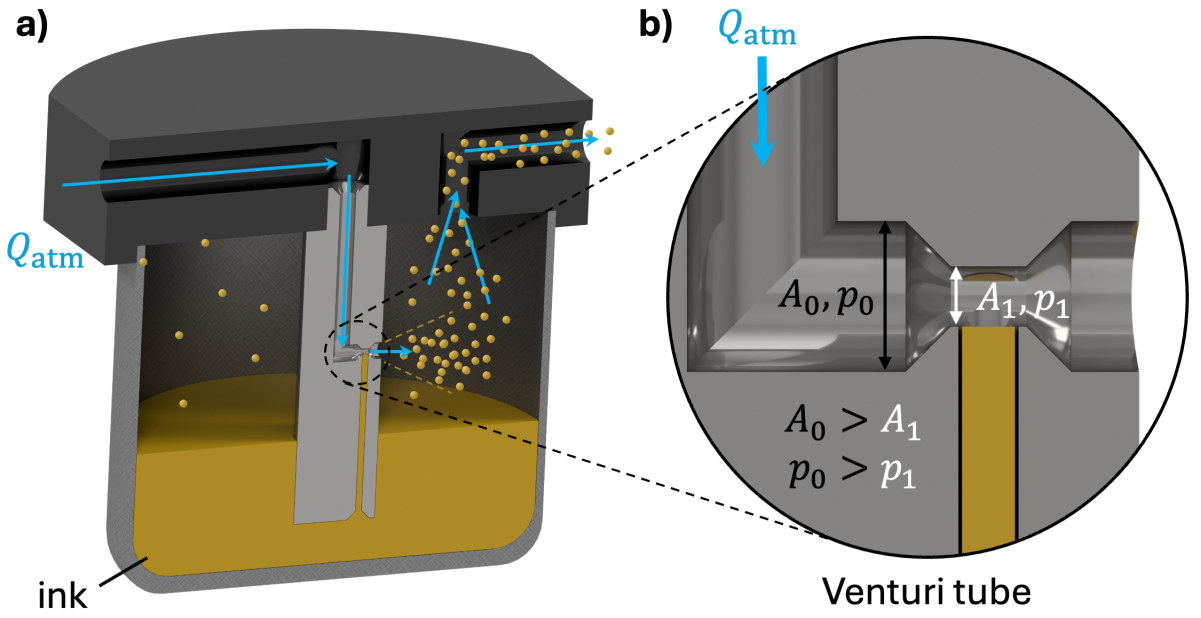

Figure 3.16: 3D illustration of the PA. a) Overview. b) Close-up view of the Venturi tube. The ink is drawn into the Venturi tube by the underpressure ($p_1 < p_0$) created by a reduction of the tube's cross-section area ($A_1 < A_0$). Aerosols are generated upon release and are transported to the nozzle by the carrier gas stream Q_{atm}.

high-viscosity inks such as Cu NP (CI-006, Novacentrix) [5], it was replaced with the UA due to the increased complexity and material waste. Additionally, all inks used were either directly compatible with UA or could be optimized for ultrasonic atomization.

3.5.2. Interruption

In contrast to DoD IJP, the aerosol is continuously generated and jetted, similar to CIJ printing. Two distinct mechanisms exist to interrupt the aerosol jet stream and prevent aerosol deposition on the target substrate: diverting and shuttering. First, the jetting operation condition is shown in Figure 3.17 a. The

nozzle is divided into a top and a bottom chamber, which are connected by a central tube. The aerosol jet or atomizer stream (Q_{atm}) enters the top chamber and continues to the second chamber. Here, the sheath gas Q_{sht} is added by a side opening and guides Q_{atm} out of the nozzle. This is called aerodynamic focusing, which will be discussed in detail in the following paragraph. When an interruption is required, a boost gas stream (Q_{bst}) is added to the bottom chamber as depicted in Figure 3.17 b. This pushes Q_{atm} back, prevents it from exiting the top chamber, and diverts it through a third opening. After filtering, an additional MFC diverts the exiting gas stream to an exhaust. Alternatively, a mechanical shutter system can be used. The shutter is a simple scoop that, when needed, moves directly into the aerosol jet stream after the jet exits the nozzle. Consequently, it intercepts aerosols, thereby preventing their deposition on the target substrate. Both interruption mechanisms can be used independently or in synchronization. For high Q_{atm} values, diversion alone is sufficient and recommended, as prolonged shutter use quickly fills the scoop, thereby causing ink to overflow. In contrast, at lower Q_{atm} values, there is often a long time between the deactivation of the diversion mechanism and the stabilization of the aerosol jet stream. To prevent printing the initially unstable jet, a shutter can be used to delay the print by intercepting the jet for a specified stabilization duration. For extremely small Q_{atm}, diversion may be ignored entirely, and only the shutter may be used as the material accumulation in the scoop is negligible.

3.5.3. Aerodynamic Focusing

A high-velocity gas jet stream exiting a small nozzle undergoes jet expansion or divergence. This would limit the minimal printable feature size. To mitigate this expansion, the enveloping sheath gas stream is used to aerodynamically focus the aerosol stream. The optimal sheath flow rate Q_{sht} depends on the nozzle diameter, and keeps the streams' cross-section diameter tight for printing fine features. Second, the sheath stream prevents direct contact between the aerosol stream and the nozzle's inner surface, thereby reducing variations in printing outcomes and clogging.

For process stability, the aerosol stream should remain laminar. Within the nozzle, the flow speed limit for laminar flow can be estimated from the Reynolds number. After the aerosol jet leaves the nozzle, the aerosol jet remains laminar inside the potential core region for a Re-dependent distance until jet breakdown happens due to turbulent diffusion [125]. Early turbulence is the primary factor in overspay, which should generally be avoided. Overspay is an unwanted phenomenon in which satellite drops are deposited beside the printing point. Large overspray may form connections to neighboring structures, leading to undesirable behavior, such as short circuits, when printing conductive materials.

3.5.4. Printing and Optimization Procedure

To efficiently print a targeted material with small, high-quality features, multiple device parameters are optimized. The parameters are listed in Table 3.3, and the detailed printing and optimization process is discussed next with a summarizing flow chart depicted in Figure A1. Using the UA, the optimization process to obtain structures with specific lateral resolution and height is as follows. First, the appropriate ink is selected. If no ready-to-use ink is available, the ink is formulated and optimized, particularly with

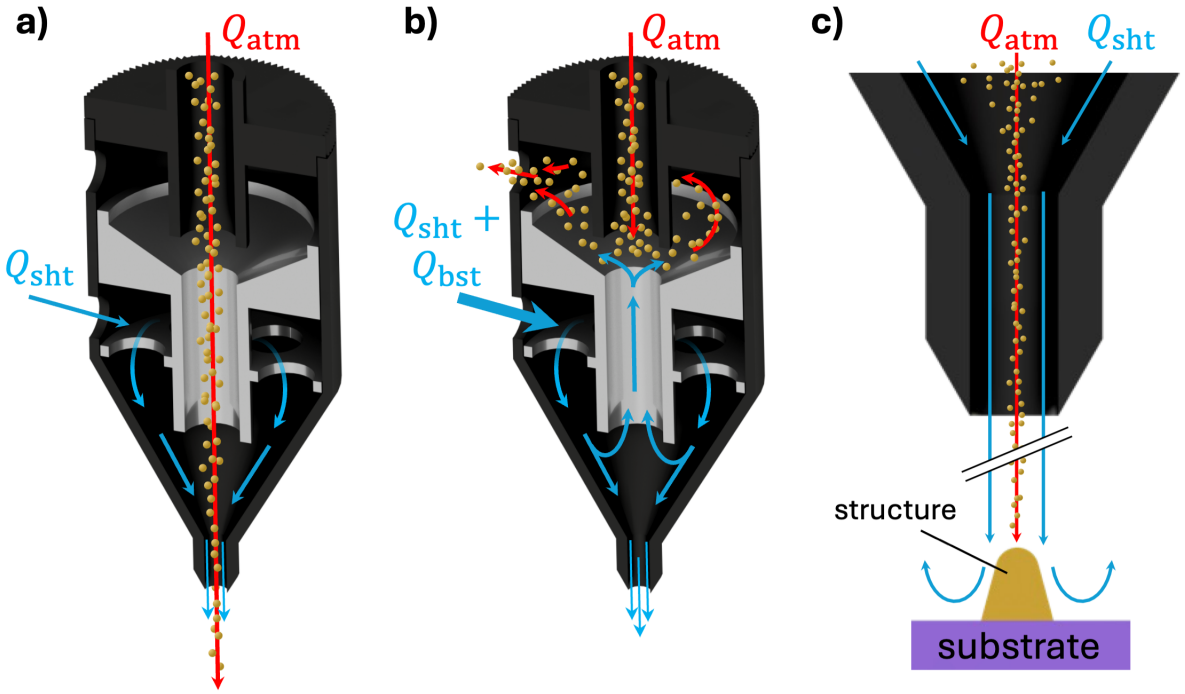

Figure 3.17: 3D illustration of the nozzle during different operation modes. a) During jetting, Q_{atm} transports the aerosols, whereas the Q_{sht} is added to prevent the aerosols from touching the inner surface of the nozzle tip and for aerodynamic focusing. b) By adding Q_{bst} to prevent the aerosols from entering the lower chamber. Subsequently, the incoming aerosols are diverted out through the exit orifice in the top chamber. c) Q_{sht} aerodynamic focuses the aerosol jet onto the target, preventing jet divergence and thereby narrowing the printed structures.

Table 3.3: Process parameters of the AJ printer. This table is specialized for the UA.

parameter	symbol	unit
atomizer flowrate	Q_{atm}	[sccm]
sheath flowrate	Q_{sht}	[sccm]
divert flowrate	Q_{bst}	[sccm]
boost flowrate	Q_{dvrt}	[sccm]
atomizer temp.	T_{atm}	[°C]
bubbler temp.	T_{bub}	[°C]
plate temp.	T_{plate}	[°C]
print speed	v	[mm s^{-1}]
opening timing	τ_{open}	[ms]
closing timing	τ_{close}	[ms]

respect to viscosity, until aerosol generation is sufficient. Usually, this entails diluting high-loading ink mixtures to balance aerosol and material densities within the aerosols. Different nozzle diameters (D) are available, ranging from 2 mm down to 100 µm. The nozzle size primarily determines the achievable minimum and maximum feature size l according to $\frac{D}{10} \leq l \leq \frac{D}{2}$. To achieve faster printing, the nozzle diameter should be selected as large as possible while still meeting the required feature sizes. Before printing, the temperatures T_{bub} and T_{atm} can be independently adjusted. To prevent continuous drying

of the ink inside the atomizer, usually T_{bub} is set to a slightly higher value than T_{atm}. Furthermore, T_{plate} can be optionally set to control the drying behavior of the printed structures. Some inks require higher T_{plate} for rapid drying to retain printed shapes, whereas other inks require lower T_{plate} to prevent crack formation. Next, the atomizer and sheath flow rates (Q_{atm} and Q_{sht}) are adjusted within the heuristic limits $Q_{atm} \leq D \cdot 0.5 \frac{\text{sccm}}{\mu\text{m}}$ and $Q_{sht} \geq 2 \cdot Q_{atm}$. At the same time, the printing speed v is optimized to achieve the desired print quality without exceeding the machine's acceleration limits. Therefore, to achieve higher print speeds, sharp corners should be avoided and replaced with rounded corners with a minimum radius. This is usually the most critical and time-consuming step, as multiple parameters: line dimensions, edge roughness and overspray, and shape consistency are affected at the same time. To increase the line width, a larger nozzle can be used and Q_{atm} increased, whereas Q_{sht} and v should be decreased. Usually, edge roughness and overspray are caused by an overly dry aerosol jet. This can be mitigated by increasing Q_{atm}-to-Q_{sht} and T_{bub}-to-T_{atm} ratios. Inconsistent line widths are commonly the result of excessively wet aerosol or excessive material, causing the printed ink to overflow onto the substrate before it solidifies. In case of overly wet aerosol, the previous wetting procedures can be applied in the opposite direction. In case of too much material, the Q_{atm} should be decreased, whereas Q_{sht} and v need to be increased. This optimization follows no strict, systematic, sequential process but rather an iterative procedure that alternates between printing and observation/measurement. Once the printed lines are of satisfactory shape and quality, the next step is to optimize the opening delay τ_{open} and closing delay τ_{close}. The opening delay is the time between enabling jetting and the start of movement. This delay is required for the AJ to stabilize and is, on average, in the range of 50 ms. If τ_{open} is too low, rough and non-uniform tails can be observed at the line start as depicted in Figure 3.18. Conversely, if the value is too high, material accumulates at the start, leading to bulge build-up during start. The close delay τ_{close} describes the time between the interruption at the end of the print and the subsequent movement. If τ_{close} is too low, the next movement causes tail formation in the new direction due to remaining aerosol jet flow. There is no upper limit on this τ_{close}, and it is kept as low as possible to enable faster printing.

3.5.5. Layout Design and Scripting

There are multiple ways to operate the AJP device. First, for simple preliminary testing, especially to ensure a stable aerosol jet and for rough line-width estimates, the device is operated manually. Next, for more precise, systematic, and parametrized testing, such as optimizing print speed and open and close timings, Python scripting is used. Finally, if all satisfactory parameters are found, more complex layout patterns can be printed by converting a DXF layout design.

For Python scripting, a custom library (ezaj) has been developed in this work, which can be used to add primitive geometries such as lines, arcs, and polylines to a layout. These geometries are treated as individual entities, and each can have different print settings, such as print speed, open and close timings. In contrast, more complex layout patterns are designed parametrically in Inventor (Autodesk) and imported into AutoCAD (Autodesk) as DXF files. Afterwards, the Optomec plugin VMTools is used to further process the layout. The plugin sets global parameter values for open and close delay timings, whereas the printing speed is defined in the KEWA software. In contrast, different geometries

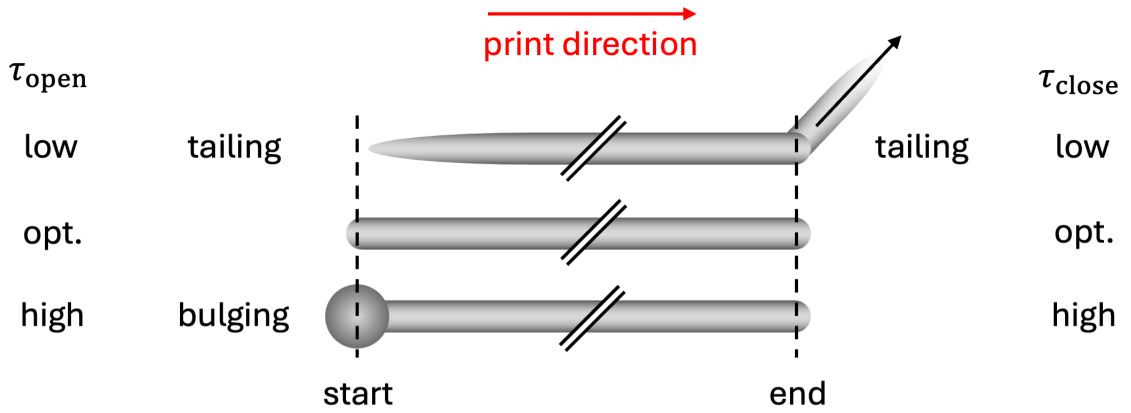

(a) Illustration of printed lines with different open and closing delay settings. The top line is printed with too short delays, which causes tailing artifacts. The center line is printed with optimal settings. The bottom row is printed with too long delays, which results in bulging at the start.

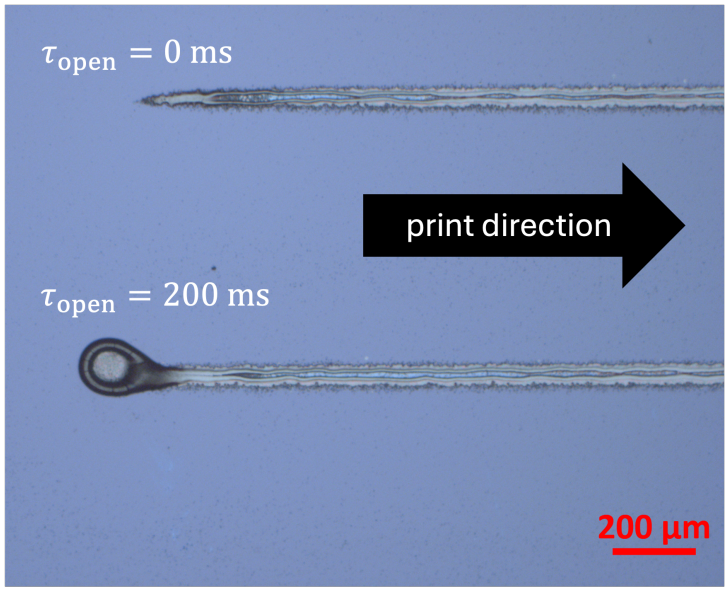

(b) AJ printed indium tin oxide (ITO) lines with open delay timing intentionally set to values leading to tailing and bulging.

Figure 3.18: Print artifacts caused by improper open and close delay timings (τ_{open}, τ_{close}).

can have individual print settings, such as printing speed, open delay, and close delay, when Python scripting is used. Both methods support hatch filling of closed structures to obtain solid patches by providing the previously determined line width and overlapping tolerances. Next, filleting is applied at every corner to avoid exceeding device acceleration limits. Finally, the complete layout is exported to a proprietary and machine-specific script file (.prg) and loaded into the KEWA software, ready for printing. A summarizing decision flow chart is depicted in Figure A2.

3.6. Material Postprocessing for Digital Printing

After the printing process, the material requires post-processing. It is common first to dry the printed materials to remove residual (co-)solvents. This can be either achieved by heating the substrate to a moderate temperature or by evaporation in a vacuum chamber. However, severe crack formation has been observed in some inks, as evidenced by preliminary experiments as shown in Figure 3.19. Therefore, unless otherwise stated, printed NP-based inks are sintered directly at the end temperature,

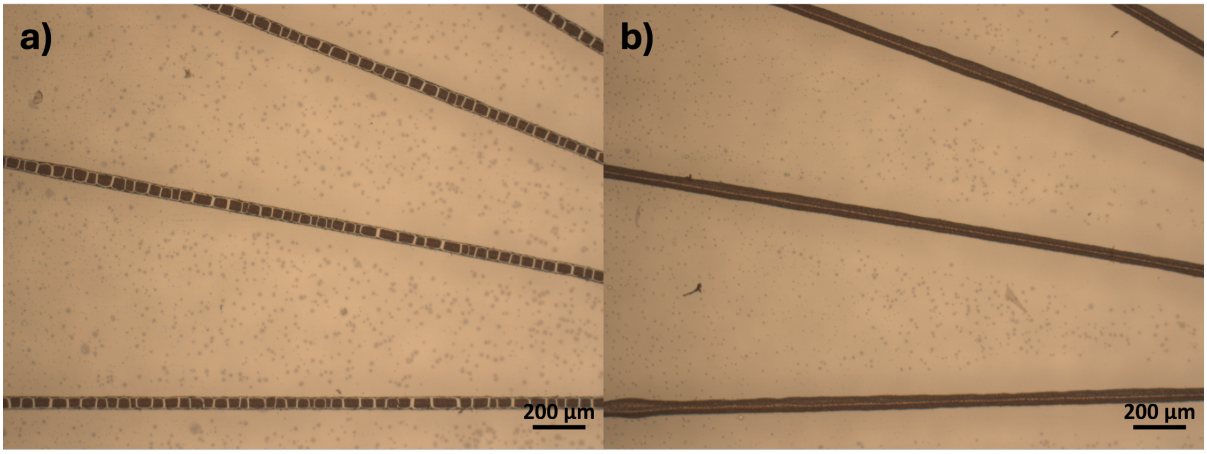

Figure 3.19: Impact of slow drying on printed Ag lines. a) Cracks form on Ag electrodes when drying at a low temperature before sintering. b) Direct sintering at high temperature results in no crack formation.

skipping both drying and temperature ramping steps.

Precursor-based materials require annealing, whereas NP-based inks require sintering; these are distinct processes. During annealing, the precursor material undergoes a chemical transformation, ultimately yielding the desired target material. In contrast, sintering is a process that increases the density of a material without causing a chemical change. In this work, NPs are heated to a high temperature but below their melting point. The NPs fuses and bonds, thereby decreasing porosity. In the case of metallic NPs, the conductivity also increases as a result. This is either achieved conventionally with hot plates or, more recently, with a flash sinter device such as the PulseForge 1200 (Novacentrix), which uses light pulses to heat the surfaces of the printed structures. This has the advantage of increased substrate compatibility, as the heat transfer direction (top-to-bottom) has a smaller impact on the substrate than hot plates with a bottom-to-top heat transfer direction. Additionally, depending on the printed structure's dimensions and material properties, the sintering rate may be many times higher than that of conventional heating. As part of a supervised student thesis, photonic sintering was conducted and evaluated on Cu NP ink [5]. However, in this work, photonic sintering was not used for the relevant inks because of the following two reasons. One reason is that all used substrates are compatible with the required annealing and sintering temperatures. The other reason is that the current processing bottleneck was not in the sintering steps but in the printing steps. Therefore, for both annealing and sintering, conventional hotplates are used.

3.7. Gas Mixing System

The gas mixing system (GMS) was used to obtain target gas streams with several parameters, including flow rate, target gas concentration, and relative humidity. The GMS consists of a network of pneumatic valves, which are in turn controlled by electrically actuated solenoid valves to avoid heating gases when directly using solenoid valves. In addition, multiple MFCs controls precisely various flow rates across the network as shown in Figure 3.20. Dry zero air was supplied by a generator (TG 12-UP, Sylatech),

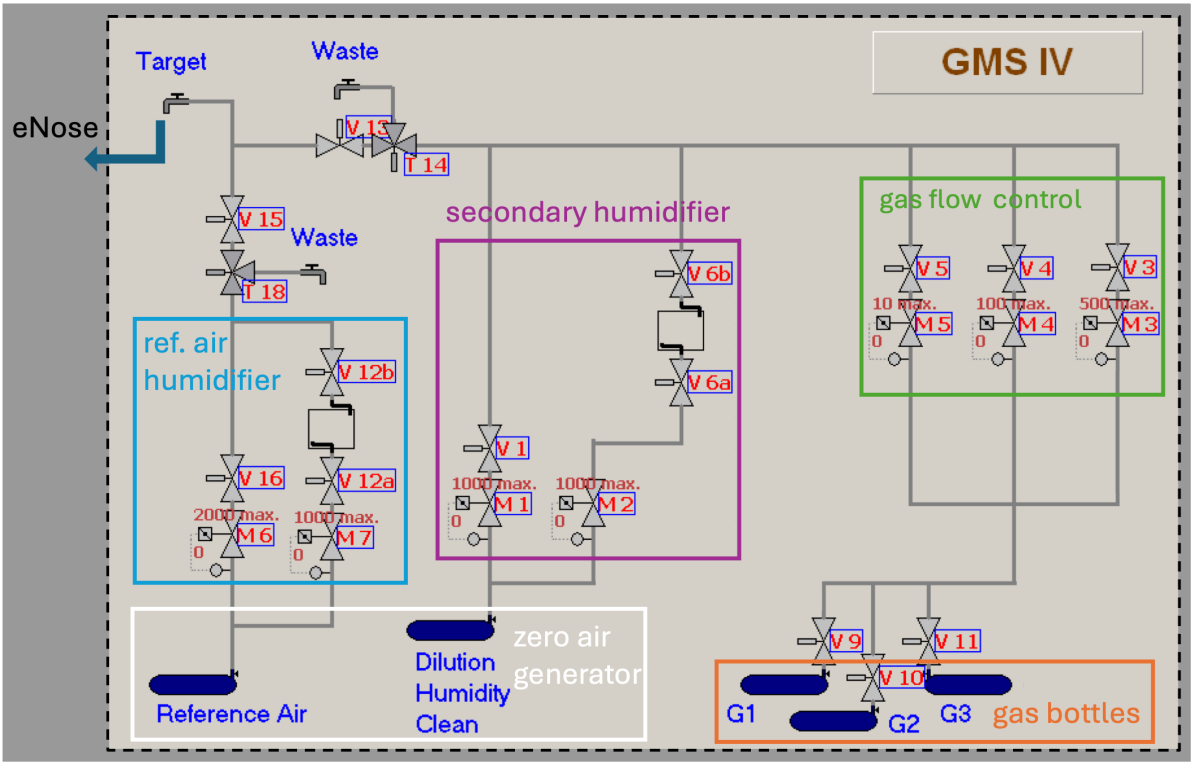

(a) Schematic overview of the relevant components.

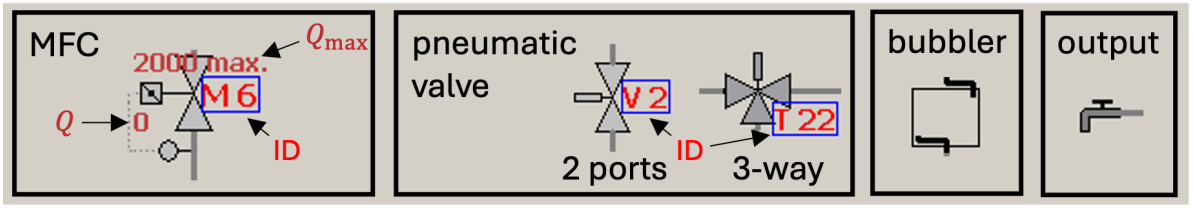

(b) Symbol legend.

Figure 3.20: Schematic overview of the GMS.

which can be humidified to near saturation by passing it through a bubbler. Predefined segments can be automatically run in sequence with adjustable durations for repeatable measurement series.

Reference Air Reference air is used for baseline measurements and is generated by a separate pipe system to avoid contamination of the reference air system. The reference air output with a flow rate of Q and the relative humidity H_{rel} is generated by mixing a dry Q_{dry} and a fully saturated (100 RH%) Q_{sat}

zero air stream as illustrated in Figure 3.21a. The MFCs are set such that Equation 3.13 and Equation 3.14 hold.

$$Q = Q_{\text{dry}} + Q_{\text{sat}} \tag{3.13}$$

$$H_{\text{rel}} = \frac{Q_{\text{sat}}}{Q} \tag{3.14}$$

Target Gas Different target gases, including IPA (C_3H_8O), benzene (C_6H_6), and carbon monoxide (CO), are supplied by corresponding gas bottles which have an initial concentration c_0 between 200 ppm and 500 ppm as illustrated in the schematic in Figure 3.21b. To obtain a target concentration c ($c \leq c_0$, unit: ppm), the initial gas from the gas bottle is diluted. Additionally, as with reference air, both the flow rate Q and the relative humidity are controlled by a secondary humidifier system (see Figure 3.20). Equation 3.15, Equation 3.16, Equation 3.17 represent the set of equations which can be solved to obtain the desired outcomes.

$$Q = Q_{\text{dry}} + Q_{\text{sat}} + Q_{\text{gas}} \tag{3.15}$$

$$c = \frac{Q_{\text{gas}}}{Q} c_0 \tag{3.16}$$

$$H_{\text{rel}} = \frac{Q_{\text{sat}}}{Q} \tag{3.17}$$

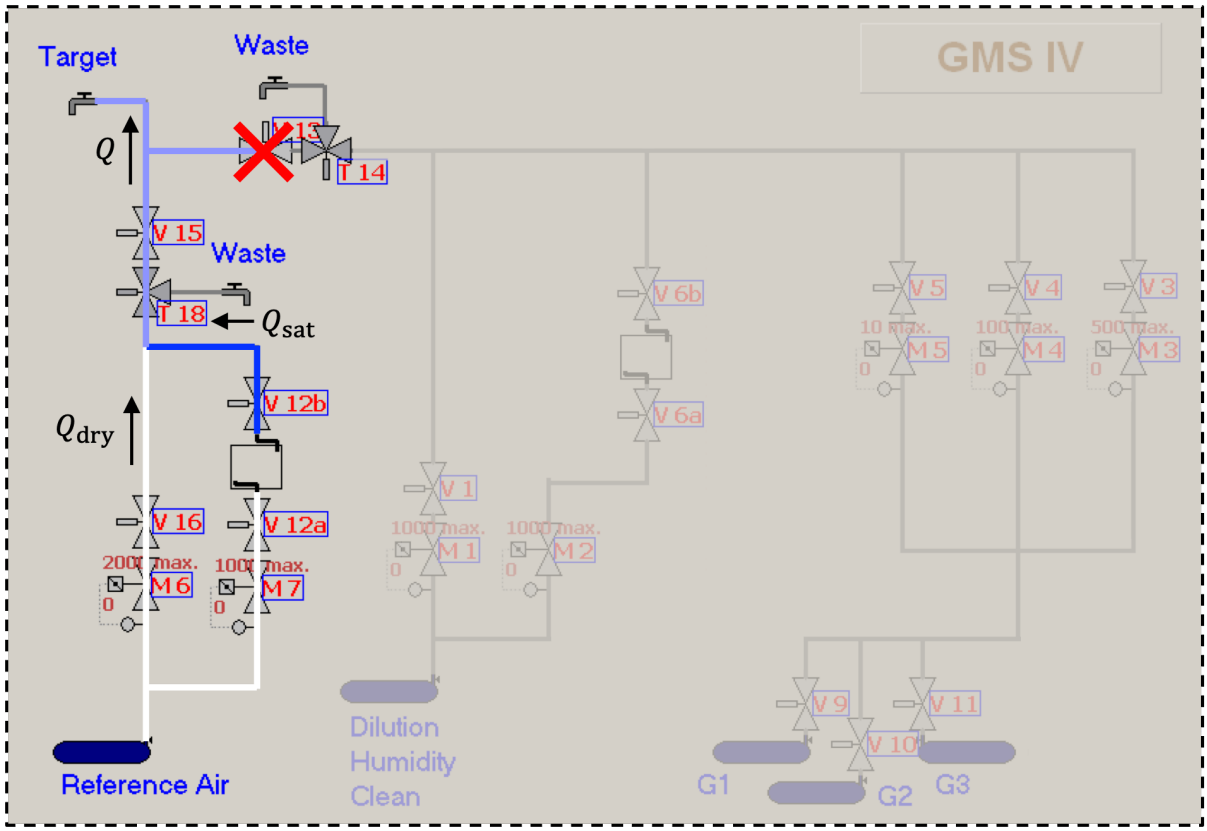

(a) Humidified reference air flow paths. During operation, the reference air section is isolated by valve 13.

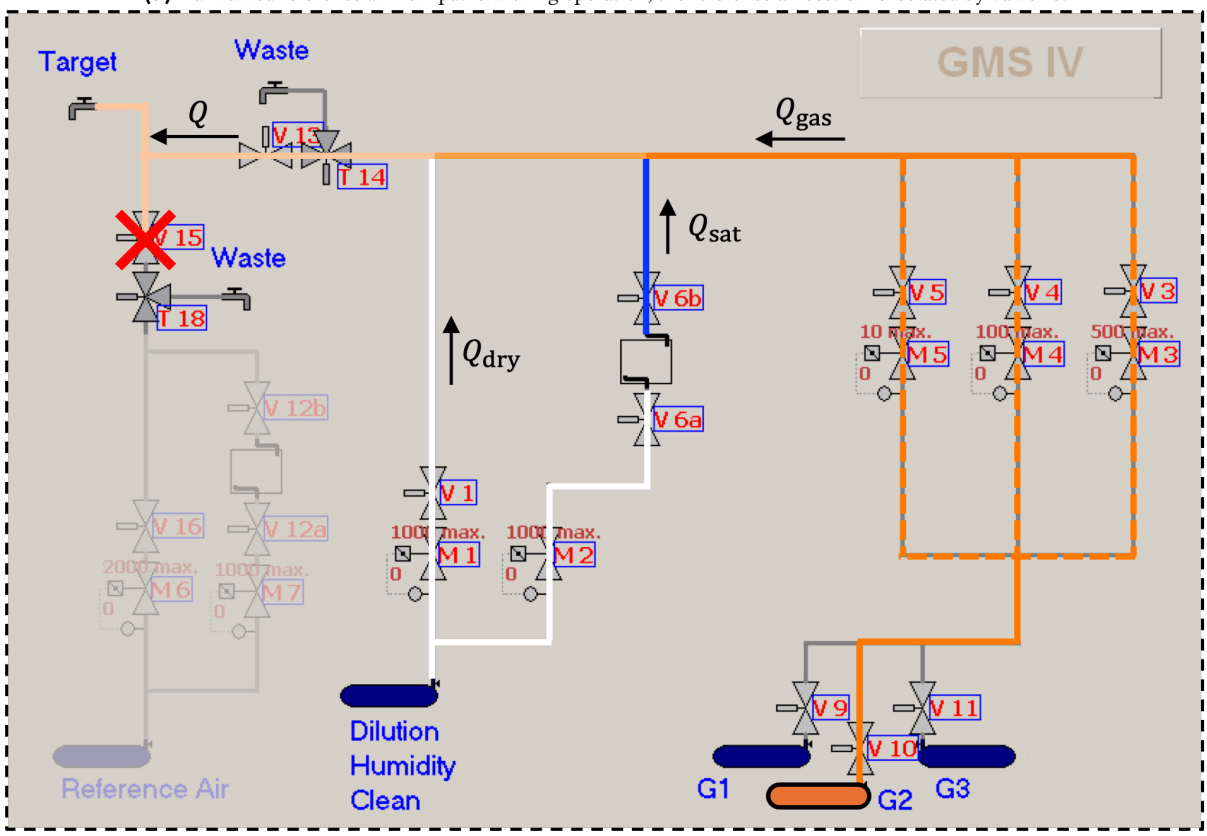

(b) Target gas flow paths. The MFCs 3, 4, and 5 are utilized depending on the required Q_{gas}. During operation, the reference air system is protected by valve 15.

Figure 3.21: Standard flow paths for GMS.

4. Relative Humidity Sensing Using Electrospun V_2O_5 Nanofibers

The chemiresistive and field-effect-based sensor technologies employed in this work for the electronic nose (eNose) are susceptible to small changes in ambient humidity. Therefore, unmonitored humidity interferes with the sensing process. Hence, continuous, reliable, and precise measurement of relative humidity with minimal cross-sensitivity to the tested analyte gases is mandatory for eNose applications. Among the vast range of potential chemiresistive materials, vanadium pentoxide (V_2O_5), a transition metal oxide (TMOX), is of particular interest due to its large carrier mobilities and catalytic behaviour. Meanwhile, electrospinning is a versatile fabrication method specialized for the synthesis of hierarchically structured and mesoporous nanofiber (NF). The annealing temperature (T_{anl}) has a profound impact on the morphology and chemical composition of the nanofibers (NFs), which in turn affects the relative humidity sensing performance, which is established for $T_{\mathrm{anl}} = 400\,^{\circ}\mathrm{C}$, $500\,^{\circ}\mathrm{C}$ and $600\,^{\circ}\mathrm{C}$ in this chapter. The best-performing sensor exhibits a linear calibration curve, high sensitivity, and fast response and recovery times. At the same time, it shows minimal response to test gases, indicating high selectivity for humidity. Parts of this chapter were previously published in Advanced Sensor Research (2025) [1].

4.1. Introduction

As discussed in Section 2.1, relative humidity describes how much water vapor is in the air relative to the maximum storable amount at a given temperature. Its precise control is crucial for diverse applications across biomedical, chemical, environmental, and industrial domains, including the healthcare, automotive, mining, agriculture, and food processing sectors [61, 126–130]. Moreover, the eNose sensor systems developed in this thesis are sensitive to even small changes in relative humidity. These changes interfere with the sensing process by altering sensing characteristics, making accurate and reliable classification difficult, if not impossible. Therefore, a reliable, energy-efficient, and high-performance humidity sensor is desired. Current progress largely depends on advancements in sensing materials, device architecture, transduction mechanisms, and fabrication technologies. Among these, the synthesis and testing used to identify high-performing candidates remain central to achieving state-of-the-art sensing performance.

Relative humidity sensing can be accomplished through various mechanisms: electrical (capacitive, chemiresistive, and field-effect-based), mechanical (surface acoustic wave and quartz crystal microbalance), and optical (colorimetric, fluorescence, and polarization/absorbance), as mentioned in Section 2.2. Among these technologies, the most commercially developed are chemiresistive sensors, which stand

out for their simplicity, cost-effectiveness, and long-term stability [40]. A wide range of materials, including metal oxide (MOX), polymers, carbon allotropes, and inorganic-organic hybrids, have been explored as chemiresistive sensing elements [40]. However, each material family faces limitations and drawbacks. Ceramic oxides often exhibit large hysteresis, low sensitivity, and slow response/recovery times, in addition to biological toxicity [131]. Similarly, carbon allotropes display poor selectivity and signal drift, resulting in poor reproducibility [131–134]. While polymers exhibit rapid, sensitive responses at high humidity, they still suffer from hysteresis and reduced performance at low humidity [135, 136]. Furthermore, water solubility remains a concern at high humidity levels [136]. As previously discussed in Section 2.2.1, chemiresistive sensors are widely used for gas sensing, where the impact of humidity is desired to be minimized. In addition to the primary sensing material, their surfaces can be modified by other materials. Known candidates used for modification include noble metals (Au [137], Al [138], Pd [139], and Pt [140]) or metal oxides (NiO [141], CuO [142]). While most modifications enhance gas-sensing performance in terms of sensitivity and selectivity, they sacrifice humidity-sensing capability. Similarly, hydrophobic coatings, such as polydimethylsiloxane (PDMS), can enhance environmental stability but can also restrict the diffusion of water molecules into the active layer, thereby diminishing sensitivity to humidity [143]. Among the listed chemiresistive materials, TMOX, a subclass of MOX, represents an outstanding material family for chemiresistive sensing applications [144–149]. TMOX-based devices can be fabricated compactly at low cost. Vanadium pentoxide, vanadium(V) oxide, or vanadia (V_2O_5), is a semiconducting TMOX with a d^0 electron configuration. It has attracted considerable interest due to its layered crystal structure, which exhibits distinct catalysis and adsorption-desorption properties. V_2O_5, the thermodynamically most stable vanadium oxide variant, is an n-type semiconductor with an optical bandgap of 2.3 eV. Its application areas range from batteries, bolometers, to electrochromic/photochromic displays, and photovoltaic electrodes [144–149]. The chemiresistive property of V_2O_5 originates from the reversible reduction of V^{5+} to V^{4+} under exposure to reducing gases [150]. However, conventional V_2O_5-based sensors commonly require UV or thermal excitation but degrade under these operating conditions, thereby limiting their operational stability and, consequently, their reliability in industrial settings [151, 152].

In addition to the chemical composition of the sensing material, its (nano)structure profoundly affects sensing performance. Compared to conventional 2D thin films, 1D nanomaterials such as nanowire (NW), nanorod (NR), nanotube (NT), and nanofiber (NF) have garnered significant attention for sensing applications due to their large mass-specific surface area, high carrier mobility, and pronounced surface reactivity [152–154]. Compared to conventional 2D thin films, these novel 1D materials require specialized synthesis methods. They are categorized into catalytic growth methods (vapor-liquid-solid (VLS) and solution-liquid-solid (SLS)), chemical solution methods (solution-phase decomposition, hydrothermal synthesis, molten-salt synthesis, electrospinning), and template-assisted methods. Previous studies have explored various V_2O_5-based nanomaterials for relative humidity sensing. Tadeo et al. reported ultrasonically nebulized thin films which can measure relative humidity in the range of 25 RH% to 76 RH%[155]. Pawar et al. demonstrated V_2O_5 nanosheets (NSs) sensing capability over a wider relative humidity range of 4 RH% to 97 RH%, albeit with poor linearity and high noise [156]. Charlotte and Viannie achieved rapid response and recovery times (60 s and 21 s) using nanoparticle-based sensors [157]. More recently, Cho et al. directly deposited V_2O_5 nanobelts via O_2-assisted physical vapor transport (PVT), which exhibits sensitivity to both humidity and gaseous analytes [158]. A novel and promising

synthesis method is electrospinning (ES) because of its ability to synthesize hierarchical-structured NFs with high porosity [159, 160]. Electrospinning (ES) is a versatile technique that can be used to synthesize a wide range of materials, including polymers, ceramics, carbon materials, and metals [159]. For ES, a polymeric precursor solution is ejected under a high electric field, forming a fine jet that solidifies into fibers. This fiber is subsequently annealed to obtain crystalline nanostructures. The result is a densely interconnected network of highly porous NFs exhibiting a wide range of pore sizes. This, in turn, allows efficient gas diffusion without sacrificing effective surface area, making it ideal for gas- and humidity-sensing applications.

During annealing, vanadium may not exclusively oxidize to vanadium pentoxide but also to vanadium dioxide[1] (VO_2). The reducing power of organic compounds in the precursor mixture has been identified as one of the contributing factors [161–163]. At the same time, the exact ratio between V_2O_5 and VO_2 also depends on the annealing temperature [163]. The precise control of this ratio is paramount for humidity-sensing applications due to the extreme differences in sensing behaviour of V_2O_5 and VO_2 [158, 163]. Additionally, the exact morphology of the NFs also depends on the annealing temperature, which in turn impacts the sensing performance [163]. Therefore, the intricate correlations between annealing temperatures, structural characteristics, and the sensing performance of electrospun V_2O_5 NFs are studied in this chapter.

4.2. Materials and Methods

4.2.1. V_2O_5 Nanofiber Synthesis by Electrospinning and Thermal Annealing

ES was chosen due to its ability to synthesize hierarchically porous NFs. Details of the ES process are discussed extensively in Section 3.1.2.

Precursor Polyacrylonitrile (PAN) (0.3 g mL^{-1}, M_W = 360 000 g mol^{-1}) and vanadyl acetylacetonate ($VO(acac)_2$) (0.1 g mL^{-1}) were dissolved in dimethylformamide (DMF). All components were purchased from Sigma-Aldrich and used as received. The mixture was magnetically stirred for at least 30 h to obtain a homogeneous precursor solution suitable for ES.

Electrospinning The spineret consisted of a 10 mL glass syringe fitted with a 200 µm stainless-steel needle. The syringe was automatically pushed during ES to achieve a constant flow rate of 2 mL h^{-1}. The stationary collector was composed of a grounded aluminum plate. A high-voltage source applied 10 kV between the metallic spineret needle and the collector during the active ES process. The jetting direction of ES setup was horizontal, e.g., the spineret was horizontally oriented, and the needle tip height matched approximately the collector center height. The working distance between the needle tip and the collector plane was set to 10 cm. This parameter set led to the formation of the Taylor cone and to stable, continuous single-jet operation.

[1] vanadium(IV) oxide

Annealing The NFs were stripped off the collector and were subsequently subjected to heat treatment in a programmable furnace to remove the polymer matrix and promote oxidation of vanadium, resulting in annealed V_2O_5 NFs. Annealing was expected to produce different mole fractions of V_2O_5 and VO_2 according to Equation 4.1, depending on the annealing temperature T_{anl} as previously mentioned.

$$n_{VO(acac)_2}\,VO(acac)_2 \xrightarrow[\text{ambient air}]{\Delta T} n_{V_2O_5}\,V_2O_5 + n_{VO}\,VO + \text{byproducts} \tag{4.1}$$

$n_{VO(acac)_2} = 2 \cdot n_{V_2O_5} + n_{VO}$ complies stochiometrically. Assuming no oxygen vacancies, the V^{5+}-to-V^{4+} ratio or the V_2O_5-to-VO_2 ratio is consequently given by $n_{V_2O_5}\, n_{VO}^{-1}$. Different samples were annealed separately at $T_{anl} = 400\,°C$, $500\,°C$ and $600\,°C$ to evaluate the effect of annealing temperature on structural and humidity sensing properties. The furnace was heated at a rate of $2\,°C\,min^{-1}$ and the final annealing temperature T_{anl} was maintained for 15 min. The material was allowed to cool inside the furnace overnight.

4.2.2. Microstructural and Compositional Analysis

The electrospun materials were characterized using multiple methods to assess the effect of annealing temperature on various material properties. These methods are presented in this section.

Electron microscopy The morphology and surface features of the NFs were analyzed by field-emission scanning electron microscopy (FE-SEM) (Hitachi 4800S). Additionally, the chemical composition was analyzed via energy-dispersive X-ray spectroscopy (EDS) and elemental mapping. High-resolution transmission electron microscopy (TEM) (Philips G20 Twin, USA) was used to study the nanostructure and crystalline growth at different annealing conditions. Selected area diffraction (SAD) patterns were recorded to identify lattice planes and confirm crystallinity. Moreover, the N_2 adsorption/desorption isotherms of the V_2O_5 NFs were analyzed using a high-vacuum physioption analyzer (Autosorb, Anton Paar). In turn, the Brunauer-Emmett-Teller (BET) surface area A_{BET}, average pore diameter $\overline{D}_{pore}$, and total pore volume V_{pore} were automatically calculated.

X-ray diffraction The crystal structure of the annealed V_2O_5 nanofibers was examined by X-ray diffraction (XRD) (Bruker D8 ADVANCE, $\lambda = 1.5418$ Å). The data were collected in the Bragg's angle (2θ) range of 10° to 70° with a step size of 0.02° and a scan rate of $2\,°\,min^{-1}$. The obtained diffraction patterns were subsequently analyzed by Rietveld[2] refinement using the TOPAS (V3, Bruker-AXS) software suite and the PDXL software from Rigaku. Using the results from XRD, the crystalite size D of the material was calculated using Equation 4.2 [164].

$$D = \frac{K\lambda}{\sqrt{\beta^2 - \beta'^2}\,\cos\theta} \tag{4.2}$$

[2] An exemplary fit is presented in Figure A3 for $T_{anl} = 500\,°C$ and the fitting parameters for all annealing temperatures are presented in Table A1

Here, K is a crystallite shape-dependent factor which is usually set to $K = 0.9$ [165], λ is the X-ray wavelength, 2θ is the Bragg's angle, β is the full width at half maximum peak, and β' is the correction of instrumental effects [166].

X-ray photoelectron spectroscopy The surface chemical states of the V_2O_5 nanofibers were analyzed using X-ray photoelectron spectroscopy (XPS) (Thermo Fisher K-Alpha+). Measurements were performed with a monochromatic Al Kα X-ray source (400 µm spot size). Charge compensation during analysis was achieved using 8 eV electrons and low-energy Ar^+ ions. The spectra were processed using Thermo Avantage software, employing Voigt peak fitting (binding-energy uncertainty of ±0.2 eV) and Scofield sensitivity factors for quantitative analysis. All binding energies were referenced to the C1s peak (C — C, C — H at 285.0 eV and verified using standard metallic Cu, Ag, and Au peaks.

4.2.3. Sensor Fabrication

Humidity sensing tests were conducted using the standard chemiresistive sensor platform (CSP) presented in Section 3.2. The V_2O_5 NFs were added to a small vial and ultrasonically dispersed in methanol (CH_3OH) for 10 min, resulting in a V_2O_5-NF suspension. 100 µL was deposited onto the interdigitated electrodes (IDE) area of the chemiresistive sensor platform (CSP) according to Section 3.2. No further postprocessing, such as heat treatment, was conducted. An image of the final sensor chip is presented in Figure 4.1.

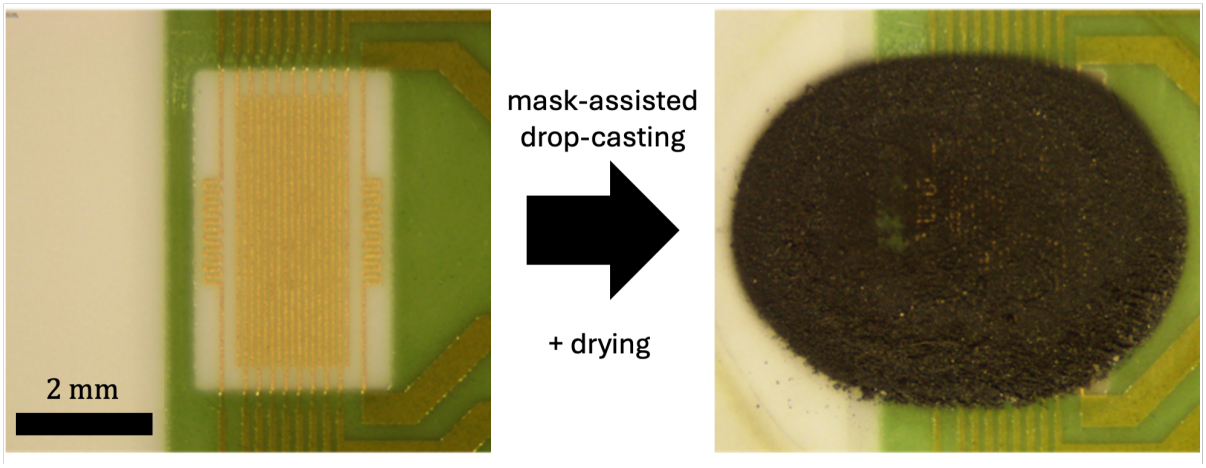

Figure 4.1: Mask assisted drop casting of V_2O_5 NFs on CSP. Left: bare IDE area of the CSP before deposition. Right: IDE covered with electrospun and annealed V_2O_5 NFs forming 16 chemiresistive sub-sensors.

4.2.4. Experimental Setup

To analyze the relative humidity sensing performance, different relative humidity levels in the 10 RH% to 90 RH% range in 20 RH% steps were supplied by the gas mixing system (GMS) (for technical details, refer to Section 3.7). Additionally, dry air ($H_{rel} = 0$ RH%) was used as the baseline reference. The

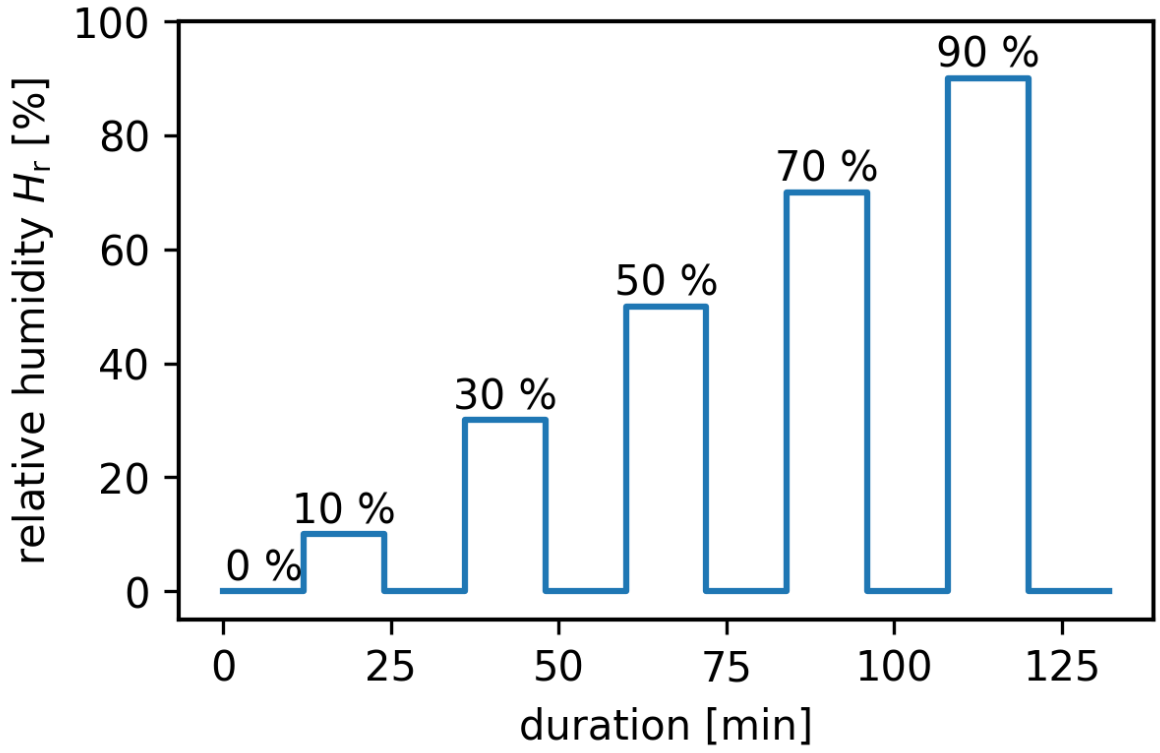

Figure 4.2: Targeted relative humidity profile. The GMS is set to provide discrete levels of 10 RH% to 90 RH% in 20 RH% steps. 0 RH% is used inbetween as baseline reference.

duration of each segment was 12 min. Relative humidity measurements were carried out at room temperature (RT) without any external excitation (e.g., heating or UV irradiation). Details about CSP, read-out, and logging in are described in Section 3.2. Measured sub-sensor resistances span a wide range from hundreds of Ω up to several hundred MΩ. Therefore, the relative response (RR) was selected as the primary response metric to enable comparability across all measurements. The humidity sensing characteristics RR, sensitivity, response time, and recovery time were evaluated according to Section 2.3. The sensitivity unit is [RR% $RH\%^{-1}$], which can be considered dimensionless.

4.3. Results and Discussion

4.3.1. Microstructural Properties

Morphology Morphological analysis by FE-SEM (Figure 4.3) and TEM (Figure 4.4) reveals porous and hollow 1D NFs at 400 °C with irregular outer diameters between 110 nm to 150 nm. The fibers exhibit rough, porous surfaces, likely originating from incomplete polymer decomposition, evaporation, and partial vanadium oxidation and crystallization. In contrast, V_2O_5 NFs annealed at 500 °C show more defined surfaces while still being fibrous and porous with diameters between 200 nm to 500 nm. Numerous pores with diameters in the range of 50 nm to 80 nm are visible, attributed to polymer

outgassing during annealing, but the NFs are not hollow compared to 400 °C. Moreover, at T_{anl} = 600 °C, the morphology transitions to particle-like, globular structures with diameters ranging from 200 nm to over 1 µm, caused by rapid crystal growth and coalescence. These results demonstrate that the fiber morphology and porosity can be fine-tuned by controlling the annealing temperature.

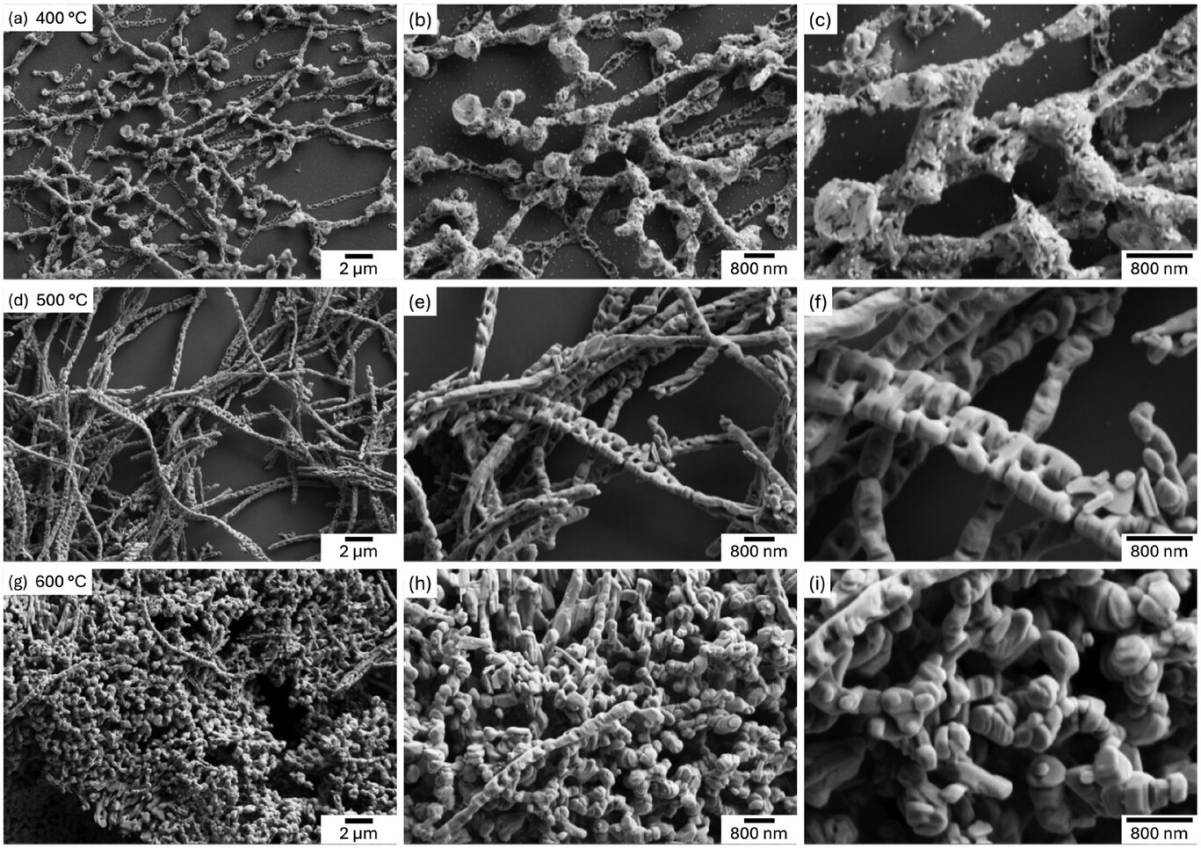

Figure 4.3: FE-SEM images of V_2O_5 NFs. (a-c) T_{anl} = 400 °C. (d-f) 500 °C. (g-i) 600 °C. The magnification increases from left to right. Reprinted from [1] under CC BY 4.0.

Crystal structure In addition to the TEM analysis in Figure 4.4, the XRD patterns and the calculated crystal parameters are presented in Figure 4.5 and Table 4.1, respectively. Across all annealing temperatures, the observed diffraction peaks are well matched to the orthorhombic V_2O_5 crystal structure in the Pmmn space group (JCPDS card no. 77-2418). Additionally, the refined lattice parameters from Table 4.1 match almost perfectly with reported values for V_2O_5 (a_0 = 11.516 Å, b_0 = 3.5656 Å, c_0 = 4.3727 Å, and V_0 = 179.55 Å^3) [96], indicating orthorhombic V_2O_5 as the primary component. Next, the structural changes across different annealing temperatures are discussed. Samples annealed at 400 °C display notably less intense diffraction peaks corresponding to the (200), (001), (110), and (400) crystal planes of V_2O_5. Additionally, lattice fringes corresponding to interplanar spacings of $d_{(200)}$ = 0.58 nm and $d_{(001)}$ = 0.71 nm are identified, confirming the coexistence of multiple orientations at T_{anl} = 400 °C. Moreover, the SAD patterns display diffuse and random interference patterns. All these findings indicate a polycrystalline character of V_2O_5 NFs annealed at 400 °C. Suprisingly, the crystallite size of

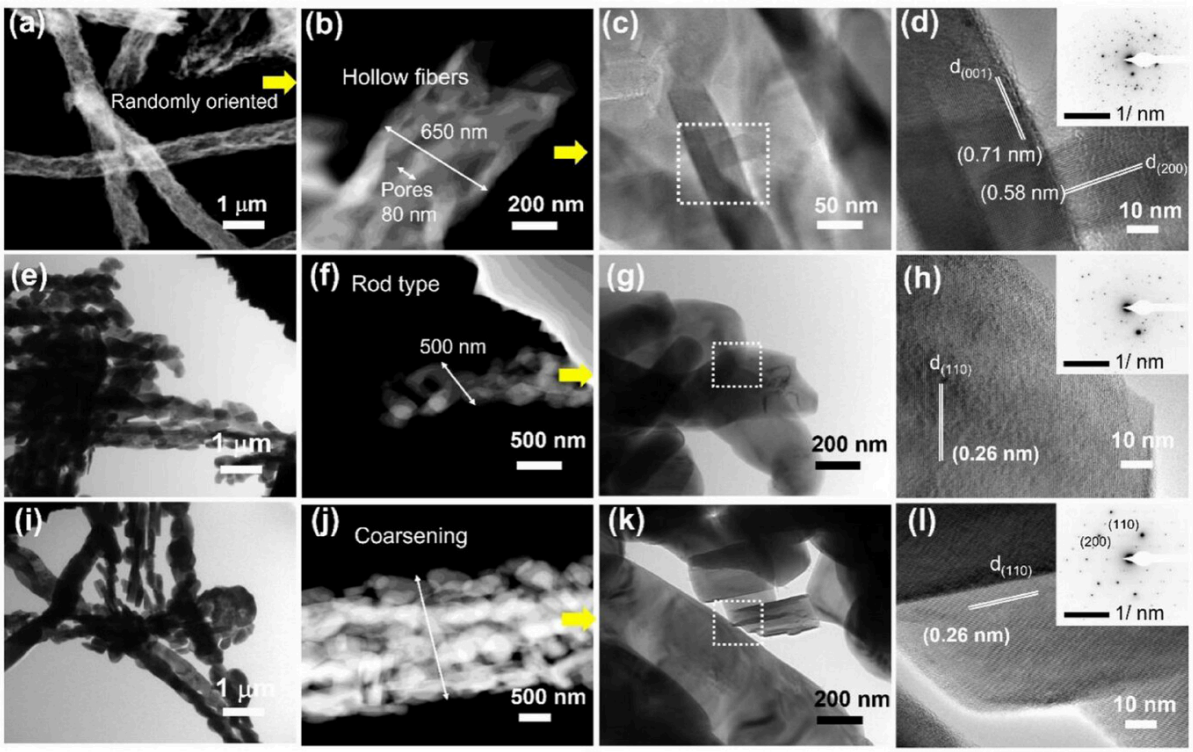

Figure 4.4: TEM and SAD analysis of V_2O_5 NFs. (a-d) T_{anl} = 400 °C. (e-h) 500 °C. (i-l) 600 °C. The first three columns show corresponding TEM images at different magnifications, and the rightmost column shows the corresponding SAD patterns. Reprinted from [1] under CC BY 4.0.

115 nm is the largest at T_{anl} = 400 °C. In contrast, annealing at 500 °C and 600 °C yields more intense peaks, indicating improved crystallinity. The most prominent peaks at 2θ = 20.32° (001) and 26.4° (110) suggest preferential growth along these directions at 500 °C and 600 °C. [167]. Lattice fringes in the TEM analysis with a d-spacing of 0.26 nm appear predominantly in fibers annealed at 500 °C and 600 °C, matching the (110) plane of V_2O_5 (JCPDS #41-1426). Corresponding SAD patterns (Figure 4.4, l) show clear spots, further confirming the enhanced crystallinity with increasing annealing temperature. The combination of smaller crystallites and high local crystallinity, which competitively influences the sensing performance [168, 169], is a first indication of good sensing performance of the NFs annealed at T_{anl} = 500 °C.

Table 4.1: XRD results. The average crystallite size $\overline{D}$, lattice constants (a_0, b_0, and c_0), and volume V_0 of the unit cell of V_2O_5 NFs annealed at 400 °C, 500 °C and 600 °C are presented.

T_{anl} [°C]	$\overline{D}$ [nm]	a_0 [Å]	b_0 [Å]	c_0 [Å]	V_0 [Å^3]
400	115	11.5158	3.5667	4.3803	179.9138
500	95	11.5143	3.5649	4.3747	179.5697
600	107	11.5148	3.5654	4.3753	179.6273

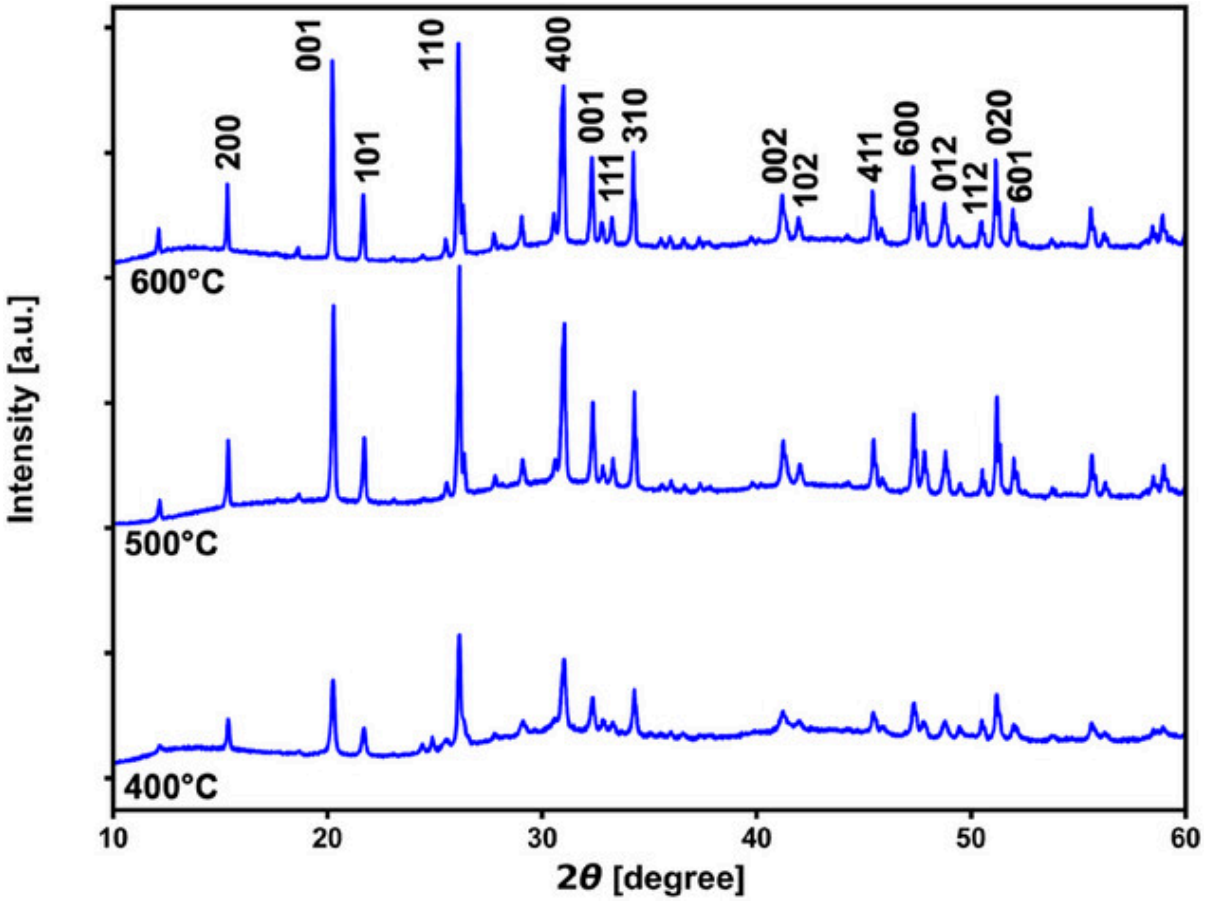

Figure 4.5: XRD patterns of V_2O_5 NFs. The XRD patterns are shown from bottom to top for samples annealed at 400 °C, 500 °C and 600 °C, respectively. Reprinted from [1] under CC BY 4.0.

Physisorption Analysis N_2 adsorption-desorption isotherms of the V_2O_5 NFs, annealed at 400 °C, 500 °C and 600 °C, exhibit type II behavior according to the International Union of Pure and Applied Chemistry (IUPAC) classification as evidenced in Figure 4.6. The type II classification supports the predominant existence of mesopores (2 nm to 50 nm) [170, 171]. Additionally, the narrow adsorption-desorption hystereses observed in Figure 4.6 a) to c) are an indication of the coexistence of larger pores, which form a hierarchical pore structure in combination with the mesopores [172]. A detailed BET analysis, which is presented in Table 4.2, reveals that the average pore diameter $\overline{D}_{\text{pore}}$ decreases with increasing annealing temperature from 22.901 nm at 400 °C to 12.173 nm at 600 °C. At the same time, the mass-specific total pore volume A_{BET} also decreases from 74.3 mm^3 at 400 °C to 50.2 mm^3 at 600 °C. In contrast, the mass-specific BET surface area A_{BET} rises with at higher annealing temperatures going from 12.992 m^2g^{-1} at 400 °C, to 14.811 m^2g^{-1} at 500 °C, and 16.507 m^2g^{-1} at 600 °C. The simultaneous decrease in pore size and increase in surface area indicate a significant increase in pore density at higher annealing temperatures. The isotherm and BET analysis indicates that the electrospun V_2O_5 NFs are well suited for humidity sensing due to the large surface area and high porosity, from which a high sensitivity is expected. Moreover, the hierarchical porosity should enable rapid gas diffusion.

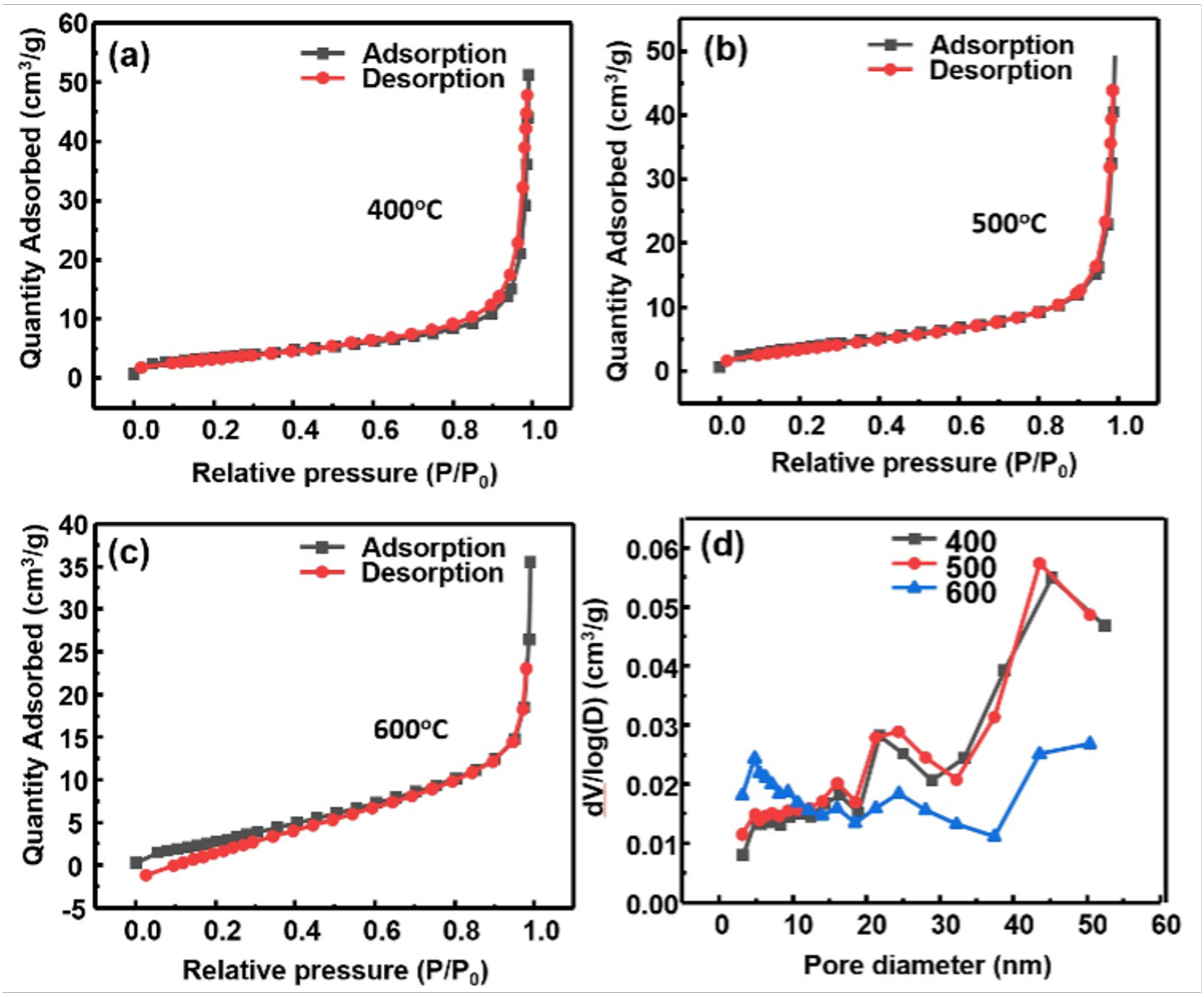

Figure 4.6: Adsorption and desorption analysis for V_2O_5 NFs. N_2 isotherms for samples annealed at 400 (a), 500 (b), and 600 °C (c). Pore diameter distribution is shown in (d). Reprinted from [1] under CC BY 4.0.

Table 4.2: BET results for V_2O_5 NFs. The average pore diameter ($\overline{D}_{\text{pore}}$), mass specific pore volume ($V_{\text{m,pore}}$), and BET-area (A_{BET}) are presented for samples annealed at 400 °C, 500 °C and 600 °C.

T_{anl} [°C]	$\overline{D}_{\text{pore}}$ [nm]	$V_{\text{m,pore}}$ [$\text{cm}^3\,\text{g}^{-1}$]	A_{BET} [$\text{m}^2\,\text{g}^{-1}$]
400	22.901	0.074382	12.992
500	19.688	0.072896	14.811
600	12.173	0.050236	16.507

4.3.2. Chemical Composition

The elemental mapping in EDS analysis, as presented in Figure 4.7, confirms the presence of V and O for all samples. Compared to the other samples, an increased concentration of residues and impurities, including C, Cu, and Ni, is found for the NFs annealed at 400 °C. Carbon in particular indicates incomplete reaction of PAN and $VO(acac)_2$ at 400 °C

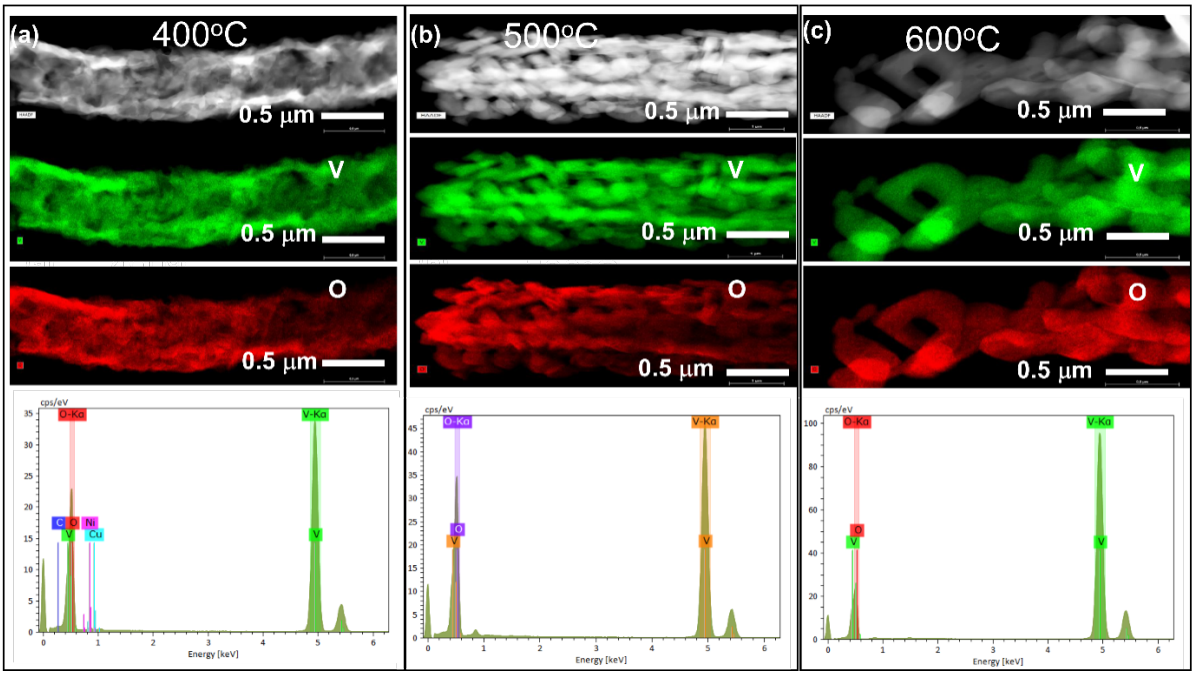

Figure 4.7: EDS analysis V_2O_5 NFs. a) T_{anl} = 400 °C. b) 500 °C. c) 600 °C. Reprinted from [1] under CC BY 4.0.

The XPS analysis confirms the presence of V and O accompanied by carbon residues, as shown in Figure 4.8. High-resolution core level spectra (refer to Figure 4.9) reveal the two V2p doublets at 517.7 eV (V^{5+}) and 516.2 eV (V^{4+}). The corresponding O1s signal to the V2p doublets is centered at 530.4 eV and is identified as lattice oxygen. Additionally, less intense peaks associated with C—O and C=O bonds are also revealed beside the main O1s peak. High-resolution core-level spectra of C1s confirm the C—O bond and detect O=C—O, C—C, and C—H bonds for all samples as depicted in Figure A4, indicating the non-negligible presence of organic residues. Quantitative calculations of the atomic concentrations show that V_2O_5 NFs annealed at 400 °C tend to contain a higher fraction of V^{4+} compared to the ones annealed at 500 and 600 °C despite the initial oxidation state of $VO(acac)_2$ being V^{5+}. This observation matches the previous reports, which associate this behavior with the reducing power of the organic precursors in the electrospun $VO(acac)_2$/PAN NFs [161–163] but needs further study to uncover the underlying oxidation mechanism. When increasing the annealing temperature to 500 and 600 °C the V^{4+} to V^{5+} ratio decreases to approximately 1/17. In contrast, the O(530.4 eV)/V_{total} ratio increases slightly from 2.2 to 2.4, indicating a reduction of oxygen vacancies and an approach toward stoichiometric V_2O_5 at higher annealing temperatures. The presence of surface contaminations makes the direct linking of O1s and oxygen vacancies difficult. The lower V^{4+}-to-V^{5+} ratio at higher annealing temperatures may indicate a composition-dependent difference in humidity-sensing properties.

4.3.3. Humidity Sensing Properties

The median sub-sensor's transient responses of V_2O_5 NFs annealed at 400 °C, 500 °C and 600 °C are presented in Figure 4.10 a, c, and e, respectively. Additionally, the corresponding H_{rel}-dependent RRs

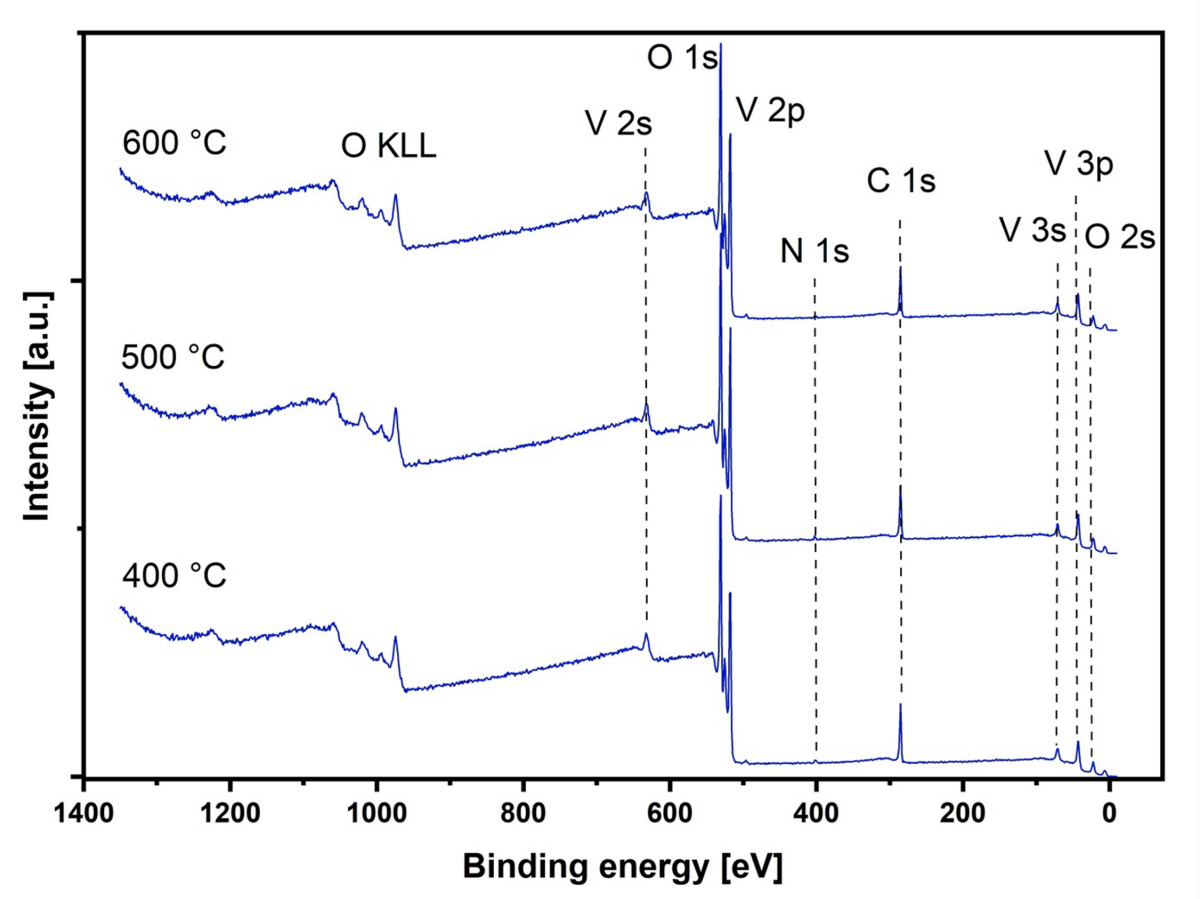

Figure 4.8: Complete XPS survey scan of V_2O_5 NFs. Annealing temperatures from bottom to top: 400 °C, 500 °C and 600 °C. Reprinted from [1] under CC BY 4.0.

and the linearly fit calibration curves are shown in Figure 4.10 b, d, and f. At $T_{anl} = 400\,°C$, the sensor exhibits a higher median resistance at reference condition ($H_{rel} = 0\,RH\%$) compared to the ones annealed at 500 °C and 600 °C. A signal drift is observed for all samples. At $T_{anl} = 400\,°C$, the sensor shows a conventional positive humidity coefficient (PHC) response[3] only for $H_{rel} = 10\,RH\%$. Conversely, between 30 RH% to 90 RH%, the responses of the sub-sensor exhibit an initial positive spike in resistance, followed by a steady decrease. The final value at the end of the 12 min segment is close to the baseline value. A correlation between the analyte concentration and spike height has been reported for NO_2 sensing using VO_2 nanowires (NWs) [173]. This finding is in line with the higher VO_2 concentration at $T_{anl} = 400\,°C$ revealed by the previous XPS analysis (Section 4.3.2). This spike-height-based analysis method may be transferable to H_{rel} sensing in this case, but requires further study. Because the RRs are calculated from the last samples of each measurement segment, no meaningful calibration curve and sensitivity can be calculated from the RR values, as shown in Figure 4.10 b). Because of these factors, the V_2O_5 NFs annealed at 400 °C is disregarded for further considerations. In contrast, sensors using V_2O_5 NFs annealed at 500 °C and 600 °C display conventional PHC responses across all tested

[3] Conventional response behaviour as defined in Section 2.3.1.

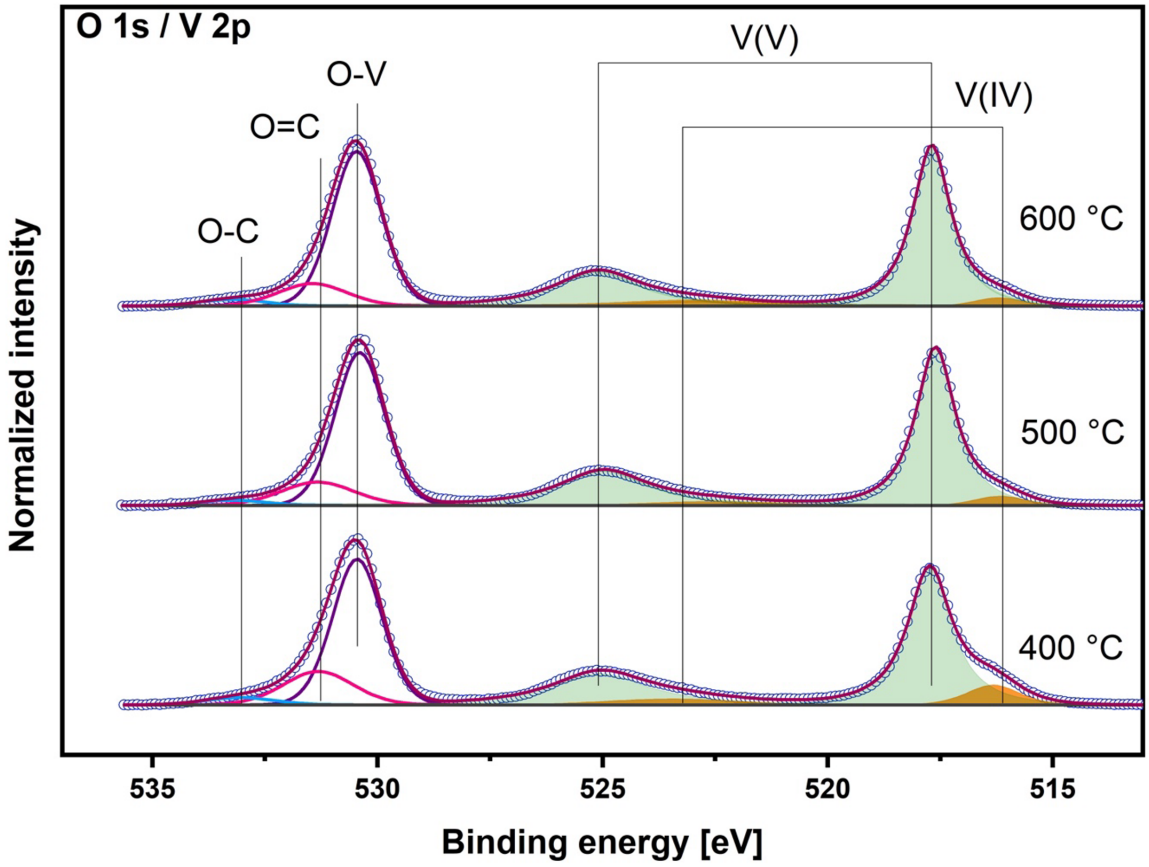

Figure 4.9: Normalized O1s and V2p core level XPS spectra of V_2O_5 NFs. Annealing temperatures from bottom to top: 400 °C, 500 °C and 600 °C. Reprinted from [1] under CC BY 4.0.

humidity values from 10 RH% to 90 RH% as shown in Figure 4.10 c and e. Additionally, the calibration curves exhibit excellent linearity. The slopes of the calibration curves, which represent the sensitivities [RR% RH%$^{-1}$], are calculated to be approximately 1.35 (T_{anl} = 500 °C) and 1.05 (T_{anl} = 600 °C). The maximum recorded sensitivity of a single sub-sensor is 1.427 (T_{anl} = 500 °C). Subsequently, the limit of detection (LoD) is calculated by linearly extrapolating the calibration curve considering a 3σ noise threshold. sub-sensors using V_2O_5 NFs annealed at 500 °C exhibit an average limit of detection (LoD) of approximately 3.5 RH% which increases to 8 RH% at 600 °C. The lowest LoD of 1.8 RH% is recorded for V_2O_5 NFs annealed at 500 °C. Therefore, for chemiresistive H_{rel} sensing, T_{anl} = 500 °C is identified as the optimal annealing temperature for electrospun V_2O_5 NF due to exhibiting the highest sensitivity and lowest LoD among all tested samples.

Next, the 90 % response ($\tau_{\text{resp,90}}$) and recovery ($\tau_{\text{recov,90}}$) time analysis is conducted using V_2O_5 NFs annealed at the previously determined optimal T_{anl} = 500 °C as presented in Figure 4.11. At H_{rel} = 10 RH%, the median response time is approximately 35 s, while 16 s is the lowest recorded value. At $H_{\text{rel}} \geq$ 30 RH%, the average reponse time values rises to around 70 s. The median and maximum values increase with higher H_{rel}. At H_{rel} = 10 RH%, the median recovery time is approximately 65 s, while 53 s is the lowest recorded value. In the range 30 RH% $\leq H_{\text{rel}} \leq$ 70 RH%, the average recovery times

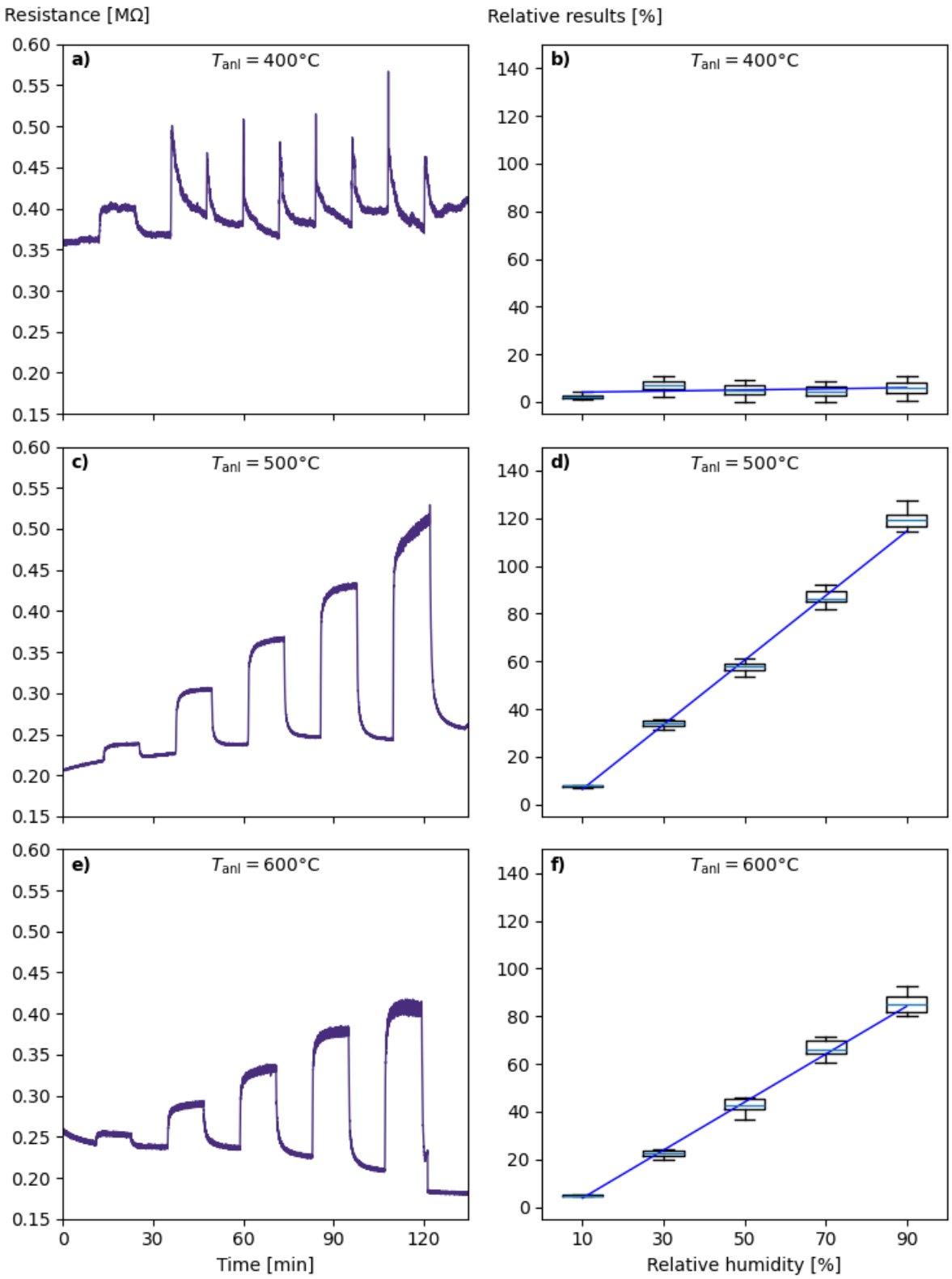

Figure 4.10: V_2O_5 relative humidity (RH) response analysis. (a, b) T_{anl} = 400 °C. (c, d) 500 °C. (e, f) 600 °C. a), b), and c) Transient sensor responses. b), d), and f) Relative responses at discrete RH levels (10 °C, 30 °C, 50 °C, 70 °C and 90 °C).

rise to approximately 125 s. At 90 RH%, the recovery time further increases to approximately 234 s. However, the high initial dynamics may be used to detect RH changes rapidly. The sensitivity, LoD,

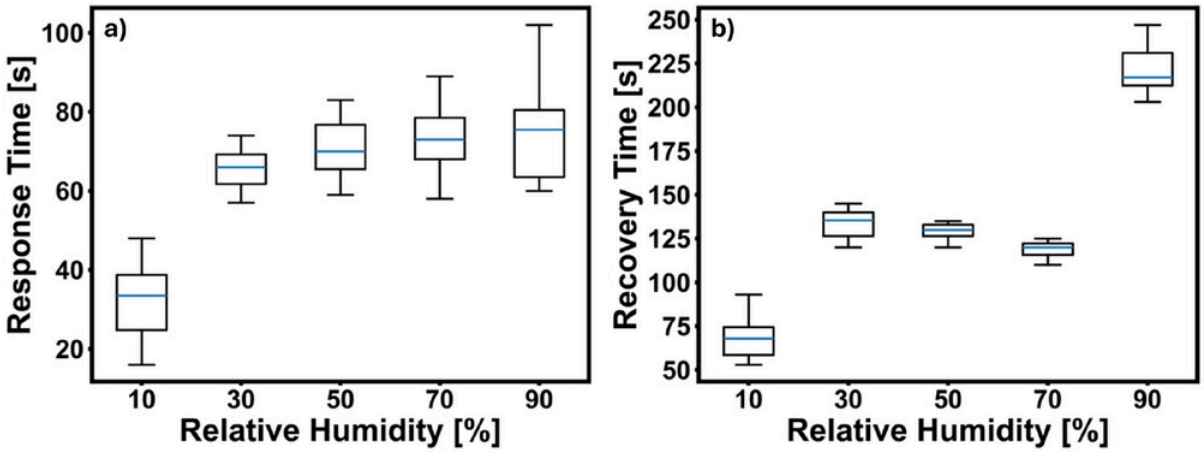

Figure 4.11: Response and recovery time analysis. a) Response time and b) recovery time at different H_{rel} levels of V_2O_5 NFs annealed at 500 °C. Reprinted from [1] under CC BY 4.0.

response, and recovery time of electrospun V_2O_5 NFs of this work are compared to other reported V_2O_5 nanomaterials in Table 4.3. Among the V_2O_5 nanomaterials, the electrospun V_2O_5 NF annealed at T_{anl} = 500 °C stands out with the highest sensitivity in the H_{rel} range between 10 RH% to 90 RH% (Table 4.3a). The LoD is excellent but slightly above the LoD of V_2O_5 nanobelts [158]. Additionally, electrospun V_2O_5 NF (T_{anl} = 500 °C) exhibit the fastest response time. The average response time is similar to thin films [155] and nanoparticles [157], and still far superior compared to NSs [156] and nanobelts [158] (Table 4.3b). The recovery time is slower than that of thin films and nanoparticles, but again faster than that of NSs and nanobelts.

Positive Humidity Coefficient Interestingly, the V_2O_5 NFs shows a positive humidity coefficient (PHC), which is atypical for n-type semiconductors. Two potential contributing mechanisms are discussed below. First, a transition between PHC and negative humidity coefficient (NHC) has been observed for WO_3 [174] and TiO_2 [175, 176] when the oxygen vacancy concentration is synthetically changed. Similarly, the oxygen concentration, derived from XPS (Section 4.3.2), of V_2O_5 NFs increases with higher annealing temperatures and approaches the expected stoichiometric value corresponding to the V^{4+} and V^{5+} concentrations. Here, a similar hydroxyl-forming mechanism may decrease the number of conducting electrons stemming from oxygen vacancies, thereby increasing resistance and leading to the observed PHC. Second, the residual carbon found in the XPS and EDS has been reported to exhibit PHC [177–181]. Further study is required to identify and confirm the exact mechanism behind the observed PHC.

Gas Independence Finally, the V_2O_5 NFs annealed at 500 °C exhibit negligible cross-sensitivity to four tested gases (1 ppm to 100 ppm) at 50 RH% as depitced in Figure 4.12.

The response to these gases is further analyzed and depicted in Figure 4.13a. Here it is observed that

Table 4.3: Comparison of V_2O_5 nanomaterials for humidity sensing.

(a) Synthesis method, sensitivity ($s_{rel,RH}$), and LoD

V_2O_5 morphology	Synthesis method	$s_{rel,RH}$ [a] [RH%]	LoD [b] [RH%]
thin film [155]	ultrasonic nebulization	0.261	none [c]
NS [156]	hydrothermal	0.422	none [d]
nanoparticle [157]	microwave annealing	0.357	none [e]
nanobelt [158]	O_2-assisted PVT	0.093	1.0
nanofiber [f] (T_{anl} = 500 °C)	electrospinning	1.427	1.8 [g]

[a] derived from linear regression according to Section 2.3.2
[b] if possible, derived from linear extrapolation of the calibration curve
[c] no value extracted due to negative LoD value
[d] no value extracted due to non-linearity
[e] no value extracted due to lack of data or plot
[f] **this work**
[g] considering a 3 standard deviation (SD) noise threshold as mentioned in Section 2.3.3

(b) Response $\tau_{resp,90}$ and recovery $\tau_{recov,90}$ time.

V_2O_5 morphology	$\tau_{resp,90}$ [s]	$\tau_{recov,90}$ [s]
thin film (TF)	35 to 60	7 to 54
NS	240	300
nanoparticle (NP)	60	21
nanobelt	177	341
nanofiber (T_{anl} = 500 °C)	16 to 100	53 to 250

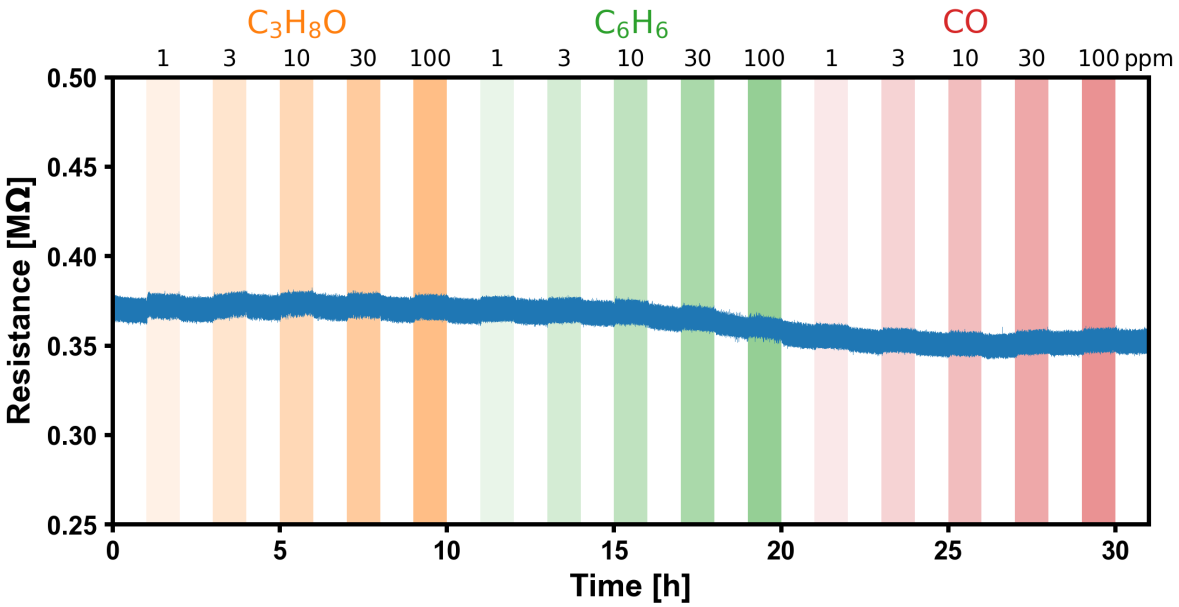

Figure 4.12: Neglible gas response of V_2O_5 NFs. The gases isopropyl alcohol (IPA), benzene, and carbon monoxide at different concentrations between 1 ppm to 100 ppm and at H_{rel} = 50 RH% were measured. Each measurement segment lasted one hour.

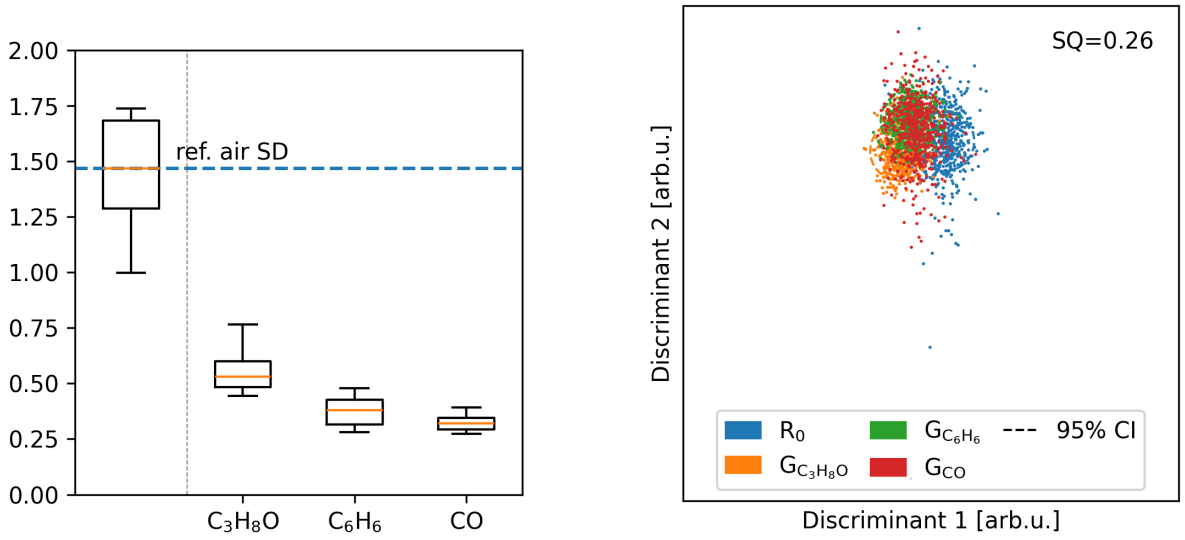

(a) Relative response of the three different gases. The relative SD (noise) of reference air is shown on the left side. All gas responses are below the standard deviation.

(b) Linear discriminant analysis (LDA) plot of the classes referene air (R_0), IPA ($G_{C_3H_8O}$), benzene ($G_{C_6H_6}$), and carbon monoxide (G_{CO}), gases at 100 ppm and at 50 RH%.

Figure 4.13: Gas response and classification analysis.

the RRs of the sub-sensors are strictly below the baseline noise, let alone the usually employed 3σ threshold. Furthermore, all classes overlap severely such that no clear separation is possible, leading to a low separation quotient (SQ) (LDA) of only 0.26 as shown in the LDA plot in Figure 4.13b.

The resulting confusion matrix (CM) from the test results is shown in Figure 4.14. As expected from

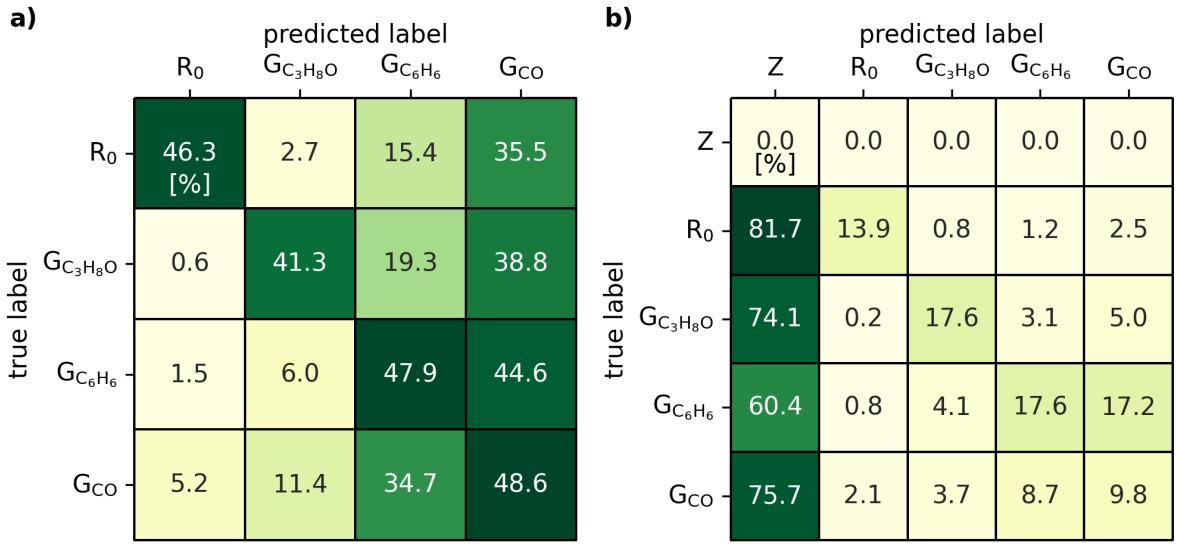

Figure 4.14: CMs of the gas classification test results. a) Only employing minimal distance-based classification. Macro average F1 = 0.48. b) Additional spherical decision boundary (95 % confidence interval (CI)). Macro average F1 = 0.23. Novelty/outlier label: Z.

previous results, the classes can not be reliably classified. If only the minimum distance is considered for classification (refer to Section 2.4.3), classes are correctly classified between 40 % to 50 % of the time, as shown in Figure 4.14 a. Many classes are misclassified as carbon monoxide, resulting in a macro-averaged F1-score of 0.48. Even worse, the majority of observations lie outside a spherical decision boundary with a 95 % CI, which leads to predominantly novelty/outlier predictions, as evidenced in Figure 4.14 b. Consequently, the macro-averaged F1-score drops to approximately 0.23.

In the following, multiple potential reasons are stated, but the exact reason and the underlying mechanism for the low sensitivity to gases are not fully elucidated and require further study. First, V_2O_5 has been shown to show low sensitivity towards hydroxylic organics such as 1-Propanol [182]. Additionally, its sensitivity depends heavily on the present humidity, which is attributed to a thin adsorbed water layer [182]. V_2O_5 is reported to be strongly hydrophilic, with simulation results showing that chemisorption is dominated by H_2O adsorption on vanadium sites of oxygen vacancies, followed by the formation of surface-level hydroxyl sites [183]. After chemisorption, more water may quickly physisorb on the NF surface to form molecular multilayers. These adsorption mechanisms would strongly compete with those of other gases, thereby lowering sensitivity. In addition, many target gases interact only weakly with V_2O_5 at room temperature and require high temperatures (300 °C to 400 °C) to function properly [184].

This finding supports the potential to use electrospun V_2O_5 NFs in a broader range of environments without risking mismeasurement due to cross-sensitivity.

4.4. Summary

V_2O_5 NFs were successfully synthesized by electrospinning a precursor material ($VO(acac)_2$ dissolved in PAN/DMF). The electrospun NFs were subsequently thermally annealed separately at 400 °C, 500 °C and 600 °C to study the impact of and connection between annealing temperature T_{anl}, morphology, chemical composition, and RH sensing properties of V_2O_5 NFs.

XRD analysis confirms the formation of orthorhombic V_2O_5 across all samples, with crystallite size decreasing at higher T_{anl}. FE-SEM and TEM investigations reveal a clear morphological evolution from hollow, fibrous structures at 400 °C to denser, globular morphologies at 500 °C and 600 °C, indicating temperature-dependent growth dynamics. Additionally, TEM shows increased local crystallinity at higher T_{anl}. N_2 adsorption-desorption isotherms indicate hierarchical mesopores with increased mass-specific surface area and pore density at higher T_{anl} according to BET analysis. XPS data indicates a positive correlation between V^{5+}/V^{4+} ratio and T_{anl}. At the same time, oxygen vacancy concentration seems to decrease with increasing T_{anl}. These results demonstrate that T_{anl} is an effective parameter for fine-tuning the crystallinity, morphology, porosity, and chemical composition of electrospun V_2O_5 nanofibers.

Next, the T_{anl}-dependent RH sensing performance was investigated using an IDE-based platform. Unlike other common chemiresistive MOX sensors, the V_2O_5 NF sensors were operated at RT without any external excitation, such as heating or UV irradiation. For T_{anl} = 400 °C, the sensor shows

non-stable responses for $H_{\mathrm{rel}} > 10\,\mathrm{RH\%}$. In contrast, at 500 °C and 600 °C, the sensors display stable sensing behaviour for all tested RH levels (10 RH% to 90 RH%) with low baseline resistance values. The sensing performance peaks at $T_{\mathrm{anl}} = 500\,^{\circ}\mathrm{C}$, showing stable operation, excellent sensitivity ($\max s_{\mathrm{rel,RH}} = 1.427\,\mathrm{RR\%\,RH\%^{-1}}$), rapid response ($\min \tau_{\mathrm{resp,90}} = 16\,\mathrm{s}$ at $H_{\mathrm{rel}} = 10\,\mathrm{RH\%}$) and recovery ($\min \tau_{\mathrm{recov,90}} = 53\,\mathrm{s}$ at $H_{\mathrm{rel}} = 10\,\mathrm{RH\%}$) time, alongside a highly linear calibration curve. The electrospun V_2O_5 NFs displays a PHC, an atypical behavior for an n-type semiconductor such as V_2O_5. Hydroxyl group formation and residual carbon are identified as potential reasons for the PHC. In summary, a connection between T_{anl}, microcrystal structure, chemical composition, and the humidity-sensing properties of ES V_2O_5 NFs was established in this chapter. Chemiresistive sensors using NFs ($T_{\mathrm{anl}} = 500\,^{\circ}\mathrm{C}$) exhibit outstanding relative humidity sensing performance, including high linear response, high sensitivity, and low cross-sensitivity.

5. Chemiresistive Electronic Nose using SnO_2 Nanowires for Gas Sensing and Mold-Detection

After the relative humidity can be reliably determined by the gas-independent V_2O_5 humidity sensor, the next step is to proceed to gas sensing using the electronic nose (eNose) technology. Next, the vapor-liquid-solid (VLS) grown SnO_2 nanowires (NWs) are used in an eNose system and are evaluated to sense and distinguish three gases besides the reference air: isopropyl alcohol (IPA), benzene, and carbon monoxide, showing elevated sensitivity towards IPA. Linear discriminant analysis (LDA) can clearly distinguish between all gases, resulting in perfect classification if no decision boundaries are used. At the same time, the F1-score remains high (0.978) even when a 95 % confidence interval is used as the decision boundary. Finally, the eNose is used to detect and identify indoor mold, which may pose a significant health risk to humans and animals. Compared to traditional sampling-based methods, the eNose is fast while remaining reliable and accurate. For a more general analysis, the eNose is applied to two mold species across two culture media. Various analysis strategies are explored to improve LDA performance, yielding a peak F1-score of 0.984. Thereby, the reliable and accurate detection and identification of different mold species using the chemiresistive eNose is demonstrated. Parts of this chapter were previously published in Advanced Sensor Research (2025) [2].

5.1. Introduction

Gas sensing plays a key role in environmental and industrial monitoring and in health diagnostics [73, 185]. An electronic nose uses arrays of partially selective sensors, combined with pattern-recognition algorithms, to recognize previously trained odors, which consist of multiple volatile compounds.

Among chemiresistive metal oxide (MOX) materials, tin dioxide (SnO_2) is one of the most widely used. As a wide-bandgap (3.6 eV) n-type semiconductor, SnO_2 exhibits strong sensitivity to oxidizing and reducing gases through surface adsorption-desorption processes that modulate its electrical conductivity as described in Section 2.2.1. Therefore, it is sensitive to a wide variety of gases while remaining chemically stable under a broad range of conditions. These features make it an excellent candidate for integration into an eNose system for the recognition of complex gas mixtures. Furthermore, 1D NWs, which form dense networks, further enhance the gas sensing performance of SnO_2 through their extremely high surface-to-volume ratio, efficient charge carrier transport along a single crystalline

path, and strong modulation of conductivity upon surface reactions. These properties make SnO_2 NWs an ideal chemiresistive sensing material.

The VLS method is a robust yet inexpensive synthesis route for obtaining SnO_2 NW with high aspect ratios. During VLS, a precursor material is evaporated and adsorbs into a liquid catalyst droplet. Finally, the droplet supersaturates, and the material crystallizes beneath the droplet, continuously forming the NW. The detailed process is described in Section 3.1.3. One key parameter, the positioning of the substrates relative to the precursor source, strongly influences the local precursor concentration in the substrates' proximity. This, in turn, affects NW diameter and, consequently, the sensing characteristics. The gas-sensing performance of VLS-grown SnO_2 NWs is then analyzed through their response magnitude, response time, and recovery time under controlled gas mixtures.

In terms of application, the chemiresistive SnO_2-NW based eNose is applied for indoor mold detection, which is crucial for maintaining healthy living conditions [186, 187]. Compared with conventional sampling methods, which are reliable but time-consuming and costly [186], the eNose system is expected to quickly detect mold presence and reliably identify the species. Two mold species from different genera on two distinct substrates are evaluated for a more general assessment. A special focus was placed on optimizing the machine learning method to enable the eNose to reliably recognize complex volatile organic compound (VOC) profiles of different mold species.

5.2. Materials and Methods

5.2.1. SnO_2 Nanowire Synthesis via Vapor-Liquid-Solid Process

SnO_2 was selected as the sole chemiresistive sensing material, widely used and well known for its superior gas-sensing capabilities across various applications [105]. To further enhance the sensing performance, the NW structure was selected for the exceptionally high surface area and porosity of NW-networks. The SnO_2 NWs were fabricated by the standard VLS process, which is described in Section 3.1.3, including the operation parameters pressure, temperature, and gas flow rate in each phase. The optimization was performed as part of a supervised student thesis [7]. The placement of the SnO precursor powder was fixed at the center of the tube oven. It has been observed that the relative placement of the Si substrates had a profound impact on several NW properties, including NW count per area, average NW diameter, and morphology. The following placements were tested: outside the precursor boat on a secondary upside-down alumina boat (behind-boat), above the precursor boat (above-boat), and behind the precursor inside the precursor boat (inside-boat) as depicted in Figure 5.1The directions are stated concerning the gas (Ar and O_2) flow direction. A fuzzy layer was visible on top of the substrates, indicative of NWs. Additionally, the whitish coloration on the substrate increased from the center towards the edges, suggesting a greater accumulation of material along the edges. In contrast, the inside-boat substrates showed no fuzzy structure but rather displayed rough particles.

Next, the morphologies of the VLS-grown SnO_2 NWs were analyzed by scanning electron microscopy (SEM). The corresponding electron micrographs of a behind- and above-boat placements sample are

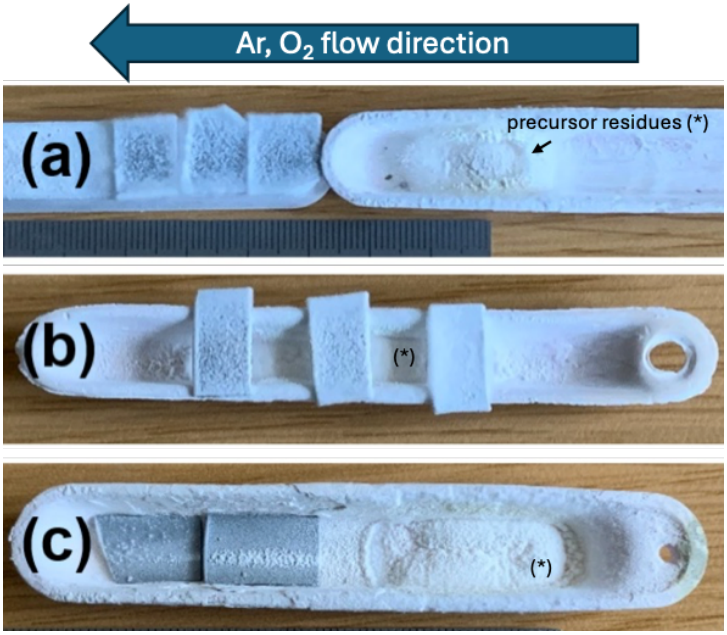

Figure 5.1: Different Si-substrate placements for VLS. Images are taken after the VLS. a) behind-boat, b) above-powder (c) inside-boat. Adapted from [7].

shown in Figure 5.2. Both the behind-boat placement (a) and the above-boat placement (b) produced

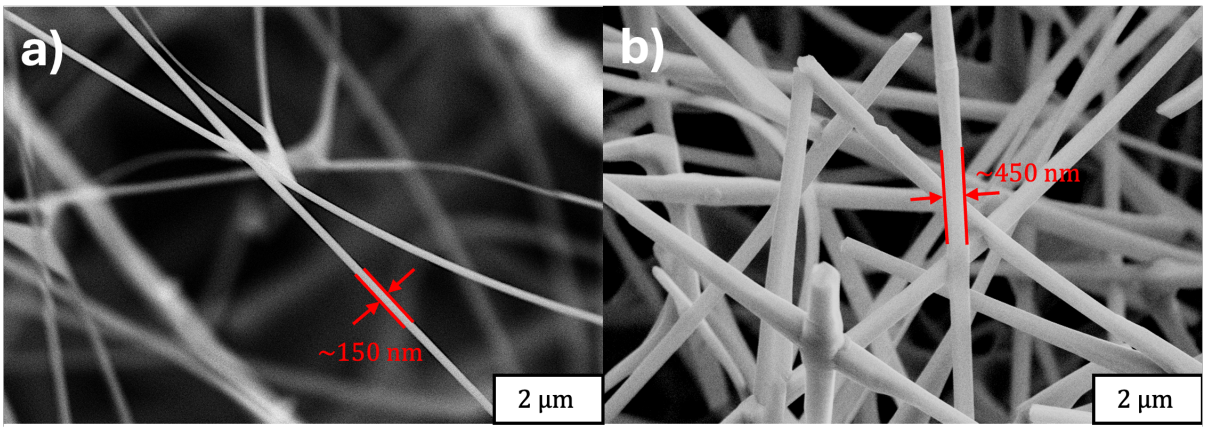

Figure 5.2: SEM images of VLS-grown SnO_2 NWs of different substrate placements. a) Behind-boat. b) Above-boat. Data collected from [7].

material with distinguishable 1D wire or whisker morphology. The behind-boat placement exhibited a lower average NW diameter (100 nm to 300 nm) compared to the above-boat placement (300 nm to 500 nm). In contrast, the inside-boat placement did not produce NW but rather an irregular and globular morphology as shown in Figure A5. In preliminary tests, the inside-boat material could not be used for chemiresistive sensing due to its extremely high resistivity. This further indicates a polycrystalline structure with grain boundaries that limit conductivity. Therefore, the inside-boat placement was disregarded for further analysis. As shown in Figure 5.1 and Figure 5.2, the SnO_2 NW thickness seemed to decrease with increasing distance to the precursor source. The SEM images were analyzed in more

detail by the open-source ImageJ software in combination with the DiameterJ plugin to obtain the NW distribution. The scaling of the SEM images was manually fit to the scale bar, which is automatically provided by the SEM software. DiameterJ generated several differently parametrized and segmented black-and-white images, from which the best one is selected. Finally, DiameterJ automatically analyzed the wire dimension distribution using the centerline formulation and subsequent center-to-edge distance analysis. The resulting normalized NW distributions are presented in Figure 5.3. It can be discerned that the NW diameter decreases from 448 nm (above-boat) to 85 nm (behind-boat) on average at the center area of the substrates (Figure 5.3 a). A larger variation of nanowires was also observed for the above-boat placement samples. Furthermore, a slight increase in NW diameter was observed at the edge area compared to the center area (Figure 5.3 b). Further increasing the source-to-target distance

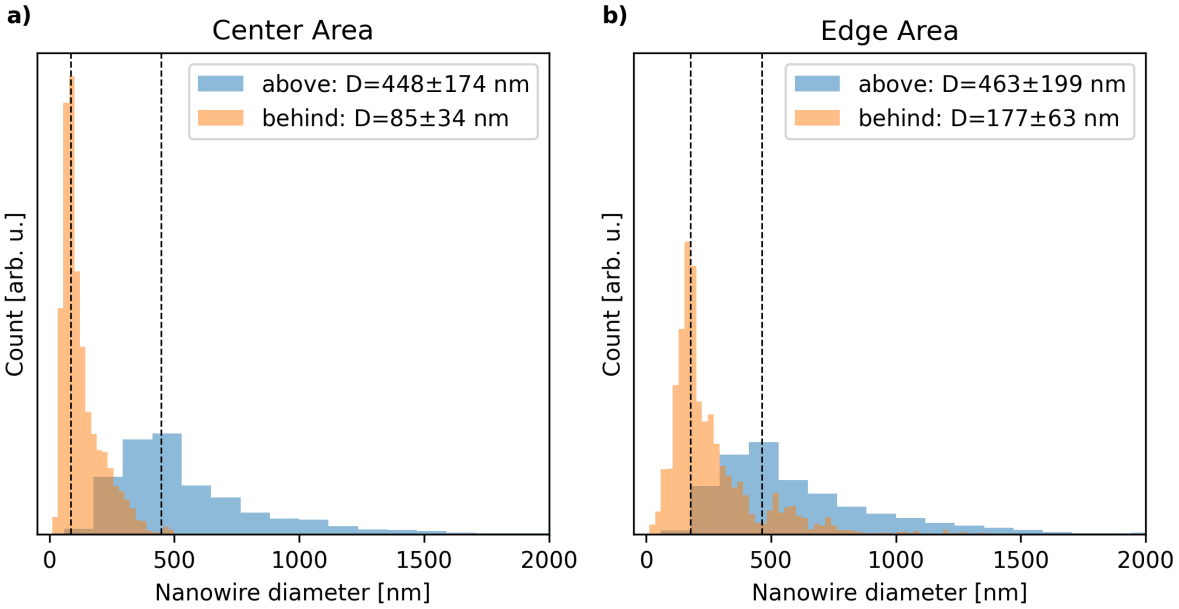

Figure 5.3: Position dependent NW diameter distribution. Data collected from [7].

eventually led to insufficient NW growth, as depicted in Figure A6. Consequently, the behind-boat positioning was selected with a distance range of 4 cm to 7 cm as the preferred substrate placement for all subsequent VLS processes.

5.2.2. Sensor Fabrication

After the VLS process, the SnO_2 nanofibers (NFs) were collected by carefully stripping them from the Si-substrates using a scalpel. The collected SnO_2 NWs were dispersed in IPA by magnetic stirring for at least 10 min to obtain a SnO_2 suspension that can be deposited in subsequent steps. The IPA based SnO_2-NW-suspension was deposited on top of the interdigitated electrodes (IDE) array of the chemiresistive sensor platform (CSP) by mask-assisted drop casting, forming 16 sub-sensors. Due to rapid sedimentation, deposition was performed immediately after magnetic stirring, and special care was taken to collect only from approximately half the height of the suspension to avoid depositing large

amounts of sediment. After drop-casting, the material was left to dry at room temperature (RT) for more than 30 min, and the mask was subsequently removed. The SnO_2 NWs were electrically connected to the IDE, forming 16 chemiresistive sub-sensors. Images of the IDE area before and after deposition are shown in Figure 5.4. The sensor was operated at RT, and the SnO_2 NWs were excited using UV

Figure 5.4: SnO_2 NWs on top of IDE array after deposition. Adapted from [2] under CC BY 4.0.

irradiation ($\lambda = 365\,\text{nm}$, irradiance $\approx 15\,\text{mW}\,\text{cm}^{-2}$) to promote gas-MOX interactions. Additionally, the excitation reduced the electrical resistivity of SnO_2 to a conveniently measurable range of several MΩ. In a measurement period of approximately 1 s, all 16 sub-sensor values were measured and logged, resulting in $N = 16$ features consisting of resistance values.

5.2.3. Humidity Sensing Setup

IPA, benzene, and carbon monoxide at 100 ppm concentration in addition to reference air were supplied by the gas mixing system (GMS) at a constant relative humidity of 50 RH%. The detailed description of the GMS setup is presented in Section 3.7. The flow rate was kept constant at 500 sccm. Each gas measurement segment took 30 min. Before and after each gas measurement segment, reference air at 50 RH% was measured as the baseline.

5.2.4. Mold Sample Preparation

Preparation Domatec GmbH conducted all mold and reference sample preparations as part of a ZIM[1] project. This subsection reports the detailed preparation procedures as stated by Domatec GmbH. The mold species *Stachybotrys chartarum* (*S. chartarum*) and *Chaetomium globosum* (*C. globosum*)

[1] Central Innovation Programme for small and medium-sized enterprises, German: **Z**entrales **I**nnovationsprogramm **M**ittelstand (ZIM)

were obtained from the Landesgesundheitsamt Baden-Württemberg (State Health Authority of Baden-Württemberg, Germany). For each mold species, two distinct culture media were used: whole wheat flour agar and gypsum board agar. For the whole wheat flour agar, 30 g flour and 15 g agar-agar were first weighed, then mixed with 1000 mL distilled water, and finally autoclaved (Varioclav 135S, HP Labortechnik GmbH) at 121 °C for 15 min to ensure sterility. For the gypsum board agar, the gypsum board was first mechanically ground into a fine powder. Similar to the wheat flour agar, 30 g of the gypsum powder was mixed with 15 g agar-agar, and subsequently dissolved in 1000 mL distilled water, followed by autoclavation under identical conditions as the whole wheat flour agar. At this stage, each culture medium was in liquid form and was then cast into sterile culture bottles (DURAN 1000 mL, GLS 80, DWK Life Sciences) under sterile conditions. The culture media solidified after cooling to RT, forming a stable growth surface. Then the culture bottles were separately inoculated with the selected mold strains, *Stachybotrys chartarum* (*S. chartarum*) and *Chaetomium globosum* (*C. globosum*). Each sterile bottle was inoculated in a Class II biological safety cabinet (Airstream ESCO Class II Biological Safety Cabinet) to prevent cross-contamination. The spores were applied directly to the surface of the culture medium using a sterile inoculation loop. Subsequently, the inoculated bottles were incubated at (25 ± 3) °C at a H_{rel}. The incubation lasted at least 10 days, during which the surface of the culture medium was colonized by mold. Stationary growth was ensured through regular inspections. For reference purposes, additional bare culture medium samples were prepared by omitting the mold inoculation and incubation steps. In total, six different types of samples were fabricated: gypsum-agar substrate reference, wheat-agar substrate reference, *S. chartarum* on gypsum-agar substrate, *S. chartarum* on wheat-agar substrate, *C. globosum* on gypsum-agar substrate, and *C. globosum* on wheat-agar substrate as depicted in Figure 5.5.

Storage The samples were delivered to Karlsruhe Institute of Technology (KIT) in insulated boxes and stored at RT with the bottle cap closed. They were also shielded from direct sunlight to prevent UV-irradiation from harming the molds.

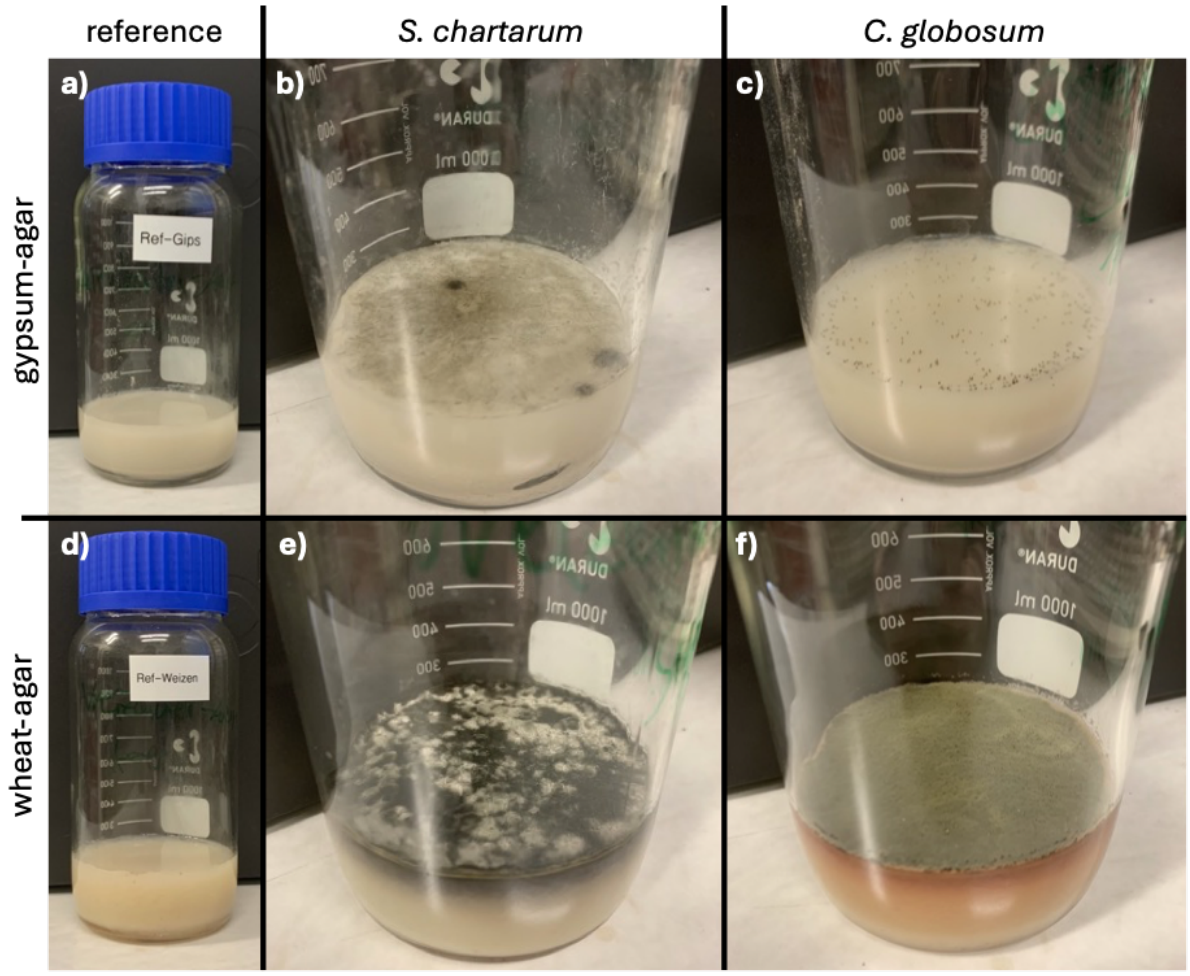

Figure 5.5: Mold and culture media samples. The samples were received from domatec GmbH. a) gypsum-agar reference, b) *S. chartarum* on gypsum-agar, c) *C. globosum* on gypsum-agar, d) wheat-agar reference, e) *S. chartarum* on wheat-agar, f) *C. globosum* on wheat-agar.

5.2.5. Mold Measurement Setup

The eNose was operated in a laboratory setup that consists of the GMS (refer to Section 3.7) and a custom-built pipe system, as depicted in Figure 5.6. The GMS provided humidified zero air at 700 sccm. This zero air was either directed into the mold sample bottles and transported the mold microbial volatile organic compounds (MVOCs) to the eNose or used as the baseline reference air via a bypass.

As depicted by Figure A7, polytetrafluoroethylene (PTFE) membrane filters with a pore size of 0.2 µm were used to prevent spore contaminations (*S. chartarum* ≥ 4 µm [188], *C. globosum* ≥ 6 µm [189]). Six distinct samples, including two agar-based culture medium references without mold and four mold samples, were measured by the eNose. Additionally, reference air was measured as the baseline. All samples, in addition to reference air, were summarized and assigned to class symbols in Table 5.1a. A measurement series consisted of alternating segments of baseline and sample measurements as presented in Table 5.1b. Samples and baseline measurement duration were set to 30 min and 10 min,

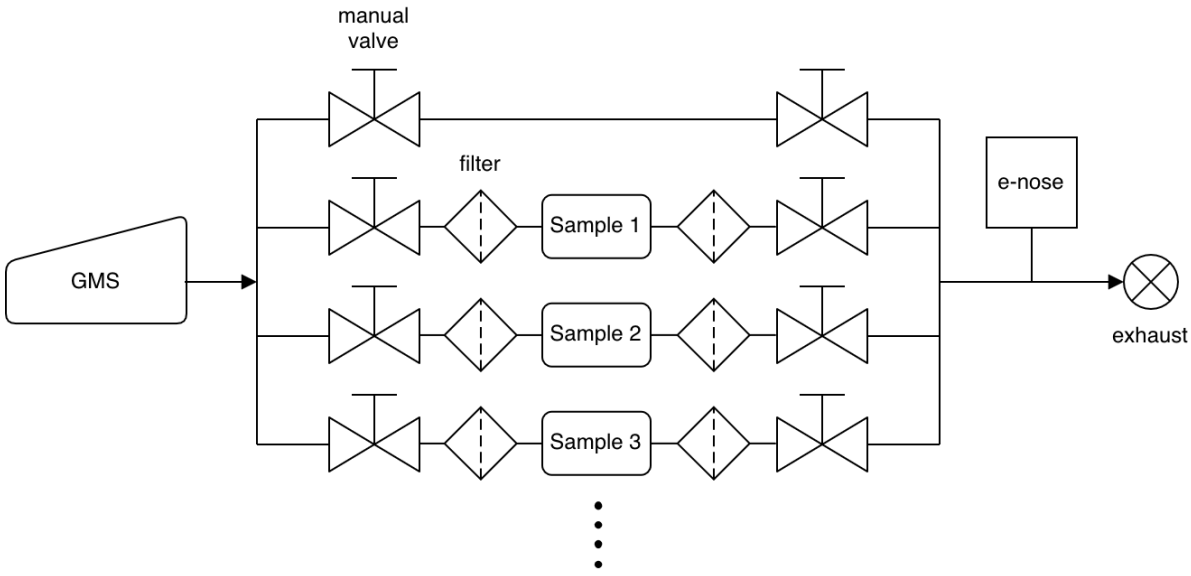

Figure 5.6: Piping diagram of the mold measurement setup. Refer to Section 3.7 for details of the GMS.

respectively. The shorter baseline measurement duration was justified by a faster response signal stabilization (shorter $\tau_{\text{resp},90}$). For each mold species, eight measurement series were conducted over two weeks.

Table 5.1: Mold measurement series. Each series consists of individual measurement segments.

(a) Measured samples and corresponding classes

Class	Description	Mold	Culture medium
R_0	reference air	none	none
R_G	gypsum-agar reference	none	gypsum
R_W	wheat-agar reference	none	wheat
S_G	*S. chartarum* on gypsum-agar	*S. chartarum*	gypsum
S_W	*S. chartarum* on wheat-agar	*S. chartarum*	wheat
C_G	*C. globosum* on gypsum-agar	*C. globosum*	gypsum
C_W	*C. globosum* on wheat-agar	*C. globosum*	wheat

(b) Segment order of measurement series

i_{segment}	Class c	Dur. [min]
1	R_0	10
2	R_G	30
3	R_0	10
4	S_G or C_G	30
5	R_0	10
6	R_W	30
7	R_0	10
8	S_W or C_W	30
9	R_0	10

(c) Initial data distribution accumulated over several measurement series

Class c	M_c	Rel. distr. [%]
R_0	17030	46.54
R_G	5418	14.81
R_W	4816	13.16
S_G	2408	6.58
S_W	2107	5.76
C_G	2408	6.58
C_W	2408	6.58
total	36595	100

5.2.6. Data Analysis

5.2.6.1. Target Gas

The resistance values were recorded using the Kamina Observer (KamObs) software (refer to Section 3.2), whereas detailed response analysis and machine learning were performed using custom Python scripts.

Response Analysis To ensure comparability across measurement segments, linear baseline corrections were applied to each sub-sensor signal to extract relative response, response time, and recovery time. Thereafter, the exponential function as described in Equation 2.12 (Section 2.3.1) was fit for the response and recovery measurement data. This is performed individually for each subsensor and for each measurement segment. Finally, the relative response (RR), response time, and recovery time were calculated from the exponential fit. To ensure that only response and recovery time were extracted from reasonable fits, entries were excluded when the RR is less than 3 times the observed baseline standard deviation.

Classification Analysis From the measurement segments, the latest 10 min were extracted. Consequently, the following classes were labeled reference air (R_0), IPA ($G_{C_3H_8O}$), benzene ($G_{C_6H_6}$), and carbon monoxide (G_{CO}). Due to the different measurement frequency, more observations were labeled as R_0 compared to other gas class labels. Therefore, the data were first randomly undersampled (`RandomUnderSampler`, imblearn 0.13.0, `random_state=42`) to match the minority-class observation count of $M_c = 88$ per class. Next LDA was evaluated by leave-one-out cross-validation (LOOCV) (`LeaveOneOut`, sklearn 1.5.2). In each LOOCV iteration, a LDA model was trained using $M - 1$ observations and tested using the left-out observation. Using the accumulated test results of the LOOCV, the classification metrics precision (PRC), recall (REC), and F1-score (F1) were evaluated (`classification_report`, sklearn). Additionally, normalized confusion matrixs (CMs) were evaluated using `confusion_matrix` from sklearn.

5.2.6.2. Mold Classification

Due to the large initial dynamic, only the most stationary data from the latest 5 min of each measured segment were extracted and labeled. The resulting feature matrix $\boldsymbol{X} \in \mathbb{R}^{M \times N}$ and the corresponding label array $\boldsymbol{y} \in \mathbb{G}^M$ consisted of $M = 36595$ observations with $N = 16$ (columns). The set of classes was defined as $\mathbb{G} = \{R_0, R_G, R_W, S_G, S_W, C_G, C_W\} \mid C = 7$.

Similar to the gas measurements, the collected dataset was imbalanced, as shown in Table 5.1c. This was primarily caused by different occurrence frequencies of measurement segments of reference air (R_0), culture media references (R_G and R_W), and mold-containing samples, as evidenced by Table 5.1b. Additionally, differences in resistance values may have affected the sample frequency of the readout electronics as mentioned in Section 3.7. As previously mentioned in Section 2.4, imbalanced datasets may negatively impact classification performance. This is also the case specifically for LDA [190]. For

this reason, the dataset was downsampled so that the sample size of each class matches that of the minority class, which is S_W with 2107 samples. $\boldsymbol{X}$ was element-wise logarithmically (to the base of 10) transformed. Class-specific QQ-plots showed that, although the feature data only loosely conformed to a normal distribution, the deviations were tolerable for LDA [87]. No further preprocessing was performed.

The dataset was shuffled and split in a stratified fashion into

- training $(\boldsymbol{X}_{\text{train}}, \boldsymbol{y}_{\text{train}})$ sets and
- test $(\boldsymbol{X}_{\text{test}}, \boldsymbol{y}_{\text{test}})$ sets.

A relative test size of $M_{\text{test}}/M = 10\,\%$ was used. The classification metrics PRC, REC, and F1-score, in addition to CM, were evaluated on the test dataset. For LDA specifically, the decision boundaries of each class were implemented with a fixed 95 % confidence interval (refer to Section 2.4.3). Feature selection was performed by using a 10-fold cross-validation (CV) using only $\boldsymbol{X}_{\text{train}}$. The number of discriminants (N') was fixed to $C - 1$, which is the maximum (refer to Section 2.4.3).

Python (3.13.0) was used for data analysis. In addition, the following packages were used for calculations: NumPy (2.1.3), SciPy (1.14.1), scikit-learn (1.5.2), and imbalanced-learn (0.13.0). For all functions that include any randomization, the `random_state` variable was set to 42 for reproducibility.

5.3. Results and Discussion

5.3.1. Gas Sensing

5.3.1.1. Response Analysis

A representative median response curve of IPA ($G_{C_3H_8O}$), benzene ($G_{C_6H_6}$), and carbon monoxide (G_{CO}) is depicted in Figure 5.7 a. For all gases at 100 ppm, the response curves exhibit a rapid increase in resistance upon exposure. The resistance signal also returns to baseline quickly when reference air is reapplied.

Among the target gases, IPA exhibits the highest median response, followed by benzene, and carbon monoxide shows the lowest response. This is also reflected in the detailed RR analysis shown in Figure 5.7 b. Here, the RR to IPA averages approximately 0.8, with a maximum of over 2.0. A large spread is observed with the interquartile range (IQR) ranging from approximately 0.25 to 1.00. In contrast, the sensor exhibits a RR of less than 0.5 to benzene and carbon monoxide. Still, the minimal RR for benzene is above the average $3\sigma_0$ threshold (horizontal dotted lines). Here σ_0 is the baseline's standard deviation (SD). Carbon monoxide shows the lowest RR below 0.25. Some sub-sensor's RRs fall below the $3\sigma_0$ threshold. Therefore, the sensor shows an elevated average selectivity towards IPA. Yet, due to differences in selectivity among the subsensors, benzene and carbon monoxide can be achieved with high selectivity, as will be shown in Section 5.3.1.2.

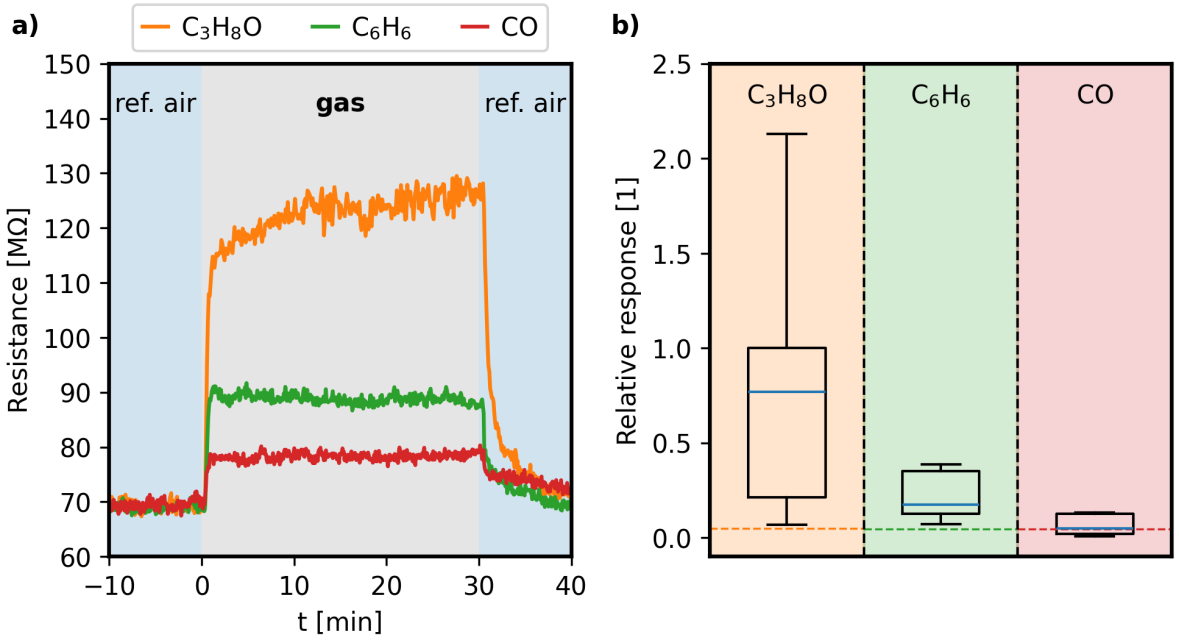

Figure 5.7: SnO_2 NW sensor gas response. Tested target gases: IPA ($G_{C_3H_8O}$), benzene ($G_{C_6H_6}$), and carbon monoxide (G_{CO}) at 100 ppm. a) Baseline corrected transient response curves. b) Box-plot of RRs. The dotted horizontal lines near zero represent the three times the averaged baseline standard deviation (0.0475, 0.0444, 0.0442).

Furthermore, the (90 %) response and recovery times are analyzed, and the results are presented in Figure 5.8. Response times when measuring IPA are widely distributed across the subsensors, with a

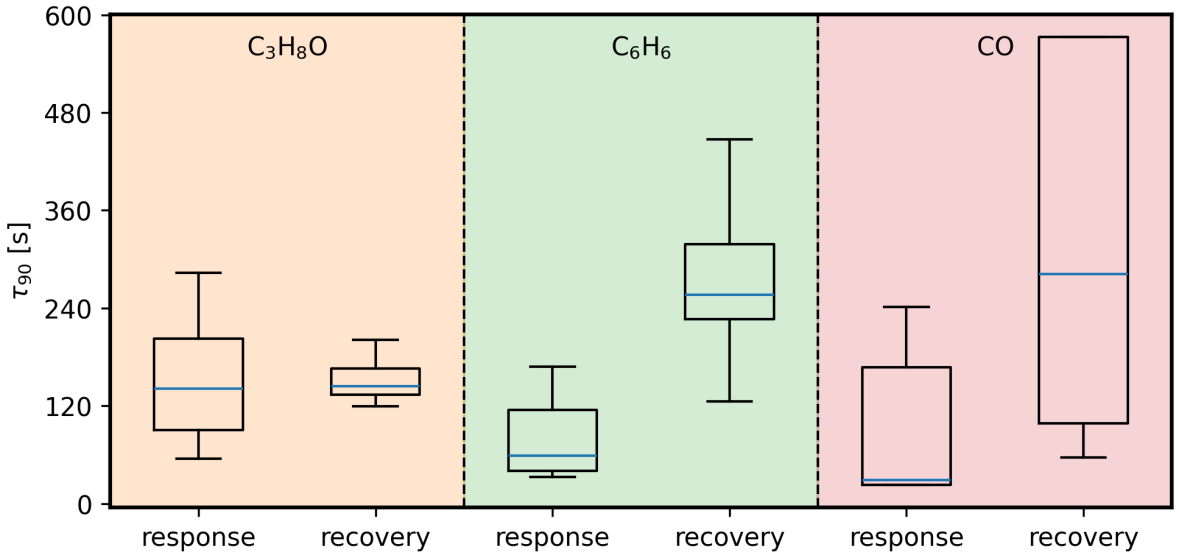

Figure 5.8: Response and recovery time analysis. Tested target gases: IPA ($G_{C_3H_8O}$), benzene ($G_{C_6H_6}$), and carbon monoxide (G_{CO}).

median of just over 2 min, whereas the lowest observed response time is around 1 min. The recovery

time values show a similar median but lower variability. For benzene, the sensor exhibits a lower median response time of approximately 60 s but a significantly longer recovery time of over 4 min. The sensor responds quickly to carbon monoxide, with median and minimum response times below 60 s. Still, some sub-sensors exhibit higher response times over 2.5 min. The highest durations are observed when recovering from carbon monoxide at just under 10 min. However, the median value is only half of that. Differences in response and recovery behaviour indicate significant differences in gas adsorption and desorption interactions between SnO_2 NW and the tested gases, with a higher selectivity towards IPA.

5.3.1.2. Classification Analysis

A representative LDA model, which is trained on all (M instead of $M-1$) observations, transforms the data as shown in the LDA map in Figure 5.9. As previously discussed in Section 2.4.3, the columns of the transformation matrix are scaled such that the 95 % confidence interval (CI) of each class is represented by a multidimensional sphere. All classes are clearly well separated and occupy distinct regions in

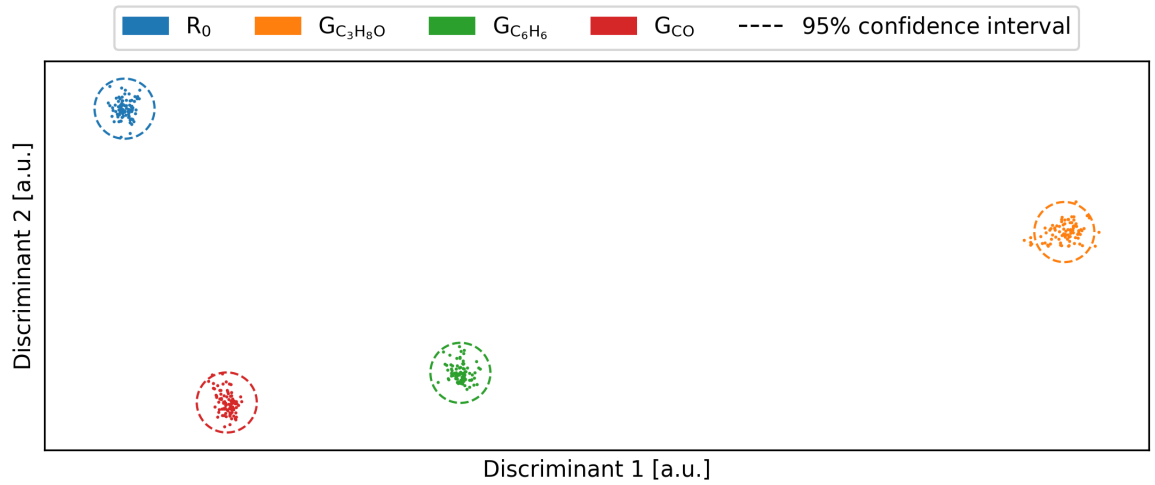

Figure 5.9: LDA plot showing discrimination between gas classes. Target gases: reference air (R_0), IPA ($G_{C_3H_8O}$), benzene ($G_{C_6H_6}$), and carbon monoxide (G_{CO}). The 95 % CIs are represented by dotted circles.

the first two discriminants of the LDA space. IPA is especially far distant from the other classes. At the same time, it exhibits greater within-class spread, with some data points lying outside the 95 % CI. Meanwhile, the data points of all other classes are well confined within their respective CI.

The normalized CM from the accumulated predictions of the LOOCV is shown in Figure 5.10. If classification is purely based on the distance to the class centroid, the LDA classifies without error, as shown in Figure 5.10 a. Conversely, if novelty (Z) detection is desired, a spherical decision boundary based on 95 % CI is used. Test observations of IPA, benzene, and carbon monoxide are occasionally positioned outside of the decision boundary. The novelty proportion is small ($\leq$ 3.4 %) for benzene and carbon monoxide, but non-neglible for IPA (11.4 %). This indicates a higher sensor noise when

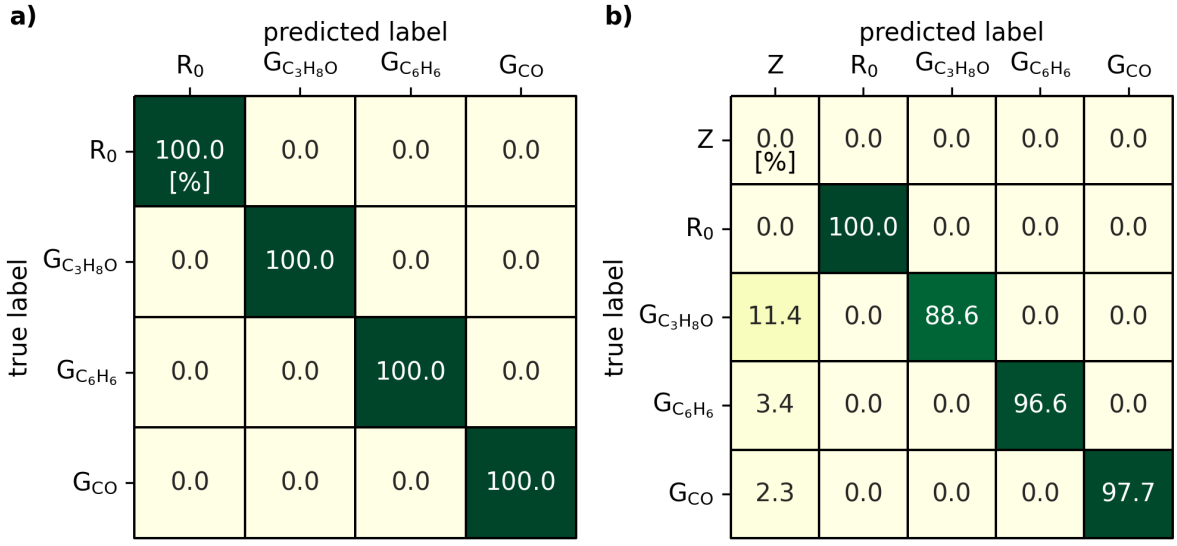

Figure 5.10: CMs of the gas classification test results. a) Without a decision boundary. b) With decision boundary. Z is the novelty label.

sensing IPA. The corresponding classification metrics precision PRC, recall REC, and F1-score (F1) are displayed in Table 5.2. As expected, all metrics are equal to 1.0 for the LDA model without a

Table 5.2: Gas classification report. The results of LDA models with and without spherical decision boundary are presented.

	No DB			DB: 95 % CI			
Class c	PRC	REC	F1	PRC	REC	F1	$M_{\text{test},c}$
R_0	1.000	1.000	1.000	1.000	1.000	1.000	88
$G_{C_3H_8O}$	1.000	1.000	1.000	1.000	0.886	0.940	88
$G_{C_6H_6}$	1.000	1.000	1.000	1.000	0.966	0.983	88
G_{CO}	1.000	1.000	1.000	1.000	0.957	0.978	88
macro avg.	1.000	1.000	1.000	1.000	0.957	0.978	$\sum = 352$

decision boundary (left). In contrast, with the decision boundary enabled, the recall for $G_{C_3H_8O}$, $G_{C_6H_6}$, and G_{CO} decreases, consistent with the CM observations. The usage of decision boundaries does not introduce misclassifications between classes. Therefore, precision remains 1.0 across all classes and the F1-scores averages to 0.978. Therefore, the eNose in combination with LDA is a highly reliable system for distinguishing among the gases IPA, benzene, and carbon monoxide.

5.3.2. Mold Detection and Identification

Impact Analysis of Relative Humidity During preliminary tests [4], an optimal relative humidity of $H_{\text{rel}} = 90\,\text{RH\%}$ was determined, in contrast to the more commonly used 50 RH%. The rationale for applying such an unusually high relative humidity is to mitigate various issues caused by drying of the culture media. These issues are presented in Figure 5.11 and discussed next. In the short term, evaporated water significantly increases the relative humidity of the carrier gas. This results in a

substantial difference in the measured resistance. For example, when using a carrier gas at 50 RH%, the reference air (baseline) was measured to be around tens of MΩ, in contrast to tens of MΩ observed for other samples as shown in Figure 5.11 a. Even the mean noise ($SD \approx 72\,k\Omega$) of reference air is over 20 times larger than the mean differences ($SD \approx 3\,k\Omega$) between the samples. The difference between reference air and other classes and the noise of the reference air overshadows the comparably minor differences between other classes, which consequently leads to a bad separation between the samples as presented in Figure 5.11 b. In the long term, the culture media dried continuously, reducing the relative humidity of the carrier gas and leading to drift in the chemiresistive signal. Moreover, changes in the stored water content of the culture media may alter the mold's metabolic expression, further contributing to a signal drift. If not controlled, this would result in a significant decline in mold density and ultimately in the death of the mold colonies. Moreover, the transfer of water from the culture medium to the carrier gas produced a substantial difference in the measured resistance values between reference air and all other samples. Due to short-term classification impairments and long-term signal drift, a high relative humidity of 90 % was selected.

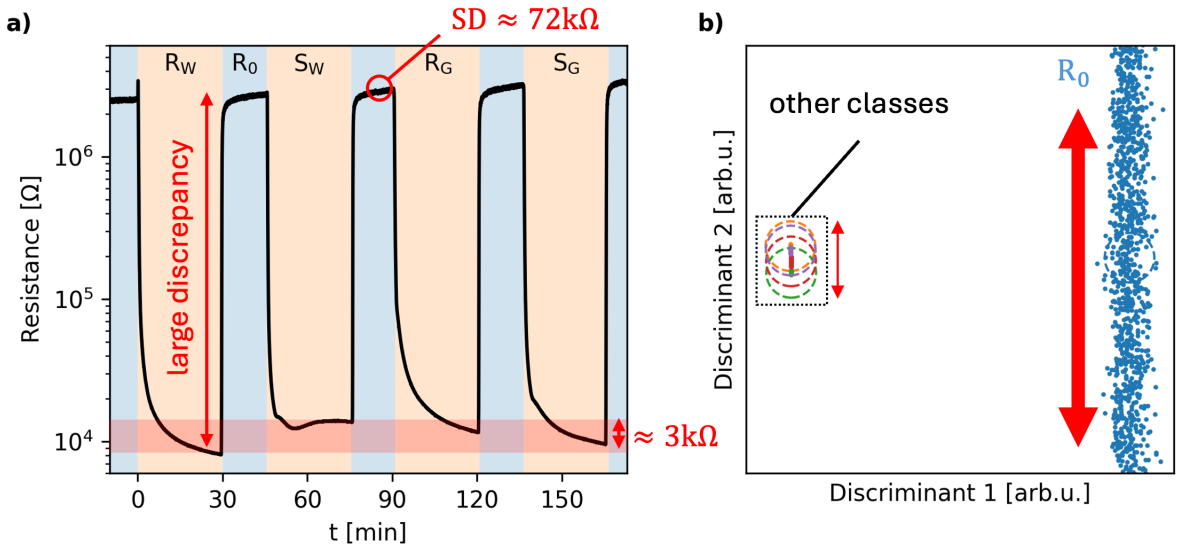

Figure 5.11: Impact of low relative humidity (RH) on mold measurements. a) Transient response showing large differences between reference air resistance and other samples. b) Noise of reference air overshadows the data of the culture medium and mold samples. Therefore, a higher RH is chosen.

5.3.2.1. Transient Sensor Response

The transient sensor responses of *S. chartarum* (a) and *C. globosum* (b) are shown in Figure 5.12. The median resistance for R_0 ($H_{rel} = 90$ RH%) is approximately 30 MΩ. Sample transient responses start with an initial spike in resistance, followed by a steadily falling signal over 30 min. The responses do not fully stabilize within this time frame, but the final values are still usable for classification, as shown later. In contrast, the signal recovers rapidly when the reference air is applied again (baseline). The sub-sensors are showing negative humidity coefficient (NHC) as expected for n-type SnO_2.

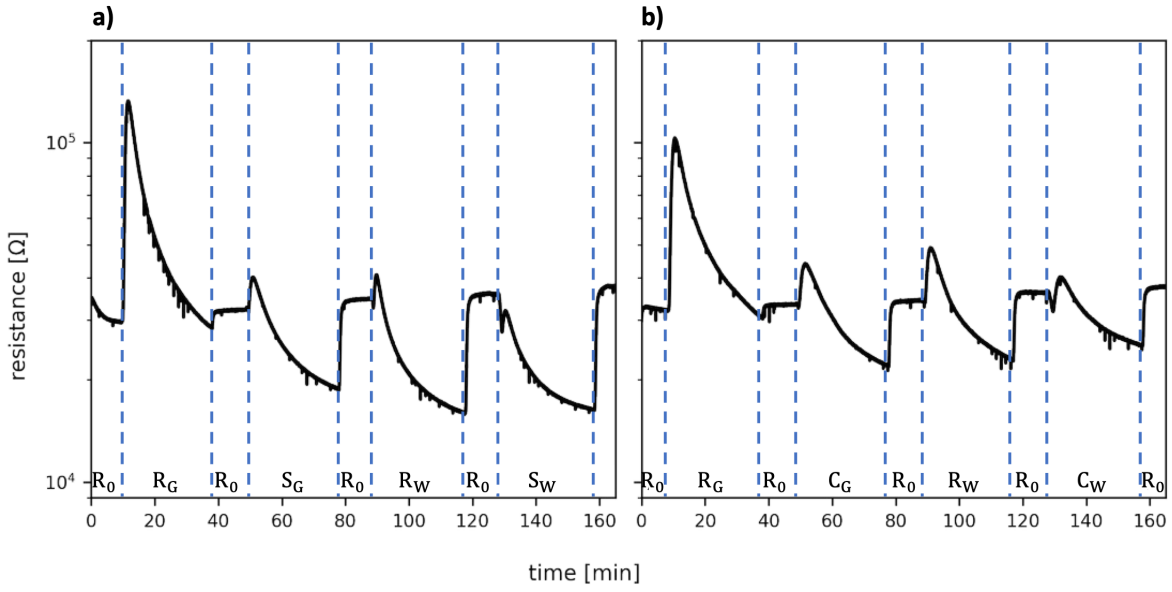

Figure 5.12: Examplanary mold measurement sensor responses. Two representative measurement series showing the median sub-sensor signal (out of the 16 sub-sensors). a) Measurement of *S. chartarum* samples, b) Measurement of *C. globosum* samples. Adapted from [2] under CC BY 4.0.

5.3.2.2. Conventional LDA Model (LDA-0)

First, the classification performance of a conventional LDA model is assessed. For future convenience, this model is abbreviated as LDA-0. LDA-0 is trained and tested with all seven initially defined classes. Using only $\boldsymbol{X}_{\text{train}}$ and $\boldsymbol{y}_{\text{train}}$, feature selection is performed iteratively to remove features that negatively impact classification performance. This can be interpreted as ignoring bad sub-sensors. Here, two out of the initial 16 features are removed. The remaining 14 features are considered for further processing. Training (dots) and test (crosses) data are shown in Figure 5.13 a, which are projected to the 2D discriminant space (d1, d2). Except for S_W (pink) and C_W (purple), all other classes overlap severely in the displayed discriminant space, leading to low REC values. Despite this, the LDA model can still distinguish the different classes to a certain degree, as shown in the CM (Figure 5.13 b) and the classification report (Table 5.3), partially due to the contribution of other discriminants which are not shown in the 2D projection. A high number of misclassifications is observed among the no-mold classes (R_0, R_G, and R_W), resulting in lower F1-score than in the mold-containing classes. In contrast, the classes S_W and C_W show perfect 1.0 PRC, meaning no other classes are being misclassified as these two, resulting in the highest F1-scores (> 0.94) out of the seven classes. This finding aligns with the observations in the LDA plot in Figure 5.13 a). A non-negligible part of the test data is classified as novelty by the LDA-0 model. This occurs most often for the classes R_0 and C_W, indicating higher signal-to-noise or greater deviation in their data. Practically, the LDA can classify all seven classes, although the performance is limited. Therefore, different performance-improving approaches are tested in the following subsections.

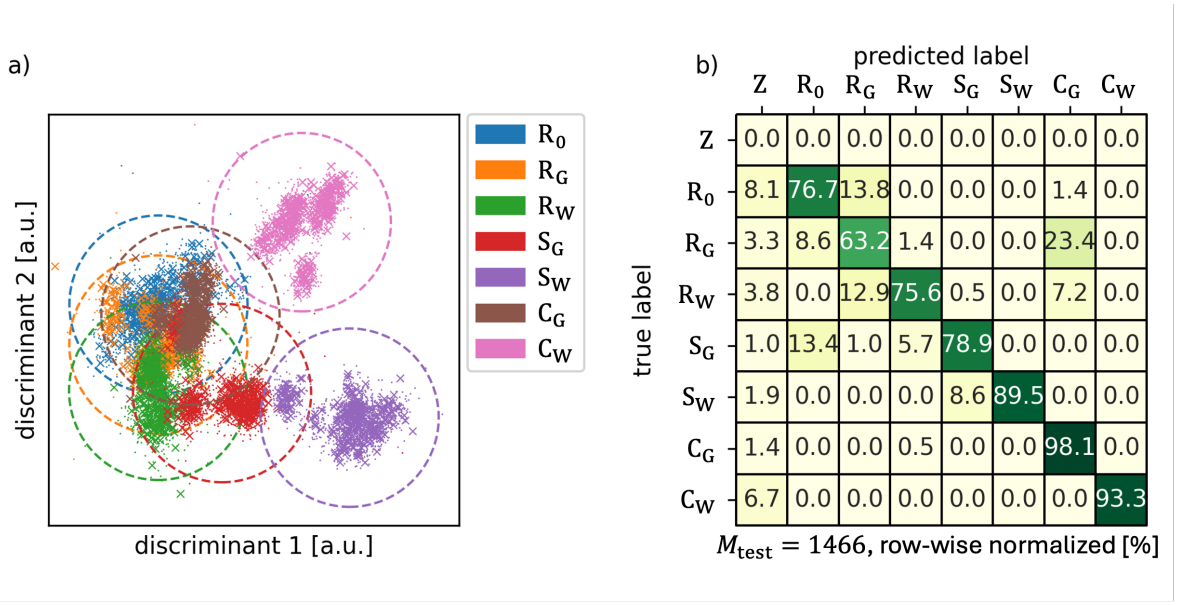

Figure 5.13: Classification results of the LDA-0 model, including all seven classes. a) Projected data points in the discriminant space of the two highest-ranked discriminants (out of six). Training data are shown as dots, and test data as crosses. The decision boundaries of each class are shown as dashed circles in the same color as the represented class. Test samples out of decision boundaries are labeled as novelty (Z). Adapted from [2] under CC BY 4.0.

Table 5.3: Classification report of the LDA-0 model. All seven classes are included each with ≈ 210 test observations.

Class c	PRC	REC	F1	$M_{\text{test},c}$
R_0	0.778	0.767	0.772	210
R_G	0.695	0.632	0.662	209
R_W	0.908	0.756	0.825	209
S_G	0.897	0.790	0.840	209
S_W	1.000	0.895	0.945	210
C_G	0.754	0.981	0.852	209
C_W	1.000	0.933	0.966	210
macro avg.	0.862	0.822	0.837	$\sum_c M_{\text{test},c} = 1466$

5.3.2.3. Substrate-Independent LDA Model (LDA-SI)

Mold detection and identification are the two most important tasks, whereas identification of the culture medium need not be performed by the eNose. Hence, a simpler LDA model can be created by removing the classes' substrate dependence. For this, the labels R_0, R_G, and R_W are merged and re-labled as reference (R), S_G and S_W are merged as (S), and C_G and C_W are merged as (C). This substrate-independent model is subsequently abbreviated as LDA-SI. Feature selection selects seven out of the 16 initial features. The resulting LDA plot is shown in Figure 5.14 a. The three classes (R, S, and C) exhibit less overlap than those in the LDA-0 model. The R class has some data points outside its own and inside other classes' decision boundaries, which leads to misclassifications that are evidenced by the corresponding CM in Figure 5.14 b. This also results in lower REC values for S and C, as shown

in the classification report (Table 5.4). S has a single out-of-bounds data cluster at the center of R, as evidenced by misclassifications to R in the CM. The data points of C are well contained within its decision boundary, with only a negligible number of outliers. Consequently, the REC of C is over 0.99. All classification metrics for C are higher than those for S. Compared to the LDA-0 model, samples are rarely detected as novel (Z). This finding indicates that the mold is primarily responsible for the detectable signal, while the substrates have a lesser impact.

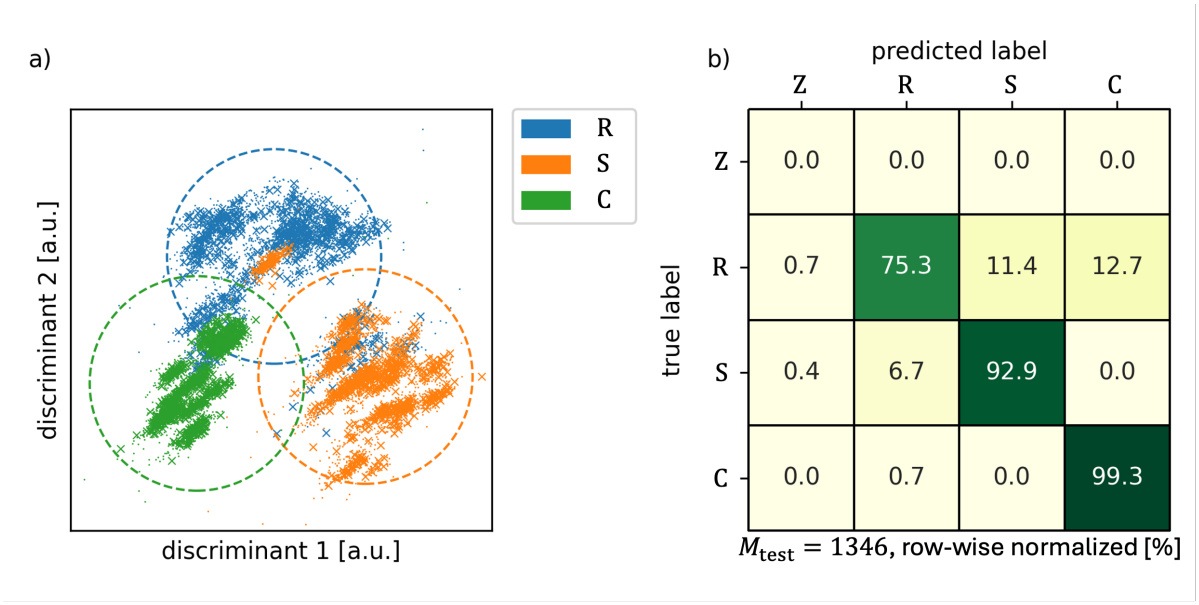

Figure 5.14: LDA-SI model test results. R is the union of $\{R_0, R_G, R_W\}$. S is the union of $\{S_G, S_W\}$. C is the union $\{C_G, C_W\}$. a) LDA plot with decision boundary shown as dashed circles. b) Normalized CM. Adapted from [2] under CC BY 4.0.

Table 5.4: Classification report of the LDA-SI model. R is the union of $\{R_0, R_G, R_W\}$. S is the union of $\{S_G, S_W\}$. C is the union $\{C_G, C_W\}$.

Class c	PRC	REC	F1	$M_{test,c}$
R	0.911	0.753	0.824	449
S	0.891	0.929	0.910	449
C	0.887	0.993	0.937	448
	$\overline{\text{PRC}}$	$\overline{\text{REC}}$	$\overline{\text{F1}}$	$\sum_c M_{test,c}$
	0.896	0.892	0.890	1346

5.3.2.4. Substrate-Specific LDA Model (LDA-SS)

In a real-world application, the growth substrate is usually known in advance. Therefore, a simplified substrate-specific LDA model (LDA-SS) can be constructed by excluding irrelevant classes. In our case, two different models are possible: the gypsum-specific (LDA-G) and the wheat-specific (LDA-W) model. LDA-G contains the classes R_{0G} (R_0 and R_G merged), S_G, and C_G. Likewise, LDA-W contains R_{0W} (R_0 and R_W merged), S_W, and C_W. From the 16 features, nine are optimally selected for LDA-G and eight

for LDA-W. The test results (LDA plots and CMs) of LDA-G and LDA-W are visualized in Figure 5.15 and Figure 5.16, respectively. Additionally, the classification reports of both models are presented in

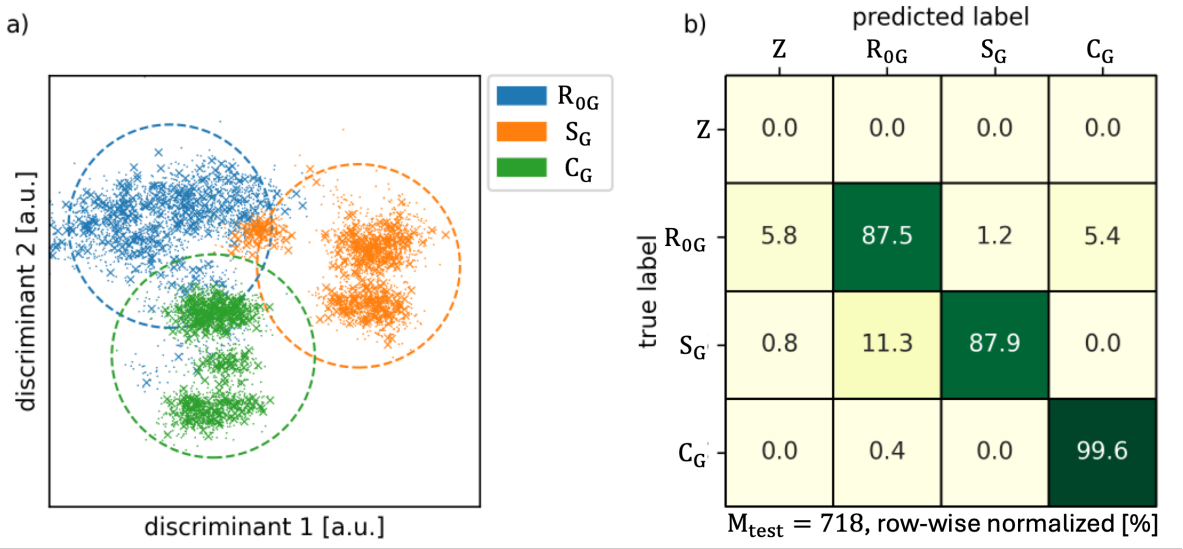

Figure 5.15: Classification results of gypsum-specific LDA model (LDA-G). a) LDA plot. b) CM. R_{0G} is the union of $\{R_0, R_G\}$.

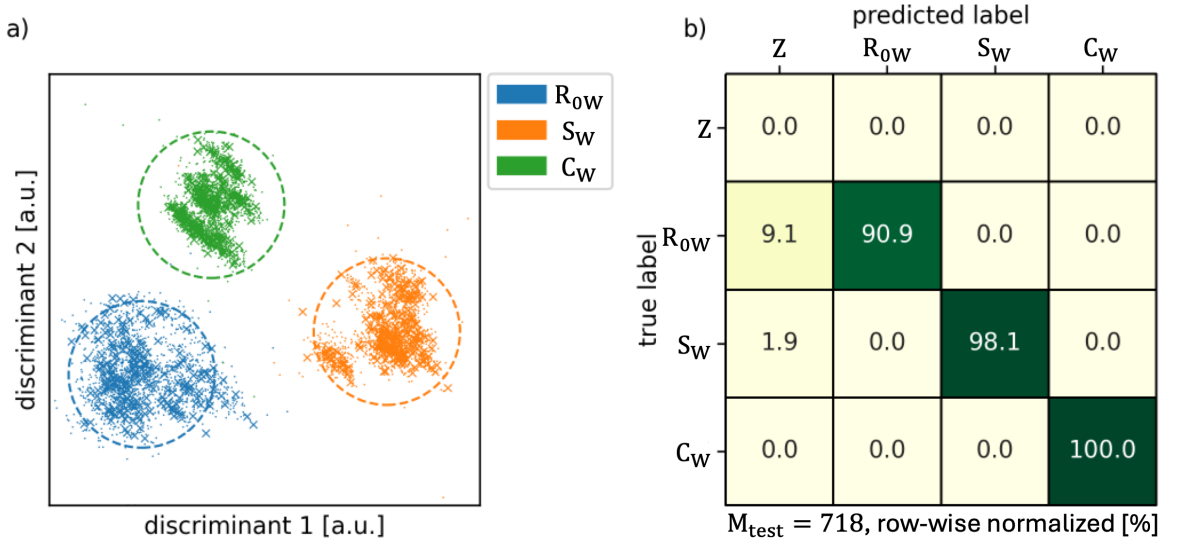

Figure 5.16: Classification results of wheat-specific LDA model (LDA-W). a) LDA plot. b) CM. R_{0W} is the union of $\{R_0, R_W\}$.

Table 5.5.

The LDA plot of LDA-G (Figure 5.15 a) shows less between-class overlap compared to LDA-0. The LDA-W model achieves a greater spatial separation between the classes as apparent in the LDA plot

Table 5.5: Classification report of LDA-SS models. R_{0G} is the union of $\{R_0, R_G\}$ and R_{0W} is the union of $\{R_0, R_W\}$.

(a) Gypsum specific LDA-G

Class c	PRC	REC	F1	$M_{\text{test},c}$
R_{0G}	0.882	0.875	0.879	240
S_G	0.986	0.879	0.929	239
C_G	0.948	0.996	0.971	239
macro avg.	0.939	0.916	0.926	$\sum_c M_{\text{test},c} = 718$

(b) Wheat specific LDA-W

Class c	PRC	REC	F1	$M_{\text{test},c}$
R_{0W}	0.100	0.901	0.952	209
S_W	1.000	0.981	0.990	210
C_W	1.000	1.000	1.000	209
macro avg.	1.000	0.963	0.981	$\sum_c M_{\text{test},c} = 628$

(Figure 5.16 a). Here, all three classes are well contained within their respective decision boundaries, with no overlap. Compared to the LDA-SI model (Figure 5.14), the no-mold classes (R_{0G} and R_{0W}) have fewer outliers, which translates into a significant increase in average REC for both LDA-SS models, as shown in Table 5.5. On gypsum, S_G shows a considerably higher PRC (0.986) compared to REC (0.879) which originates from misclassifications as R_{0G} evidenced in the CM (refer to Figure 5.15 b and Figure 5.16 b). R_{0G} and R_{0W} are the only classes that are detected as novelty for both LDA-SS models in a non-negligible amount (approximately 6 % to 9 %). Compared to LDA-0 and LDA-SI, both LDA-G and LDA-W achieve a higher average F1-score of 0.926 and 0.981, respectively.

5.3.2.5. LDA-Ensemble with Softmax Regressor (LDA-SR)

In the previous section, it was shown that a simplified LDA model (LDA-SS) with fewer classes naturally performs better on the included classes. This idea can be generalized by removing the restriction to eliminating only substrate-specific classes. Given C distinct classes, the number of possible combinations of at least two classes with non-repeating elements and disregarding order is calculated by Equation 5.1 (proven in Theorem A1).

$$N_{\text{m}} = 2^C - C - 1 \tag{5.1}$$

using the binomial theorem. Hence, an ensemble of N_{m} distinct LDA models can be created, where each LDA model is trained on a unique set of classes. It is noted that the ensemble always includes a model that contains all classes, which is equal to LDA-0. At this stage, the ensemble produces an output array in the form of $\mathbb{G}^{N_{\text{m}}}$ containing individual class predictions as an intermediate result. Thereafter, a softmax regression (SMR) takes the N_{m} predictions as input and re-predicts one of the C classes. This combined LDA-ensemble and SMR algorithm is subsequently abbreviated as LDA-SMR. One undesirable side effect of the SMR is that the novelty detection function of the LDA models is intrinsically eliminated.

Therefore, an additional majority-voting algorithm is implemented to reintroduce the novelty-detection function. The SMR prediction is accepted if more than half of the relevant LDA models in the ensemble match. Otherwise, the prediction is rejected and declared novel. $N_{\mathrm{m},c}$, the number of relevant LDA models for each class is calculated by Equation 5.2 (proven by Theorem A2).

$$N_{\mathrm{m},c} = 2^{C-1} - 1 \tag{5.2}$$

For $\mathbb{G} = \{\mathrm{R_0}, \mathrm{R_G}, \mathrm{R_W}, \mathrm{S_G}, \mathrm{S_W}, \mathrm{C_G}, \mathrm{C_W}\}$ ($C = 7$) in this case and according to Equation 5.1 and Equation 5.2, a total of 120 distinct LDA models are possible in which $N_{\mathrm{m},c} = 63$ are relevant for each class. Consequently, the intermediate prediction array is in the form of $\mathbb{G}^{120}$. The detailed model structure is shown in Figure 5.17. Individual LDA models of the ensemble are trained without any hyperparameter optimization or feature selection. Next, the SMR is hyperparameter-tuned and trained using the LDA ensemble predictions of the training data. Here, the optimal regularization strength is 0.09. Feature selection is performed on the complete LDA-SR, eliminating 20 of the initial 120 features of the intermediate prediction from the LDA ensemble. This can be interpreted as removing 20 bad-performing LDA models. Finally, the complete LDA-SR model is tested. The CM of the test result without majority voting is shown in Figure 5.18 a, and the classification report is presented in Table 5.6. The model achieves superb PRC and REC, and consequently exceptionally high F1-scores across all classes. No significant misclassification is observed. Only a negligible number of test samples are detected as novelty when majority voting is enabled, as shown in the CM (Figure 5.18 b). As expected, no REC value changes occur from the majority voting, since the novelty label Z has no occurrences in the test data set. Compared to LDA-0, LDA-SI, and LDA-SS, all classification performance metrics improved considerably, especially for low-performing classes. Consequently, the performance disparity between classes decreases. It must be noted that compared to other presented models, the LDA-SR is more

Table 5.6: Classification report of the LDA-SR model. In parentheses are the corresponding values, without majority voting, if they differ.

Class c	PRC	REC	F1	$M_{\mathrm{test},c}$
$\mathrm{R_0}$	0.966 (0.981)	0.957	0.962 (0.969)	210
$\mathrm{R_G}$	0.9361 (0.949)	0.981	0.958 (0.965)	209
$\mathrm{R_W}$	1.000	0.981	0.990	209
$\mathrm{S_G}$	0.995	0.981	0.988	209
$\mathrm{S_W}$	0.995	0.995	0.995	210
$\mathrm{C_G}$	0.995	0.995	0.995	209
$\mathrm{C_W}$	1.000	0.984	0.984 (0.986)	210
	$\overline{\mathrm{PRC}}$	$\overline{\mathrm{REC}}$	$\overline{\mathrm{F1}}$	$\sum_c M_{\mathrm{test},c}$
	0.984 (0.988)	0.984	0.984 (0.984)	1466

computationally expensive for large class counts C due to the exponentially growing number of LDA models $M \propto 2^C$ in the ensemble, according to Equation 5.1. As shown in this case, one way to reduce the number of models is to eliminate bad-performing LDA models by feature selection. Additionally, the number of classes can be reduced manually, similar to the approaches for LDA-SI and LDA-SS. Still,

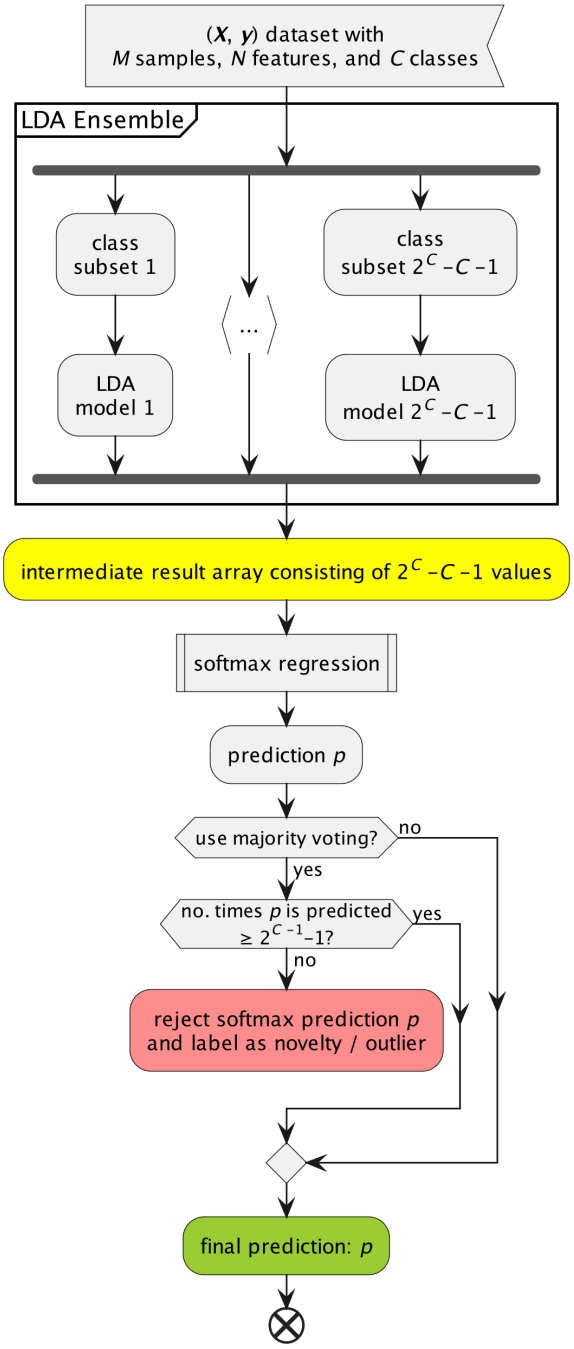

Figure 5.17: Data flow chart of the LDA-SR algorithm. The model consists of multiple LDA models, which are trained using unique data and class subsets.

because the computations for individual LDA models are mostly efficient matrix operations (refer to Section 2.4.3), the ensemble is fast during both training and application in this case.

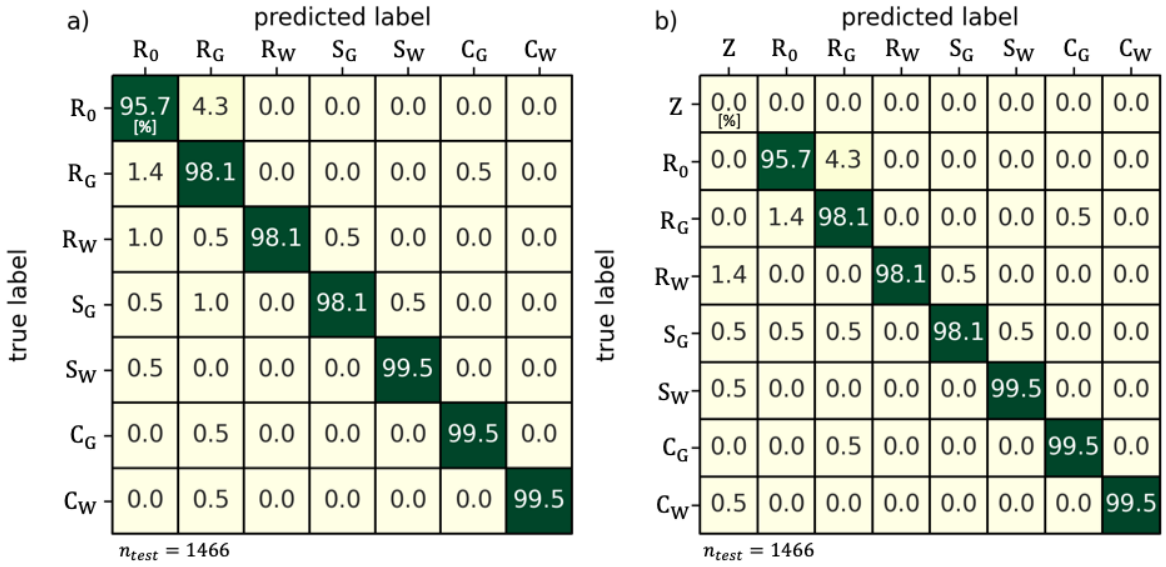

Figure 5.18: CMs of LDA-SR models. a) without majority voting, b) with majority voting.

5.4. Summary

SnO_2 NWs were VLS-grown with diameters below 200 nm. An CSP based eNose equiped with these SnO_2 NWs were tested using the target gases IPA, benzene, and carbon monoxide and exhibits higher responsivity to IPA. In addition, the gas-dependent response and recovery times were analyzed, showing swift response times but slower recovery times. The eNose in combination with LDA were evaluated for gas recognition by LOOCV.

The corresponding LDA plot shows all classes clearly separated, resulting in exceptional classification performance. If no decision boundary is used, the LDA makes no classification errors. The F1-score remains high at over 0.978 even if a decision boundary using 95 % confidence interval is employed, confirming that the SnO_2-based eNose is well suited for gas sensing purposes.

Finally, the eNose was evaluated for mold detection and identification of two common indoor mold species, *S. chartarum* and *C. globosum*, in laboratory conditions on two different substrates (agar mixed with either shredded gypsum or wheat). A conventional LDA model, trained on all seven initial classes, achieves only a mediocre results with an average F1-score of 0.837 due to severe class overlap evidenced in the corresponding LDA plot. Consequently, different approaches were tested to improve the LDA's classification performance. The LDA model can be simplified by either merging classes to remove the substrate dependency or by creating LDA models specific to each substrate. Both approaches improve classification performance compared to LDA-0.

Moreover, a novel ensemble classifier (LDA-SR) comprising individual LDA models and a subsequent softmax regressor is implemented and evaluated. LDA-SR is further extended by applying a majority-

vote algorithm to preserve novelty detection. LDA-SR achieves an exceptional F1-score of 0.986 despite containing all seven classes.

Therefore, it has been demonstrated that the chemiresistive eNose in combination with an optimized LDA-based algorithm can reliably detect and identify mold species across different growth media.

6. Digitally Printed Single-ChemFET-based Electronic Nose

Following the exploration of the two chemiresistive sensors in the previous two chapters, this chapter focuses on the development of a novel sensing technology: chemically-sensitive field-effect transistor (ChemFET). A ChemFET can be voltage modulated to artificially generate features for classification tasks instead of relying on physical sub-sensor. Because the ChemFET comprises multiple components made of different materials with distinct properties and requirements, a hybrid digital printing process involving both inkjet printing (IJP) and aerosol jet printing (AJP) is developed. Next, the fabricated ChemFET is structurally and electrically characterized. Finally, its performance in sensing and classification of three different test gases is analyzed. The electronic nose (eNose) shows exceptionally high sensitivity towards isopropyl alcohol (IPA) and benzene. A single voltage-modulated ChemFET provides sufficient features for eNose applications and is comparable to a multi-sub-sensor chemiresistive eNose in classification performance. In addition, the classification performance of Random Forest (RF) is found to be higher than that of linear discriminant analysis (LDA). A feature importance analysis reveals significant differences in information gain across operating points. Parts of this chapter were previously published in Advanced Sensor Research (2025)

6.1. Introduction

Besides the previously used chemiresistive sensors, ChemFETs are another electrical sensing technology that stand out for their enhanced sensitivity and selectivity, as well as their lower power consumption [40, 191–193]. Conventional chemiresistive eNoses require multiple sub-sensors to maximize selectivity and minimize cross-sensitivity.

Alternatively, features can be generated by modulating the operating temperature [8, 194], but at the cost of a significantly reduced measurement cycle frequency, depending on the thermal design and power budget. Similarly, ChemFET can generate a set of features using only a single sub-sensor by modulating the applied voltages U_{GS} and U_{DS}. Still, unlike temperature-modulated chemiresistive metal oxide (MOX)-sensors, voltage modulation can be performed rapidly and power-efficiently. Furthermore, the modulation may render conventional excitation approaches, such as heating or UV irradiation, obsolete, thereby enabling further power savings. Two distinct ChemFET variants exist: gate- and channel-sensor. The gate-sensor variant employs a conventional top-gate transistor structure, in which the gate is exposed to the analyte, thereby altering its work function. In return, the change in the transistor's characteristics can be measured [72]. Metals such as palladium (Pd) are commonly used as gate materials. In contrast, the channel-sensor variant instead exposes the channel semiconductor.

This generally results in higher sensitivity than the indirect gate-sensor variant. Different channel materials can be used, ranging from semiconducting polymers (polyaniline and polystyrenesulfonic acid [195]) to carbon allotropes (graphene [196], single-walled carbon nanotubes [97]) to inorganic MOX semiconductors such as SnO_2 nanowires (NWs) [197, 198]. Among the semiconducting MOXs, In_2O_3 is a promising candidate for ChemFETs because of its tried-and-tested chemiresistive sensing properties [137, 199, 200] in addition to its printability [201–205].

As noted in Chapter 3, printing enables rapid prototyping, which is particularly useful during the research stage. inkjet printing (IJP) can be used to print functional materials with layer heights in the nanometer range, which is required, for example, for the fabrication of thin-film transistors. Meanwhile, aerosol jet printing (AJP) is used to print fine electrodes owing to its continuous-jetting mechanism, which is more efficient than IJP's dropwise deposition. Additionally, the AJP can handle a wider range of inks with viscosities up to 1000 cP, while being significantly less susceptible to nozzle clogging due to the protective sheath gas stream [121]. Here, a combined IJP-AJP hybrid approach is employed, leveraging the advantages of both printing technologies to efficiently and flexibly fabricate ChemFETs for eNose-applications. Additionally, the gas-sensing performance of a single ChemFET eNose is evaluated using two machine-learning algorithms and ultimately compared with that of other chemiresistive and field-effect-based sensors.

6.2. Materials and Methods

6.2.1. Device Structure

The ChemFET was structured as a bottom-gate thin-film transistor (TFT) as illustrated by the fabrication process and schematic layer stack cross-section in Figure 6.1. Without any top passivation, this layer structure intentionally allowed the analyte molecules to interact directly with the exposed thin-film semiconductor (In_2O_3), thereby exerting a stronger impact on the channel and ultimately leading to a higher sensitivity. A low-resistive p-type Si-wafer bulk was used as the bottom gate, whereas the 90 nm SiO_2 was used as the gate insulator. In_2O_3 was chosen as the semiconducting channel material and was deposited as a thin film on top of SiO_2 gate insulator. Next, the top electrodes were deposited on top of the In_2O_3 thin film. The top electrodes consisted of two different materials, ITO and Ag, and were used for the following reasons. Compared to ITO, Ag is a better-conducting material but was observed in preliminary tests to form a hindering Schottky barrier at the In_2O_3-Ag interface. This observation is consistent with previous reports [206]. The Schottky barrier prevented any significant U_{GS}-dependent change in channel conductivity. To circumvent this, ITO was chosen as an intermediate material as previous reports show no Schottky behaviour at Ag-ITO interfaces [207, 208]. Consequently, the resulting layout had the following junctions (from top to bottom): Ag-ITO and ITO-In_2O_3.

The following sections will elaborate on the hybrid AJP-IJP fabrication process, which efficiently addresses the challenge of vastly different layer thickness requirements for the In_2O_3 channel and the (ITO and Ag) top electrodes.

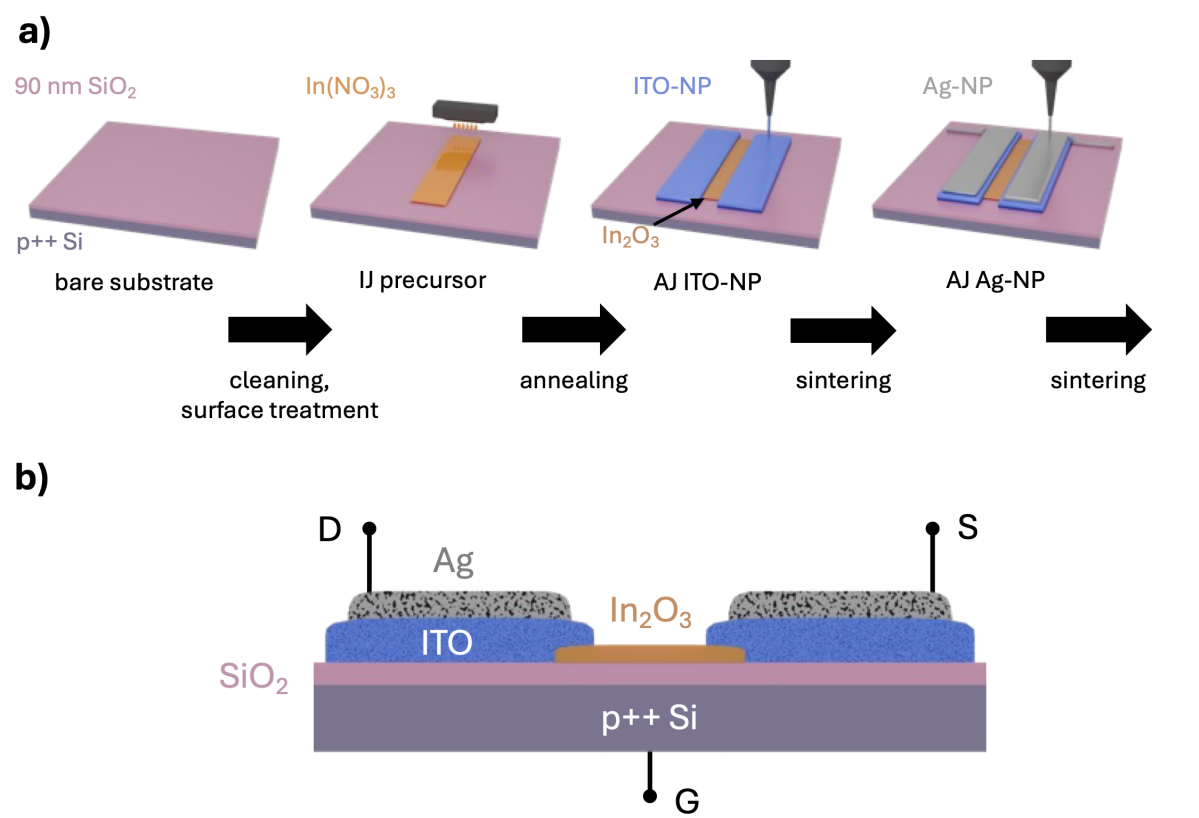

Figure 6.1: Illustration of ChemFET's layer structure and fabrication process. a) Fabrication process including IJP of the In_2O_3 precursor for the channel semiconductor and AJP of indium tin oxide (ITO) and Ag nanoparticles (NPs) as electrodes. b) Cross-section layout of a single ChemFET with source (S), drain (D), and gate (G) contacts. Adapted from [3] under CC BY 4.0.

6.2.2. Printing of Semiconducting Channel

The semiconducting In_2O_3 thin film is the core functional structure of the ChemFET. The channel layer thickness, which is commonly below 30 nm, has an especially profound impact on several field-effect transistor (FET)-characteristics, such as threshold voltage (U_{th}), and on/off-ratio [70]. For In_2O_3-TFTs specifically, even sub 1 nm layer thicknesses has been reported [209]. In this work, IJP was chosen as the deposition method to fabricate the In_2O_3 thin film via a precursor route.

Ink A diluted version of $In(NO_3)_3$ based precursor was used based on existing recipes [210–212] to match the used printhead and layer thickness requirements. First, 0.2 wt% glycerol and 0.8 wt% deionized water were mixed to an inkjet (IJ)-printable solvent. 0.05 M $In(NO_3)_3$ ($\geq$ 99.99 %, Thermo Scientific) was subsequently dissolved in the glycerol-water solvent by continuous magnetic stirring for at least two hours. A transparent ink was obtained as a result. The viscosity of the precursor ink was determined to be 2.1 cP at 30 °C using a rotational viscosimeter (Anton Paar ViscoQC300L).

Substrate preparation A heavily p-doped (boron, 0.001 Ω cm to 0.01 Ω cm, MicroChemicals GmbH) Si wafer was used as the substrate. The wafer was additionally coated ex works with a polished 90 nm SiO_2 layer. First, the Si/SiO_2-wafer (diameter: 100 mm, thickness: 525 µm) was first diced into quadratic 18 mm × 18 mm substrates. Next, the diced substrates were ultrasonically cleaned in acetone and subsequently in IPA for 10 min each. The cleaned substrates were next surface-treated in a plasma oven for 10 s (100 % O_2, 0.3 mbar, 100 % power) to improve the wetting behavior for the subsequent IJP process. This step was especially critical for the IJP process. Droplets printed on an untreated substrate surface form separated dots (Figure 6.2 a). At insufficient treatment durations (≈ 2 second), holes and

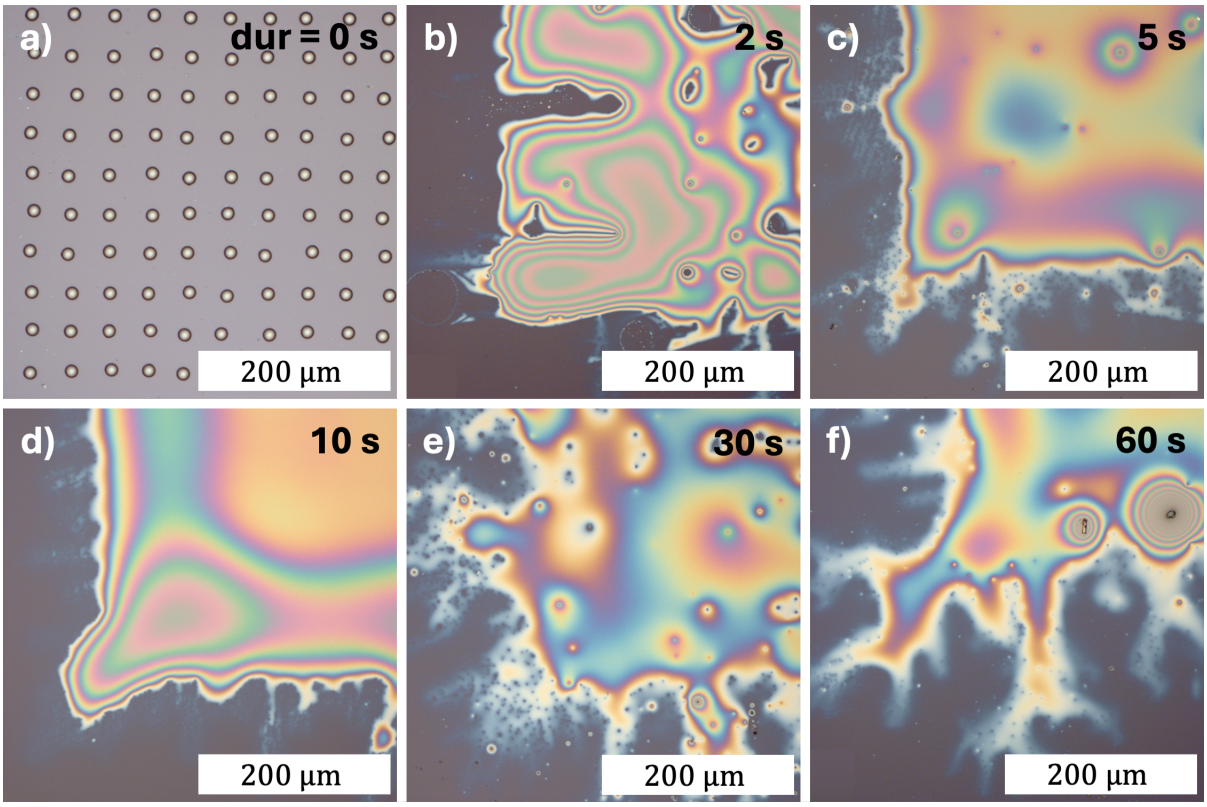

Figure 6.2: Microscope images showing the impact of different plasma activation duration for IJP. The plasma durations from a) to f) are (off) 0 s, 2 s, 5 s, 10 s, 30 s and 60 s, respectively. The interference-induced colors qualitatively indicate different layer heights. Optimal duration is between 5 s to 10 s. Other process parameters: 100 % O_2, 0.3 mbar, 100 % power, polished SiO_2 surface.

uneven surfaces formed (Figure 6.2 b). Within an optimal duration range of approximately 5 s to 10 s, the targeted shapes can be printed with connected surfaces (Figure 6.2 c and d). Further increasing the treatment duration led to uncontrolled dendrite growth (Figure 6.2 e and f). Consequently, for this work, a fixed plasma treatment duration of 10 s was used.

Inkjet printing The In_2O_3 precursor was IJ printed onto the cleaned and plasma-treated substrates using a research-class IJ printer (SUSS LP50 PiXDRO) with a 1 pL droplet volume cartridge (DMC-11601). The printing parameters are listed in Table 6.1. Elevating the nozzle temperature to 30 °C was required

Table 6.1: IJP settings for printing In_2O_3 precursor.

(a) Printing parameters excluding pulse wave profile.

parameter	value
nozzle temp.	27 °C
substrate temp.	30 °C
ink pressure	−8 mbar
ejection freq.	3000 Hz
DPI	400 DPI to 800 DPI
printing mode	y, unidirectional
quality factor	1

(b) Pulse wave profile.

parameter	symbol	value
first pulse voltage	U_0	3 V
second pulse voltage	U_1	0 V
ejection pulse voltage	U_2	24 V
first pulse ramp duration	τ_{r0}	1 µs
first pulse hold duration	τ_{h0}	1 µs
second pulse ramp duration	τ_{r1}	1 µs
second pulse hold duration	τ_{r1}	0 µs
ejection pulse ramp duration	τ_{r2}	6 µs
ejection pulse hold duration	τ_{h2}	10 µs
recovery ramp duration	τ_{r3}	5 µs
recovery hold duration	τ_{h3}	0 µs

for stable droplet formation. Furthermore, the plate temperature was optimized to 30 °C to avoid the coffee ring effect and enhance process repeatability as depicted in Figure 6.3.

Annealing Finally, the substrates were annealed on a hotplate at 300 °C for 1 h in ambient air. Afterwards, the substrates are left on the hotplates to cool naturally to room temperature (RT) overnight. Preliminary tests showed that incomplete crystallization occurs at 200 °C or lower. Conversely, annealing under the same conditions at 400 °C resulted in overly high conductivity of the In_2O_3 thin film at the off-state.

Characterization Optical microscope images of the printed films were taken. The In_2O_3 thin films were measured using a stylus-based profilometry (Dektak XT).

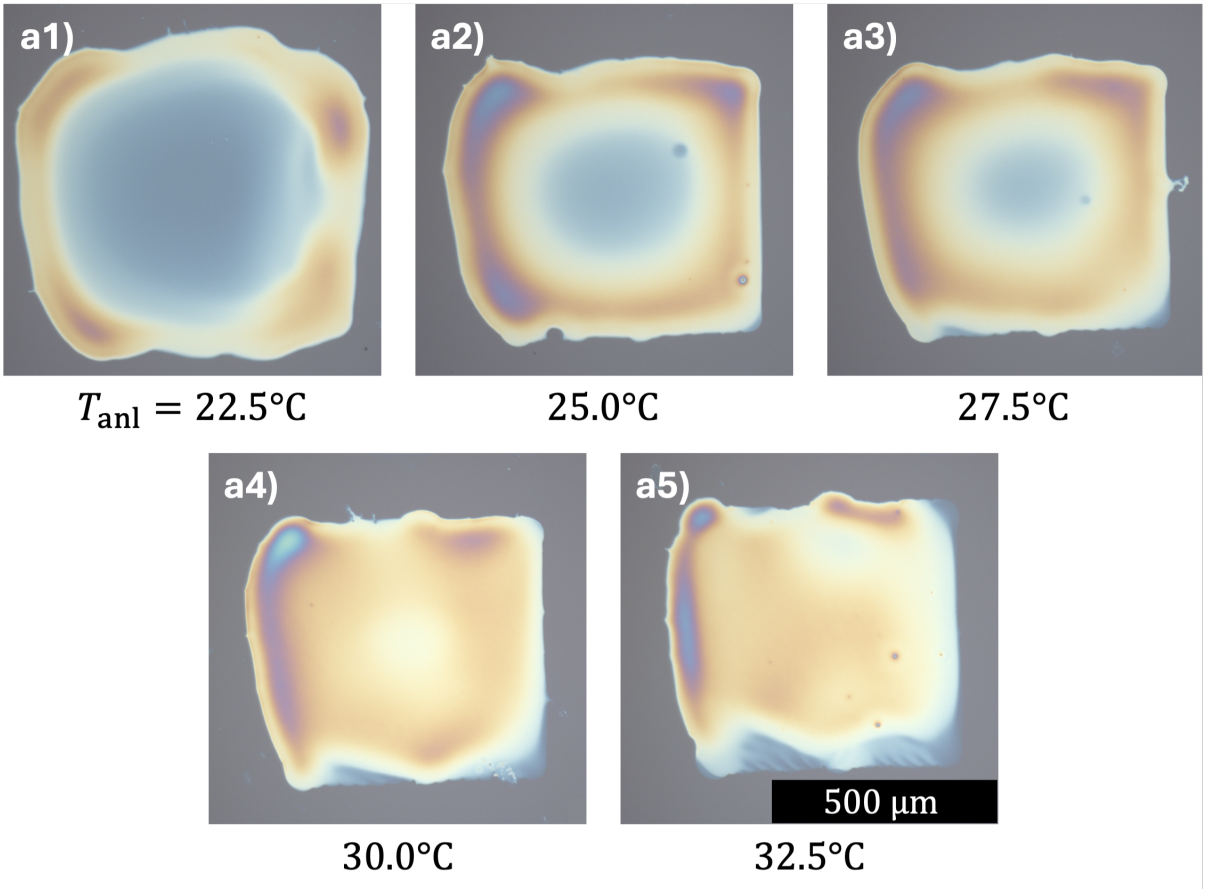

Figure 6.3: Microscope images of IJ printed In_2O_3 patches with different substrate temperatures. The interference-induced colors qualitatively indicate different layer heights. 30 °C is used for the fabrication of the In_2O_3 thin film in this chapter.

6.2.3. Printing of Conductive Electrodes

Next, the Ag top electrodes and the intermediate ITO layer were aerosol jet (AJ) printed on top of the IJ printed In_2O_3 thin film.

Inks NP-based inks were used for all AJ printed structures. The water-based Ag-NP ink (Metalon® JS-A221AE, Novacentrix) was a commercially available AJP-specialized ink. According to the manufcaturer, typical values for NP size, Ag content and viscosity were 35 nm, 50 wt% and 10 cP to 20 cP, respectively [213]. The Ag-NP ink is used without any modifications.

For the ITO ink, a water-based ITO-NP dispersion (US Research Nanomaterials Inc.) with an average particle size of 18 nm was used as the starting material. With the initial ITO-loading (20 wt%), the ultrasonic atomizer (UA) of the AJ printer was unable to generate a sufficient number of printable aerosols. At around 10 wt% loading, the AJP using the ultrasonic atomizer (UA) was possible, but resulted in unacceptable overspray and rough structures. The optimal loading was determined to be around 5 wt%, characterized by a good balance among aerosol density, NP concentration, and overspray

behaviour. Still, overspray could not be completely avoided, and a simple solution is presented later in this section. Only deionized water was used for dilution.

Aerosol jet printing The ITO-NP and Ag-NP inks were both printed with an AJ printer (AJ 5X, Optomec). The 300 µm nozzle was chosen to be as large as possible and as small as needed to print the required structure sizes while minimizing print time. The sheath-to-atomizer flow rate ratios, in addition to the atomizer and bubbler temperatures, were iteratively adjusted for each ink individually according to the general procedure described in Section 3.5 to obtain lines within an appropriate width range with satisfactory smoothness and acceptable overspray. The optimization process was primarily focused on the ITO-NP ink, as the commercial Ag-NP ink was well optimized and printable across a broad range of operating conditions. Table 6.2 lists the optimized values of AJP process parameters. The

Table 6.2: Optimized parameters of AJP. Parameters may differ depending if printing ITO or Ag NPs.

Parameter	Optimal value	
	ITO	Ag
Q_{sht}/Q_{atm}	6.5	4
T_{atm}	25 °C	
T_{bub}	26 °C	
T_{plate}	40 °C	RT
v	5 mm s^{-1}	

high plate temperature (T_{plate}) of 40 °C ensured rapid solidification of printed structures, significantly improving shape consistency by preventing deformations caused by nearby jet pressure. However, if T_{plate} was too high, crack formation was observed, similar to the drying processes described in Section 3.6. In contrast, the Ag ink did not require elevated T_{plate} and was printed at RT without precise temperature control. Furthermore, the minimum radius of printed structures was kept above 25 µm to ensure operation within acceleration limits and shape consistency. As previously mentioned, overspray was unavoidable, specifically for the ITO ink, as shown in Figure 6.4 a. Still, the majority of the visible overspray particles could be removed by blowing the substrate surface with an air blow gun (N_2) as evidenced by Figure 6.4 b. The remaining particles sparsely populated the surface and caused no negative effects, such as short circuits.

Sintering Printed ITO and Ag structures were sintered separately and directly after printing for one hour at 300 °C and 200 °C, respectively. No preceding thermal or vacuum drying was performed, especially for Ag, where cracks would form during drying as mentioned in Section 3.3. All sintering steps were done on hot plates under ambient conditions. The intermediate ITO layer had the additional advantage of enabling subsequent Ag prints without a plasma activation step between them. The difference in surface hydrophilicity of In_2O_3 and SiO_2 caused the printed Ag electrodes to disconnect at the junction as depicted in Figure A9.

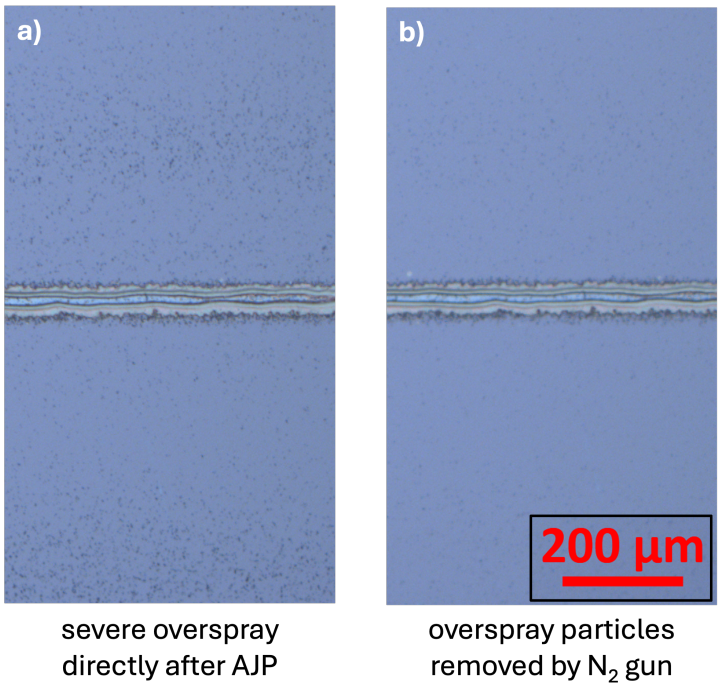

Figure 6.4: Removal of overspray particles. Light microscope images of AJ printed lines. a) Directly after AJP. b) After briefly blowing the surface using an air blow gun (N_2). The majority of large visible residues can be removed this way.

Characterization A ChemFET was cut using focused ion beam (FIB), and scanning electron microscopy (SEM) images of the cross-sections were obtained (Zeiss Crossbeam 1540 EsB). Furthermore, the electrodes were analyzed by a stylus-based profilometry (Dektak XT).

6.2.4. Experimental Setup

Housing The finished eNose chip was operated in a custom-designed and custom-machined housing, as illustrated in Figure 6.5 a and b. The purpose of the housing was

1. to create a well-defined gas-mixing chamber for reproducible results and
2. to enable a stable electrical connection of surface electrodes.

The housing was comprised of three main parts: the bottom part (white), the top part (gray), and the electronics (green PCB with soldered components). The eNose chip was placed and aligned in a precise cutout at the center of the bottom part. The top part was then aligned (lateral tolerance: ±0.2 mm) and secured by four screws. Above the sensing area, a stadium-shaped[1] cutout served as the gas mixing chamber. To the bottom, the chamber was sealed against the polished SiO_2 surface by a fluorocarbon-based fluoroelastomer materials (FKM) gasket. Similarly, a secondary FKM gasket sealed the chamber to the top against a lid that was closed during operation but could be opened for inspection. The airtight sealing was required to prevent uncontrolled leakage.

The ChemFET was printed on the sensing area, with electrodes extending to the outer edges. Spring-loaded pogo pins established electrical contact with the electrodes at well-defined patches when the top part was screwed against the bottom part. The sensor was operated at RT without any excitation sources such as heating or UV irradiation. The housing top part was machined from a single piece of stainless steel. Therefore, in combination with the FKM gaskets, the gas mixing chamber has minimal chemical interaction with the used target analytes (IPA, benzene, and carbon monoxide) within the normal operation conditions [214]. Additionally, the chamber completely isolated the gas stream from the electrical components. This not only prevented damage to these components but also prevented the eNose sensor from measuring chemical molecules due to uncontrolled and interfering outgassing of these components.

Electrical Measurement The ChemFET was powered by a multi-channel power supply (Rigol DP832A) and was measured using a multimeter (Keithley 2001). Both the power supply and the multimeter were connected to (USB-A) and controlled by PC. The multimeter used an IEEE-488.2-to-USB converter. Figure 6.5 d presents the schematic electrical read-out layout. The power supply U_{GS} and U_{DS} were controlled by a multichannel power supply (Rigol DP832A) with the common ground connected to the source of the ChemFET. I_{DS} was measured by a multimeter (Keithley 2001). The ChemFET was first electrically characterized via standard output and transfer measurements. In the output characteristics, the primary variable (U_{DS}) was swept from 0 V to 30 V in 1 V steps at each secondary variable (U_{GS}) value ranging from 0 V to 30 V in 2 V increments. The transfer curve was composed of a forward and a backward U_{GS} sweep ranging from 0 V to 30 V in 1 V steps at a constant drain-source voltage (U_{DS} = 30 V). For the eNose application, each observation data vector consisted of three distinct transfer measurements as depicted in Figure 6.6. A single measurement cycle (multidimensional data point) consisted of three transfer characteristics at different U_{DS} values

[1] 2D shape with a rectangle between two half-circles

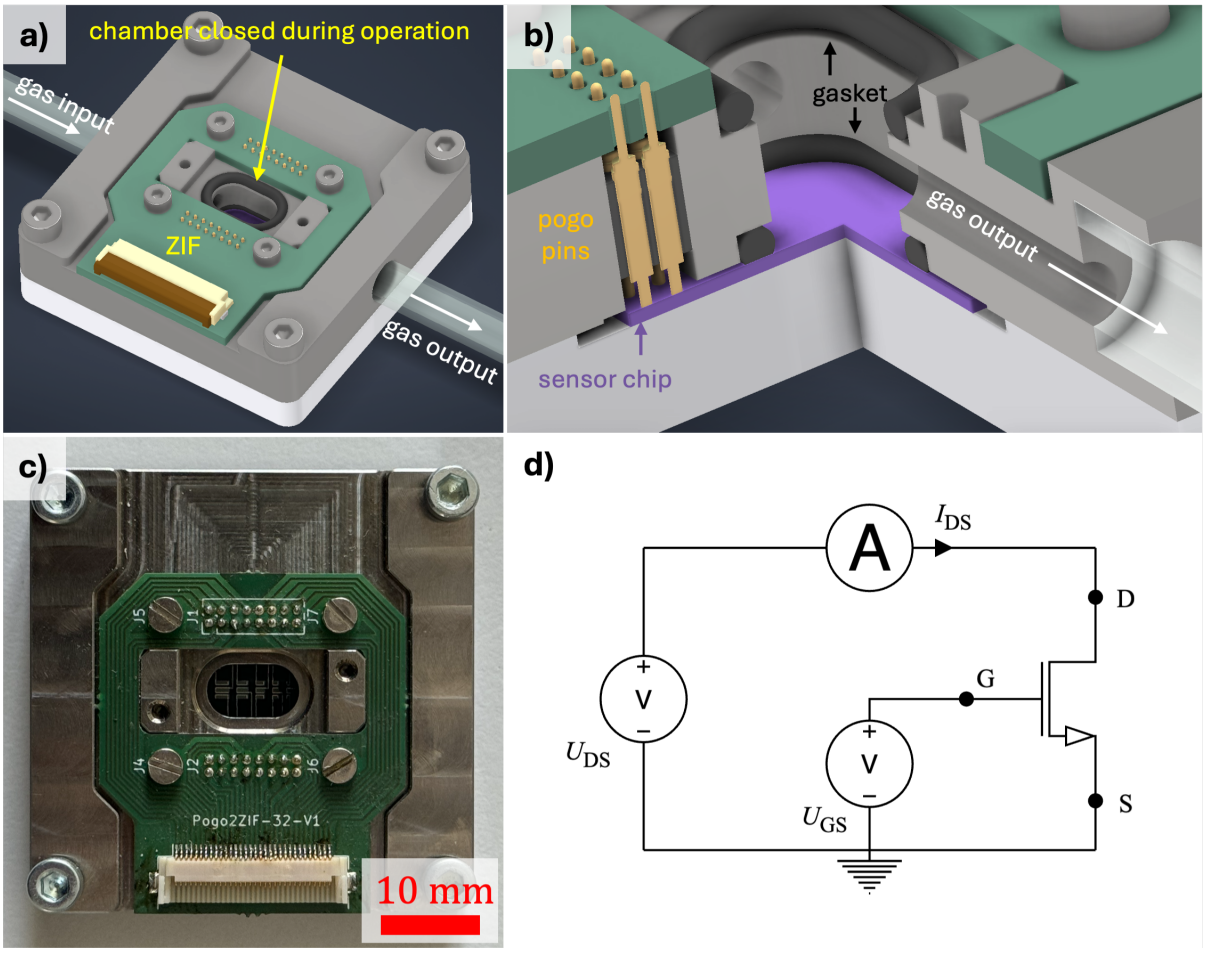

Figure 6.5: Custom designed and machined housing and electrical connections. a) CAD illustration of the housing and PCB, b) quarter-section view focusing on the sensor chamber, c) machined housing and soldered printed circuit board (PCB), d) electrical circuit diagram of the ChemFET measurement setup

(10 V, 20 V and 30 V). Each transfer curve was composed of a forward and a backward U_{GS} sweep ranging from 0 V to 30 V in 1 V increments. This resulted in a 180-dimensional[2] observation data vector containing I_{DS} values as elements. The complete measurement cycle took approximately 30 s. The data was recorded on a measurement PC using PyVISA (Python).

For power-consumption considerations of the eNose, the complete system was modeled as a perfect power supply, the ChemFET, cables, and a current-measurement device. Because of the low gate currents ($I_{GS} \ll I_{DS}$) and the low switching frequency (< 1 Hz), the switching and gate losses were negligible compared to the conduction losses. The total serial voltage U_{tot} and the total serial current I_{tot} were extracted from the measurements. Consequently, the total current was $I_{tot} = I_{DS} = I_{cable} = I_{ammeter}$ and the total voltage was $U_{tot} = U_{DS} + U_{cable} + U_{ammeter}$. Because the resistance of the ChemFET dominated the resistance of the cables and the ammeter ($R_{ChemFET} \gg R_{cable}, R_{ammeter}$), the corresponding voltages U_{cable} and $U_{ammeter}$ were neglible compared to U_{DS}. Therefore, the total power loss of the system could

[2] (number of transfers) × (sweeps per transfer) × (values per sweep) = 3 × 2 × 30 = 180

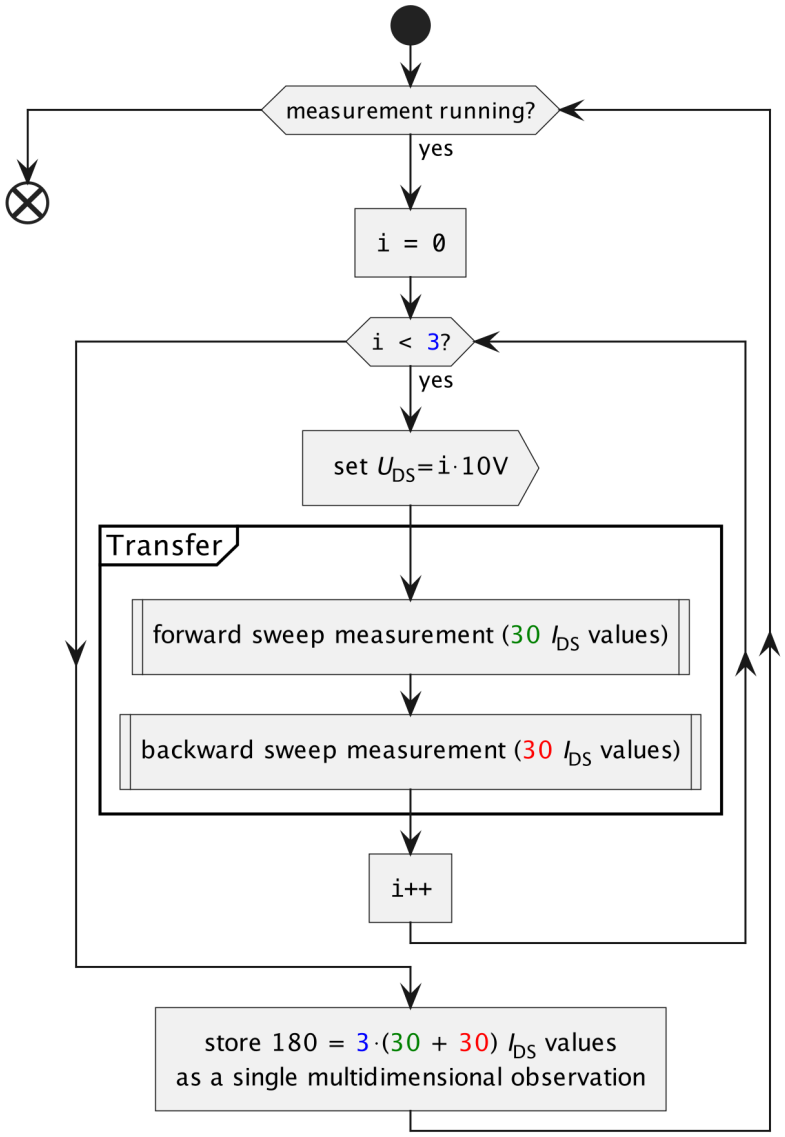

Figure 6.6: Flow chart of ChemFET measurement process. In total 180 I_{DS} values are captured per cycle.

be estimated as the average power loss of the ChemFET, which could be calculated by averaging over the complete cycle according to Equation 6.1.

$$P_{\text{loss,tot}} = \frac{1}{180}\sum_{i=1}^{180} P_i = \frac{1}{180}\sum_{i=1}^{180} U_{\text{DS}} I_{\text{DS}} \tag{6.1}$$

Gas Measurement Series The gas mixing system (GMS), as previously discussed in Section 3.7, supplied the baseline reference air in addition to the three distinct gases, IPA (C_3H_8O), benzene (C_6H_6), and carbon monoxide (CO), at a constant relative humidity of 50 RH%. The concentration of the three gases was set to 100 ppm. Reference air was always measured between gas measurements as a

baseline. Additionally, the measurement series started and ended with baseline measurements. Gas measurements were taken in random order at the same frequency over one week.

6.2.5. Data Analysis

Data analysis was performed using Python (3.12), and default parameters were used for all subsequently mentioned functions if not otherwise stated.

Data Collection and Preprocessing From each 30 min measurement segment, the most stationary data from minutes 19 to 29 were collected and labeled with a 1 min safety margin. This resulted in a feature matrix $\boldsymbol{X} \in \mathbb{R}^{M \times N}$ and a label array $\boldsymbol{y} \in \mathbb{G}^{M}$ where $M = 820$ was the number of samples, $N = 180$ the number of features, and $\mathbb{G} = \left\{\mathrm{R_0}, \mathrm{G_{C_3H_8O}}, \mathrm{G_{C_6H_6}}, \mathrm{G_{CO}}\right\}$ ($C = 7$) the set of classes. Similar to Chapter 5, the data was not equally distributed among the three classes. Reference air ($\mathrm{R_0}$) accounts for $\approx 60\,\%$ of the data, with the remaining 40 % almost evenly distributed among the three gas classes ($\mathrm{G_{C_3H_8O}}$,$\mathrm{G_{C_6H_6}}$, and $\mathrm{G_{CO}}$) as presented in Table 6.3. As previously mentioned, individual feature values were logarithmically transformed I_{DS} values. Randomized undersampling was performed using `RandomUnderSampler` from imblearn (0.14.0), with `random_state` set to 42 for repeatability.

Table 6.3: Initial data sample distribution of all classes. The dataset is severely imbalanced, with the majority of observations belonging to $\mathrm{R_0}$.

Class c	Description	M_c	Rel. distr. [%]
$\mathrm{R_0}$	reference air	484	59.0
$\mathrm{G_{C_3H_8O}}$	isopropyl alcohol	112	13.7
$\mathrm{G_{C_6H_6}}$	benzene	111	13.5
$\mathrm{G_{CO}}$	carbon monoxide	113	13.8
	total	820	100

Training and Testing Given the relatively small sample size, LOOCV was used to evaluate the models. This was accomplished using the `LeaveOneOut` class from scikit-learn (1.7.2). In each LOOCV iteration the undersampled dataset ($\boldsymbol{X}$,$\boldsymbol{y}$) was split into training ($\boldsymbol{X}_{\mathrm{train}} \in \mathbb{R}^{M-1 \times N}$, $\boldsymbol{y}_{\mathrm{train}} \in \mathbb{G}^{M}$) and test data ($\boldsymbol{X}_{\mathrm{test}} \in \mathbb{R}^{1 \times N}$, $\boldsymbol{y}_{\mathrm{train}} \in \mathbb{G}^{1}$). Additionally, the current loop variable `i` was used to set the `random_state` (`random_state = i`) for repeatable randomness. The linear discriminant analysis (LDA) was implemented in Python, as described in Section 2.4.3, and trained directly on the complete training dataset at each iteration. `RandomForestClassifier` (scikit-learn) was used as the Random Forest (RF) algorithm. In contrast to LDA, the RF was first subjected to hyperparameter tuning by means of cross-validated random search using `RandomizedSearchCV` (scikit-learn). The random search was performed using `random_state = i` over 60 iterations (`n_iter = 10`) with a 5-fold stratified and shuffled cross-validation (CV). The search space was spanned by the following RF hyperparameters, as listed in Table 6.4, along with their data types and ranges. After training, the models were evaluated on a single test observation per LOOCV iteration. The test results were stored separately for each model and

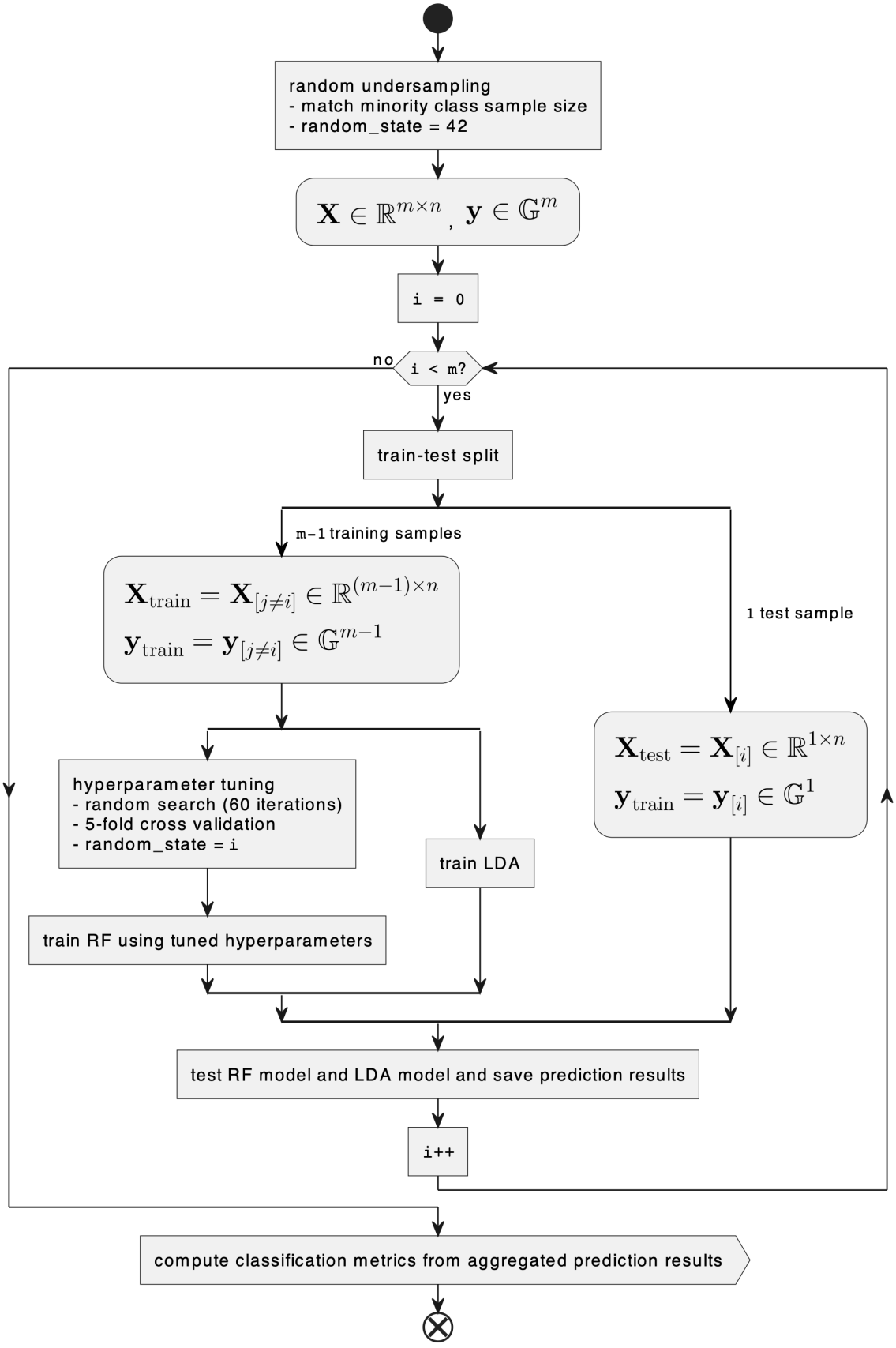

Figure 6.7: Data analysis flow chart of the ChemFET eNose. During each iteration of the leave-one-out cross-validation (LOOCV) loop, the `random_state` variable is set to the loop variable `i` for repeatability.

Table 6.4: Tuned hyperparameters for RF models. All values are of integer type.

Hyperparameter	Variable name	Value range
no. trees	`n_estimators`	[100, 1000]
max. tree depth	`max_depth`	[5, 50]
min. req. samples for splitting	`min_samples_split`	[2, 15]
min. req. samples per leaf node	`min_samples_leaf`	[1, 10]
max. no. leaf nodes	`max_leaf_nodes`	[8, 120]

accumulated across the entire LOOCV loop. The true label array was equal to the initial label array $\boldsymbol{y}_{\text{true}} = \boldsymbol{y}$. The LOOCV test results were gathered in a predicted label array $\boldsymbol{y}_{\text{pred}} \in \mathbb{G}^M$ with the same shape as the $\boldsymbol{y}$. These two label arrays, $\boldsymbol{y}_{\text{true}}$ and $\boldsymbol{y}_{\text{pred}}$, were used to compute the classification metrics, as described in the next paragraph.

The actual and predicted label arrays derived from the LOOCV test results were used to compute the normalized confusion matrix (CM) and classification metrics using the scikit-learn functions `confusion_matrix` and `classification_report`, respectively. PRC, REC, and F1-score were evaluated as classification metrics.

Feature Importance A feature importance analysis was conducted to assess the relative information gain across different operating points (U_{DS} and U_{GS}). Because of the singular test data in each LOOCV iteration, permutation feature importance could not be calculated. Instead, for LDA, the feature importances were computed as the normalized contributions of each feature in the projection matrix as described in Section 2.4.3. For RF, the pre-implemented impurity-based feature importances were calculated during training and were directly used.

Finally, models were trained and tested again using low-impact features, with corresponding impacts below a certain threshold removed. This threshold was swept from 5 to 50 percentile in 5 percentile increments. For each percentile, a new LOOCV loop was performed for LDA and RF, and the accumulated test results were analyzed.

LDA Plot To visualize the data clustering and separation, a LDA plot was created. For this plot, a separate but representative LDA model was trained on the complete data set ($\boldsymbol{X}$,$\boldsymbol{y}$). This means that, compared with each LDA model in the LOOCV iterations, it had only one additional training observation. Subsequently, the LDA plots were created using the highest-ranked discriminants. Additionally, the 95 % confidence interval was visualized as circles around each of the class centroids in the LDA plots. The circular shape resulted from deliberate standardized scaling of the discriminants, as discussed in Section 2.4.3.

6.3. Results and Discussion

6.3.1. Structural Characterization

Using a stylus profilometer, the In_2O_3 films IJ printed at 600 DPI, 800 DPI and 1000 DPI are measured as depicted in Figure 6.8a. The In_2O_3 film thickness increases from 5 nm at 600 DPI to 9 nm 1000 DPI. As discussed in Section 3.4, the layer thickness should correlate with DPI^2 within certain limits. The observation only weakly correlates with ($\approx 10/1000\text{nm}\,\text{DPI}^{-2}$) due to inconsistencies at 600 DPI and due to overflow at 1000 DPI. The structural continuity of the In_2O_3 thin film is not guaranteed when the film thickness falls below approximately 600 dpi, which is indicated by the increased standard deviation as seen in Figure 6.8a. In contrast, single Ag lines are approximately 2 µm high and 100 µm wide as depicted in Figure 6.8b. The M-shape is a result of a strong AJ stream pushing material away from the center. A microscope image of the printed ChemFET is shown in Figure 6.9 a. From the top view, the

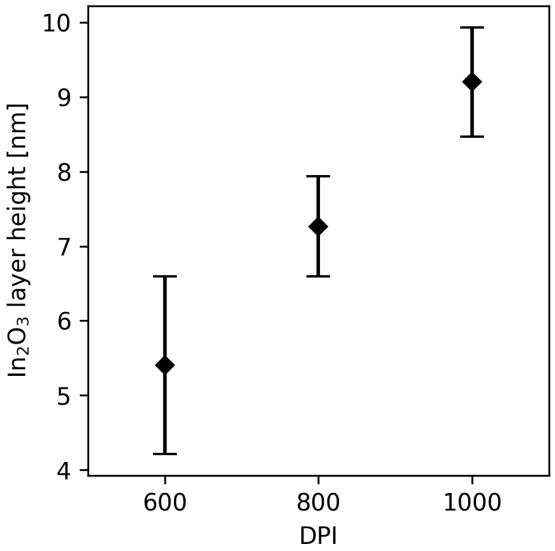

(a) DPI-dependence of In_2O_3 layer thickness. The low layer heights are approaching the device limits, leading to a high noise-to-signal ratio. Additionally, at 600 DPI or below, continuity of the thin film (TF) is not guaranteed. At 1000 DPI or above, overflow occurs, which impacts the lateral shape integrity. Therefore, the optimal dpi setting of 800 DPI is used.

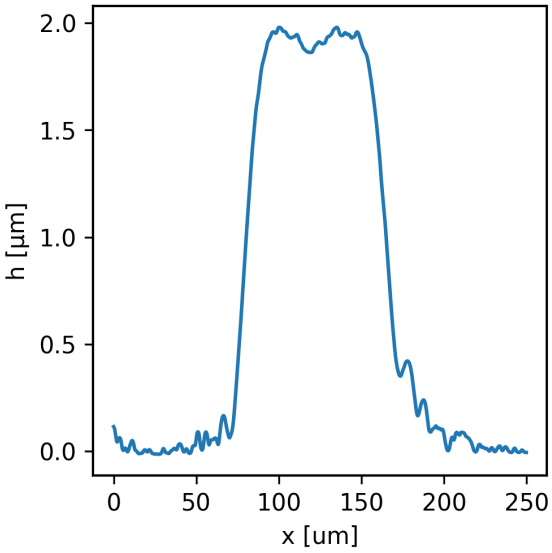

(b) Ag electrode profile measurement showing line thicknesses of around 2 µm. The profile is M-shaped due to the jet stream's pushing force.

Figure 6.8: Profile analysis of IJ and AJ printed structures.

In_2O_3 layer is barely distinguishable due to its nanometer-thickness. The ITO layer is almost entirely covered by the Ag layer. A 50 µm gap ($=l_{ch}$) is visible between the top electrodes. An SEM image of a FIB cut cross-section is shown in Figure 6.9 b and c. The NP-nature of the Ag (first layer from the top) and ITO (second layer from the top) materials, and the difference in their NP-sizes, are visible on Figure 6.9 b. In the zoomed view of Figure 6.9 c, SiO_2 can be distinguished from Si. Additionally, the In_2O_3 layer is hinted at by the thin whitish layer between ITO and SiO_2.

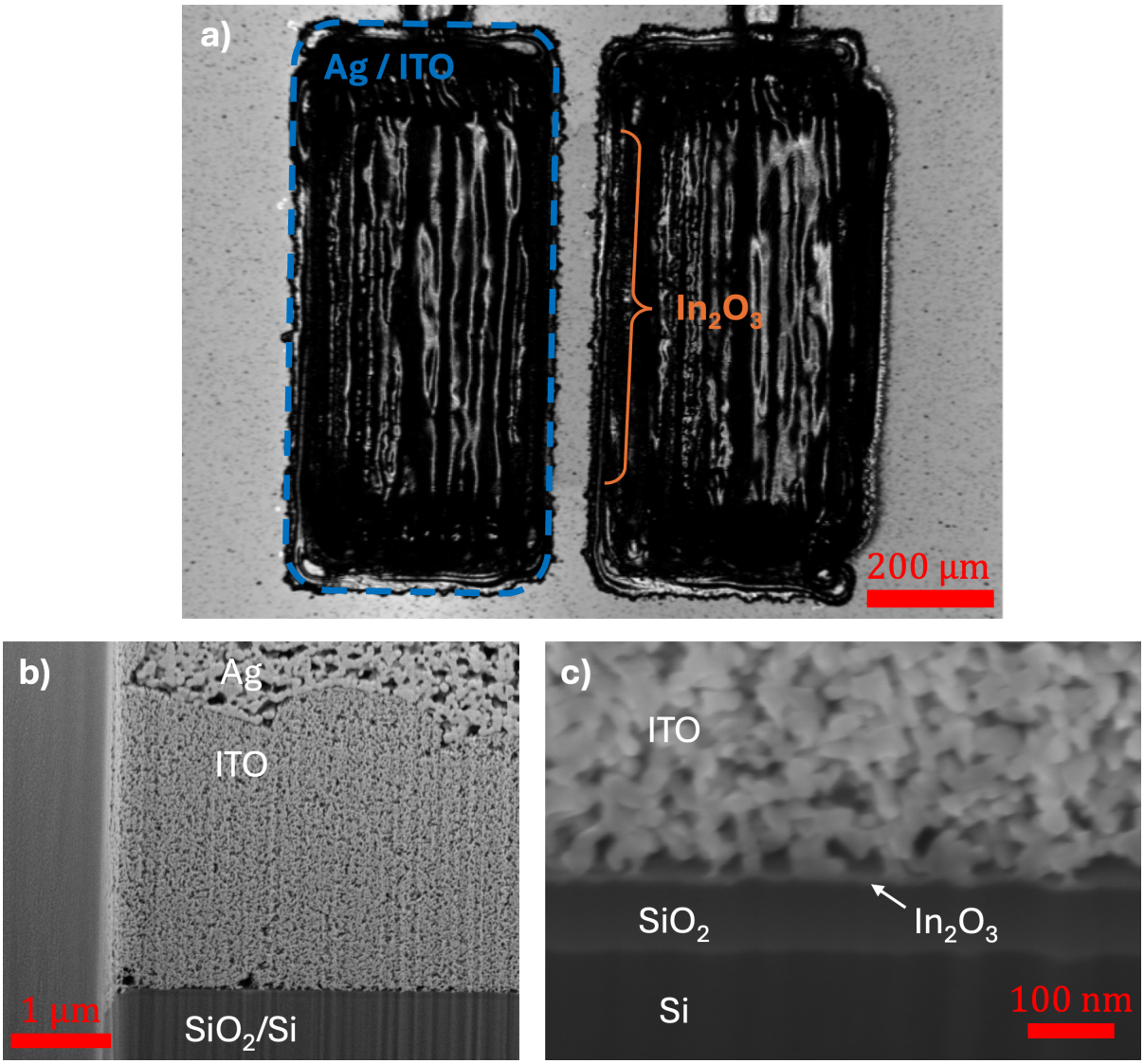

Figure 6.9: Structure of a printed ChemFET. a) Top view. The In_2O_3 layer is barely visible. b) and c) cross-sectional FIB-SEM image of the ChemFET. b) overview of the complete stack including the Ag and ITO electrode and the substrate. The In_2O_3 layer is not visible at this magnification. c) Zoomed view of the ITO-In_2O_3-SIO_2 interface. In_2O_3 forms the thin whitish layer, which is barely distinguishable. Adapted from [3] under CC BY 4.0.

6.3.2. Electrical Characterization

Preliminary tests showed that the off current increases rapidly with increasing In_2O_3 layer thickness. At the same time, the on current does not increase significantly, which consequently leads to an overall decrease in the on/off ratio. Therefore, the fabrication of the ChemFET was subsequently performed at 800 DPI as further reduction in film thickness (600 DPI or below) would result in the previously mentioned structural inconsistencies. Figure 6.10 shows the output and transfer characteristics of a printed (800 DPI) ChemFET under reference conditions (reference air at $H_{\mathrm{rel}} = 50\,\mathrm{RH\%}$). In the

output characteristic (Figure 6.10 a), the linear region at lower U_{DS} values and the saturation region at higher U_{DS} values are both distinguishable. An on/off-ratio of 2.3×10^5 is extracted from the transfer characteristic at $U_{DS} = 30\,V$ (Figure 6.10 b). Using linear extrapolation of $I_{DS}{}^{\frac{1}{2}}$ (red) during the forward sweep, the threshold voltage is calculated to be $U_{th} = 12.67\,V$. Hysteresis effects are observed in

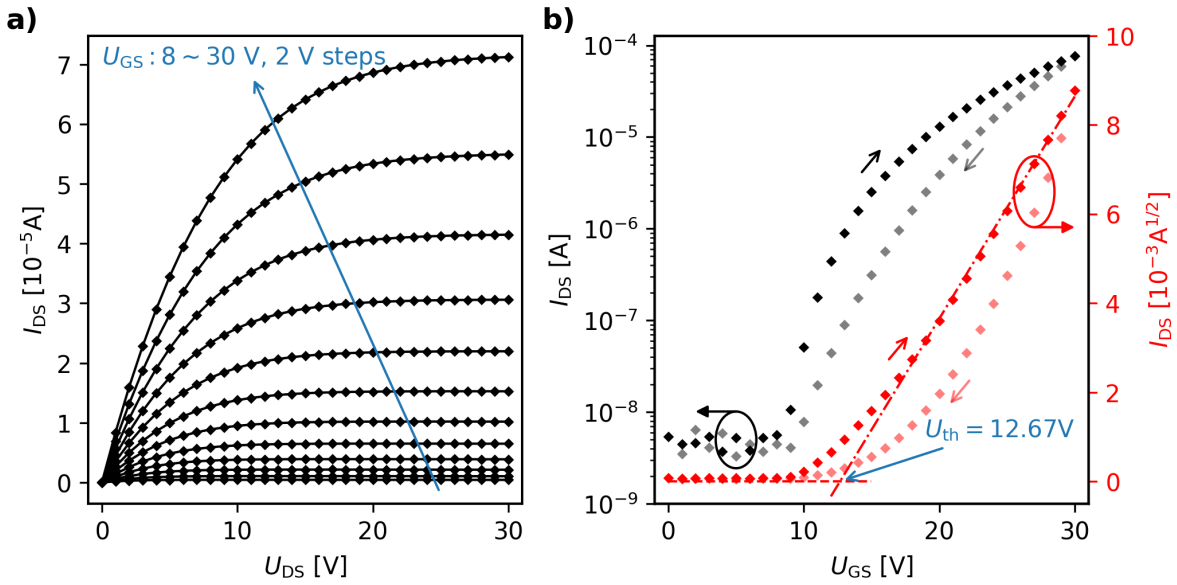

Figure 6.10: FET characteristics of the printed ChemFET. a) Output characteristics with $\Delta U_{GS} = 2\,V$ steps. b) Transfer characteristics at $U_{DS} = 30\,V$. The ChemFET is measured at RT using reference air at $H_{rel} = 50\,RH\%$. The data point transparency of the backward sweep is set to 0.5 to distinguish it from the forward sweep. Adapted from [3] under CC BY 4.0.

the transfer characteristics. However, this is not necessarily a detrimental characteristic for eNose applications and may even bear additional information for classification, which will be discussed in more detail later. The observed U_{th} drift over prolonged measurements is a more critical issue. For TFTs, this drift in threshold voltage $\Delta U_{th}(t)$ is caused by charge trapping and can be modeled by a stretched-exponential function (Equation 6.2)[70], where τ and β are constants, and $\Delta U_{th\infty} = \lim_{t\to\infty} U_{th}$ is the asymptotic limit.

$$\Delta U_{th}(t) = \Delta U_{th\infty} \cdot \left[1 - e^{-\left(\frac{t}{\tau}\right)^{\beta}}\right] \tag{6.2}$$

Figure 6.11 shows the recorded change in threshold voltage over 14 h and the corresponding fitted curve according to Equation 6.2. The threshold voltage shifts rapidly initially and approaches the limiting value at approximately the two-hour mark. After approximately six hours, the signal stabilizes. Consequently, relevant gas measurements are performed after a stabilization time of at least eight hours.

6.3.3. Gas Response

A representative transient response curve of the ChemFET sensor at the operating point $U_{DS} = 30\,V$ and $U_{GS} = 30\,V$ is shown in Figure 6.12 a. I_{DS} decrease rapidly when the ChemFET is exposed to of

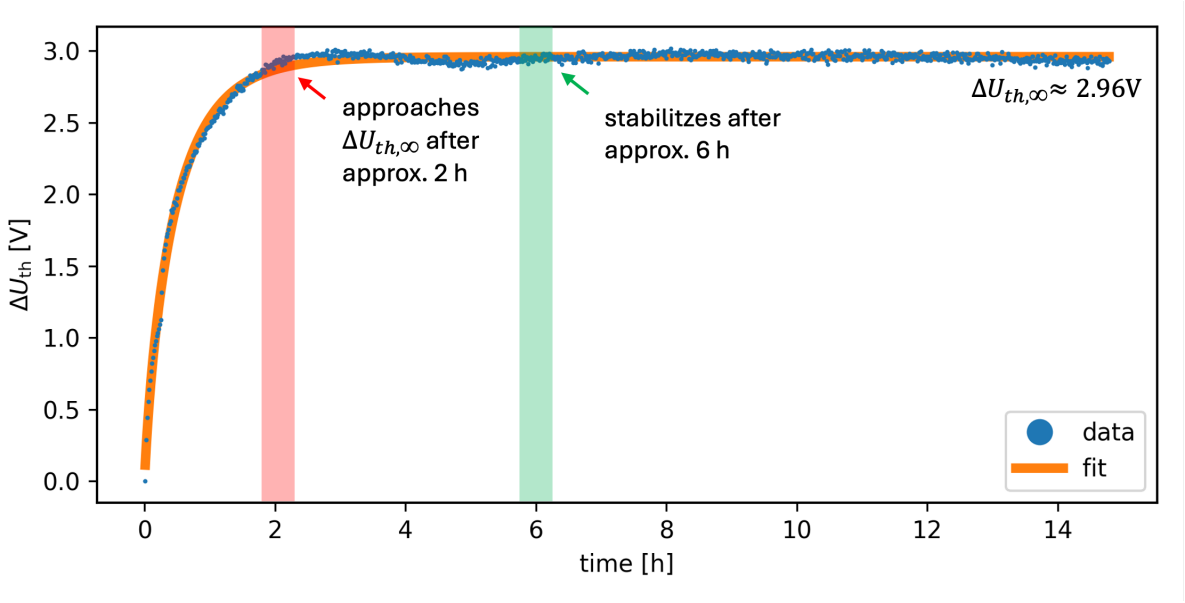

Figure 6.11: Gate bias-induced drift in threshold voltage U_{th}. Equation 6.2 is fitted to the measurement data ($\Delta U_{\text{th}\infty} \approx$ 2.96 V, $\tau \approx$ 0.46 h, and $\beta \approx$ 0.85). Adapted from [3] under CC BY 4.0.

the three measured gases, IPA (C_3H_8O), benzene (C_6H_6), and carbon monoxide (CO). The stabilized I_{DS} values during approximately the last 10 min for benzene (green) and isopropyl alcohol (orange) are reduced to around 0.1 µA to 1 µA. In contrast, carbon monoxide exhibits a much higher value of around 10 µA. The difference in response dynamics before stabilization depends on the previous gas, indicating a memory effect in the system. The relative responses (RRs) for each gas at 100 ppm are calculated to be around 10^2 for IPA and benzene (refer to Figure 6.12 b), which are exceptionally high. In contrast, carbon monoxide displays a lower but still respectable value of approximately $10^{0.7} \approx 5$, but also exhibits a lower variation.

Next, the response and recovery times are evaluated. Due to the non-negligible deviation from the exponential model proposed in Section 2.3, no fit was performed on the response curves. Instead, response times are extracted when the RR reaches 0.9 of the stabilized value. Because the low-frequency signal is not guaranteed to be monotonic (refer to Figure 6.12 a), the search is performed backwards in time. In contrast, the response time is roughly monotonic and therefore well fit by an exponential function. The results are presented in Figure 6.13. The sensor's average response time is approximately 8 min, 4 min and 12 min for IPA, benzene, and carbon monoxide, respectively. The high standard deviations stem from the previously mentioned differences in response dynamics. Meanwhile, response times are more consistent, with fewer variations, which aligns with the transient curves in Figure 6.12 a. They average to 6 min, 7 min and 3 min, for IPA, benzene, and carbon monoxide, respectively. Overall, the ChemFET sensor exhibits moderate response times and recovery times.

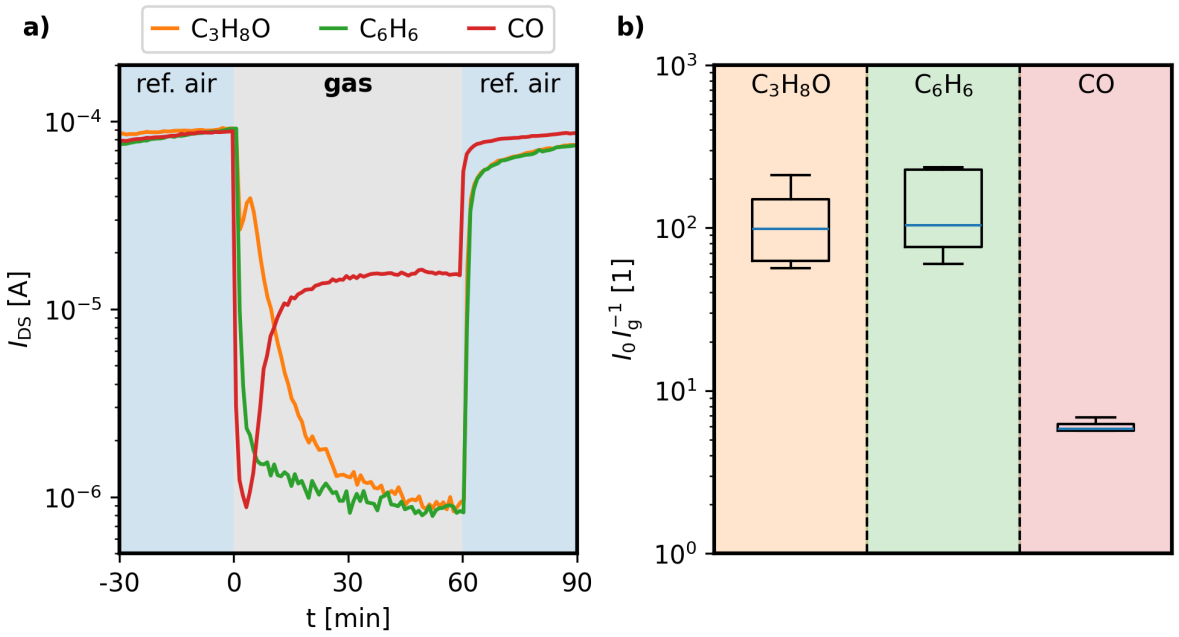

Figure 6.12: Response analysis of the ChemFET
The ChemFET was operated at $U_{DS} = 30\,V$ and $U_{GS} = 30\,V$. a) Representative transient responses to benzene (C_6H_6), isopropyl alcohol (C_3H_8O), and carbon monoxide (CO). Baseline: reference air (R_0). b) Relative response analysis showing the mean values and the standard deviation. The values are calculated from 5 analyzed segments for each gas and stem from a single measurement series.

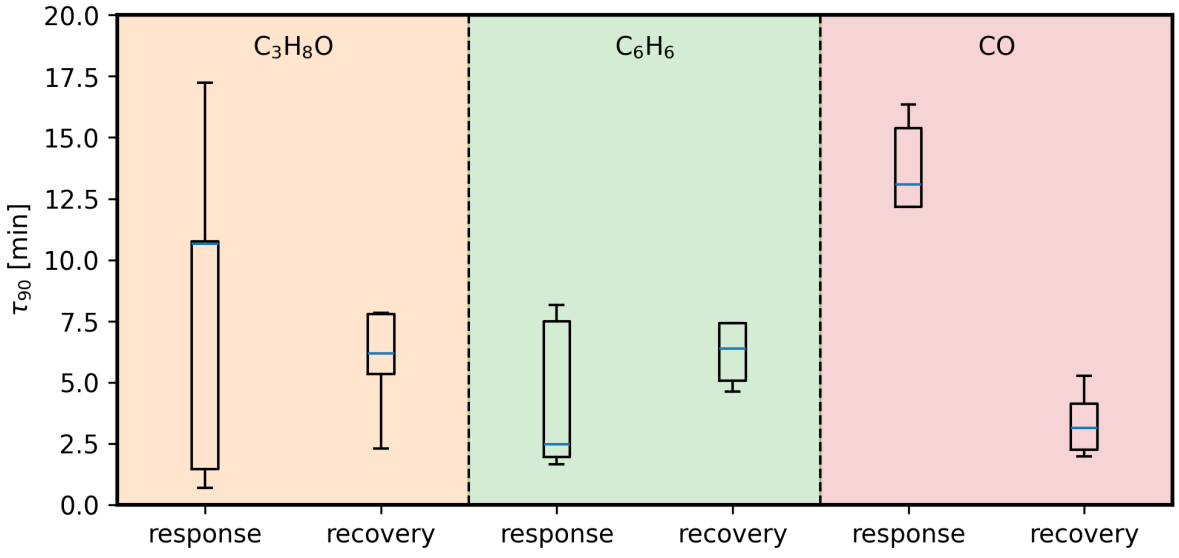

Figure 6.13: Response and recovery time analysis of the ChemFET. The ChemFET was operated at $U_{DS} = 30\,V$ and $U_{GS} = 30\,V$.

6.3.4. Feature Generation and Classification

In Figure 6.14, the observed feature patterns of the four different classes are compared by averaging all observations of each corresponding class. The feature patterns, which are logarithmically transformed I_{DS} values, are composed of valleys in the off state regions $U_{GS} \lesssim U_{th}$ and peaks around the on state regions $U_{GS} \gtrsim U_{th}$. In the off regions, no significant differences in features are observed between the classes. In contrast, notable variations between the classes occur when increasing U_{GS} beyond the threshold voltage U_{th}. The classes R_0 (reference air) and G_{CO} (carbon monoxide) are clearly distinguished from $G_{C_3H_8O}$ (IPA) and $G_{C_6H_6}$ (benzene). Conversely, only minor differences are observed between $G_{C_3H_8O}$ and $G_{C_6H_6}$. Interestingly, the symmetry of the peaks also differs slightly between the classes.

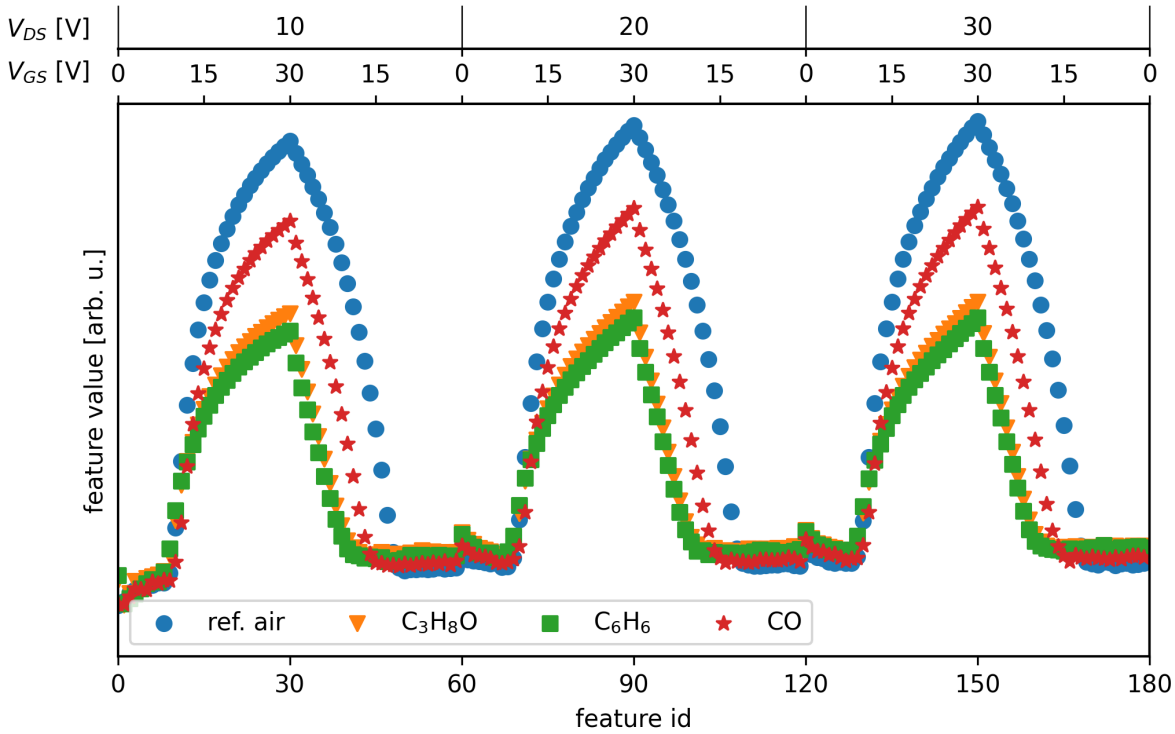

Figure 6.14: Feature pattern comparison between R_0,$G_{C_3H_8O}$, $G_{C_6H_6}$, and G_{CO}. The corresponding U_{DS} and U_{GS} values for each feature are displayed at the top of the plot. Machine learning algorithms use the distinct feature patterns of the four different classes to discriminate between them. Adapted from [3] under CC BY 4.0.

LDA The LDA plots in Figure 6.15 visualize the data clusters for the four classes in the discriminant space. The data clusters of R_0 (blue) and G_{CO} (red) occupy distinct areas in the LDA plot and are well separated. In contrast, the data clusters of IPA and benzene severely overlap in the first two discriminants, as shown in Figure 6.15 a. Only the third discriminant can separate both classes, as presented in Figure 6.15 b. The observed separations of the class clusters in the LDA plot are reflected in the CM (Figure 6.16) and in the classification report (Table 6.5). LDA achieves 1.0 PRC and REC for R_0 and G_{CO} due to the excellent separation in the discriminant space. In contrast, a high amount of misclassifications between these $G_{C_3H_8O}$ and $G_{C_6H_6}$ can be seen in the CM, resulting in relatively

low PRC and REC values of 0.63 to 0.67. All in all, the LDA achieves a macro-averaged PRC, REC, and F1-score of 0.82. The equality of PRC and REC results from the fact that only $G_{C_3H_8O}$ and $G_{C_6H_6}$ are being misclassified to each other.

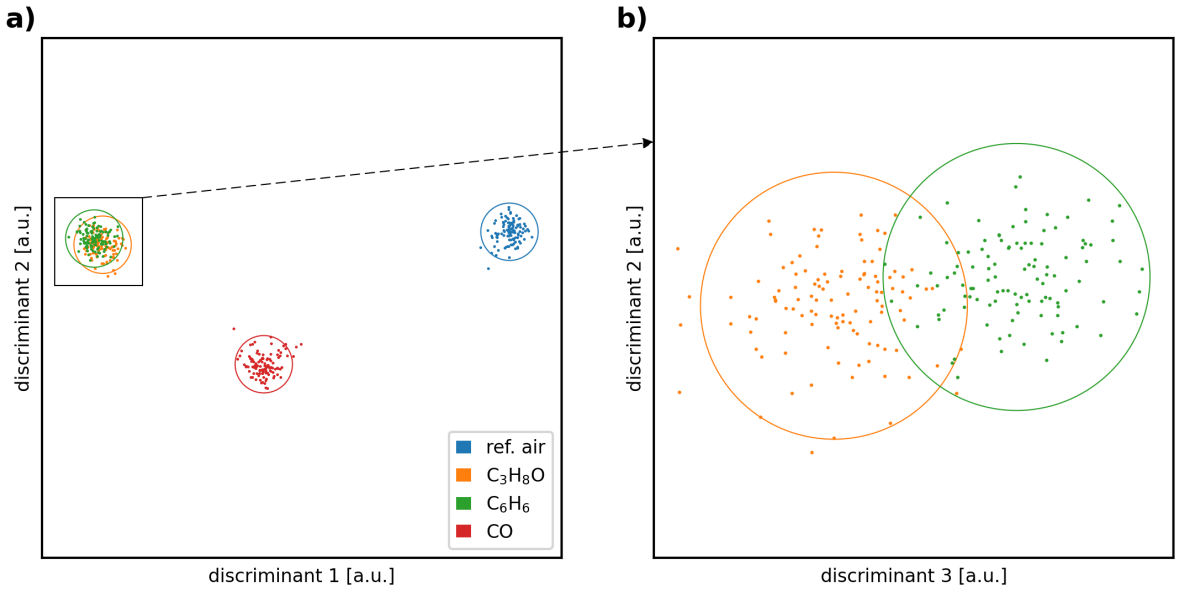

Figure 6.15: Representative LDA plot. The LDA model was trained on the complete dataset. a) LDA map of the first (d1) and second-ranked (d2) discriminants, including all gas classes. b) LDA map of the second (d2) and third-ranked (d3) discriminants that focuses only on Isopropyl alcohol and benzene. The discriminant axes are scaled such that 95 % confidence intervals are represented as circles around the class centers. Reprinted from [3] under CC BY 4.0.

Random Forest Similar to LDA, both R_0 and G_{CO} are perfectly classified as shown in the CM in Figure 6.16 b. Consequently, the model exhibits PRC = 1.0 and REC = 1.0 as presented in Table 6.5. Approximately 23 % of the tested $G_{C_3H_8O}$ is being misclassified as $G_{C_6H_6}$, whereas only 8 % of $G_{C_6H_6}$ is misclassified as $G_{C_3H_8O}$. On average, the RF achieves an F1-score of 0.92.

Table 6.5: LOOCV classification report of LDA and RF.. Adapted from [3] under CC BY 4.0.

	LDA			RF			
Class	PRC	REC	F1	PRC	REC	F1	M_c
R_0	1.00	1.00	1.00	1.00	1.00	1.00	111
$G_{C_3H_8O}$	0.64	0.67	0.65	0.90	0.76	0.82	111
$G_{C_6H_6}$	0.65	0.63	0.64	0.79	0.92	0.85	111
G_{CO}	1.00	1.00	1.00	1.00	1.00	1.00	111
macro avg.	0.82	0.82	0.82	0.92	0.92	0.92	$\sum = 444$

Comparison between LDA and RF Both LDA and RF accurately classify reference air and carbon monoxide, indicating that the ChemFET uniquely responds to these gas compositions, resulting in a distinguishable feature pattern, which was displayed in Figure 6.14. In contrast, both models make

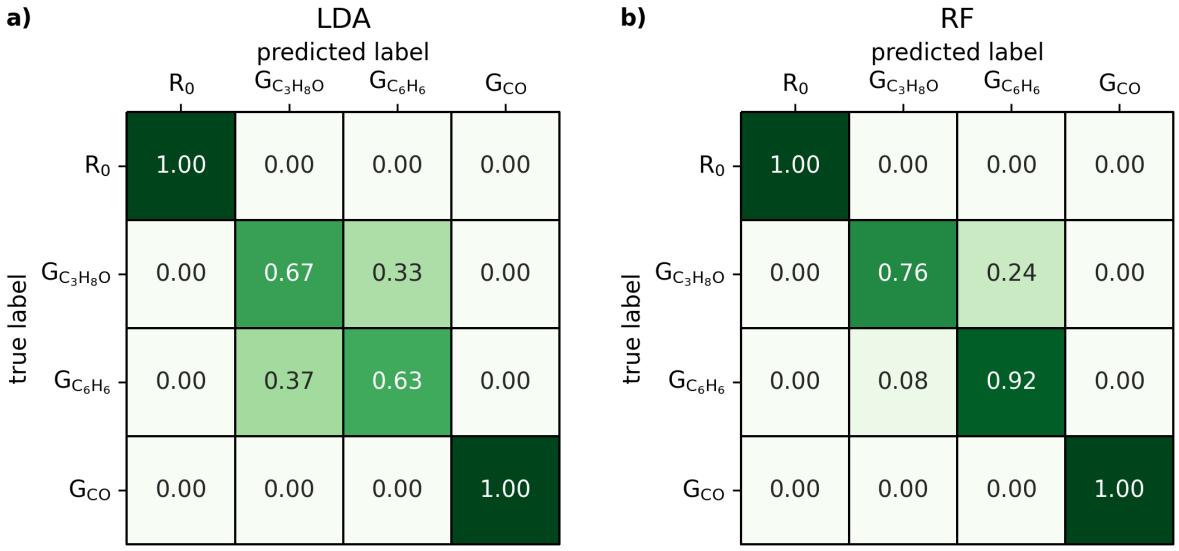

Figure 6.16: Normalized confusion matrices of the LOOCV test results.. a) LDA. b) RF. Reprinted from [3] under CC BY 4.0.

classification errors when classifying IPA and benzene. Compared to LDA, RF increases the class-specific F1-score by 0.19 for $G_{C_3H_8O}$ and by 0.22 for $G_{C_6H_6}$. This is most notable in the reduction of misclassifications (equal to an increase in REC) for $G_{C_6H_6}$ and the increase in PRC for $G_{C_3H_8O}$. According to these results, RF is clearly the better performing algorithm for the tested ChemFET in combination with the tested gases. However, the improved performance is achieved at the cost of higher computational complexity and, consequently, increased computational time, particularly during the hyperparameter tuning step, which the LDA does not require.

6.3.5. Feature Importance Analysis

The feature importances are calculated (LDA) or collected (RF) from all trained models of the LOOCV. To analyze which operation point results in the maximal informational gain, the feature importance values (y-axis) are plotted against the corresponding U_{GS} values (x-axis) in Figure 6.17 and against the corresponding U_{DS} values (x-axis) in Figure 6.18, respectively. Both LDA (Figure 6.17 a) and RF (Figure 6.17 b) show near-zero feature importances in the off-state region ($U_{GS} \lesssim U_{th}$). Conversely, the feature importance rises in the on state $U_{GS} \gtrsim U_{th}$ and peaks around the maximal voltage $U_{GS} = 30\,V$. Three hypothesized causes are presented below, which may explain the observed behaviour. First, the drain-channel-source connection of the ChemFET simplifies to a resistor in the off-state. Hence, the ChemFET can be seen as a chemiresistor with resistance values corresponding to $R_{DS} = U/I_{DS}$[3]. Without external excitation sources, such as heating or UV irradiation, the chemiresistor fails to respond to the presented gas. Additionally, the low I_{DS} values (high resistance) approach the measurement limits. Second, the U_{GS}-induced electric field (E-field) may directly affect the ionosorption behavior of gas molecules, including oxygen ion species. In turn, this would increase selectivity for gases. Third,

[3] For a simplified model ignoring electrode and interface resistances

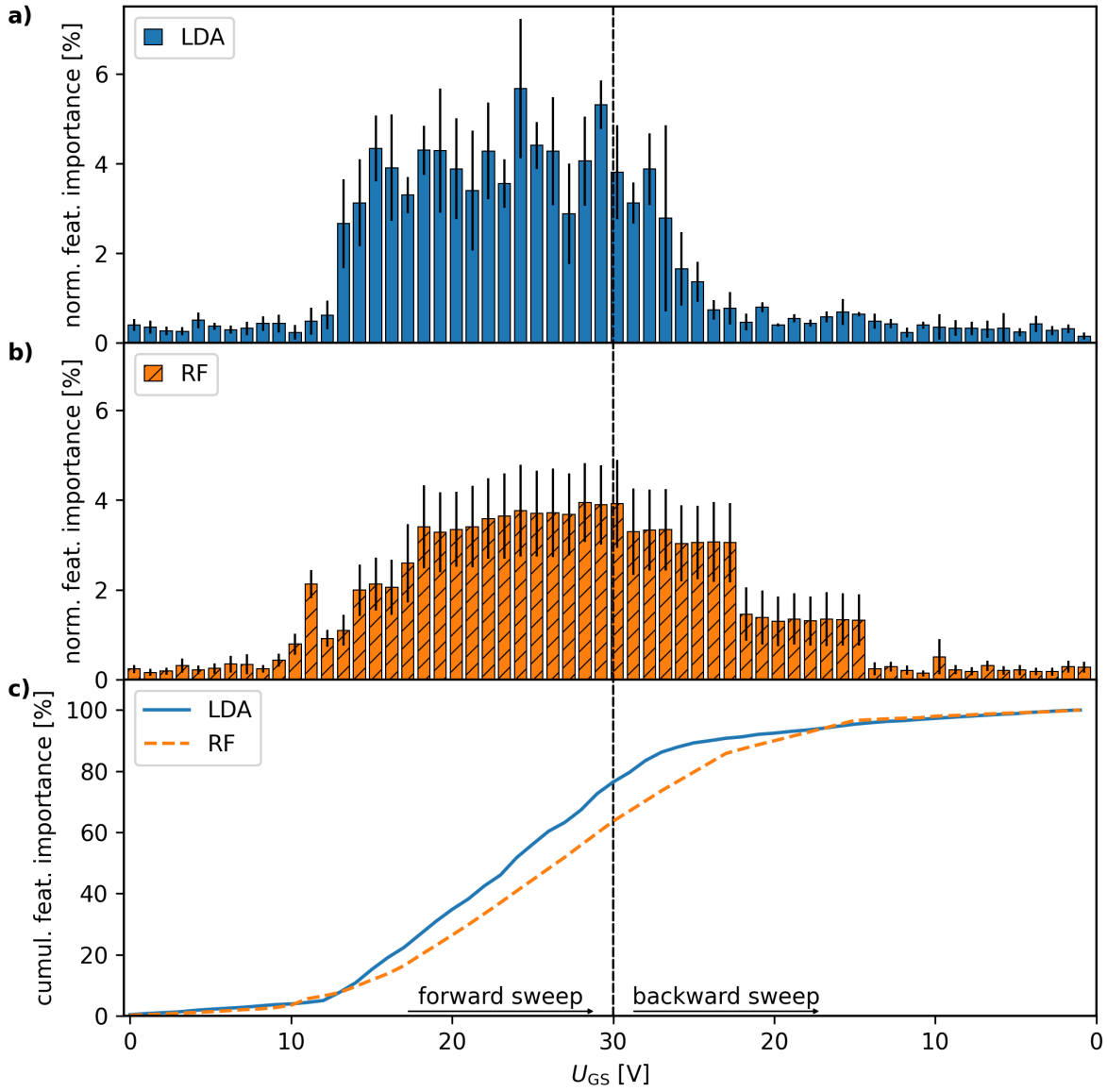

Figure 6.17: Normalized U_{GS} dependent feature importances. a) LDA. b) RF. The bars show the mean values, and the lines show the standard deviations. Cumulative feature importance is shown in c. Reprinted from [3] under CC BY 4.0.

physorption-induced characteristic changes (charge depletion or accumulation) may be amplified at higher gate voltages. Furthermore, Figure 6.17 c shows that both LDA and RF exhibit asymmetric behavior, with higher cumulative feature importances during the forward sweep of U_{GS}. Additionally, LDA displays a higher skewness.

In contrast, no significant dependence is observed between the feature importance and U_{DS} (refer to Figure 6.18).

The evaluation results of models with low-ranking features removed are presented below. Due to computational complexity and time, the RF was not subjected to hyperparameter-tuning again but

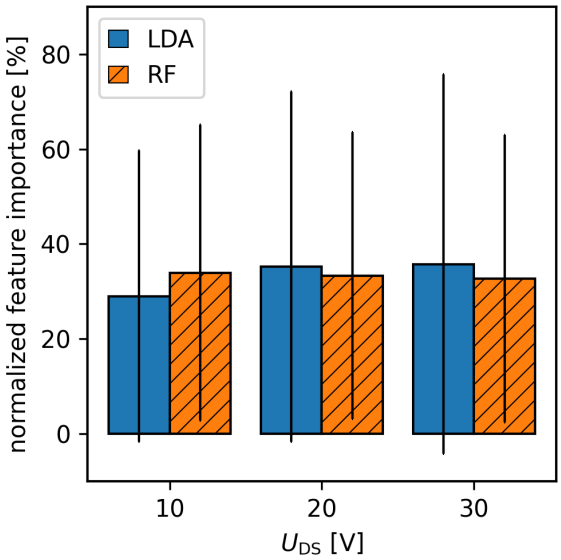

Figure 6.18: Normalized U_{DS} dependent feature importances for LDA and RF
The bars show the mean values, and the lines show the standard deviations. Reprinted from [3] under CC BY 4.0.

instead used the averaged values from the previous LOOCV iterations as listed in Table A2. Within the searched percentiles, both LDA and RF achieve the maximum F1-scores at the same threshold percentile ($p_{th} = 35$). Only minor improvements are observed for both LDA and RF. The F1-score of LDA increases from 0.83 to 0.85 and from 0.92 to 0.94 for RF.

These findings indicate that approximately a third of the features provide no informational gain. At the same time, the signal noise at these operating points is not overly disruptive to classification. Therefore, many operation points (U_{DS}, U_{GS} combinations) may be skipped to increase measurement frequency without sacrificing classification performance.

6.3.6. Comparison of the ChemFET and Chemiresistor

Gas Sensing Performance The ChemFET and the chemiresistive SnO_2 NW-based eNose systems from the previous chapter are compared regarding multiple metrics. They are additionally compared against other reported sensors. The comparison, including the sources, is presented in Table 6.6.

Compared to its direct predecessor, using the same chemiresistive sensor platform (CSP) [109] and operated at RT with UV excitation, the improved vapor-liquid-solid (VLS) and deposition process leads to an up to over six-fold improvement in RR for IPA at the same conditions. Additionally, the RR increases by more than twofold in the best case when targeting benzene. In contrast, targeting carbon monoxide, only the best subsensors can keep up, while the median response is lower. Compared with gas-specific chemiresistive sensors, the SnO_2 NW sensor in this work only matches other SnO_2-based sensors in IPA response. In contrast, the responses to benzene and carbon monoxide are comparably weak. Moreover, only the best subsensors can compete with the reported response and recovery times,

Table 6.6: Comparison table of resistive and field-effect-based gas sensors. For an arbitrary base s_0 and gas response signal s_g, the default unmarked response value is $|s_g - s_0|\, s_0^{-1}$. The asterix $*$ denotes the alternative calculation $\max\{s_g, s_0\} \cdot \min\{s_g, s_0\}^{-1}$. If not directly published, values are extracted by graph analysis and marked by a preceding $\approx$. Values in parentheses are linearly extrapolated data to 100 ppm. The maximum and minimum values reported in this work are denoted by a preceding $\uparrow$ and $\downarrow$, respectively. Otherwise, the median values are listed.

type	mat. and morph.	op. cond.	gas	c [ppm]	resp. [1]	$\tau_{resp,90}$ [s]	$\tau_{recov,90}$ [s]	ref.
resistor	SnO_2 NW	RT, UV	C_3H_8O	100	≈ 0.35	-	-	[109]
			C_6H_6	100	≈ 0.16	-	-	
			CO	100	≈ 0.11	-	-	
	SnO_2 NF	325 °C	C_6H_6	100	$\approx 4.69^*$	-	-	[215]
	V_2O_5-SnO_2 NF	325 °C	C_6H_6	100	$\approx 8.63^*$	3	47	
	SnO_2 NR	196 °C	C_3H_8O	100	$\approx 2.5^*$	8	13	[216]
	SnO_2 NP	300 °C	CO	100	$\approx 1.7^*$	6	-	[217]
	Ce-In_2O_3 NS	220 °C	C_3H_8O	100	93^*	14	15	[218]
			CO	100	8.09^*	-	-	
	RuO_2-In_2O_3 TF	90 °C	C_6H_6	50	123.1^*	34	42	[219]
FET	CNT	RT	C_3H_8O	100	0.26	< 120	-	[220]
	CNT	RT	C_6H_6	2	≈ 4.13 (252.4)	318	> 3600	[221]
	organic NW	RT	CO	40	≈ 0.23 (0.58)	-	-	[222]
resistor	SnO_2 NW	RT, UV	C_3H_8O	100	$\uparrow 2.13$	$\downarrow 55$	$\downarrow 77$	**this work**
					0.77	141	144	
			C_6H_6	100	$\uparrow 0.39$	$\downarrow 33$	$\downarrow 126$	
					0.17	59	256	
			CO	100	$\uparrow 0.13$	$\downarrow 23$	$\downarrow 57$	
					0.05	29	282	
FET	In_2O_3 TF	RT	C_3H_8O	100	$\uparrow 127.79^*$	$\downarrow 41$	$\downarrow 137$	
					70.14^*	639	371	
			C_6H_6	100	$\uparrow 215.08^*$	$\downarrow 99$	$\downarrow 277$	
					117.39^*	148	382	
			CO	100	$\uparrow 5.86^*$	$\downarrow 81$	$\downarrow 119$	
					5.51^*	785	188	

whereas the median values are several times slower. However, the reported chemiresistive sensors were operated exclusively at elevated temperatures ranging from 90 °C to 325 °C with a median of 200 °C. This will limit their power efficiency compared to the UV excitation used in the present work. Compared to the ChemFET, which is also operated at RT, the chemiresistor exhibits a higher response to IPA and a comparable response to carbon monoxide, but severely underperforms for benzene.

The ChemFET in this work exhibits exceptionally high responses to IPA and benzene, which are among the best reported for chemiresistive and chemfet sensors. This is even more remarkable, considering that the ChemFET is operated at room temperature and without UV irradiation. The difference is extreme in direct comparison with the carbon nanotube (CNT)-based ChemFET for IPA sensing, with a nearly 500-fold increase in sensitivity. The carbon monoxide response is the second highest reported case (Ce-In_2O_3), and approximately 10-times higher compared to the organic NW based ChemFET.

In terms of response and recovery times, the ChemFET can match those reported for ChemFET devices. However, as in the chemiresistive SnO_2 sensor in this work, the response and recovery times remain mediocre at best. This is, as observed in Table 6.6, a general issue across all RT-operated sensors, indicating that proper heating not only increases sensitivity but also enhances gas-interaction dynamics.

Gas Classification Performance Next, the classification performance of the multi-sub-sensor chemiresistive SnO_2-NW-based and single ChemFET-based eNose systems is compared. To ensure comparability, only the LDA results are used for comparison. The multi-sub-sensor chemiresistive eNose achieves higher discrimination between the tested gases as shown in the respective LDA plots (Figure 5.9 and Figure 6.15). If no decision boundaries are enabled, the chemiresistive eNose makes no errors across all classes, whereas the single ChemFET achieves this only for reference air and carbon monoxide. Still, the results from the ChemFET are respectable, considering that only a single (sub-)sensor is used compared to an array of sub-sensors as is the case for the chemiresistive sensor. This is illustrated by artificially reducing the number of sub-sensor of the chemiresistive sub-sensors (features) that the LDA model receives, as shown in Figure 6.19. If using the best two sub-sensor, the LDA map shows similar separations as the single ChemFET (Figure 6.19 b). Whereas the two worst sub-sensor results in a much larger within-class to between-class spread (Figure 6.19 b). Surprisingly, the LDA model using the "bad" sub-sensor has a higher average SQ, which results from the coincidental combination of sub-sensor. Differences in the tested gases and gas concentrations prevent a direct comparison of classification performance with other eNose systems.

Power Consumption According to Equation 6.1, the total power loss of a ChemFET is estimated to be in the range of 10 µW at reference conditions due to higher average I_{DS}. For the tested gases, the estimated power loss drops to the 1 µW range because of the lower average I_{DS}. In contrast, the power consumption of the UV-activated SnO_2-NW is dominated by the ultraviolet (UV)-light-emitting diode (LED), which is in the range of 50 mW [109]. Therefore, the ChemFET is more than three orders of magnitude more efficient than the UV-activated chemiresistive eNose, which in turn is already

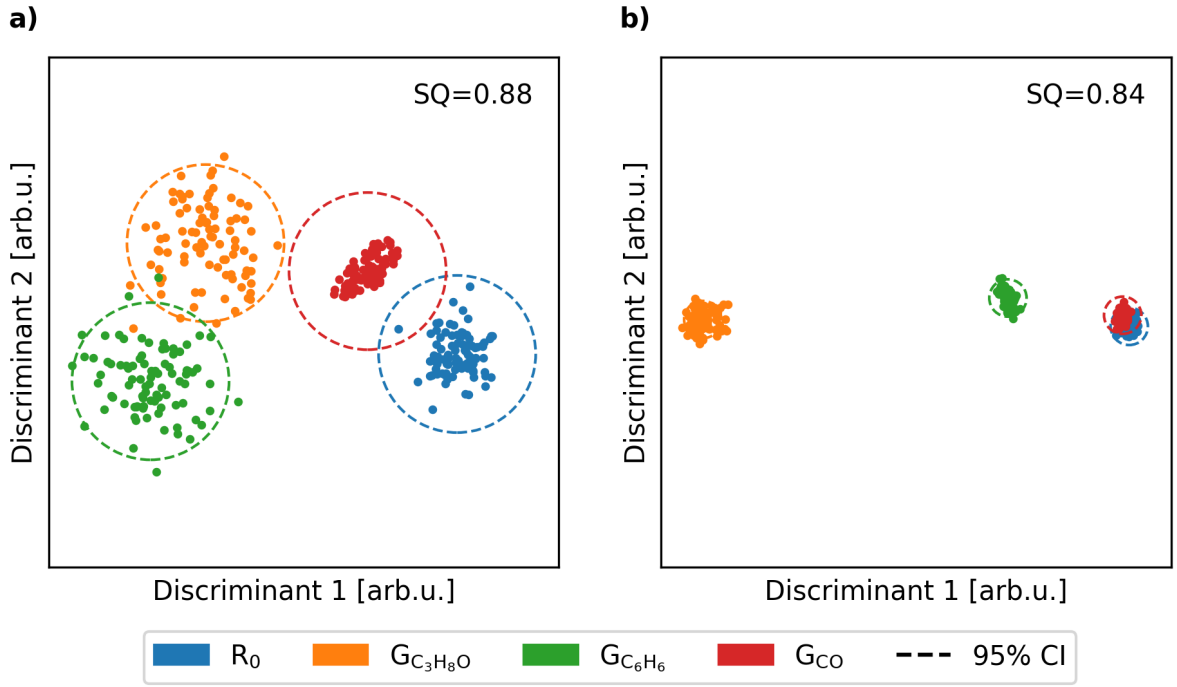

Figure 6.19: LDA plots for the chemiresistive sensor using only two sub-sensor. a) Only using the two least impactful sub-sensor. b) Only using the two most impactful sub-sensor. The corresponding average separation quotient (SQ) is listed in the top-right corner.

over two orders of magnitude more efficient compared to the heated Karlsruher Mikronase (KAMINA) (4.5 W to 9.0 W) [109].

6.4. Summary

In this chapter, an eNose sensor based on a single ChemFET was successfully fabricated through a hybrid digital printing process in which a several-nanometer-thick semiconducting In_2O_3 channel layer was IJ printed. In contrast, the micrometer-thick top electrodes were AJ printed. The ChemFET was exposed to IPA, benzene, and carbon monoxide while being operated at room temperature without any external stimuli such as heating or UV irradiation.

Its response towards IPA and benzene is exceptionally high, with a relative response of ≈ 200. For classification measurements, the drain-source current (I_{DS}) was recorded at different gate-source (U_{GS}) and drain-source (U_{DS}) voltages, yielding a total of 180 features per observation. Subsequently, the machine learning algorithms, LDA and RF, were repeatedly trained and tested using LOOCV. The test results reveal that both models can accurately classify reference air and carbon monoxide without misclassification. However, the classification capability to distinguish IPA and benzene is limited for LDA, resulting in a moderate overall F1-score of 0.82. In contrast, RF achieves higher PRC and REC, particularly for benzene, leading to an improved overall F1-score of 0.92. A dedicated feature-importance analysis reveals a strong correlation with U_{GS} above the threshold (U_{th}). By removing low-importance features, the F1-score can be further increased to 0.94 (RF).

A final comparison between the chemiresistive SnO_2-NW, the ChemFET, and past literature reports reveals that the ChemFET in this chapter exhibits outstanding sensitivity, particularly towards IPA and benzene. But the multi-sub-sensors chemiresistive eNose from the previous chapter still performs better on classification tasks than the single-sensor ChemFET. The power consumption of the ChemFET is estimated to be at least three orders of magnitude lower than that of UV and high-temperature chemiresistors.

Overall, the ChemFET eNose demonstrates exceptional sensitivity and ultra-low power consumption, achieving remarkable classification performance, given that it uses only a single sensor rather than multi-sub-sensor configurations.

7. Conclusion and Outlook

7.1. Conclusion

Drawing inspiration from the biological olfactory system and addressing the growing demand for reliable, accurate, and efficient odor sensing, this doctoral thesis advances chemiresistive and ChemFET-based eNose technologies through innovations in nanomaterial synthesis, digital printing, and machine learning.

Relative humidity is a key environmental variable that strongly affects the sensing behavior of many gas and eNose sensors, including those developed in this work. Therefore, to adequately monitor relative humidity, a V_2O_5-nanofiber (NF)-based relative humidity sensor was developed in Chapter 4. The electrospun NF were thermally annealed and characterized at different temperatures. Subsequently, the optimal annealing temperature is determined to be 500 °C. At this annealing temperature, the humidity sensor using V_2O_5 NFs, exhibits a linear calibration curve within a wide sensing range between 10 RH% to 90 RH%, fast response and recovery time, and exceptionally high sensitivity of 1.427, which outperforms other reported cases using chemiresistive V_2O_5 nanomaterials. Moreover, the sensor operates efficiently at RT without external excitation, such as heating or UV irradiation. Conversely, the sensor exhibits high selectivity for humidity while showing minimal response to the target gases IPA, benzene, and carbon monoxide. Despite the strictly laboratory setting with controlled relative humidity in this work, the findings in this chapter strongly support the deployment of electrospun V_2O_5 NF alongside gas and eNose sensors for humidity-independent sensing in field applications. In a rudimentary first step, this can be achieved by simply adding the relative humidity (RH) signal as an additional feature column to the dataset.

Next in Chapter 5, a chemiresistive SnO_2 NWs-based eNose has been developed. Here, the SnO_2 NWs were VLS-grown with optimized substrate positioning and showed higher sensitivity to IPA than to the other tested gases. The chemiresistive eNose, in combination with LDA, can clearly distinguish among gases, with minimal to no misclassification errors. To capitalize on the eNose's good classification performance, it was applied to indoor mold detection and identification of two common indoor mold species, *Stachybotrys chartarum* (*S. chartarum*) and *Chaetomium globosum* (*C. globosum*). Additionally, each mold species was grown on two different agar-based media to simulate different environments. It is shown that systematic data-partitioning strategies are required to improve LDA performance for reliable classification. However, the highest classification performance (F1 $\approx$ 0.986) is achieved using a novel LDA ensemble. In conclusion, the SnO_2 NW-based eNose, combined with an optimized LDA algorithm, demonstrates excellent gas discrimination and highly reliable mold detection and identification, achieving near-perfect classification performance for both applications.

Finally, in Chapter 6, the sensor technology advances to ChemFETs. The ChemFET was fabricated by combining IJP and AJP, exploiting their complementary advantages to print components with distinct requirements, such as a nanometer-thick In_2O_3 channel and micrometer-thick electrodes. By systematic gate-source and drain-source voltage modulation, a single RT-operated ChemFET without UV activation can generate a sufficient number of features to classify the target gases. However, a basic LDA algorithm struggles to distinguish between IPA and benzene reliably. In contrast, a hyperparameter-optimized RF model achieves considerably higher classification metrics (F1 $\approx$ 0.92). An in-depth analysis reveals a strong correlation between feature importance and gate-source voltage in the on-state of the ChemFET. This result suggests that a considerable number of operation points may be omitted without negatively affecting the classification performance of the ChemFET-based eNose.

A detailed comparison of the two eNose systems – SnO_2 NW chemiresistor and In_2O_3 TF ChemFET – highlights the advantages and drawbacks of both technologies. The ChemFET exhibits remarkable sensitivity, not only vastly outperforming other ChemFET but also competing with, and in some cases surpassing, high-temperature-operated sensors. However, in terms of classification performance, the chemiresistive SnO_2 NW-based eNose using multiple sub-sensor remains superior. The high power-efficiency of these two RT-operated sensors, due to the lack of heating, comes at the cost of mediocre response and recovery times, resulting from reduced gas-interaction dynamics, which is expected for RT-operated sensors.

Taken together, this thesis establishes a versatile toolbox of advanced fabrication and synthesis methods, complementary sensor technologies, and tailored machine learning pipelines that jointly enable high-performing, robust, and application-oriented machine olfactory sensing.

7.2. Outlook

Blending of Sensor Technologies and Functional Materials The integration and blending of diverse sensor transduction mechanisms, different materials, and material morphologies are logical next steps. As separately explored across this thesis, each combination has its own advantages which can be systematically exploited in an integrated solution. It is noted that this integration is not expected to increase the average sensitivity to specific analytes but should instead increase the diversity of sub-sensor sensing characteristics, thereby improving classification performance. Especially, a boost in classification performance in field applications is expected if humidity can be measured independently, as in the case of the V_2O_5 NF sensor. Additionally, efficient and effective data analysis for maximal information extraction when combining data from different domains remains an interesting

In-Field Applicable Devices and Systems As noted above, a mobile, cost-effective, in-field-applicable device is desired, such as for mold detection. Similar systems are commercially available but remain very expensive, such as the Portable Electronic Nose (PEN) system ($\approx$ 83 000 \$, AIRSENSE Analytics GmbH, Germany) [223]. In addition to the eNose sensor chip, the complete readout and evaluation must be developed. Moreover, a pneumatic sniffing mechanism must be developed and fabricated. It must be able to draw in gaseous analyte samples and direct the sample to the eNose sensor. At the same time,

the system is expected to include a reference gas or reference air generator for baseline measurements. Extensive testing must be performed to validate device accuracy and reliability. Meanwhile, the need for and frequency of recalibrations will significantly impact the system's commercial feasibility.

Automated Material Screening One of the most promising directions for advancing nearly all eNose and gas-sensing technologies is the exploration of novel sensing materials to identify materials with higher sensitivity, higher selectivity, or other advantageous properties. Manually selecting and testing different materials and material combinations is a never-ending, time-consuming task that does not guarantee success. Therefore, an automated material screening system that can continuously test different materials and material combinations is not only desirable but also obligatory to compete in an era of an ever-increasing number of new materials and possibilities. Additionally, instead of random material selection, a machine learning-based approach can save significant time and costs in the long run by systematically selecting test samples while balancing exploration and exploitation.

A. Appendix

A.1. Figures

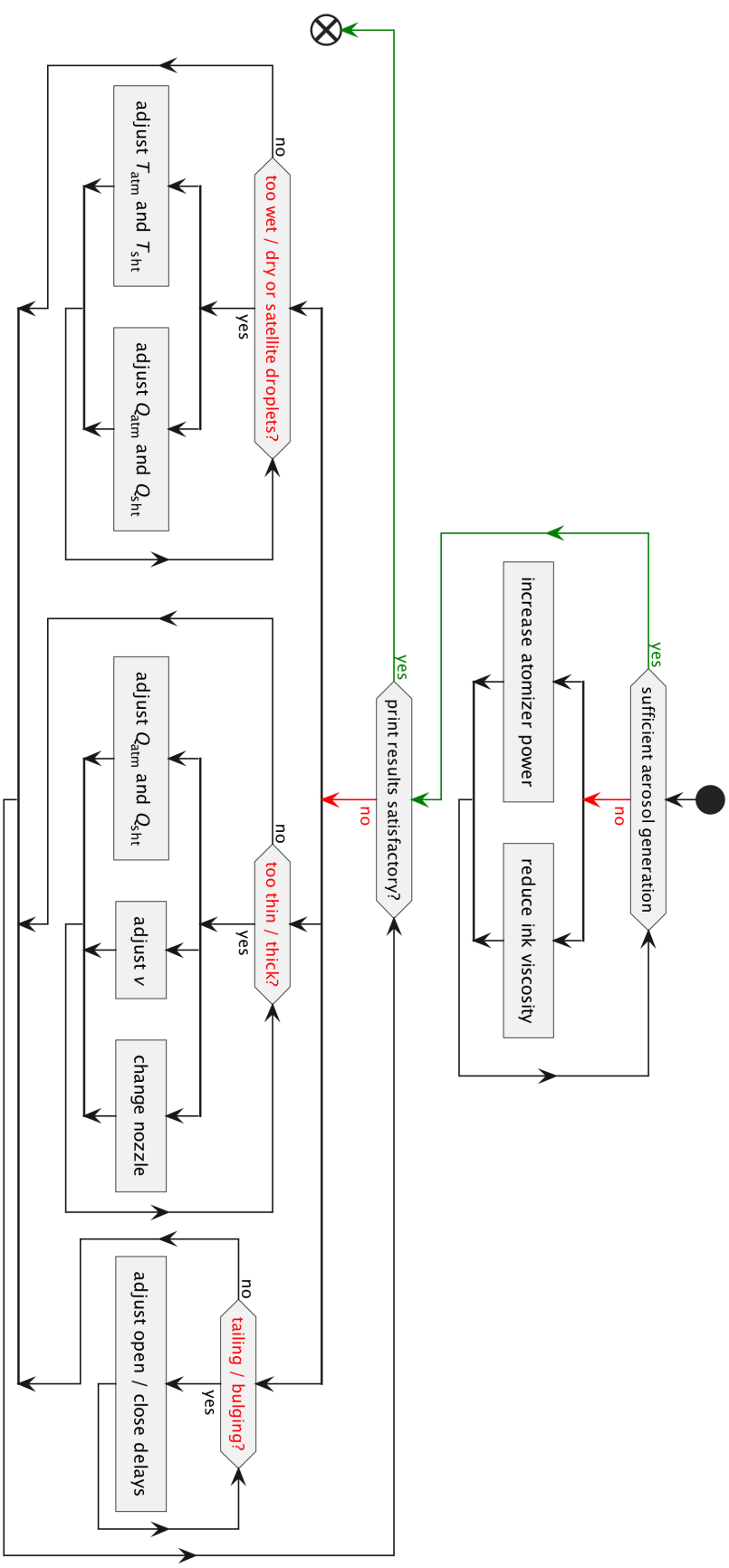

Figure A1: AJP optimization flow chart. First, sufficient printable aerosols need to be generated. Thereafter, individual issues are resolved by adjusting various process parameters.

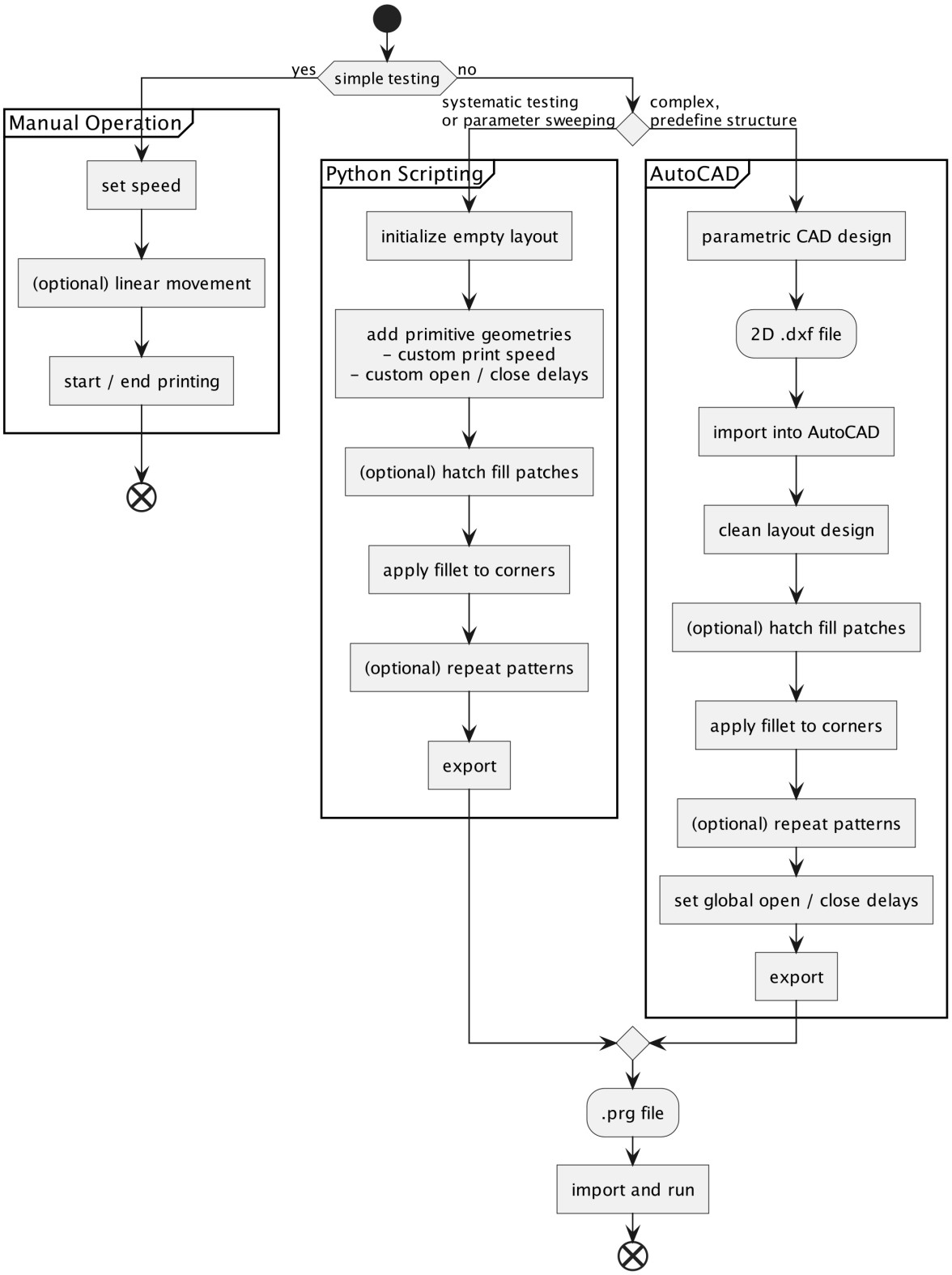

Figure A2: Decision and workflow for AJ printer operation. Depending on the operation's complexity, the AJ printer can either be manually operated or automatically operated using a prg script file.

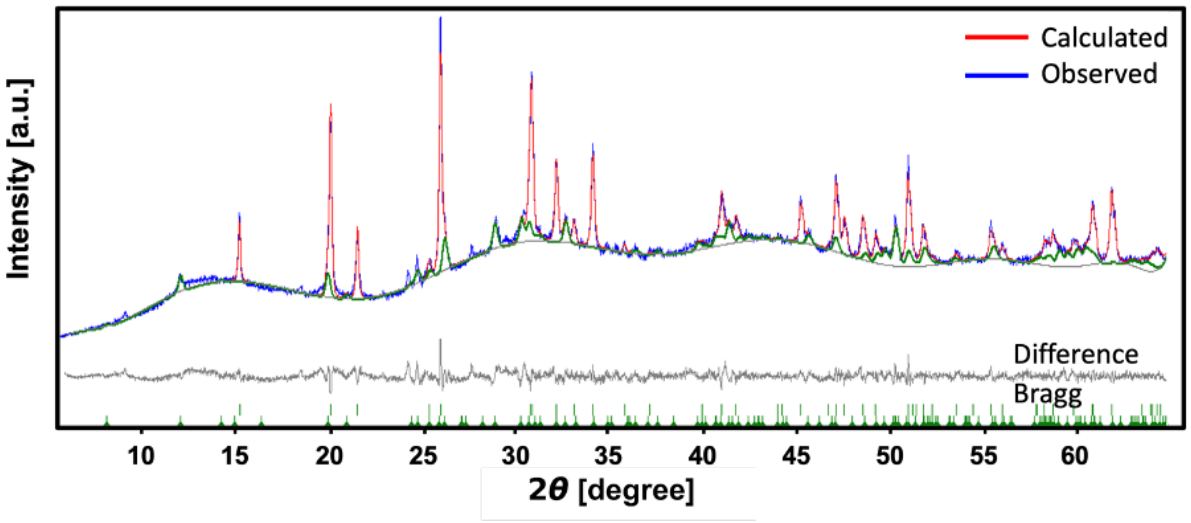

Figure A3: Examplanary Rietveld refinement of XRD patterns for V_2O_5 NFs. This sample was annealed at $T_{anl} = 500\,^{\circ}C$. Reprinted from [1] under CC BY 4.0.

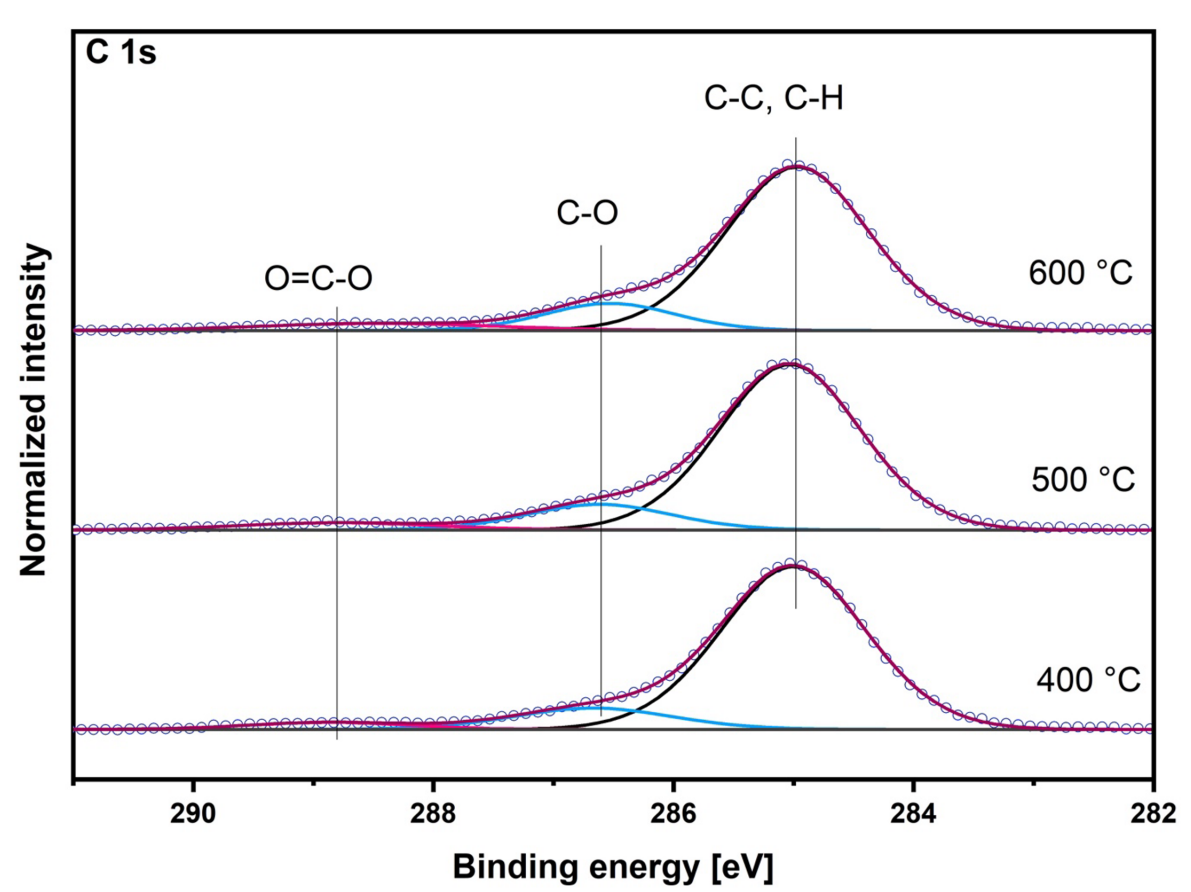

Figure A4: Normalized C1s core level X-ray photoelectron spectroscopy (XPS) spectra of V_2O_5 NFs. The samples were annealed at 400 °C, 500 °C and 600 °C. Reprinted from [1] under CC BY 4.0.

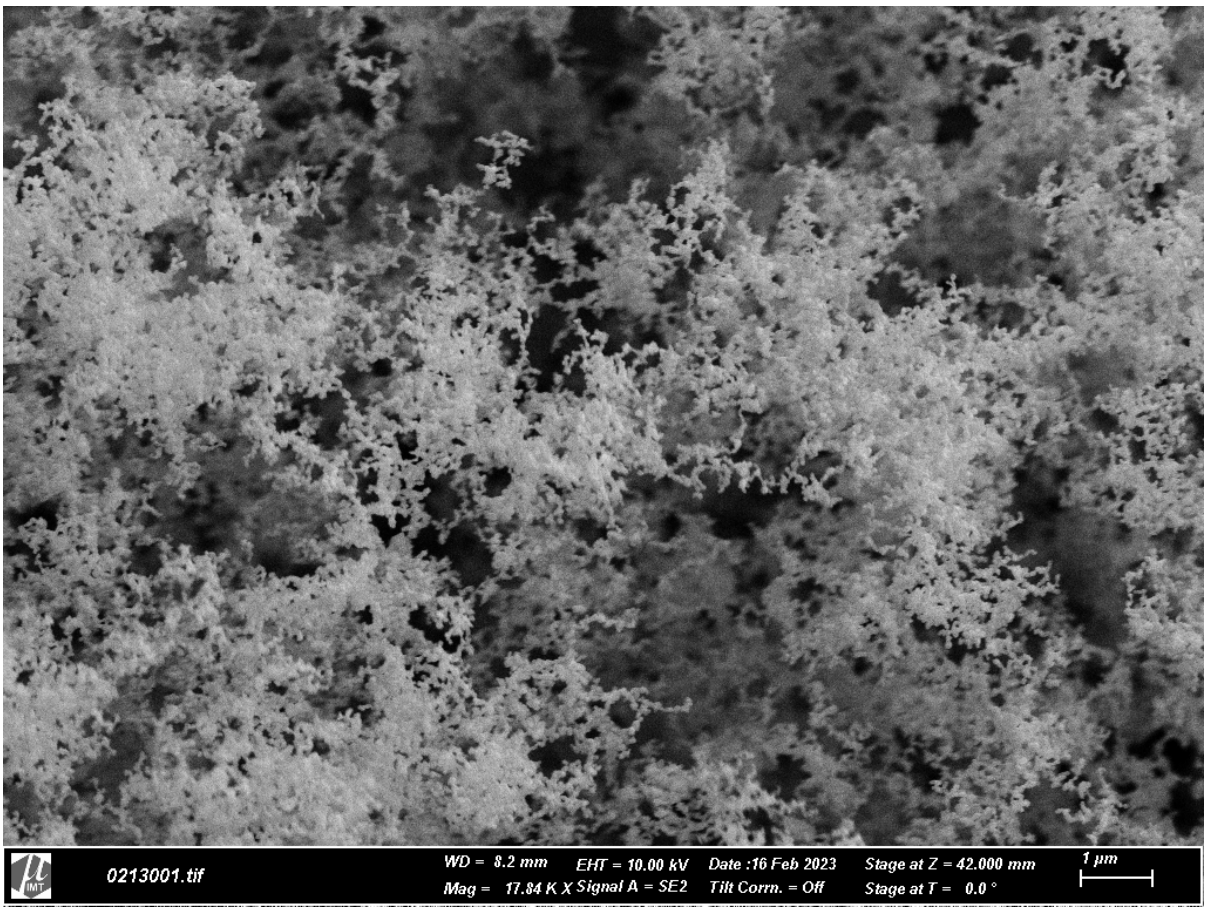

Figure A5: SEM image of VLS-grown materials at the inside-boat position. Particle-like structures are observed on substrates placed inside the ceramic boats

Figure A6: Dewetting of Au thin film with insufficient SnO_2 NW growth. This is caused by a large source-to-target distance. Data collected from [7].

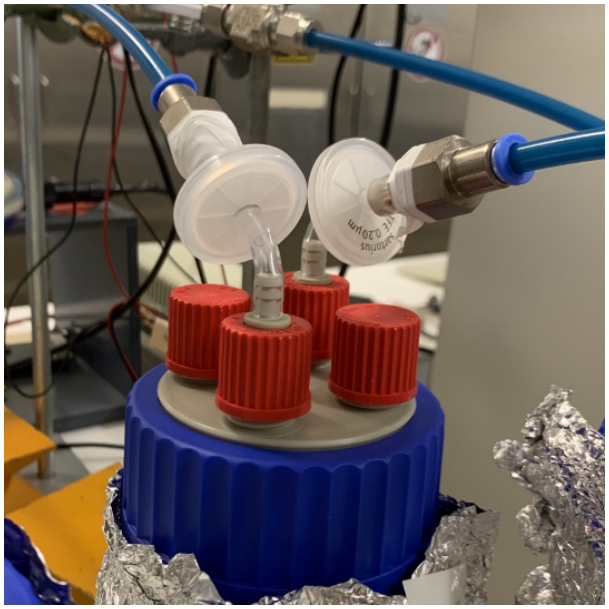

Figure A7: Cap and filters on top of the sample bottles. PTFE membrane filters with 0.2 µm pore size are used.

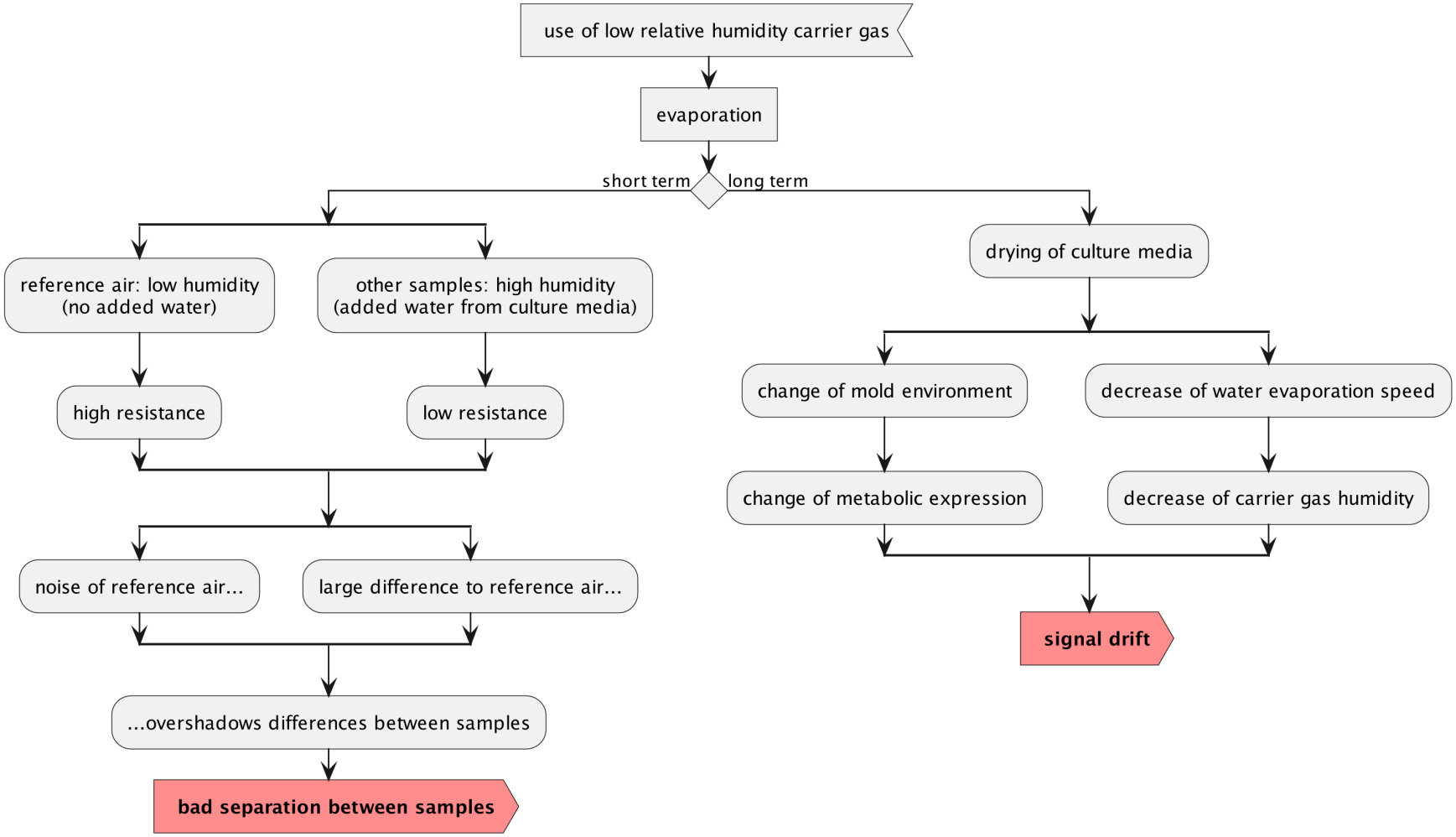

Figure A8: Impact of using low relative humidity carrier gas. In the short term, a low humidity leads to bad separation between different mold and culture media samples. In the long term, this causes signal drift.

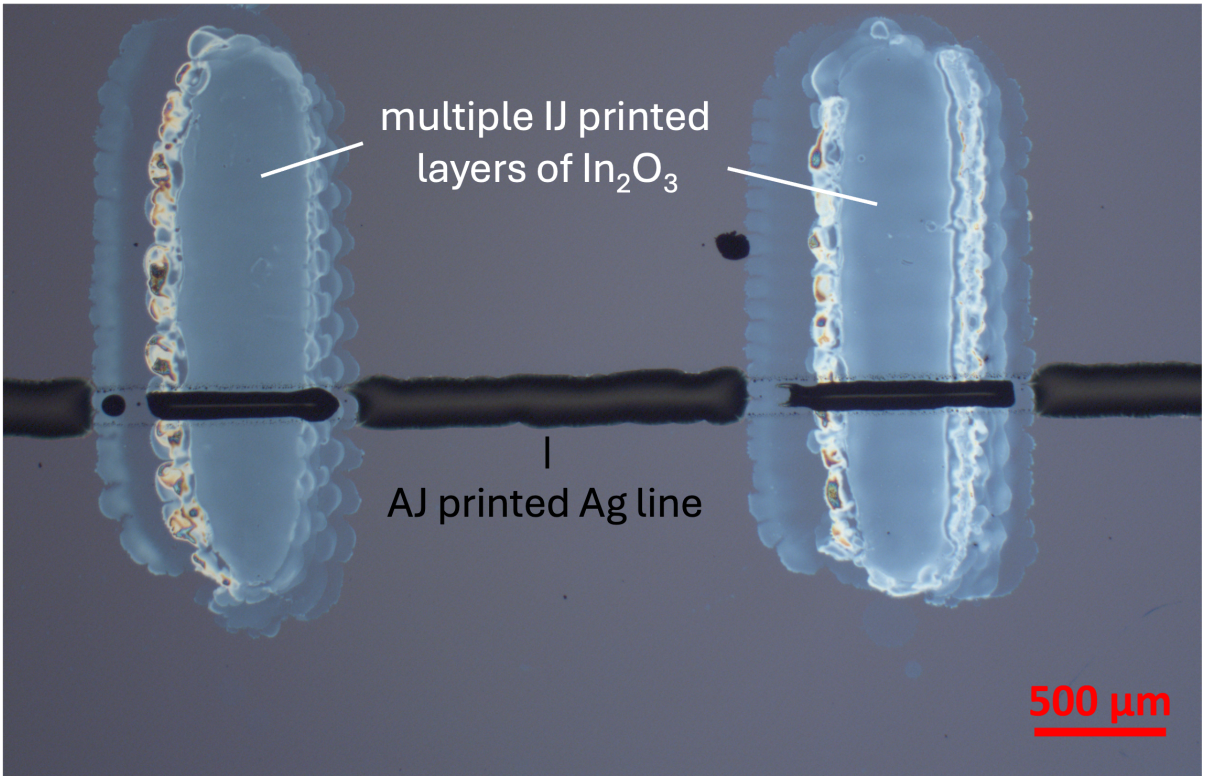

Figure A9: Interruption of Ag lines when AJ printed on In_2O_3 patches. Compared to SiO_2 background, the IJ printed In_2O_3 patches are hydrophobic, resulting in asymmetric ink flow post-printing.

A.2. Tables

Table A1: Rietveld Analysis Fitting Parameters.

T [°C]	GoF[a]	R_{exp}	R_{wp}	R_p	wDW[b]
400	1.93	1.99	3.84	2.91	0.69
500	3.02	2.05	6.18	3.86	0.49
600	2.85	2.12	6.03	4.45	0.49

[a] Goodness of fit
[b] weighted Durbin Watson

Table A2: Average hyperparameters of RF models from the initial LOOCV.

Hyperparameter	Variable name	Mean value
number of trees	`n_estimators`	500
maximum tree depth	`max_depth`	28
min. req. sample node for splitting	`min_samples_split`	5
min. req. samples per leaf node	`min_samples_leaf`	1
max. number of leaf nodes	`max_leaf_nodes`	67

A.3. Equations, Theorems and Proofs

Theorem A1. *Given C classes, the number of possible combinations with at least two elements is $N_m = 2^C - C - 1$ without repetition and disregarding order.*

Proof. Using the binomial sum $\sum_{k=0}^{n} \binom{n}{k} = 2^n$, N_m can be derived according to:

$$\begin{aligned} N_m &= \sum_{k=2}^{C} \binom{C}{k} \\ &= \sum_{k=0}^{C} \binom{C}{k} - \binom{C}{1} - \binom{C}{0} \\ &= 2^C - C - 1 \end{aligned}$$

□

Theorem A2. *Given C classes, and N_m models according to Theorem A1, the number of models $N_{m,c}$ containing a specific class c eqals $2^{C-1} - 1$.*

Proof. First, it can be deduced that $N_{m,c}$ is constant and independent of c because all classes are equally distributed. Hence, the total number of class occurrences can be calculated by

- right-hand side (RHS): multiplying $N_{m,c}$ and C, or
- left-hand side (LHS): adding the number of classes for each model individually

$$N_{\mathrm{m},c} \cdot C = \sum_{k=2}^{C} \binom{C}{k} \cdot k$$

$N_{\mathrm{m},c}$ is derived by rearranging the equation and using the binomial sum.

$$\begin{aligned}
N_{\mathrm{m},c} &= \frac{\sum_{k=2}^{C} \left[\binom{C}{k} \cdot k \right]}{C} \\
&= \sum_{k=2}^{C} \left[\binom{C}{k} \cdot \frac{k}{C} \right] \\
&= \sum_{k=2}^{C} \left[\frac{C!}{k!(C-k)!} \cdot \frac{k}{C} \right] \\
&= \sum_{k=2}^{C} \left[\frac{(C-1)!}{(k-1)!(C-k)!} \right] \\
&= \sum_{k=2}^{C} \left[\frac{(C-1)!}{(k-1)!((C-1)-(k-1))!} \right] \\
&= \sum_{k=2}^{C} \binom{C-1}{k-1} \\
&= \sum_{k=1}^{C-1} \binom{C-1}{k} \\
&= \sum_{k=0}^{C-1} \binom{C-1}{k} - \binom{C}{0} \\
&= 2^{C-1} - 1
\end{aligned}$$

□

List of Figures

List of Tables

List of Publications

Peer-Reviewed Journal Publications (First Author)

[1] H. Yang, M. Islam, V. Trouillet, M. Sommer, J. G. Korvink, U. Lemmer, and B. Sharma, "Electrospun Vanadium Pentoxide (V2O5) Nanofibers for Enhanced Humidity Sensing", *Advanced Sensor Research*, vol. 4, no. 6, p. 2 500 040, Jun. 2025. DOI: 10.1002/adsr.202500040 Accessed: Dec. 8, 2025.

[2] H. Yang, M. Sommer, S. Bauer, and U. Lemmer, "Electronic Nose for Indoor Mold Detection and Identification", *Advanced Sensor Research*, e00124, Dec. 2025. DOI: 10.1002/adsr.202500124 Accessed: Dec. 29, 2025.

[3] H. Yang, M. Sommer, S. A. Singaraju, P. Arya, G. Cadilha Marques, J. Aghassi-Hagmann, and U. Lemmer, "Hybrid-Printed Single-ChemFET Electronic Nose Enabled by Machine Learning - Under Review", *Advanced Sensor Research*, 2026.

Supervised Student Theses

[4] T. Lu, "Schimmeldetektion mittels elektronischer Nase: eine Analyse des Einflusses verschiedener Wachstumsuntergründe", Bachelor Thesis, Karlsruher Institute of Technology (KIT), Karlsruhe, Germany, Nov. 2023.

[5] Y. Mao, "Optimization of Mechanical and Electrical Property for Printed Electrodes with Copper Nanoparticles", M.Sc. thesis, Karlsruher Institute of Technology (KIT), Karlsruhe, Germany, Jul. 2024.

[6] T. Krause, "Implementierung eines Neuronalen Netzwerks für die elektronische Nase", M.Sc. thesis, Karlsruher Institute of Technology (KIT), Karlsruhe, Germany, Nov. 2024.

[7] G. Liu, "Sensing Performance Analysis and Comparison of Different Chemiresistive Metal Oxide Nanostructures used for Electronic Noses", M.Sc. thesis, Karlsruher Institute of Technology (KIT), Karlsruhe, Germany, Apr. 2022.

References

[8] H. Liu, R. Wu, Q. Guo, Z. Hua, and Y. Wu, "Electronic Nose Based on Temperature Modulation of MOS Sensors for Recognition of Excessive Methanol in Liquors", *ACS Omega*, vol. 6, no. 45, pp. 30 598–30 606, Nov. 2021, ISSN: 2470-1343, 2470-1343. DOI: 10.1021/acsomega.1c04350 Accessed: Nov. 23, 2025.

[9] K. C. Hoover, "Smell with inspiration: The evolutionary significance of olfaction", *American Journal of Physical Anthropology*, vol. 143, no. S51, pp. 63–74, 2010, ISSN: 00029483. DOI: 10.1002/ajpa.21441 Accessed: Feb. 4, 2026.

[10] S. Boesveldt and V. Parma, "The importance of the olfactory system in human well-being, through nutrition and social behavior", *Cell and Tissue Research*, vol. 383, no. 1, pp. 559–567, Jan. 2021, ISSN: 0302-766X, 1432-0878. DOI: 10.1007/s00441-020-03367-7 Accessed: Feb. 4, 2026.

[11] S. M. A. Elkholi, M. K. Abdelwahab, and M. Abdelhafeez, "Impact of the smell loss on the quality of life and adopted coping strategies in COVID-19 patients", *European Archives of Oto-Rhino-Laryngology*, vol. 278, no. 9, pp. 3307–3314, Sep. 2021, ISSN: 0937-4477, 1434-4726. DOI: 10.1007/s00405-020-06575-7 Accessed: Feb. 4, 2026.

[12] L. E. DeGreeff and K. Peranich, "Canine olfactory detection of trained explosive and narcotic odors in mixtures using a Mixed Odor Delivery Device", *Forensic Science International*, vol. 329, p. 111 059, Dec. 2021, ISSN: 03790738. DOI: 10.1016/j.forsciint.2021.111059 Accessed: Feb. 4, 2026.

[13] T. Talou, A. Gaset, M. Delmas, M. Kulifaj, and C. Montant, "Dimethyl sulphide: The secret for black truffle hunting by animals?", *Mycological Research*, vol. 94, no. 2, pp. 277–278, Mar. 1990, ISSN: 09537562. DOI: 10.1016/S0953-7562(09)80630-8 Accessed: Feb. 4, 2026.

[14] J. Cheng, J. Sun, L. Shi, and C. Dai, "An effective method fusing electronic nose and fluorescence hyperspectral imaging for the detection of pork freshness", *Food Bioscience*, vol. 59, p. 103 880, Jun. 2024, ISSN: 22124292. DOI: 10.1016/j.fbio.2024.103880 Accessed: Jan. 12, 2026.

[15] M. Xu, X. Hu, H. Zhang, T. Miao, L. Ma, J. Liang, Y. Zhu, H. Zhu, Z. Cheng, and X. Sun, "Detection and Pattern Recognition of Chemical Warfare Agents by MOS-Based MEMS Gas Sensor Array", *Sensors*, vol. 25, no. 8, p. 2633, Apr. 2025, ISSN: 1424-8220. DOI: 10.3390/s25082633 Accessed: Feb. 4, 2026.

[16] A. Anyfantis and S. Blionas, "An Analysis on the Performance of a Mobile Platform with Gas Sensors for Real Time Victim Localization", *Sensors*, vol. 21, no. 6, p. 2018, Mar. 2021, ISSN: 1424-8220. DOI: 10.3390/s21062018 Accessed: Feb. 4, 2026.

[17] H. H. Ali, "Gas Chromatography: Principles, Medicine and Pharmaceutical, Energy, Fuel Applications and Environmental Analysis", *SAR Journal of Medical Biochemistry*, vol. 6, no. 04, p. 94, Aug. 2025, ISSN: 27077721, 27096882. DOI: 10.36346/sarjmb.2025.v06i04.005 Accessed: Feb. 4, 2026.

[18] H.-J. Hübschmann, *Handbook of GC-MS: Fundamentals and Applications*, 1st ed. Wiley, Jun. 2025, ISBN: 978-3-527-35403-0 978-3-527-84764-8. DOI: 10.1002/9783527847648 Accessed: Feb. 5, 2026.

[19] O. Gould, N. Drabińska, N. Ratcliffe, and B. De Lacy Costello, "Hyphenated Mass Spectrometry versus Real-Time Mass Spectrometry Techniques for the Detection of Volatile Compounds from the Human Body", *Molecules*, vol. 26, no. 23, p. 7185, Nov. 2021, ISSN: 1420-3049. DOI: 10.3390/molecules26237185 Accessed: Feb. 5, 2026.

[20] *E2M*, https://www.bruker.com/en/products-and-solutions/cbrne-detectors/gc-ms/e2m.html. Accessed: Feb. 5, 2026.

[21] J. W. Gardner and P. N. Bartlett, "A brief history of electronic noses", *Sensors and Actuators B: Chemical*, vol. 18, no. 1-3, pp. 210–211, Mar. 1994, ISSN: 09254005. DOI: 10.1016/0925-4005(94)87085-3 Accessed: Feb. 5, 2026.

[22] A. B. Fialkov, A. Gordin, and A. Amirav, "Extending the range of compounds amenable for gas chromatography–mass spectrometric analysis", *Journal of Chromatography A*, vol. 991, no. 2, pp. 217–240, Apr. 2003, ISSN: 00219673. DOI: 10.1016/S0021-9673(03)00247-4 Accessed: Feb. 5, 2026.

[23] L. Cheng, Q.-H. Meng, A. J. Lilienthal, and P.-F. Qi, "Development of compact electronic noses: A review", *Measurement Science and Technology*, vol. 32, no. 6, p. 062 002, Jun. 2021, ISSN: 0957-0233, 1361-6501. DOI: 10.1088/1361-6501/abef3b Accessed: Jan. 12, 2022.

[24] Z. Zhai, Y. Liu, C. Li, D. Wang, and H. Wu, "Electronic Noses: From Gas-Sensitive Components and Practical Applications to Data Processing", *Sensors*, vol. 24, no. 15, p. 4806, Jul. 2024, ISSN: 1424-8220. DOI: 10.3390/s24154806 Accessed: Feb. 5, 2026.

[25] A. Mujahid and F. Dickert, "Surface Acoustic Wave (SAW) for Chemical Sensing Applications of Recognition Layers", *Sensors*, vol. 17, no. 12, p. 2716, Nov. 2017, ISSN: 1424-8220. DOI: 10.3390/s17122716 Accessed: Jan. 12, 2026.

[26] T. Julian, S. N. Hidayat, A. Rianjanu, A. B. Dharmawan, H. S. Wasisto, and K. Triyana, "Intelligent Mobile Electronic Nose System Comprising a Hybrid Polymer-Functionalized Quartz Crystal Microbalance Sensor Array", *ACS Omega*, vol. 5, no. 45, pp. 29 492–29 503, Nov. 2020, ISSN: 2470-1343, 2470-1343. DOI: 10.1021/acsomega.0c04433 Accessed: Jan. 15, 2025.

[27] V. Shah, J. Bhaliya, G. M. Patel, and P. Joshi, "Room-Temperature Chemiresistive Gas Sensing of SnO2 Nanowires: A Review", *Journal of Inorganic and Organometallic Polymers and Materials*, vol. 32, no. 3, pp. 741–772, Mar. 2022, ISSN: 1574-1443, 1574-1451. DOI: 10.1007/s10904-021-02198-5 Accessed: Oct. 28, 2025.

[28] M. Agarwal, M. D. Balachandran, S. Shrestha, and K. Varahramyan, "SnO2 Nanoparticle-Based Passive Capacitive Sensor for Ethylene Detection", *Journal of Nanomaterials*, vol. 2012, pp. 1–5, 2012, ISSN: 1687-4110, 1687-4129. DOI: 10.1155/2012/145406 Accessed: Jan. 12, 2022.

[29] A. Kaiser, E. T. Ceja, F. Huber, U. Herr, and K. Thonke, "Highly Sensitive H2S Sensing with Gold and Platinum Surface-Modified ZnO Nanowire ChemFETs", in *The 1st International Electronic Conference on Biosensors*, MDPI, Nov. 2020, p. 7. DOI: 10.3390/IECB2020-07070 Accessed: Jan. 15, 2026.

[30] T.-I. Jeong, T. M. Nguyen, E. Choi, A. Gliserin, T. M. T. Nguyen, S. Kim, S. Kim, H. Kim, G.-H. Bak, N.-Y. Kim, V. Devaraj, E. Choi, J.-W. Oh, and S. Kim, "Multichannel Hierarchical Analysis of Time-Resolved Hyperspectral Data for Advanced Colorimetric E-Nose", *ACS Sensors*, vol. 9, no. 6, pp. 2869–2876, Jun. 2024, ISSN: 2379-3694, 2379-3694. DOI: 10.1021/acssensors.3c02663 Accessed: Jan. 12, 2026.

[31] S. Esfahani, A. Tiele, S. O. Agbroko, and J. A. Covington, "Development of a Tuneable NDIR Optical Electronic Nose", *Sensors*, vol. 20, no. 23, p. 6875, Dec. 2020, ISSN: 1424-8220. DOI: 10.3390/s20236875 Accessed: Jan. 12, 2026.

[32] Q. Liu, H. Cai, Y. Xu, Y. Li, R. Li, and P. Wang, "Olfactory cell-based biosensor: A first step towards a neurochip of bioelectronic nose", *Biosensors and Bioelectronics*, vol. 22, no. 2, pp. 318–322, Aug. 2006, ISSN: 09565663. DOI: 10.1016/j.bios.2006.01.016 Accessed: Jan. 12, 2026.

[33] A. D. Wilson and M. Baietto, "Applications and Advances in Electronic-Nose Technologies", *Sensors*, vol. 9, no. 7, pp. 5099–5148, Jun. 2009, ISSN: 1424-8220. DOI: 10.3390/s90705099 Accessed: Jan. 12, 2026.

[34] T. Sanislav, G. D. Mois, S. Zeadally, S. Folea, T. C. Radoni, and E. A. Al-Suhaimi, "A Comprehensive Review on Sensor-Based Electronic Nose for Food Quality and Safety", *Sensors*, vol. 25, no. 14, p. 4437, Jul. 2025, ISSN: 1424-8220. DOI: 10.3390/s25144437 Accessed: Feb. 5, 2026.

[35] S.-Y. Jeong, J.-S. Kim, and J.-H. Lee, "Rational Design of Semiconductor-Based Chemiresistors and their Libraries for Next-Generation Artificial Olfaction", *Advanced Materials*, vol. 32, no. 51, p. 2 002 075, Dec. 2020, ISSN: 0935-9648, 1521-4095. DOI: 10.1002/adma.202002075 Accessed: Feb. 6, 2026.

[36] F. S. Fedorov, N. P. Simonenko, V. Trouillet, I. A. Volkov, I. A. Plugin, D. P. Rupasov, A. S. Mokrushin, I. A. Nagornov, T. L. Simonenko, I. S. Vlasov, E. P. Simonenko, V. G. Sevastyanov, N. T. Kuznetsov, A. S. Varezhnikov, M. Sommer, I. Kiselev, A. G. Nasibulin, and V. V. Sysoev, "Microplotter-Printed On-Chip Combinatorial Library of Ink-Derived Multiple Metal Oxides as an Electronic Olfaction Unit", *ACS Applied Materials & Interfaces*, vol. 12, no. 50, pp. 56 135–56 150, Dec. 2020, ISSN: 1944-8244, 1944-8252. DOI: 10.1021/acsami.0c14055 Accessed: Mar. 11, 2024.

[37] P. M. Bulemo, D.-H. Kim, H. Shin, H.-J. Cho, W.-T. Koo, S.-J. Choi, C. Park, J. Ahn, A. T. Güntner, R. M. Penner, and I.-D. Kim, "Selectivity in Chemiresistive Gas Sensors: Strategies and Challenges", *Chemical Reviews*, vol. 125, no. 8, pp. 4111–4183, Apr. 2025, ISSN: 0009-2665, 1520-6890. DOI: 10.1021/acs.chemrev.4c00592 Accessed: Jan. 12, 2026.

[38] M. Tonezzer, T. T. L. Dang, N. Bazzanella, V. H. Nguyen, and S. Iannotta, "Comparative gas-sensing performance of 1D and 2D ZnO nanostructures", *Sensors and Actuators B: Chemical*, vol. 220, pp. 1152–1160, Dec. 2015, ISSN: 09254005. DOI: 10.1016/j.snb.2015.06.103 Accessed: Feb. 6, 2026.

[39] P. Zhang, Y. Xiao, J. Zhang, B. Liu, X. Ma, and Y. Wang, "Highly sensitive gas sensing platforms based on field effect Transistor-A review", *Analytica Chimica Acta*, vol. 1172, p. 338 575, Aug. 2021, ISSN: 00032670. DOI: 10.1016/j.aca.2021.338575 Accessed: Jan. 8, 2025.

[40] J. Zhang, L. Liu, Y. Yang, Q. Huang, D. Li, and D. Zeng, "A review on two-dimensional materials for chemiresistive- and FET-type gas sensors", *Physical Chemistry Chemical Physics*, vol. 23, no. 29, pp. 15 420–15 439, 2021, ISSN: 1463-9076, 1463-9084. DOI: 10.1039/D1CP01890F Accessed: Jan. 8, 2025.

[41] R. Henrion and G. Henrion, *Multivariate Datenanalyse*. Berlin, Heidelberg: Springer Berlin Heidelberg, 1995, ISBN: 978-3-642-57792-5. DOI: 10.1007/978-3-642-57792-5 Accessed: Jan. 17, 2025.

[42] G. G. Teixeira, L. G. Dias, N. Rodrigues, Í. M. Marx, A. C. Veloso, J. A. Pereira, and A. M. Peres, "Application of a lab-made electronic nose for extra virgin olive oils commercial classification according to the perceived fruitiness intensity", *Talanta*, vol. 226, p. 122 122, May 2021, ISSN: 00399140. DOI: 10.1016/j.talanta.2021.122122 Accessed: Jan. 15, 2025.

[43] Y. Tan, Y. Chen, Y. Zhao, M. Liu, Z. Wang, L. Du, C. Wu, and X. Xu, "Recent advances in signal processing algorithms for electronic noses", *Talanta*, vol. 283, p. 127 140, Feb. 2025, ISSN: 00399140. DOI: 10.1016/j.talanta.2024.127140 Accessed: Sep. 15, 2025.

[44] A. Jiarpinijnun, K. Osako, and U. Siripatrawan, "Visualization of volatomic profiles for early detection of fungal infection on storage Jasmine brown rice using electronic nose coupled with chemometrics", *Measurement*, vol. 157, p. 107 561, Jun. 2020, ISSN: 02632241. DOI: 10.1016/j.measurement.2020.107561 Accessed: Jan. 15, 2025.

[45] P. Peng, X. Zhao, X. Pan, and W. Ye, "Gas Classification Using Deep Convolutional Neural Networks", *Sensors*, vol. 18, no. 1, p. 157, Jan. 2018, ISSN: 1424-8220. DOI: 10.3390/s18010157 Accessed: Jan. 15, 2025.

[46] H. Ma, T. Wang, B. Li, W. Cao, M. Zeng, J. Yang, Y. Su, N. Hu, Z. Zhou, and Z. Yang, "A low-cost and efficient electronic nose system for quantification of multiple indoor air contaminants utilizing HC and PLSR", *Sensors and Actuators B: Chemical*, vol. 350, p. 130 768, Jan. 2022, ISSN: 09254005. DOI: 10.1016/j.snb.2021.130768 Accessed: Jan. 15, 2025.

[47] C. Fang, H.-Y. Li, L. Li, H.-Y. Su, J. Tang, X. Bai, and H. Liu, "Smart Electronic Nose Enabled by an All-Feature Olfactory Algorithm", *Advanced Intelligent Systems*, vol. 4, no. 7, p. 2 200 074, Jul. 2022, ISSN: 2640-4567, 2640-4567. DOI: 10.1002/aisy.202200074 Accessed: Jan. 15, 2025.

[48] J. Goschnick, "An electronic nose for intelligent consumer products based on a gas analytical gradient microarray", *Microelectronic Engineering*, vol. 57–58, pp. 693–704, Sep. 2001, ISSN: 01679317. DOI: 10.1016/S0167-9317(01)00553-6 Accessed: Mar. 3, 2026.

[49] C. Arnold, M. Harms, and J. Goschnick, "Air quality monitoring and fire detection with the Karlsruhe electronic micronose KAMINA", *IEEE Sensors Journal*, vol. 2, no. 3, pp. 179–188, Jun. 2002, ISSN: 1530-437X. DOI: 10.1109/JSEN.2002.800681 Accessed: Nov. 14, 2024.

[50] V. V. Sysoev, I. Kiselev, M. Frietsch, and J. Goschnick, "Temperature Gradient Effect on Gas Discrimination Power of a Metal-Oxide Thin-Film Sensor Microarray", *Sensors*, vol. 4, no. 4, pp. 37–46, May 2004, ISSN: 1424-8220. DOI: 10.3390/s40400037 Accessed: Nov. 14, 2024.

[51] J. Goschnick, I. Koronczi, M. Frietsch, and I. Kiselev, "Water pollution recognition with the electronic nose KAMINA", *Sensors and Actuators B: Chemical*, vol. 106, no. 1, pp. 182–186, Apr. 2005, ISSN: 09254005. DOI: 10.1016/j.snb.2004.05.055 Accessed: Nov. 14, 2024.

[52] C. Arnold, D. Haeringer, I. Kiselev, and J. Goschnick, "Sub-surface probe module equipped with the Karlsruhe Micronose KAMINA using a hierarchical LDA for the recognition of volatile soil pollutants", *Sensors and Actuators B: Chemical*, vol. 116, no. 1-2, pp. 90–94, Jul. 2006, ISSN: 09254005. DOI: 10.1016/j.snb.2005.12.068 Accessed: Nov. 14, 2024.

[53] J. Goschnick, V. Magapu, I. Kiselev, and I. Koronczi, "New normalization procedure to improve signal pattern discrimination power in case of different concentration dependencies of the gas sensors in an array", *Sensors and Actuators B: Chemical*, vol. 116, no. 1-2, pp. 85–89, Jul. 2006, ISSN: 09254005. DOI: 10.1016/j.snb.2005.12.067 Accessed: Mar. 3, 2026.

[54] V. V. Sysoev, J. Goschnick, T. Schneider, E. Strelcov, and A. Kolmakov, "A Gradient Microarray Electronic Nose Based on Percolating SnO2 Nanowire Sensing Elements", *Nano Letters*, vol. 7, no. 10, pp. 3182–3188, Oct. 2007, ISSN: 1530-6984, 1530-6992. DOI: 10.1021/nl071815+ Accessed: Mar. 3, 2026.

[55] D. Haeringer and J. Goschnick, "Characterization of smelling contaminations on textiles using a gradient microarray as an electronic nose", *Sensors and Actuators B: Chemical*, vol. 132, no. 2, pp. 644–649, Jun. 2008, ISSN: 09254005. DOI: 10.1016/j.snb.2008.01.068 Accessed: Mar. 3, 2026.

[56] V. Musatov, V. Sysoev, M. Sommer, and I. Kiselev, "Assessment of meat freshness with metal oxide sensor microarray electronic nose: A practical approach", *Sensors and Actuators B: Chemical*, vol. 144, no. 1, pp. 99–103, Jan. 2010, ISSN: 09254005. DOI: 10.1016/j.snb.2009.10.040 Accessed: Nov. 30, 2025.

[57] M. Adib, R. Eckstein, G. Hernandez-Sosa, M. Sommer, and U. Lemmer, "SnO2 Nanowire-Based Aerosol Jet Printed Electronic Nose as Fire Detector", *IEEE Sensors Journal*, vol. 18, no. 2, pp. 494–500, Jan. 2018, ISSN: 1530-437X, 1558-1748, 2379-9153. DOI: 10.1109/JSEN.2017.2777178 Accessed: Jan. 12, 2022.

[58] Z. Liang, F. Tian, S. Yang, C. Zhang, H. Sun, and T. Liu, "Study on Interference Suppression Algorithms for Electronic Noses: A Review", *Sensors*, vol. 18, no. 4, p. 1179, Apr. 2018, ISSN: 1424-8220. DOI: 10.3390/s18041179 Accessed: Feb. 5, 2026.

[59] Y. Wang and Y. Zhou, "Recent Progress on Anti-Humidity Strategies of Chemiresistive Gas Sensors", *Materials*, vol. 15, no. 24, p. 8728, Dec. 2022, ISSN: 1996-1944. DOI: 10.3390/ma15248728 Accessed: Feb. 6, 2026.

[60] V. Gold, Ed., *The IUPAC Compendium of Chemical Terminology: The Gold Book*, 4th ed. Research Triangle Park, NC: International Union of Pure and Applied Chemistry (IUPAC), 2019. DOI: 10.1351/goldbook Accessed: Mar. 11, 2025.

[61] H. Farahani, R. Wagiran, and M. Hamidon, "Humidity Sensors Principle, Mechanism, and Fabrication Technologies: A Comprehensive Review", *Sensors*, vol. 14, no. 5, pp. 7881–7939, Apr. 2014, ISSN: 1424-8220. DOI: 10.3390/s140507881 Accessed: Jan. 26, 2024.

[62] S. Firestein, "How the olfactory system makes sense of scents", *Nature*, vol. 413, no. 6852, pp. 211–218, Sep. 2001, ISSN: 0028-0836, 1476-4687. DOI: 10.1038/35093026 Accessed: Jan. 11, 2026.

[63] C. Bushdid, M. O. Magnasco, L. B. Vosshall, and A. Keller, "Humans Can Discriminate More than 1 Trillion Olfactory Stimuli", *Science*, vol. 343, no. 6177, pp. 1370–1372, Mar. 2014, ISSN: 0036-8075, 1095-9203. DOI: 10.1126/science.1249168 Accessed: Jan. 12, 2026.

[64] A. P. Horsfield, A. Haase, and L. Turin, "Molecular recognition in olfaction", *Advances in Physics: X*, vol. 2, no. 3, pp. 937–977, May 2017, ISSN: 2374-6149. DOI: 10.1080/23746149.2017.1378594 Accessed: Jan. 12, 2026.

[65] E. Block, "Molecular Basis of Mammalian Odor Discrimination: A Status Report", *Journal of Agricultural and Food Chemistry*, vol. 66, no. 51, pp. 13 346–13 366, Dec. 2018, ISSN: 0021-8561, 1520-5118. DOI: 10.1021/acs.jafc.8b04471 Accessed: Jan. 12, 2026.

[66] C. B. Billesbølle, C. A. De March, W. J. C. Van Der Velden, N. Ma, J. Tewari, C. L. Del Torrent, L. Li, B. Faust, N. Vaidehi, H. Matsunami, and A. Manglik, "Structural basis of odorant recognition by a human odorant receptor", *Nature*, vol. 615, no. 7953, pp. 742–749, Mar. 2023, ISSN: 0028-0836, 1476-4687. DOI: 10.1038/s41586-023-05798-y Accessed: Jan. 12, 2026.

[67] L. Zhaoping, "Olfactory object recognition, segmentation, adaptation, target seeking, and discrimination by the network of the olfactory bulb and cortex: Computational model and experimental data", *Current Opinion in Behavioral Sciences*, vol. 11, pp. 30–39, Oct. 2016, ISSN: 23521546. DOI: 10.1016/j.cobeha.2016.03.009 Accessed: Jan. 12, 2026.

[68] S. Kuroda, Y. Nakaya-Kishi, K. Tatematsu, and S. Hinuma, "Human Olfactory Receptor Sensor for Odor Reconstitution", *Sensors*, vol. 23, no. 13, p. 6164, Jul. 2023, ISSN: 1424-8220. DOI: 10.3390/s23136164 Accessed: Jan. 11, 2026.

[69] L. Liu, Y. Wang, Y. Liu, S. Wang, T. Li, S. Feng, S. Qin, and T. Zhang, "Heteronanostructural metal oxide-based gas microsensors", *Microsystems & Nanoengineering*, vol. 8, no. 1, p. 85, Jul. 2022, ISSN: 2055-7434. DOI: 10.1038/s41378-022-00410-1 Accessed: Feb. 6, 2026.

[70] Y. Zhou, *Semiconducting Metal Oxide Thin-Film Transistors*. IOP Publishing Ltd, 2021, ISBN: 978-0-7503-2556-1. DOI: 10.1088/978-0-7503-2556-1 Accessed: Aug. 19, 2025.

[71] S. Dadhich, A. D. D. Dwivedi, and A. K. Singh, "Fabrication, characterization, numerical simulation and compact modeling of P3HT based organic thin film transistors", *Journal of Semiconductors*, vol. 42, no. 7, p. 074 102, Jul. 2021, ISSN: 1674-4926, 2058-6140. DOI: 10.1088/1674-4926/42/7/074102 Accessed: Jan. 13, 2026.

[72] J. Janata, "Chemically Sensitive Field-Effect Transistors, Past, Present and Future", *ChemElectroChem*, vol. 9, no. 23, e202200784, Dec. 2022, ISSN: 2196-0216, 2196-0216. DOI: 10.1002/celc.202200784 Accessed: Jan. 8, 2025.

[73] A. K. Sharma and A. Mahajan, "Potential applications of chemiresistive gas sensors", in *Carbon Nanomaterials and Their Nanocomposite-Based Chemiresistive Gas Sensors*, Elsevier, 2023, pp. 223–245, ISBN: 978-0-12-822837-1. DOI: 10.1016/B978-0-12-822837-1.00002-2 Accessed: Jan. 16, 2026.

[74] S. Sundararajan, *Multivariate Analysis and Machine Learning Techniques: Feature Analysis in Data Science Using Python* (Transactions on Computer Systems and Networks). Singapore: Springer Nature Singapore, 2025, ISBN: 978-981-99-0352-8 978-981-99-0353-5. DOI: 10.1007/978-981-99-0353-5 Accessed: Dec. 9, 2025.

[75] P. Kumar, R. Bhatnagar, K. Gaur, and A. Bhatnagar, "Classification of Imbalanced Data:Review of Methods and Applications", *IOP Conference Series: Materials Science and Engineering*, vol. 1099, no. 1, p. 012 077, Mar. 2021, ISSN: 1757-8981, 1757-899X. DOI: 10.1088/1757-899X/1099/1/012077 Accessed: Feb. 8, 2024.

[76] A. Amin, S. Anwar, A. Adnan, M. Nawaz, N. Howard, J. Qadir, A. Hawalah, and A. Hussain, "Comparing Oversampling Techniques to Handle the Class Imbalance Problem: A Customer Churn Prediction Case Study", *IEEE Access*, vol. 4, pp. 7940–7957, 2016, ISSN: 2169-3536. DOI: 10.1109/ACCESS.2016.2619719 Accessed: Feb. 8, 2024.

[77] S. Hu, Y. Liang, L. Ma, and Y. He, "MSMOTE: Improving Classification Performance When Training Data is Imbalanced", in *2009 Second International Workshop on Computer Science and Engineering*, Qingdao, China: IEEE, 2009, pp. 13–17, ISBN: 978-1-4244-5285-9. DOI: 10.1109/WCSE.2009.756 Accessed: Feb. 8, 2024.

[78] T. Hastie, R. Tibshirani, and J. Friedman, *The Elements of Statistical Learning* (Springer Series in Statistics). New York, NY: Springer New York, 2009, ISBN: 978-0-387-84858-7. DOI: 10.1007/978-0-387-84858-7 Accessed: Dec. 9, 2025.

[79] S. Kaufman, S. Rosset, and C. Perlich, "Leakage in data mining: Formulation, detection, and avoidance", in *Proceedings of the 17th ACM SIGKDD International Conference on Knowledge Discovery and Data Mining*, San Diego California USA: ACM, Aug. 2011, pp. 556–563, ISBN: 978-1-4503-0813-7. DOI: 10.1145/2020408.2020496 Accessed: Jan. 23, 2026.

[80] M. A. Pimentel, D. A. Clifton, L. Clifton, and L. Tarassenko, "A review of novelty detection", *Signal Processing*, vol. 99, pp. 215–249, Jun. 2014, ISSN: 01651684. DOI: 10.1016/j.sigpro.2013.12.026 Accessed: Jan. 24, 2026.

[81] H. Brink, J. W. Richards, M. Fetherolf, and B. Cronin, *Real-World Machine Learning*. Shelter Island: Manning, 2017, ISBN: 978-1-61729-192-0.

[82] M. Frye, J. Mohren, and R. H. Schmitt, "Benchmarking of Data Preprocessing Methods for Machine Learning-Applications in Production", *Procedia CIRP*, vol. 104, pp. 50–55, 2021, ISSN: 22128271. DOI: 10.1016/j.procir.2021.11.009 Accessed: Jan. 7, 2026.

[83] K. Backhaus, B. Erichson, S. Gensler, R. Weiber, and T. Weiber, *Multivariate Analysis: An Application-Oriented Introduction*. Wiesbaden: Springer Fachmedien Wiesbaden, 2025, ISBN: 978-3-658-47931-2. DOI: 10.1007/978-3-658-47931-2 Accessed: Dec. 9, 2025.

[84] R. A. Fisher, "THE USE OF MULTIPLE MEASUREMENTS IN TAXONOMIC PROBLEMS", *Annals of Eugenics*, vol. 7, no. 2, pp. 179–188, Sep. 1936, ISSN: 2050-1420, 2050-1439. DOI: 10.1111/j.1469-1809.1936.tb02137.x Accessed: Nov. 30, 2025.

[85] C.-D. Kohl and T. Wagner, Eds., *Gas Sensing Fundamentals* (Springer Series on Chemical Sensors and Biosensors). Berlin, Heidelberg: Springer Berlin Heidelberg, 2014, vol. 15, ISBN: 978-3-642-54519-1. DOI: 10.1007/978-3-642-54519-1 Accessed: Nov. 28, 2025.

[86] T. Liu, L. Guo, M. Wang, C. Su, D. Wang, H. Dong, J. Chen, and W. Wu, "Review on Algorithm Design in Electronic Noses: Challenges, Status, and Trends", *Intelligent Computing*, vol. 2, p. 0012, Jan. 2023, ISSN: 2771-5892. DOI: 10.34133/icomputing.0012 Accessed: Nov. 28, 2025.

[87] T. Li, S. Zhu, and M. Ogihara, "Using discriminant analysis for multi-class classification: An experimental investigation", *Knowledge and Information Systems*, vol. 10, no. 4, pp. 453–472, Oct. 2006, ISSN: 0219-1377, 0219-3116. DOI: 10.1007/s10115-006-0013-y Accessed: Oct. 28, 2025.

[88] J. Han, M. Kamber, and J. Pei, *Data Mining: Concepts and Techniques* (Morgan Kaufmann Series in Data Management Systems), 3rd ed. Amsterdam Boston: Elsevier/Morgan Kaufmann, 2012, ISBN: 978-0-12-381479-1.

[89] *ISO 80004-1:2023: Nanotechnologies — Vocabulary — Part 1: Core vocabulary*, Terminology, Geneva, Jul. 2023.

[90] J. Chen, Q. Zhao, B. Yu, and U. Lemmer, "A Review on Quantum Dot-Based Color Conversion Layers for Mini/Micro-LED Displays: Packaging, Light Management, and Pixelation", *Advanced Optical Materials*, vol. 12, no. 2, p. 2 300 873, Jan. 2024, ISSN: 2195-1071, 2195-1071. DOI: 10.1002/adom.202300873 Accessed: Jan. 10, 2026.

[91] C. Zhang, J. He, Y. Zhang, J. Chen, Y. Zhao, Y. Niu, and C. Yu, "Cerium dioxide-doped carboxyl fullerene as novel nanoprobe and catalyst in electrochemical biosensor for amperometric detection of the CYP2C19*2 allele in human serum", *Biosensors and Bioelectronics*, vol. 102, pp. 94–100, Apr. 2018, ISSN: 09565663. DOI: 10.1016/j.bios.2017.11.014 Accessed: Jan. 10, 2026.

[92] R. Huber, "Gedruckte Temperatursensor-Arrays mit hoher räumlicher Auflösung", Ph.D. dissertation, Karlsruher Institute of Technology (KIT), Karlsruhe, Germany, 2024. DOI: 10.5445/IR/1000169183

[93] H. Yu and Z. Tan, *Introduction to Electrospinning and Nanofiber* (Synthesis Lectures on Green Energy and Technology). Cham: Springer Nature Switzerland, 2025, ISBN: 978-3-031-74310-8. DOI: 10.1007/978-3-031-74310-8 Accessed: Jan. 9, 2026.

[94] M. Augustin, M. Sommer, and V. V. Sysoev, "UV–VIS sensor system based on SnO2 nanowires", *Sensors and Actuators A: Physical*, vol. 210, pp. 205–208, Apr. 2014, ISSN: 09244247. DOI: 10.1016/j.sna.2014.02.016 Accessed: Dec. 30, 2025.

[95] S. Das and V. Jayaraman, "SnO2: A comprehensive review on structures and gas sensors", *Progress in Materials Science*, vol. 66, pp. 112–255, Oct. 2014, ISSN: 00796425. DOI: 10.1016/j.pmatsci.2014.06.003 Accessed: Jan. 12, 2022.

[96] A. Jain, S. R. Manippady, R. Tang, H. Nishihara, K. Sobczak, V. Matejka, and M. Michalska, "Vanadium oxide nanorods as an electrode material for solid state supercapacitor", *Scientific Reports*, vol. 12, no. 1, p. 21 024, Dec. 2022, ISSN: 2045-2322. DOI: 10.1038/s41598-022-25707-z Accessed: Jan. 26, 2024.

[97] E.-K. Hong and W.-J. Cho, "Semiconducting single-walled carbon nanotube network-based double-gate thin-film transistors for high-performance aqueous chemical sensor applications", *AIP Advances*, vol. 8, no. 11, p. 115 312, Nov. 2018, ISSN: 2158-3226. DOI: 10.1063/1.5059376 Accessed: Jan. 10, 2025.

[98] P. Kurzweil, "CAPACITORS | Electrochemical Double-Layer Capacitors: Carbon Materials", in *Encyclopedia of Electrochemical Power Sources*, Elsevier, 2009, pp. 634–648, ISBN: 978-0-444-52745-5. DOI: 10.1016/B978-044452745-5.00352-X Accessed: Jan. 10, 2026.

[99] J. Y. Hwang, Y. Lee, G. H. Lee, S. Y. Lee, H.-S. Kim, S.-i. Kim, H. J. Park, S.-J. Kim, B. Z. Lee, M. S. Choi, C. Jin, and K. H. Lee, "Room-temperature ammonia gas sensing via Au nanoparticle-decorated TiO2 nanosheets", *Discover Nano*, vol. 18, no. 1, p. 47, Mar. 2023, ISSN: 2731-9229. DOI: 10.1186/s11671-023-03798-5 Accessed: Oct. 2, 2023.

[100] V. Srinivasan, A. Kathiravan, M. Kathiresan, G. Krishnan, and M. A. Jhonsi, "Facile synthesis of carbon nanocubes and its applications for sensing antibiotics", *Journal of Photochemistry and Photobiology A: Chemistry*, vol. 403, p. 112 855, Dec. 2020, ISSN: 10106030. DOI: 10.1016/j.jphotochem.2020.112855 Accessed: Jan. 10, 2026.

[101] G. Paramasivam, V. V. Palem, T. Sundaram, V. Sundaram, S. C. Kishore, and S. Bellucci, "Nanomaterials: Synthesis and Applications in Theranostics", *Nanomaterials*, vol. 11, no. 12, p. 3228, Nov. 2021, ISSN: 2079-4991. DOI: 10.3390/nano11123228 Accessed: Jan. 10, 2026.

[102] S. J. Lee, H. Jang, and D. N. Lee, "Recent advances in nanoflowers: Compositional and structural diversification for potential applications", *Nanoscale Advances*, vol. 5, no. 19, pp. 5165–5213, 2023, ISSN: 2516-0230. DOI: 10.1039/D3NA00163F Accessed: Jan. 10, 2026.

[103] Y. K. Mishra and R. Adelung, "ZnO tetrapod materials for functional applications", *Materials Today*, vol. 21, no. 6, pp. 631–651, Jul. 2018, ISSN: 13697021. DOI: 10.1016/j.mattod.2017.11.003 Accessed: Aug. 12, 2022.

[104] A. Zhang, G. Zheng, and C. M. Lieber, *Nanowires: Building Blocks for Nanoscience and Nanotechnology* (NanoScience and Technology). Cham: Springer International Publishing, 2016, ISBN: 978-3-319-41979-4 978-3-319-41981-7. DOI: 10.1007/978-3-319-41981-7 Accessed: Jan. 10, 2026.

[105] E. Brunet, T. Maier, G. Mutinati, S. Steinhauer, A. Köck, C. Gspan, and W. Grogger, "Comparison of the gas sensing performance of SnO2 thin film and SnO2 nanowire sensors", *Sensors and Actuators B: Chemical*, vol. 165, no. 1, pp. 110–118, Apr. 2012, ISSN: 09254005. DOI: 10.1016/j.snb.2012.02.025 Accessed: Jan. 12, 2022.

[106] G. I. Taylor, "Disintegration of water drops in an electric field", *Proceedings of the Royal Society of London. Series A. Mathematical and Physical Sciences*, vol. 280, no. 1382, pp. 383–397, Jul. 1964, ISSN: 0080-4630, 2053-9169. DOI: 10.1098/rspa.1964.0151 Accessed: Jan. 9, 2026.

[107] R. S. Wagner and W. C. Ellis, "VAPOR-LIQUID-SOLID MECHANISM OF SINGLE CRYSTAL GROWTH", *Applied Physics Letters*, vol. 4, no. 5, pp. 89–90, Mar. 1964, ISSN: 0003-6951, 1077-3118. DOI: 10.1063/1.1753975 Accessed: Jan. 25, 2026.

[108] M. Akbari, M. Joharifar, S. Kamaei, M. A. Mohajerzadeh, and S. Mohajerzadeh, "Modeling of spatial growth of SnO2 nanowires on silicon substrates by VLS technique", *Materials Research Express*, vol. 6, no. 9, p. 095 085, Jul. 2019, ISSN: 2053-1591. DOI: 10.1088/2053-1591/ab3250 Accessed: Nov. 14, 2024.

[109] M. Adib, "UV-excited SnO2 nanowire based electronic nose", Ph.D. dissertation, Karlsruher Institute of Technology (KIT), Karlsruhe, 2021.

[110] M. Nagano, "Growth of SnO2 whiskers by VLS mechanism", *Journal of Crystal Growth*, vol. 66, no. 2, pp. 377–379, Mar. 1984, ISSN: 00220248. DOI: 10.1016/0022-0248(84)90221-5 Accessed: Dec. 30, 2025.

[111] M. Adib and M. Sommer, "UV excited SnO2 nanowire based printed e-Nose: Potential application as burning smell detector and explosive detector", in *2016 IEEE SENSORS*, Orlando, FL, USA: IEEE, Oct. 2016, pp. 1–3, ISBN: 978-1-4799-8287-5. DOI: 10.1109/ICSENS.2016.7808805 Accessed: Feb. 7, 2026.

[112] V. V. Sysoev, A. V. Lashkov, A. Lipatov, I. A. Plugin, M. Bruns, D. Fuchs, A. S. Varezhnikov, M. Adib, M. Sommer, and A. Sinitskii, "UV-Light-Tunable p-/n-Type Chemiresistive Gas Sensors Based on Quasi-1D TiS3 Nanoribbons: Detection of Isopropanol at ppm Concentrations", *Sensors*, vol. 22, no. 24, p. 9815, Dec. 2022, ISSN: 1424-8220. DOI: 10.3390/s22249815 Accessed: Feb. 7, 2026.

[113] J. L. Mead, H. Xie, S. Wang, and H. Huang, "Enhanced adhesion of ZnO nanowires during in situ scanning electron microscope peeling", *Nanoscale*, vol. 10, no. 7, pp. 3410–3420, 2018, ISSN: 2040-3364, 2040-3372. DOI: 10.1039/C7NR09423J Accessed: Mar. 1, 2026.

[114] Z. Li, D. Wang, Q. Fu, S. Zhu, M. Pan, B. Li, P. Kang, and G. Wu, "The effect of SiC nanowires on the mechanical properties of carbon fiber reinforced aluminum matrix composites", *Composites Part A: Applied Science and Manufacturing*, vol. 200, p. 109 381, Jan. 2026, ISSN: 1359835X. DOI: 10.1016/j.compositesa.2025.109381 Accessed: Mar. 1, 2026.

[115] H. Wijshoff, "Structure- and fluid-dynamics in piezo inkjet printheads", Ph.D. dissertation, s.n.], [S.l., 2008.

[116] M. A. Shah, D.-G. Lee, B.-Y. Lee, and S. Hur, "Classifications and Applications of Inkjet Printing Technology: A Review", *IEEE Access*, vol. 9, pp. 140 079–140 102, 2021, ISSN: 2169-3536. DOI: 10.1109/ACCESS.2021.3119219 Accessed: Dec. 8, 2025.

[117] Q. Zhang, "Inkjet Printing of Bragg Mirrors and Microlens Arrays for Optical Systems", Ph.D. dissertation, Karlsruher Institute of Technology (KIT), Karlsruhe, Germany, 2024. DOI: 10.5445/IR/1000169751

[118] H. Wijshoff, "Manipulating Drop Formation in Piezo Acoustic Inkjet", *NIP & Digital Fabrication Conference*, vol. 22, no. 1, pp. 79–82, Jan. 2006, ISSN: 2169-4451. DOI: 10.2352/ISSN.2169-4451.2006.22.1.art00020_1 Accessed: Jan. 27, 2026.

[119] *Optomec Milestones*, https://optomec.com/milestones/. Accessed: Mar. 6, 2026.

[120] L. De Waele, M. Di Pietro, S. Perilli, E. Mantini, G. Trevisan, M. Simoncini, M. Panella, V. Betti, M. Laffranchi, and D. Mantini, "Aerosol Jet Printing for Neuroprosthetic Device Development", *Bioengineering*, vol. 12, no. 7, p. 707, Jun. 2025, ISSN: 2306-5354. DOI: 10.3390/bioengineering12070707 Accessed: Dec. 8, 2025.

[121] G. P. Gramlich, "Aerosol Jet and Ultra Precise Dispensing Printed Millimeter Wave Interconnects", Ph.D. dissertation, Karlsruher Institute of Technology (KIT), Karlsruhe, Germany, 2025. DOI: 10.5445/IR/1000185006

[122] E. B. Secor, "Principles of aerosol jet printing", *Flexible and Printed Electronics*, vol. 3, no. 3, p. 035 002, Sep. 2018, ISSN: 2058-8585. DOI: 10.1088/2058-8585/aace28 Accessed: Feb. 14, 2025.

[123] *Optomec Aerosol Jet 5x*, https://optomec.com/aj-5x/, Apr. 2025. Accessed: Dec. 4, 2025.

[124] K. Skarżyński, J. Krzemiński, M. Jakubowska, and M. Słoma, "Highly conductive electronics circuits from aerosol jet printed silver inks", *Scientific Reports*, vol. 11, no. 1, p. 18 141, Sep. 2021, ISSN: 2045-2322. DOI: 10.1038/s41598-021-97312-5 Accessed: Dec. 8, 2025.

[125] J. Q. Feng, "Mist flow visualization for round jets in Aerosol Jet printing", *Aerosol Science and Technology*, vol. 53, no. 1, pp. 45–52, Jan. 2019, ISSN: 0278-6826, 1521-7388. DOI: 10.1080/02786826.2018.1532566 Accessed: Dec. 8, 2025.

[126] M. Srbinovska, C. Gavrovski, V. Dimcev, A. Krkoleva, and V. Borozan, "Environmental parameters monitoring in precision agriculture using wireless sensor networks", *Journal of Cleaner Production*, vol. 88, pp. 297–307, Feb. 2015, ISSN: 09596526. DOI: 10.1016/j.jclepro.2014.04.036 Accessed: Jan. 26, 2024.

[127] Y.-T. Jao, P.-K. Yang, C.-M. Chiu, Y.-J. Lin, S.-W. Chen, D. Choi, and Z.-H. Lin, "A textile-based triboelectric nanogenerator with humidity-resistant output characteristic and its applications in self-powered healthcare sensors", *Nano Energy*, vol. 50, pp. 513–520, Aug. 2018, ISSN: 22112855. DOI: 10.1016/j.nanoen.2018.05.071 Accessed: Jan. 26, 2024.

[128] S. Gupta Chatterjee, S. Chatterjee, A. K. Ray, and A. K. Chakraborty, "Graphene–metal oxide nanohybrids for toxic gas sensor: A review", *Sensors and Actuators B: Chemical*, vol. 221, pp. 1170–1181, Dec. 2015, ISSN: 09254005. DOI: 10.1016/j.snb.2015.07.070 Accessed: Jan. 26, 2024.

[129] L. Yu, Q. Zheng, H. Wang, C. Liu, X. Huang, and Y. Xiao, "Double-Color Lanthanide Metal–Organic Framework Based Logic Device and Visual Ratiometric Fluorescence Water Microsensor for Solid Pharmaceuticals", *Analytical Chemistry*, vol. 92, no. 1, pp. 1402–1408, Jan. 2020, ISSN: 0003-2700, 1520-6882. DOI: 10.1021/acs.analchem.9b04575 Accessed: Jan. 26, 2024.

[130] F. Bibi, C. Guillaume, N. Gontard, and B. Sorli, "A review: RFID technology having sensing aptitudes for food industry and their contribution to tracking and monitoring of food products", *Trends in Food Science & Technology*, vol. 62, pp. 91–103, Apr. 2017, ISSN: 09242244. DOI: 10.1016/j.tifs.2017.01.013 Accessed: Jan. 26, 2024.

[131] V. Montes-García and P. Samorì, "Humidity Sensing with Supramolecular Nanostructures", *Advanced Materials*, p. 2 208 766, 2024, ISSN: 0935-9648, 1521-4095. DOI: 10.1002/adma.202208766 Accessed: Jan. 26, 2024.

[132] T. Blank, L. Eksperiandova, and K. Belikov, "Recent trends of ceramic humidity sensors development: A review", *Sensors and Actuators B: Chemical*, vol. 228, pp. 416–442, Jun. 2016, ISSN: 09254005. DOI: 10.1016/j.snb.2016.01.015 Accessed: Jan. 26, 2024.

[133] M. Jian, C. Wang, Q. Wang, H. Wang, K. Xia, Z. Yin, M. Zhang, X. Liang, and Y. Zhang, "Advanced carbon materials for flexible and wearable sensors", *Science China Materials*, vol. 60, no. 11, pp. 1026–1062, Nov. 2017, ISSN: 2095-8226, 2199-4501. DOI: 10.1007/s40843-017-9077-x Accessed: Jan. 26, 2024.

[134] J.-M. Tulliani, B. Inserra, and D. Ziegler, "Carbon-Based Materials for Humidity Sensing: A Short Review", *Micromachines*, vol. 10, no. 4, p. 232, Mar. 2019, ISSN: 2072-666X. DOI: 10.3390/mi10040232 Accessed: Jan. 26, 2024.

[135] U. Mogera, A. A. Sagade, S. J. George, and G. U. Kulkarni, "Ultrafast response humidity sensor using supramolecular nanofibre and its application in monitoring breath humidity and flow", *Scientific Reports*, vol. 4, no. 1, p. 4103, Feb. 2014, ISSN: 2045-2322. DOI: 10.1038/srep04103 Accessed: Mar. 12, 2025.

[136] B. Adhikari and S. Majumdar, "Polymers in sensor applications", *Progress in Polymer Science*, vol. 29, no. 7, pp. 699–766, Jul. 2004, ISSN: 00796700. DOI: 10.1016/j.progpolymsci.2004.03.002 Accessed: Jan. 26, 2024.

[137] J. Fang, Z.-H. Ma, J.-J. Xue, X. Chen, R.-P. Xiao, and J.-M. Song, "Au doped In2O3 nanoparticles: Preparation, and their ethanol detection with high performance", *Materials Science in Semiconductor Processing*, vol. 146, p. 106 701, Aug. 2022, ISSN: 13698001. DOI: 10.1016/j.mssp.2022.106701 Accessed: Oct. 2, 2023.

[138] K. Suematsu, N. Ma, M. Yuasa, T. Kida, and K. Shimanoe, "Surface-modification of SnO2 nanoparticles by incorporation of Al for the detection of combustible gases in a humid atmosphere", *RSC Advances*, vol. 5, no. 105, pp. 86 347–86 354, 2015, ISSN: 2046-2069. DOI: 10.1039/C5RA17556A Accessed: Jan. 26, 2024.

[139] D. Wang, S. Ding, S. Chen, D. Shan, C. Jiang, and X. Zhang, "Pd-modified SnO2 octahedrons for humidity-independent ethanol vapor gas sensing", *Journal of Alloys and Compounds*, vol. 1028, p. 180 635, May 2025, ISSN: 0925-8388. DOI: 10.1016/j.jallcom.2025.180635

[140] Z. Zhuang, L. Zhang, C. Huang, X. Wang, H. Guo, T. Thomas, F. Qu, P. Wang, and M. Yang, "A dimethyl disulfide gas sensor based on nanosized Pt-loaded tetrakaidecahedral alpha-Fe2O3 nanocrystals", *Nanotechnology*, vol. 33, no. 40, p. 405 502, Oct. 2022, ISSN: 0957-4484, 1361-6528. DOI: 10.1088/1361-6528/ac614c Accessed: Dec. 16, 2025.

[141] H.-R. Kim, A. Haensch, I.-D. Kim, N. Barsan, U. Weimar, and J.-H. Lee, "The Role of NiO Doping in Reducing the Impact of Humidity on the Performance of SnO2-Based Gas Sensors: Synthesis Strategies, and Phenomenological and Spectroscopic Studies", *Advanced Functional Materials*, vol. 21, no. 23, pp. 4456–4463, Dec. 2011, ISSN: 1616-301X, 1616-3028. DOI: 10.1002/adfm.201101154 Accessed: Jan. 26, 2024.

[142] K.-I. Choi, H.-J. Kim, Y. C. Kang, and J.-H. Lee, "Ultraselective and ultrasensitive detection of H2S in highly humid atmosphere using CuO-loaded SnO2 hollow spheres for real-time diagnosis of halitosis", *Sensors and Actuators B: Chemical*, vol. 194, pp. 371–376, Apr. 2014, ISSN: 09254005. DOI: 10.1016/j.snb.2013.12.111 Accessed: Jan. 26, 2024.

[143] Z. Gao, G. Song, X. Zhang, Q. Li, S. Yang, T. Wang, Y. Li, L. Zhang, L. Guo, and Y. Fu, "A facile PDMS coating approach to room-temperature gas sensors with high humidity resistance and long-term stability", *Sensors and Actuators B: Chemical*, vol. 325, p. 128 810, Dec. 2020, ISSN: 09254005. DOI: 10.1016/j.snb.2020.128810 Accessed: Jan. 26, 2024.

[144] J. Xia, C. Yuan, and S. Yanagida, "Novel Counter Electrode V2O5/Al for Solid Dye-Sensitized Solar Cells", *ACS Applied Materials & Interfaces*, vol. 2, no. 7, pp. 2136–2139, Jul. 2010, ISSN: 1944-8244, 1944-8252. DOI: 10.1021/am100380w Accessed: Jan. 26, 2024.

[145] Y. Wei, M. Li, J. Zheng, and C. Xu, "Structural characterization and electrical and optical properties of V2O5 films prepared via ultrasonic spraying", *Thin Solid Films*, vol. 534, pp. 446–451, May 2013, ISSN: 00406090. DOI: 10.1016/j.tsf.2013.01.093 Accessed: Jan. 26, 2024.

[146] A. Subrahmanyam, Y. Bharat Kumar Redd, and C. L. Nagendra, "Nano-vanadium oxide thin films in mixed phase for microbolometer applications", *Journal of Physics D: Applied Physics*, vol. 41, no. 19, p. 195 108, Oct. 2008, ISSN: 0022-3727, 1361-6463. DOI: 10.1088/0022-3727/41/19/195108 Accessed: Jan. 26, 2024.

[147] W. Wu, Y. Wang, X. Wang, Q. Chen, X. Wang, S. Yang, X. Liu, J. Guo, and Z. Yang, "ChemInform Abstract: Structure and Electrochemical Performance of FeF3 /V2O5 Composite Cathode Material for Lithium-Ion Battery.", *ChemInform*, vol. 41, no. 5, chin.201005009, Feb. 2010, ISSN: 0931-7597, 1522-2667. DOI: 10.1002/chin.201005009 Accessed: Jan. 26, 2024.

[148] A. A. Akl, "Thermal annealing effect on the crystallization and optical dispersion of sprayed V2O5 thin films", *Journal of Physics and Chemistry of Solids*, vol. 71, no. 3, pp. 223–229, Mar. 2010, ISSN: 00223697. DOI: 10.1016/j.jpcs.2009.11.009 Accessed: Jan. 26, 2024.

[149] T. K. Le, M. Kang, and S. W. Kim, "A review on the optical characterization of V2O5 micro-nanostructures", *Ceramics International*, vol. 45, no. 13, pp. 15 781–15 798, Sep. 2019, ISSN: 02728842. DOI: 10.1016/j.ceramint.2019.05.339 Accessed: Jan. 26, 2024.

[150] X. Zhao, Y. Yan, L. Mao, M. Fu, H. Zhao, L. Sun, Y. Xiao, and G. Dong, "A relationship between the V4+/V5+ ratio and the surface dispersion, surface acidity, and redox performance of V2O5–WO3/TiO2 SCR catalysts", *RSC Advances*, vol. 8, no. 54, pp. 31 081–31 093, 2018, ISSN: 2046-2069. DOI: 10.1039/C8RA02857E Accessed: Jan. 26, 2024.

[151] H. Wang, J. Bai, M. Dai, K. Liu, Y. Liu, L. Zhou, F. Liu, F. Liu, Y. Gao, X. Yan, and L. Geyu, "Visible light activated excellent NO2 sensing based on 2D/2D ZnO/g-C3N4 heterojunction composites", *Sensors and Actuators B: Chemical*, vol. 304, p. 127 287, Feb. 2020, ISSN: 09254005. DOI: 10.1016/j.snb.2019.127287 Accessed: Jan. 26, 2024.

[152] C. Zhang, X. Geng, H. Liao, C.-J. Li, and M. Debliquy, "Room-temperature nitrogen-dioxide sensors based on ZnO1-x coatings deposited by solution precursor plasma spray", *Sensors and Actuators B: Chemical*, vol. 242, pp. 102–111, Apr. 2017, ISSN: 09254005. DOI: 10.1016/j.snb.2016.11.024 Accessed: Jan. 26, 2024.

[153] S. Liang, X. He, F. Wang, W. Geng, X. Fu, J. Ren, and X. Jiang, "Highly sensitive humidity sensors based on LiCl–Pebax 2533 composite nanofibers via electrospinning", *Sensors and Actuators B: Chemical*, vol. 208, pp. 363–368, Mar. 2015, ISSN: 0925-4005. DOI: 10.1016/j.snb.2014.11.035 Accessed: Jan. 26, 2024.

[154] Q. Kuang, C. Lao, Z. L. Wang, Z. Xie, and L. Zheng, "High-Sensitivity Humidity Sensor Based on a Single SnO2 Nanowire", *Journal of the American Chemical Society*, vol. 129, no. 19, pp. 6070–6071, May 2007, ISSN: 0002-7863, 1520-5126. DOI: 10.1021/ja070788m Accessed: Jan. 26, 2024.

[155] I. J. Tadeo, R. Parasuraman, S. B. Krupanidhi, and A. M. Umarji, "Enhanced humidity responsive ultrasonically nebulised V2O5 thin films", *Nano Express*, vol. 1, no. 1, p. 010 005, Jun. 2020, ISSN: 2632-959X. DOI: 10.1088/2632-959X/ab779a Accessed: Jan. 26, 2024.

[156] M. S. Pawar, P. K. Bankar, M. A. More, and D. J. Late, "Ultra-thin V2O5 nanosheet based humidity sensor, photodetector and its enhanced field emission properties", *RSC Advances*, vol. 5, no. 108, pp. 88 796–88 804, 2015, ISSN: 2046-2069. DOI: 10.1039/C5RA17253E Accessed: Feb. 18, 2025.

[157] M. R. Charlotte and L. R. Viannie, "Tailoring vanadium pentoxide nanoparticles for humidity sensing: Impact of microwave annealing", *Journal of Materials Science*, vol. 59, no. 48, pp. 22 034–22 052, Dec. 2024, ISSN: 0022-2461, 1573-4803. DOI: 10.1007/s10853-024-10485-y Accessed: Feb. 18, 2025.

[158] S. Cho, S. H. Lim, J. Oh, T.-S. Ju, S. Yang, H. H. Kim, and Y. Kim, "Synthesis-in-place of V2O5 nanobelts for wide range humidity detection", *Sensors and Actuators B: Chemical*, vol. 423, p. 136 711, Jan. 2025, ISSN: 09254005. DOI: 10.1016/j.snb.2024.136711 Accessed: Feb. 18, 2025.

[159] A. Macagnano, E. Zampetti, and E. Kny, Eds., *Electrospinning for High Performance Sensors* (NanoScience and Technology). Cham: Springer International Publishing, 2015, ISBN: 978-3-319-14406-1. DOI: 10.1007/978-3-319-14406-1 Accessed: Dec. 3, 2025.

[160] J. Xie, J. Wang, and L. Xu, "One-Step Preparation of Hierarchical Structured Nanofibers Using Coaxial Electrospinning for Lithium-Ion Batteries", *ACS Applied Polymer Materials*, vol. 7, no. 17, pp. 10 965–10 980, Sep. 2025, ISSN: 2637-6105, 2637-6105. DOI: 10.1021/acsapm.5c02539 Accessed: Dec. 16, 2025.

[161] Z. Strassberger, E. V. Ramos-Fernandez, A. Boonstra, R. Jorna, S. Tanase, and G. Rothenberg, "Synthesis, characterization and testing of a new V2O5/Al2O3–MgO catalyst for butane dehydrogenation and limonene oxidation", *Dalton Transactions*, vol. 42, no. 15, p. 5546, 2013, ISSN: 1477-9226, 1477-9234. DOI: 10.1039/c3dt32954b Accessed: Jan. 26, 2024.

[162] K. M. Koczkur, S. Mourdikoudis, L. Polavarapu, and S. E. Skrabalak, "Polyvinylpyrrolidone (PVP) in nanoparticle synthesis", *Dalton Transactions*, vol. 44, no. 41, pp. 17 883–17 905, 2015, ISSN: 1477-9226, 1477-9234. DOI: 10.1039/C5DT02964C Accessed: Jan. 26, 2024.

[163] R. Berenguer, M. O. Guerrero-Pérez, I. Guzmán, J. Rodríguez-Mirasol, and T. Cordero, "Synthesis of Vanadium Oxide Nanofibers with Variable Crystallinity and V5+/V4+ Ratios", *ACS Omega*, vol. 2, no. 11, pp. 7739–7745, Nov. 2017, ISSN: 2470-1343, 2470-1343. DOI: 10.1021/acsomega.7b01061 Accessed: Jan. 26, 2024.

[164] A. L. Patterson, "The Scherrer Formula for X-Ray Particle Size Determination", *Physical Review*, vol. 56, no. 10, pp. 978–982, Nov. 1939, ISSN: 0031-899X. DOI: 10.1103/PhysRev.56.978 Accessed: Dec. 19, 2025.

[165] A. Monshi, M. R. Foroughi, and M. R. Monshi, "Modified Scherrer Equation to Estimate More Accurately Nano-Crystallite Size Using XRD", *World Journal of Nano Science and Engineering*, vol. 02, no. 03, pp. 154–160, 2012, ISSN: 2161-4954, 2161-4962. DOI: 10.4236/wjnse.2012.23020 Accessed: Jan. 26, 2024.

[166] J. I. Langford and A. J. C. Wilson, "Scherrer after sixty years: A survey and some new results in the determination of crystallite size", *Journal of Applied Crystallography*, vol. 11, no. 2, pp. 102–113, Apr. 1978, ISSN: 0021-8898. DOI: 10.1107/S0021889878012844 Accessed: Jan. 26, 2024.

[167] D. S. Doke, S. B. Khomane, S. L. Pandhare, M. K. Dongare, F. Dumeignil, and S. B. Umbarkar, "Vanadium-based highly active and selective catalysts for oxidative dehydrogenation of ethyl lactate to ethyl pyruvate", *Applied Catalysis A: General*, vol. 587, p. 117 246, Oct. 2019, ISSN: 0926860X. DOI: 10.1016/j.apcata.2019.117246 Accessed: Dec. 18, 2025.

[168] A. Katoch, G.-J. Sun, S.-W. Choi, J.-H. Byun, and S. S. Kim, "Competitive influence of grain size and crystallinity on gas sensing performances of ZnO nanofibers", *Sensors and Actuators B: Chemical*, vol. 185, pp. 411–416, Aug. 2013, ISSN: 09254005. DOI: 10.1016/j.snb.2013.05.030 Accessed: Feb. 8, 2026.

[169] G. Korotcenkov, "Electrospun Metal Oxide Nanofibers and Their Conductometric Gas Sensor Application. Part 1: Nanofibers and Features of Their Forming", *Nanomaterials*, vol. 11, no. 6, p. 1544, Jun. 2021, ISSN: 2079-4991. DOI: 10.3390/nano11061544 Accessed: Jan. 26, 2024.

[170] J. U. Keller and R. Staudt, *Gas Adsorption Equilibria: Experimental Methods and Adsorptive Isotherms*. Boston: Springer, 2005, ISBN: 978-0-387-23598-1. Accessed: Mar. 15, 2025.

[171] J. Rouquerol, D. Avnir, C. W. Fairbridge, D. H. Everett, J. H. Haynes, N. Pernicone, J. D. F. Ramsay, K. S. W. Sing, and K. K. Unger, "Recommendations for the Characterization of Porous Solids", De Gruyter, Tech. Rep. DOI: 10.1515/iupac.66.0925 Accessed: Dec. 19, 2025.

[172] H. Liu, P. He, Z. Li, D. Sun, H. Huang, J. Li, and G. Zhu, "Crystalline Vanadium Pentoxide with Hierarchical Mesopores and Its Capacitive Behavior", *Chemistry – An Asian Journal*, vol. 1, no. 5, pp. 701–706, Nov. 2006, ISSN: 1861-4728, 1861-471X. DOI: 10.1002/asia.200600169 Accessed: Jan. 26, 2024.

[173] J. Liang, K. Zhu, R. Yang, and M. Hu, "Room temperature NO2 sensing properties of Au-decorated vanadium oxide nanowires sensor", *Ceramics International*, vol. 44, no. 2, pp. 2261–2268, Feb. 2018, ISSN: 02728842. DOI: 10.1016/j.ceramint.2017.10.186 Accessed: Dec. 29, 2025.

[174] J. Qian, Z. Peng, Z. Shen, Z. Zhao, G. Zhang, and X. Fu, "Positive impedance humidity sensors via single-component materials", *Scientific Reports*, vol. 6, no. 1, p. 25 574, May 2016, ISSN: 2045-2322. DOI: 10.1038/srep25574 Accessed: Nov. 2, 2023.

[175] R. Schaub, P. Thostrup, N. Lopez, E. Lægsgaard, I. Stensgaard, J. K. Nørskov, and F. Besenbacher, "Oxygen Vacancies as Active Sites for Water Dissociation on Rutile TiO 2 (110)", *Physical Review Letters*, vol. 87, no. 26, p. 266 104, Dec. 2001, ISSN: 0031-9007, 1079-7114. DOI: 10.1103/PhysRevLett.87.266104 Accessed: Nov. 2, 2023.

[176] S. Wendt, R. Schaub, J. Matthiesen, E. Vestergaard, E. Wahlström, M. Rasmussen, P. Thostrup, L. Molina, E. Lægsgaard, I. Stensgaard, B. Hammer, and F. Besenbacher, "Oxygen vacancies on TiO2(110) and their interaction with H2O and O2: A combined high-resolution STM and DFT study", *Surface Science*, vol. 598, no. 1-3, pp. 226–245, Dec. 2005, ISSN: 00396028. DOI: 10.1016/j.susc.2005.08.041 Accessed: Nov. 2, 2023.

[177] S. Tachibana, Y.-F. Wang, T. Sekine, Y. Takeda, J. Hong, A. Yoshida, M. Abe, R. Miura, Y. Watanabe, D. Kumaki, and S. Tokito, "A Printed Flexible Humidity Sensor with High Sensitivity and Fast Response Using a Cellulose Nanofiber/Carbon Black Composite", *ACS Applied Materials & Interfaces*, vol. 14, no. 4, pp. 5721–5728, Feb. 2022, ISSN: 1944-8244, 1944-8252. DOI: 10.1021/acsami.1c20918 Accessed: Nov. 2, 2023.

[178] A. Mansoori, S. Ahmad, S. Bansal, and M. Vashishath, "Flexible Graphite-Based Humidity Sensor Using Green Technology", *ECS Sensors Plus*, vol. 1, no. 4, p. 044 401, Dec. 2022, ISSN: 2754-2726. DOI: 10.1149/2754-2726/acadee Accessed: Nov. 2, 2023.

[179] A. Yoshida, Y.-F. Wang, S. Tachibana, A. Hasegawa, T. Sekine, Y. Takeda, J. Hong, D. Kumaki, T. Shiba, and S. Tokito, "Printed, all-carbon-based flexible humidity sensor using a cellulose nanofiber/graphene nanoplatelet composite", *Carbon Trends*, vol. 7, p. 100 166, Apr. 2022, ISSN: 26670569. DOI: 10.1016/j.cartre.2022.100166 Accessed: Nov. 2, 2023.

[180] B. Zhao, V. S. Sivasankar, S. K. Subudhi, A. Dasgupta, and S. Das, "Printed Carbon Nanotube-Based Humidity Sensors Deployable on Surfaces of Widely Varying Curvatures", *ACS Applied Nano Materials*, vol. 6, no. 2, pp. 1459–1474, Jan. 2023, ISSN: 2574-0970, 2574-0970. DOI: 10.1021/acsanm.2c05423 Accessed: Nov. 2, 2023.

[181] Z.-H. Duan, Q.-N. Zhao, C.-Z. Li, S. Wang, Y.-D. Jiang, Y.-J. Zhang, B.-H. Liu, and H.-L. Tai, "Enhanced positive humidity sensitive behavior of p-reduced graphene oxide decorated with n-WS2 nanoparticles", *Rare Metals*, vol. 40, no. 7, pp. 1762–1767, Jul. 2021, ISSN: 1001-0521, 1867-7185. DOI: 10.1007/s12598-020-01524-z Accessed: Nov. 2, 2023.

[182] I. Raible, M. Burghard, U. Schlecht, A. Yasuda, and T. Vossmeyer, "V2O5 nanofibres: Novel gas sensors with extremely high sensitivity and selectivity to amines", *Sensors and Actuators B: Chemical*, vol. 106, no. 2, pp. 730–735, May 2005, ISSN: 09254005. DOI: 10.1016/j.snb.2004.09.024 Accessed: Mar. 10, 2025.

[183] S. Indhumathi, M. Manoj Cristopher, P. Karthick, M. Dhivya Pushpa, B. Poornima, C. Gopalakrishnan, and K. Jeyadheepan, "Synthesis of stable and highly oxygen deficient V2O5 thin films for physical functionalization of nanofiltration membranes", *Materials Science in Semiconductor Processing*, vol. 100, pp. 185–191, Sep. 2019, ISSN: 13698001. DOI: 10.1016/j.mssp.2019.04.048 Accessed: Feb. 20, 2026.

[184] W.-H. Liao, Z.-J. Huang, Y.-L. Pan, and C.-L. Hsu, "High-Sensitivity MEMS Ethanol Gas Sensors Based on Laser-Machined Glass Substrates and Electrospun p-NiO Doped n-V2O5 Nanofibers", *IEEE Sensors Journal*, vol. 25, no. 7, pp. 10 594–10 601, Apr. 2025, ISSN: 1530-437X, 1558-1748, 2379-9153. DOI: 10.1109/JSEN.2025.3542249 Accessed: Feb. 20, 2026.

[185] M. Tonezzer and L. Van Duy, "Gas Sensors", in *Encyclopedia of Sensors and Biosensors*, Elsevier, 2023, pp. 185–208, ISBN: 978-0-12-822549-3. DOI: 10.1016/B978-0-12-822548-6.00113-8 Accessed: Oct. 26, 2023.

[186] J. A. Holme, E. Øya, A. K. J. Afanou, J. Øvrevik, and W. Eduard, "Characterization and pro-inflammatory potential of indoor mold particles", *Indoor Air*, vol. 30, no. 4, pp. 662–681, Jul. 2020, ISSN: 0905-6947, 1600-0668. DOI: 10.1111/ina.12656 Accessed: Dec. 29, 2025.

[187] L. Empting, "Neurologic and neuropsychiatric syndrome features of mold and mycotoxin exposure", *Toxicology and Industrial Health*, vol. 25, no. 9-10, pp. 577–581, Oct. 2009, ISSN: 0748-2337, 1477-0393. DOI: 10.1177/0748233709348393 Accessed: Dec. 29, 2025.

[188] K. Tucker, J. L. Stolze, A. H. Kennedy, and N. P. Money, "Biomechanics of conidial dispersal in the toxic mold Stachybotrys chartarum", *Fungal Genetics and Biology*, vol. 44, no. 7, pp. 641–647, Jul. 2007, ISSN: 10871845. DOI: 10.1016/j.fgb.2006.12.007 Accessed: Jan. 9, 2026.

[189] X. Wang, L. Lombard, J. Groenewald, J. Li, S. Videira, R. Samson, X. Liu, and P. Crous, "Phylogenetic reassessment of the Chaetomium globosum species complex", *Persoonia - Molecular Phylogeny and Evolution of Fungi*, vol. 36, no. 1, pp. 83–133, Jun. 2016, ISSN: 0031-5850. DOI: 10.3767/003158516X689657 Accessed: Jan. 9, 2026.

[190] J. Xie and Z. Qiu, "The effect of imbalanced data sets on LDA: A theoretical and empirical analysis", *Pattern Recognition*, vol. 40, no. 2, pp. 557–562, Feb. 2007, ISSN: 00313203. DOI: 10.1016/j.patcog.2006.01.009 Accessed: Feb. 7, 2024.

[191] A. Zulkefli, B. Mukherjee, R. Sahara, R. Hayakawa, T. Iwasaki, Y. Wakayama, and S. Nakaharai, "Enhanced Selectivity in Volatile Organic Compound Gas Sensors Based on ReS2-FETs under Light-Assisted and Gate-Bias Tunable Operation", *ACS Applied Materials & Interfaces*, vol. 13, no. 36, pp. 43 030–43 038, Sep. 2021, ISSN: 1944-8244, 1944-8252. DOI: 10.1021/acsami.1c10054 Accessed: Jan. 8, 2025.

[192] B. Sharma, A. Sharma, and J.-S. Kim, "Recent advances on H2 sensor technologies based on MOX and FET devices: A review", *Sensors and Actuators B: Chemical*, vol. 262, pp. 758–770, Jun. 2018, ISSN: 09254005. DOI: 10.1016/j.snb.2018.01.212 Accessed: Jan. 26, 2024.

[193] S. Hong, M. Wu, Y. Hong, Y. Jeong, G. Jung, W. Shin, J. Park, D. Kim, D. Jang, and J.-H. Lee, "FET-type gas sensors: A review", *Sensors and Actuators B: Chemical*, vol. 330, p. 129 240, Mar. 2021, ISSN: 09254005. DOI: 10.1016/j.snb.2020.129240 Accessed: Jan. 12, 2022.

[194] S. Zhang, Z. Yuan, and F. Meng, "Electronic Nose Under Dynamic Temperature Modulation for Highly Selective Identification of Industrial Toxic Chemicals", *IEEE Transactions on Instrumentation and Measurement*, vol. 74, pp. 1–11, 2025, ISSN: 0018-9456, 1557-9662. DOI: 10.1109/TIM.2025.3588944 Accessed: Nov. 23, 2025.

[195] Y. Jiang, H. Tai, G. Xie, and J. Yu, "Fabrication and NO2 sensing properties of ChemFET sensors with self-assembly PAN/PSSA sensitive films based on nano-Au surface", in *Sixth International Conference on Thin Film Physics and Applications*, Shanghai, China, Feb. 2008, 69843Q. DOI: 10.1117/12.792244 Accessed: Jan. 10, 2025.

[196] J. Sengupta and C. M. Hussain, "Graphene-based field-effect transistor biosensors for the rapid detection and analysis of viruses: A perspective in view of COVID-19", *Carbon Trends*, vol. 2, p. 100 011, Jan. 2021, ISSN: 26670569. DOI: 10.1016/j.cartre.2020.100011 Accessed: Jan. 10, 2025.

[197] A. Lale, A. Grappin, L. Mazenq, D. Bourrier, A. Lecestre, J. Launay, and P. Temple-Boyer, "Development of All-Around SiO2/Al2O3 Gate, Suspended Silicon Nanowire Chemical Field Effect Transistors Si-nw-ChemFET", in *Proceedings of Eurosensors 2017, Paris, France, 3–6 September 2017*, MDPI, Aug. 2017, p. 419. DOI: 10.3390/proceedings1040419 Accessed: Jan. 10, 2025.

[198] S. V. Kalinin, J. Shin, S. Jesse, D. Geohegan, A. P. Baddorf, Y. Lilach, M. Moskovits, and A. Kolmakov, "Electronic transport imaging in a multiwire SnO2 chemical field-effect transistor device", *Journal of Applied Physics*, vol. 98, no. 4, p. 044 503, Aug. 2005, ISSN: 0021-8979, 1089-7550. DOI: 10.1063/1.2001144 Accessed: Jan. 12, 2022.

[199] S. Shah, S. Hussain, S. T. U. Din, A. Shahid, J. N. O. Amu-Darko, M. Wang, Y. Tianyan, G. Liu, and G. Qiao, "A review on In2O3 nanostructures for gas sensing applications", *Journal of Environmental Chemical Engineering*, vol. 12, no. 3, p. 112 538, Jun. 2024, ISSN: 22133437. DOI: 10.1016/j.jece.2024.112538 Accessed: Jan. 20, 2025.

[200] A. Chizhov, P. Kutukov, A. Astafiev, and M. Rumyantseva, "Photoactivated Processes on the Surface of Metal Oxides and Gas Sensitivity to Oxygen", *Sensors*, vol. 23, no. 3, p. 1055, Jan. 2023, ISSN: 1424-8220. DOI: 10.3390/s23031055 Accessed: Oct. 31, 2023.

[201] N. Devabharathi, J. R. Pradhan, S. S. Priyadarsini, T. Brezesinski, and S. Dasgupta, "Inkjet-Printed Narrow-Channel Mesoporous Oxide-Based n-Type TFTs and All-Oxide CMOS Electronics", *Advanced Materials Interfaces*, vol. 9, no. 25, p. 2 200 949, Sep. 2022, ISSN: 2196-7350, 2196-7350. DOI: 10.1002/admi.202200949 Accessed: Apr. 23, 2024.

[202] L. Zhu, G. He, J. Lv, E. Fortunato, and R. Martins, "Fully solution-induced high performance indium oxide thin film transistors with ZrOx high-k gate dielectrics", *RSC Advances*, vol. 8, no. 30, pp. 16 788–16 799, 2018, ISSN: 2046-2069. DOI: 10.1039/C8RA02108B Accessed: Apr. 23, 2024.

[203] C.-H. Choi, S.-Y. Han, Y.-W. Su, Z. Fang, L.-Y. Lin, C.-C. Cheng, and C.-h. Chang, "Fabrication of high-performance, low-temperature solution processed amorphous indium oxide thin-film transistors using a volatile nitrate precursor", *Journal of Materials Chemistry C*, vol. 3, no. 4, pp. 854–860, 2015, ISSN: 2050-7526, 2050-7534. DOI: 10.1039/C4TC01568A Accessed: Apr. 23, 2024.

[204] H. Lee, X. Zhang, J. Kim, E.-J. Kim, and J. Park, "Investigation of the Electrical Characteristics of Bilayer ZnO/In2O3 Thin-Film Transistors Fabricated by Solution Processing", *Materials*, vol. 11, no. 11, p. 2103, Oct. 2018, ISSN: 1996-1944. DOI: 10.3390/ma11112103 Accessed: Aug. 8, 2023.

[205] R. Yao, X. Fu, W. Li, S. Zhou, H. Ning, B. Tang, J. Wei, X. Cao, W. Xu, and J. Peng, "Bias Stress Stability of Solution-Processed Nano Indium Oxide Thin Film Transistor", *Micromachines*, vol. 12, no. 2, p. 111, Jan. 2021, ISSN: 2072-666X. DOI: 10.3390/mi12020111 Accessed: Aug. 8, 2023.

[206] M. Nazarzadehmoafi, "Electronic properties of metal-In2O3 interfaces", May 2017. DOI: 10.18452/17771 Accessed: Oct. 3, 2023.

[207] D. Chen, Y. Jiang, Z. Sun, Y. Huang, J. Yu, and T. Chen, "ITO/Ag/ITO and ITO/Cu/ITO transparent rear contacts for semi-transparent perovskite solar cells", *Thin Solid Films*, vol. 752, p. 139 252, Jun. 2022, ISSN: 00406090. DOI: 10.1016/j.tsf.2022.139252 Accessed: Jan. 17, 2025.

[208] S. Kim, J.-H. Jang, and J.-S. Lee, "Thermally Stable and Highly Reflective ITO/Ag-Based Ohmic Contacts to p-GaN", *Journal of The Electrochemical Society*, vol. 154, no. 11, H973, 2007, ISSN: 00134651. DOI: 10.1149/1.2778862 Accessed: Jan. 17, 2025.

[209] M. Si, Y. Hu, Z. Lin, X. Sun, A. Charnas, D. Zheng, X. Lyu, H. Wang, K. Cho, and P. D. Ye, "Why In2O3 Can Make 0.7 nm Atomic Layer Thin Transistors", *Nano Letters*, vol. 21, no. 1, pp. 500–506, Jan. 2021, ISSN: 1530-6984, 1530-6992. DOI: 10.1021/acs.nanolett.0c03967 Accessed: Jan. 5, 2026.

[210] S. A. Singaraju, T. T. Baby, F. Neuper, R. Kruk, J. A. Hagmann, H. Hahn, and B. Breitung, "Development of Fully Printed Electrolyte-Gated Oxide Transistors Using Graphene Passive Structures", *ACS Applied Electronic Materials*, vol. 1, no. 8, pp. 1538–1544, Aug. 2019, ISSN: 2637-6113, 2637-6113. DOI: 10.1021/acsaelm.9b00313 Accessed: Jan. 12, 2022.

[211] S. A. Singaraju, G. C. Marques, P. Gruber, R. Kruk, H. Hahn, B. Breitung, and J. Aghassi-Hagmann, "Fully Printed Inverters using Metal-Oxide Semiconductor and Graphene Passives on Flexible Substrates", *physica status solidi (RRL) – Rapid Research Letters*, vol. 14, no. 9, p. 2 000 252, Sep. 2020, ISSN: 1862-6254, 1862-6270. DOI: 10.1002/pssr.202000252 Accessed: Jan. 12, 2022.

[212] S. A. Singaraju, "Development of Fully Printed Oxide Electronics for Flexible Substrates", Ph.D. dissertation, Karlsruher Institute of Technology (KIT), Karlsruhe, 2021. DOI: 10.5445/IR/1000131808

[213] "Metalon JS-A221AE - Technical Datasheet", Optomec Inc., Technical Datasheet. Accessed: Jan. 5, 2026.

[214] *EPDM & FKM Chemical Resistance Guide*, Ontario, Canada, 2020. Accessed: Mar. 2, 2026.

[215] C. Feng, X. Li, C. Wang, Y. Sun, J. Zheng, and G. Lu, "Facile synthesis benzene sensor based on V2O5-doped SnO2 nanofibers", *RSC Adv.*, vol. 4, no. 88, pp. 47 549–47 555, Sep. 2014, ISSN: 2046-2069. DOI: 10.1039/C4RA06120A Accessed: Feb. 3, 2026.

[216] D. Hu, B. Han, R. Han, S. Deng, Y. Wang, Q. Li, and Y. Wang, "SnO2 nanorods based sensing material as an isopropanol vapor sensor", *New Journal of Chemistry*, vol. 38, no. 6, p. 2443, 2014, ISSN: 1144-0546, 1369-9261. DOI: 10.1039/c3nj01482g Accessed: Feb. 2, 2026.

[217] C. Li, M. Lv, J. Zuo, and X. Huang, "SnO2 Highly Sensitive CO Gas Sensor Based on Quasi-Molecular-Imprinting Mechanism Design", *Sensors*, vol. 15, no. 2, pp. 3789–3800, Feb. 2015, ISSN: 1424-8220. DOI: 10.3390/s150203789 Accessed: Feb. 2, 2026.

[218] Y. Bai, H. Fu, X. Yang, S. Xiong, S. Li, and X. An, "Conductometric isopropanol gas sensor: Ce-doped In2O3 nanosheet-assembled hierarchical microstructure", *Sensors and Actuators B: Chemical*, vol. 377, p. 133 007, Feb. 2023, ISSN: 09254005. DOI: 10.1016/j.snb.2022.133007 Accessed: Feb. 3, 2026.

[219] D. S. Gavaskar, P. Nagaraju, and M. R. Reddy, "Investigations on RuO2–In2O3 nanostructured porous composite thin films for benzene detection", *Microporous and Mesoporous Materials*, vol. 345, p. 112 247, Nov. 2022, ISSN: 13871811. DOI: 10.1016/j.micromeso.2022.112247 Accessed: Feb. 4, 2026.

[220] Y. H. Ngo, M. Brothers, J. A. Martin, C. C. Grigsby, K. Fullerton, R. R. Naik, and S. S. Kim, "Chemically Enhanced Polymer-Coated Carbon Nanotube Electronic Gas Sensor for Isopropyl Alcohol Detection", *ACS Omega*, vol. 3, no. 6, pp. 6230–6236, Jun. 2018, ISSN: 2470-1343, 2470-1343. DOI: 10.1021/acsomega.8b01039 Accessed: Feb. 3, 2026.

[221] R. Cao, Z. Lu, J. Hu, and Y. Zhang, "Carbon-Based FET-Type Gas Sensor for the Detection of ppb-Level Benzene at Room Temperature", *Chemosensors*, vol. 12, no. 9, p. 179, Sep. 2024, ISSN: 2227-9040. DOI: 10.3390/chemosensors12090179 Accessed: Feb. 3, 2026.

[222] K. Datta, P. Ghosh, A. Rushi, A. Mulchandani, and M. Shirsat, "Fe nanoparticle tailored poly(N-methyl pyrrole) nanowire matrix: A CHEMFET study from the perspective of discrimination among electron donating analytes", *Journal of Physics D: Applied Physics*, vol. 48, no. 19, p. 195 301, Mar. 2015, ISSN: 0022-3727, 1361-6463. DOI: 10.1088/0022-3727/48/19/195301 Accessed: Feb. 3, 2026.

[223] H. Li, Q. Wang, L. Han, Z. Chen, G. Wang, Q. Wang, S. Ma, B. Ai, and G. Xi, "Quality characterization of tobacco flavor and tobacco leaf position identification based on homemade electronic nose", *Scientific Reports*, vol. 14, no. 1, p. 19 229, Aug. 2024, ISSN: 2045-2322. DOI: 10.1038/s41598-024-70180-5 Accessed: Mar. 2, 2026.

Acknowledgements

This dissertation would not have been possible without the support, guidance, and contributions of numerous individuals. Therefore, I express my deepest gratitude to all those who have accompanied me on this journey.

- First and foremost, I would like to thank my doctoral supervisor, Prof. Dr. Uli Lemmer (LTI), for his invaluable guidance, encouragement, and both organizational and financial support throughout all stages of this work. His expertise and mentorship, combined with the research freedom he granted me, created an ideal framework for my professional and personal development. I am especially grateful for his insightful feedback and detailed revisions, which have significantly enhanced the quality and coherence of all my works.
- I am also grateful to Prof. Dr. Manfred Kohl (IMT) for agreeing to act as my second referee and for his organizational assistance.
- My profound appreciation also extends to Dr. Martin Sommer, my topical supervisor at IMT, for his dedicated scientific supervision and continuous engagement with my research since my master's thesis. Drawing on his deep expertise, he provided valuable advice and suggestions on methodological precision and critical reasoning, ensuring scientific rigor, especially regarding the eNose topic. His detailed comments and revisions contributed substantially to the refinement of this work and the publications.

This research would not have been possible without the extensive collaborations with colleagues at KIT, to which I am deeply grateful.

- Special gratitude goes to Bharat (IMT) for his collaborative work on electrospinning, for his guidance and support on my first publication.
- I would like to thank my LTI colleagues Qiaoshuang and Jan for the introduction to and collaboration on IJP. I am also grateful to my INT colleagues, Surya, Pooja, Merve, and Dr. Gabriel Cadilha Marques, for sharing their expertise in inkjet-printed electronics and for allowing me to use many of their devices.
- I am grateful to Robert (LTI) and Georg (IHE) for sharing their deep knowledge regarding AJP.
- Special thanks go to Orlando (LTI) and Jan for their assistance with SEM imaging.
- I am grateful to Vanessa Trioulliet (IMT) for her assistance with XPS measurements.

- I would like to acknowledge the contributions of the students I had the pleasure of supervising: Guanfeng, Tianqi, Yijin M., and Thilo. Their enthusiasm and hard work enriched this research, and I hope they gained as much from our collaboration as I did.
- Especially regarding this thesis, I would like to thank my LTI colleagues Yujing, Jiaqi, Jan, Klaus, Mohamed, and Orlando for their invaluable comments and revisions.

The technical infrastructure that supported this research would not have been possible without the dedicated work of several colleagues.

- I am grateful to Hans and Mario Sütsch from LTI, and Alexandra Moritz from the IMT workshop, for their technical support and for machining complex parts.
- I also thank Achim Voigt (IMT) for his electrical support and for providing devices and components.
- I thank Felix Geiselhöringer (LTI) for always providing swift organizational assistance.
- I thank Christian, Julian, and Reza for maintaining LTI's cleanroom — a never-ending mammoth task — and also for their operational support.

Additionally, I would like to thank and acknowledge the many external collaborators I had the privilege to work with outside of KIT.

- I thank the eNose veterans, Benjamin (SEMLLDECT GmbH) and Ilia (Breitmeier Messtechnik GmbH), for their insightful expertise and the numerous fruitful discussions.
- I also thank Stefanie (domatec GmbH) for her experimental work and expertise regarding mold cultivations.

I am grateful to the excellence cluster 3DMM2O for the funding, as well as for the many beneficial and practical events, including young scientist meetings, scientific modules, and management modules.

At last, I would like to thank all the wonderful people with whom I had the privilege to share my time and many memorable moments throughout this journey.

- My friends inside and outside of KIT have made everyday life enjoyable and sustainable. During the week, I always looked forward to sharing my lunchtime with the LTI lunch group, including Jiaqi, Qiaoshuang, Yujing, Andres, Jan, Julian, Klaus, Leo, Nils, Orlando, Qihao, and Robert. During my occasional stays at IMT, I also thank Stefan for the many coffee and lunch sessions. I thank my LTI colleagues Lingyi, Yijin W., and Andres for the various fun yet challenging sports activities. Outside of KIT, I thank all my close friends for maintaining and strengthening our wonderful bonds, for our unforgettable gatherings and adventures, and for your moving encouragements.
- I owe my deepest gratitude to Isabelle, my loving partner, for her unwavering support, patience, and understanding throughout this journey, in both its highs and lows. Despite her busy schedule, she often willingly sacrificed her time to assist me in my endeavors without expecting anything in return.

- Finally, I would like to thank my whole family for their constant love, support, encouragement, and belief in me, which extends far beyond the timeframe of my doctoral research. They always nurtured my curiosity, supported my choices, and encouraged me to pursue my own path. Their willingness to provide a place of retreat, rest, and comfort during challenging phases has been invaluable in the long run. It is truly a privilege to have them as my family, and I feel especially motivated and driven to honour their selfless efforts and unwavering support.

Again, to all mentioned here and to those I may have inadvertently omitted, thank you for being part of this journey.